Wissenschaftliche Mitteilungen

aus dem
Institut für Meteorologie der Universität Leipzig
und dem
Institut für Troposphärenforschung e. V. Leipzig

ISBN 3-9804089-8-1

Meteorologische Arbeiten aus Leipzig (III)

Hrsg.: A. Raabe, K. Arnold, J. Heintzenberg

Leipzig 1998

Band 9

Inhaltsverzeichnis

Wissenschaftliche Mitteilungen aus dem Institut für Meteorologie der Universität Leipzig und dem Institut für Troposphärenforschung e.V. Leipzig, Band 9

Kürzestfristvorhersage der Windgeschwindigkeit in einem Wirbelschleppenwarnsystem für Flughäfen

Uwe Schlink, Gerd Tetzlaff

Zusammenfassung:

Die lange Lebensdauer und die hohe Intensität der Wirbelschleppen landender Großraumflugzeuge kann zu einer Gefährdung des nachfolgenden Verkehrs führen. Zur Vorhersage einer gefährdungsfreien Nutzungszeit der Landebahn, nach der die Staffelungsabstände der landenden Flugzeuge bestimmt werden, dient ein Wirbelschleppenwarnsystem. Ein wesentlicher Teil dieses Warnsystems ist die Vorhersage des quer zur Landebahn wehenden Windes. Dafür wird bisher ein auf Persistenz beruhendes Verfahren eingesetzt. Die vorliegende Arbeit zeigt, daß durch Verwendung eines autoregressiven Modells die Querwindprognose verbessert werden kann. Dazu werden die Meßdaten analysiert und die Modellparameter geschätzt. Der Einsatz der AR Prognose im Wirbelschleppenwarnsystem führt im Vergleich zur bisherigen Methode zu längeren Nutzungszeiten und vermeidet das Auftreten von Diskontinuitäten (Sprüngen) in der Vorhersage. Besonders durch letzteres wird die Akzeptanz des Warnsystems bei den Fluglotsen verbessert.

Summary:

Wake vortices of landing heavy aircraft are intensive and show long life time. They are thus capable to endanger following air traffic. The prediction of the propagation paths of wake vortices can help to identify time intervals in which it is possible to use the parallel runways independently. The wake vortex warning system has the purpose to produce such predictions. The major predictor is the wind component perpendicular to the runway. The short prediction period makes the use of the persistency for the warning system plausible. The performance of such simple prediction methods can be improved by using an autoregressive method (AR). To find the relevant parameters a data set of wind data comprising about two years observations was used. The AR-based predictions as a wake vortex warning system improves the quality of the prediction, makes them more continuous avoiding prediction jumps, and finally allows longer periods of independent use of the parallel runways.

Einleitung

Die starke Abhängigkeit des Luftverkehrs von den Wetterbedingungen wird an der Präsenz der Flughafenmeteorologen deutlich. Sie veröffentlichen Vorhersagen über die meteorologischen Bedingungen in der unmittelbaren Umgebung des Airports (Gordon, 1992). Aber auch die Flugzeuge selbst beeinflussen die Strömungs- verhältnisse direkt an der Landebahn. Jedes Flugzeug erzeugt ein Paar stark rotierender Wirbel. Sie werden als Wirbelschleppe bezeichnet und breiten sich im Nachlauf aus. Besonders bei Großraumflugzeugen kann die Intensität der beiden innerhalb der Wirbelschleppe enthaltenen Wirbelkerne so groß sein, daß nachfolgende Flugzeuge beim Einfliegen in diese Turbulenzkörper beschädigt werden oder sogar abstürzen. Einer Studie aus dem Jahre 1977 zufolge traten im Zeitraum von 1964-73 in den USA immerhin 86 Flugunfälle auf, die auf den Einfluß der Wirbelschleppen zurückzuführen waren (Franke, 1995).

Die lange Lebensdauer der Wirbelschleppen und ihre Ausbreitung in Bodennähe führen dazu, daß es nicht nur zu einer Gefährdung hintereinanderfliegender Flugzeuge kommt, sondern daß auch seitlich versetzt fliegende Maschinen durch die Wirbelschleppen in Mitleidenschaft gezogen werden können. Besonders bei dicht aneinandergrenzenden Landebahnen kommt es zu einer starken Beeinflussung durch driftende Wirbelschleppen. Deshalb müssen auch hier gegebenenfalls Staffelungsabstände eingehalten werden, was jedoch zu Kapazitätsproblemen an den betroffenen Flughäfen führen kann. Insbesondere an großen Flughäfen bedeutet Flugverkehrsplanung eine Mangelverwaltung von verfügbaren Start- und Landezeiten. Durch Zeitverzögerungen werden Zusatzkosten verursacht. Die Errichtung neuer Landebahnen ist aus geographischen, ökologischen und finanziellen Gründen nicht immer möglich.

Verbesserungen sind also im Wesentlichen nur über eine optimierte Flugverkehrs- kontrolle zu erreichen. Das bedeutet, den Anflugverkehr so zu steuern, daß Wartezeiten vermieden werden und eine maximale Nutzungszeit entsteht. Bei zu diesem Zweck verringerten Staffelungsabständen beim Landeanflug müssen jedoch die von den Wirbelschleppen ausgehenden Gefahren berücksichtigt werden.

Aus diesem Grund wurde ein Wirbelschleppenwarnsystem entwickelt (Franke, 1995). Dabei wurden das Wirbelverhalten innerhalb der atmosphärischen Grenzschicht analysiert und die für die Wirbelverlagerung wichtigen Einflußgrößen erfaßt. Der Prognosealgorithmus dieses Warnsystems ermittelt für Vorhersage- zeiträume von etwa 10 Minuten die maximal möglichen Wanderweiten. Das verwendete Wirbelverlagerungsmodell geht von einer Aufspaltung der Problemstellung in zwei Teilaufgaben aus. Einerseits muß eine Vorhersage der Wirbellebensdauer erfolgen. Zum anderen ist eine Prognose der quer zur Landebahn gerichteten Windkomponente erforderlich. Diese Kurzzeitvorhersage der 2-Minuten-Mittelwerte der Querwindgeschwindigkeit wird bei Franke (1995) mit einem Persistenzmodell mit Weibull-verteiltem Sicherheitszuschlag realisiert.

Die hier vorgestellten Untersuchungen hatten das Ziel, diese Querwindprognose zu verbessern. Dabei mußte man davon ausgehen, daß neben synoptischen Einflüssen lokale Effekte sehr dominierend sind. Letztere umfassen z.B. Stömungseffekte, die durch die Orographie und das Bodenprofil bedingt sind (Otruba et al., 1988) und die thermische Konvektion. Da die Natur der Einflußgrößen sehr vielgestaltig und komplex ist, ist zu erwarten, daß zur Vorhersage ein pragmatischer Ansatz geeignet ist, der lediglich die in der Zeitserie der Winddaten enthaltene Information nutzt (Ding et al., 1996). Wie die Analyse der Datenserien zeigt, kann dabei über ein reines Persistenzmodell hinausgegangen werden. Das entwickelte autoregressive Modell wird im Rahmen des vorhandenen Wirbelschleppenwarnsystems getestet und die Nutzungsdauer berechnet. Die gefundenen Ergebnisse werden mit den von Franke (1995) angegebenen verglichen.

Datenanalyse

Die verwendeten Ausgangsdaten wurden während verschiedener Meßkampagnen in den Jahren 1984 bis 1996 am Flughafen Fankfurt/Main beobachtet. Dazu wurde eine Kette von Propelleranemometern verwendet, deren Meßgenauigkeit ±0.05m/s und deren Anlaufgeschwindigkeit etwa 0.2m/s betrug. Jeweils drei Propeller- anemometer waren rechtwinklig zueinander am Ende eines der 7 Masten in einer Höhe von 10..12 m angebracht. Die Windgeschwindigkeiten der drei Richtungen wurden kontinuierlich registriert und von einem Datalogger mit einer Tastrate von 3Hz digitalisiert. Schließlich wurde jede Komponente über alle 7 Meßpunkte und 2 Minuten gemittelt. Für die Windvorhersage wurden die Zeitreihen von 2-Minuten-Mittelwerten des Querwindes verwendet (Abb. 1). Normalerweise sind Fluktuationen der Windgeschwindigkeit innerhalb von einigen Minuten das Ergebnis thermischer Konvektion oder durch

Wirbelerscheinungen verursacht, die an Hindernissen entstehen. Letztere würden charakteristische Frequenzen im Spektrum der Windgeschwindigkeit zur Folge haben. Solche Hindernisse existieren natürlich in der unmittelbaren Umgebung eines Flughafens nicht. Dies erklärt, daß im Frequenzspektrum ausgeprägte Zyklen nicht erkennbar sind (Abb. 4). Jedoch kann man an der Autokorrelationsfunktion (Abb. 2) erkennen, daß die Daten sehr stark autokorreliert sind. Erst nach einem Lag von etwa 200 Werten (entspricht 6,7 Stunden) sinkt die Autokorrelation in den Konfidenzbereich für den Wert Null. Eine näherungsweise Beschreibung für empirische autokorrelierte Reihen gelingt häufig durch die von Box & Jenkins (1976) entwickelten linearen ARIMA[p,d,q]-Modelle (autoregressive integrated moving average). Die Modellanpassung vollzieht sich dabei üblicherweise in den folgenden vier Phasen: Identifikation, Parameterschätzung, Diagnose und Interpretation des Modells. Daran kann die praktische Anwendung des Modells, z.B. für die Prognose, anschließen. Im weiteren werden anhand einiger Datenbeispiele die Ergebnisse dieser vier Anpassungsschritte angegeben und diskutiert.

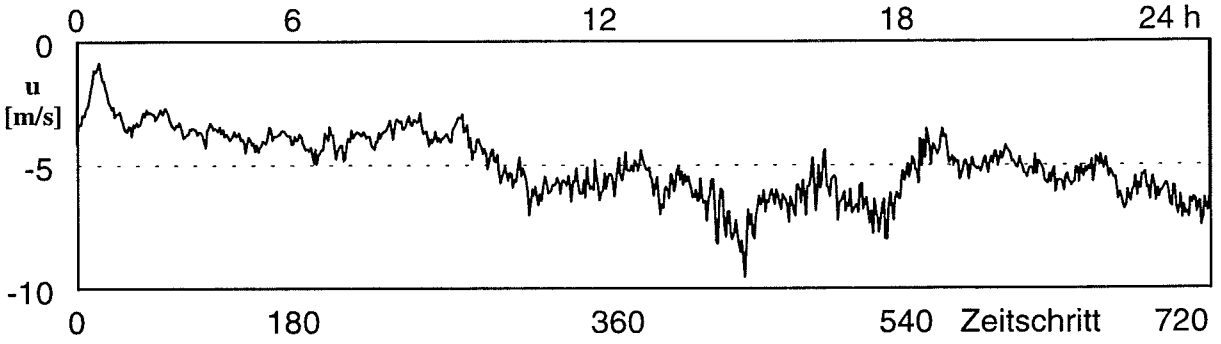

Abb. 1: Querwindkomponente u (in m/s) am ersten Meßtag

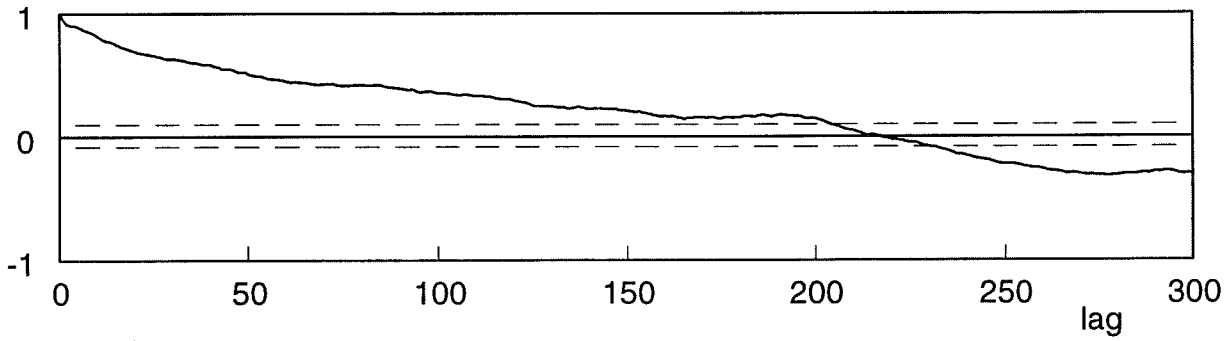

Abb. 2: Autokorrelationsfunktion (ACF) der Querwindkomponente am ersten Meßtag (gestrichelt: Konfidenzbereich für ACF=0)

Modellierung

Da die hier vorliegenden Reihen keinen deutlichen Trend oder Zyklen enthalten, also stationär sind, gilt d=0. Die Spezifikation der Ordnungen p und q erfolgt nach Box & Jenkins mit Hilfe der Autokorrelationsfunktion (ACF) (Abb. 2) und der partiellen Autokorrelationsfunktion (PACF) (Abb. 3). Das langsame Abklingen der ACF und der plötzliche Abbruch der PACF deuten auf einen AR-Prozeß hin. Darüber hinaus sind die ersten fünf PACF-Werte signifikant, da sie außerhalb des Konfidenzintervalls für Null liegen. Somit läßt sich ein ARIMA[5,0,0] ≡ AR(5)-Prozeß identifizieren.

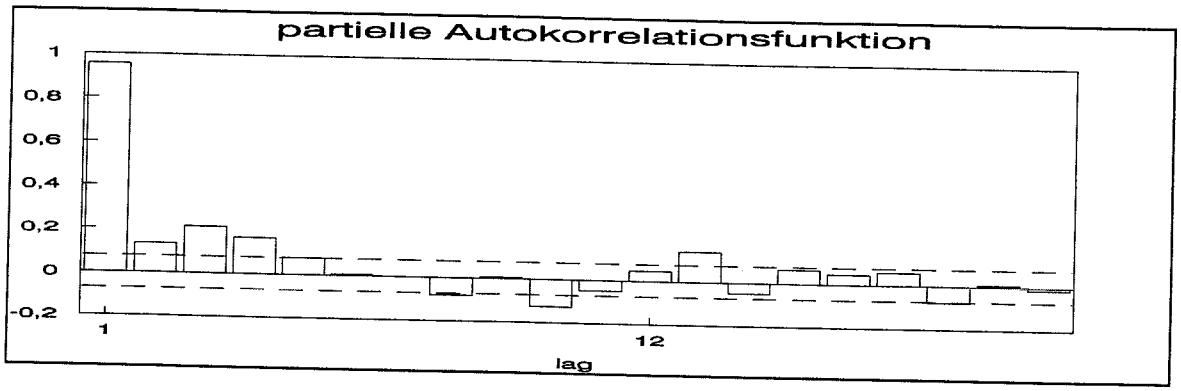

Abb. 3: Partielle Autokorrelationsfunktion der Querwindkomponente am ersten Meßtag

Für dieses AR(5)-Modell

$$(1-\Phi_1 B^1-\Phi_2 B^2-\Phi_3 B^3-\Phi_4 B^4-\Phi_5 B^5)u_t=\varepsilon_t \qquad (1)$$

sind die Parameter $\Phi_1,\Phi_2,\Phi_3,\Phi_4,\Phi_5$ sowie $\sigma^2_\varepsilon = \mathrm{var}(\varepsilon_t)$ zu bestimmen.

Eine einfache Schätzung erhält man durch die Yule-Walker-Gleichungen. Sie wird durch rekursive Iteration weiter verbessert. Um einen Überblick über das Verhalten der gesamten Winddaten zu bekommen, ist es notwendig, die Modellierung auf weitere Messungen auszudehnen.

Für den Quer- (u), den Längs- (v) und den Vertikalwind (w) von drei unabhängigen Meßtagen wurde jeweils ein AR(5)-Modell identifiziert und dessen Parameter geschätzt (Tabellen 1 bis 3).

Tabelle 1: Geschätzte Modellparameter für den Querwind

Parameter	Tag 1	Tag 2	Tag 3
Φ_1	+0.71	+0.74	+0.73
Φ_2	-0.05	+0.06	+0.15
Φ_3	+0.08	+0.12	+0.04
Φ_4	+0.13	-0.04	+0.04
Φ_5	+0.10	+0.09	-0.02
σ^2_ε	0.16	0.07	0.08
R^2_T	0.92	0.90	0.87

Tabelle 2: Geschätzte Modellparameter für den Längswind

Parameter	Tag 1	Tag 2	Tag 3
Φ_1	+0.85	+0.85	+0.88
Φ_2	+0.02	+0.05	+0.02
Φ_3	+0.07	+0.10	+0.09
Φ_4	-0.01	-0.02	-0.03
Φ_5	+0.03	-0.0001	+0.01
σ^2_ε	0.16	0.09	0.13
R^2_T	0.82	0.96	0.93

Tabelle 3: Geschätzte Modellparameter für den Vertikalwind

Parameter	Tag 1	Tag 2	Tag 3
Φ_1	+0.27	+0.32	+0.44
Φ_2	+0.22	+0.24	+0.14
Φ_3	+0.23	+0.10	+0.16
Φ_4	+0.14	+0.11	+0.03
Φ_5	+0.06	+0.15	+0.12
σ^2_ε	0.003	0.002	0.002
R^2_T	0.68	0.69	0.62

Der Schätzfehler der iterativen Bestimmung der Parameter $\Phi_1,\Phi_2,\Phi_3,\Phi_4,\Phi_5$ ist $\leq \pm 0.05$. Diese, für die Schätzung der Modellparameter angegebene Genauigkeit bezieht sich lediglich auf die Iteration der Parameter. Fehler infolge einer nicht korrekten Modellidentifikation sind nicht enthalten. Hierzu muß stets das AIC Kriterium herangezogen werden (siehe Abschnitt Modelldiagnose).

Eine abschließende Entscheidung über die Adäquatheit eines angepaßten Modells wird anhand von Maßzahlen, die die Güte eines Modells charakterisieren getroffen. Mit Hilfe einer solchen Modelldiagnose ist nun zu prüfen, ob die Meßreihe tatsächlich als eine typische Realisierung dieses geschätzten AR(5)-Prozesses aufgefaßt werden kann. Dazu wird beispielsweise das durch das Modell erzeugte Frequenzspektrum mit dem Spektrum (Periodogramm) der Meßreihe verglichen. In Abb. 4 sind beide im logarithmischen Maßstab eingezeichnet. Man erkennt, daß das Modell den prinzipiellen (geglätteten) Verlauf des gemessenen Spektrums wiedergibt. Die auftretenden Differenzen zwischen Modell und Meßdaten sind im Residualterm εt enthalten. Ihr Beitrag wird durch den ebenfalls in den Tabellen 1 bis 3 angegebenen Parameter $\sigma^2\varepsilon$ quantifiziert.

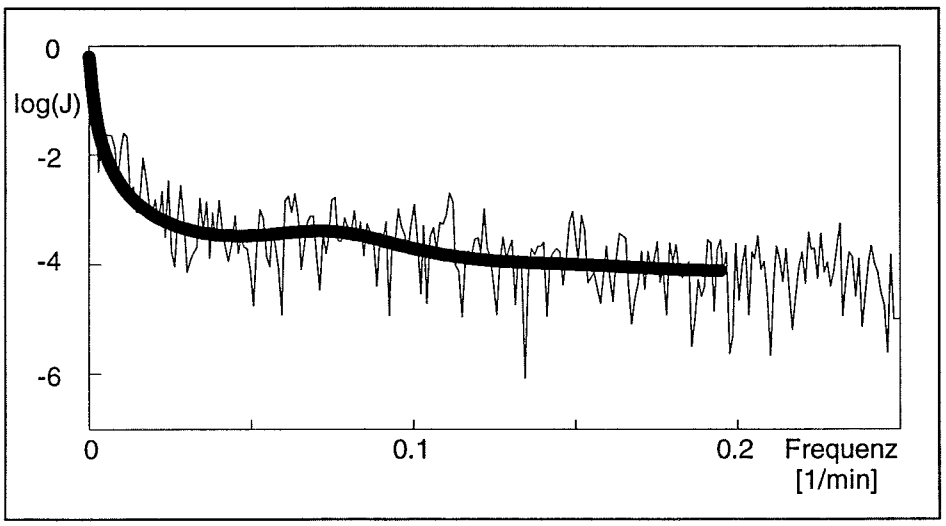

Abb. 4: Periodogramm des Querwindes des 1. Tages und Spektrum des angepaßten AR(5)-Modells (dicke Linie) in logarithmischer Darstellung, (J = relative spektrale Intensität)

Ein Gütekriterium, welches sich direkt aus den Residuen ableitet ist

$$R_T^2 = 1 - \frac{\sum \varepsilon_t^{\,2}}{\sum (u_t - \overline{u})^2}, \qquad (0 \le R_T^2 \le 1). \tag{2}$$

Es setzt die Varianz (2. Moment) der Residuen ε_t ins Verhältnis zur Varianz der Meßdaten und ist somit ein normalisiertes Maß dafür, welcher Anteil der Datenvarianz durch das angepaßte Modell erklärt wird. Bei den in den Tabellen 1 und 2 gegebenen Resultaten zeigt sich mit $R^2_T \approx 0.90$, daß etwa 90 % der Meßdatenvarianz durch die AR(5)-Modelle beschrieben wird. Bemerkenswert ist dabei der deutlich niedrigere Wert $R^2_T \approx 0.65$ bei der Modellierung des Vertikalwindes (vgl. Tab. 3). Da hier gleichzeitig σ^2_ε sehr klein ist, muß also die Varianz der vertikalen Windstärke einen besonders kleinen Wert annehmen.

Interpretation

Der Modellparameter Φ_1 drückt die Korreliertheit zwischen benachbarten Meßwerten aus. Plötzliche, 'schroffe' Änderungen können bei z. B. $\Phi_1 \approx 0.7$ nicht auftreten - das Windsystem besitzt eine mehr oder weniger große Trägheit oder Persistenz. Der aktuelle Meßwert baut auf 70% des Windwertes vom vorherigen Zeitschritt auf. Die zu höheren lags gehörenden Terme des AR-Modells stellen eine längerwirkende 'Rückkopplung' innerhalb des Prozesses dar. Durch solche Rückkopplungen können auch automatisch Periodizitäten in den Realisierungen des Modells entstehen. Ihre Intensität und Periode hängen natürlich von den Modellparametern ab. In Abb. 4 deutet sich solch ein Effekt im Spektrum an. Das implizite Enthaltensein von Periodizitäten in autoregressiven Prozessen wurde erstmals von Slutzky (1927) und Yule (1927) erkannt.

Vergleicht man die Modellparameter für die drei Windrichtungen, so zeigt sich ein deutlich anisotropes Verhalten: Besonders beim Vertikalwind nimmt Φ_1 wesentlich niedrigere Werte an (vgl. Tab. 3 mit Tab. 1 und 2). Die aktuelle Windstärke ist also im Vergleich zum Horizontalwind weniger stark von ihrem vorhergehenden Wert bestimmt (weniger autokorreliert). Die Streubreite des Residualterms ist, wie bereits oben festgestellt wurde, ebenfalls kleiner. Diese beiden Resultate stehen im Einklang mit der Vorstellung von einer horizontalen Schichtung der Atmosphäre. Dabei ist die vertikale Komponente sowohl in ihrer über längere Zeitabschnitte gleichförmigen (autokorrelierten) Bewegung, als auch in den unsystematischen Schwankungen (Streuung) weniger ausgeprägt, als dies bei den horizontalen Komponenten der Fall ist.

Prognose

Für den hier vorliegenden Fall eines AR(5)-Modells

$$(1 - \Phi_1 B^1 - \Phi_2 B^2 - \Phi_3 B^3 - \Phi_4 B^4 - \Phi_5 B^5) u_t = \varepsilon_t \tag{3}$$

ergibt sich die Einschrittprognose

$$\hat{u}_{t+1} = \Phi_1 u_t + \Phi_2 u_{t-1} + \Phi_3 u_{t-2} + \Phi_4 u_{t-3} + \Phi_5 u_{t-4}, \tag{4}$$

und die Prognose über zwei Schritte, bei der ein bereits prognostizierter Wert eingeht, lautet

$$\hat{u}_{t+2} = \Phi_1 \hat{u}_{t+1} + \Phi_2 u_t + \Phi_3 u_{t-1} + \Phi_4 u_{t-2} + \Phi_5 u_{t-3} . \qquad (5)$$

In diesem Sinne wird fortgesetzt.
Die Prognose ist stets eine gewichtete Summe aus zurückliegenden Beobach- tungen, da man ja auch den ersten prognostizierten Wert in (11) wieder durch die fünf letzten Beobachtungswerte aus (10) ersetzen kann. Die Vertrauensbereiche für die AR(5)-Vorhersagen über T Zeitschritte berechnen sich gemäß Box & Jenkins (1979) zu

$$\hat{u}_{t+T}(\pm) = \hat{u}_{t+T} \pm u_{1-\alpha/2} \sigma_\varepsilon P_T(\Phi_1,...,\Phi_5) \qquad (6)$$

dabei ist $u_{1-\alpha/2}$ das Quantil der standardisierten Normalverteilung für eine Sicherheit von (1-α/2). $P_T(\Phi_1,...,\Phi_5)$ symbolisiert ein Polynom aus Potenzen der Modellparameter $\Phi_1,...,\Phi_5$. Mit zunehmendem Prognosehorizont T wird P_T und damit auch der Vertrauensbereich in Abhängigkeit von den Modellparametern größer. Zur Illustration dieses Prognoseansatzes wurden für den Querwind (u) des ersten Meßtages mit den bereits oben geschätzten Parameterwerten AR(5)-Vorhersagen berechnet (siehe Abb. 5). Die fett gezeichnete Kurve stellt die Meßwerte dar, die dünn gezeichneten geben die Vertrauensbereiche der Prognosen wieder. Je länger der Vorhersagezeitraum ist, um so breiter wird der Konfidenzbereich. Gleichzeitig werden Abweichungen vom mittleren Niveau immer weniger deutlich vorhergesagt. Das bedeutet, daß mit zunehmendem Vorhersagezeitraum die Prognosekurven immer glatter werden.

Die innere Prognosekurve greift nur einen Zeitschritt (2 min) in die Zukunft. Dagegen sagt das äußere Kurvenpaar den Verlauf über 5 Zeitschritte (10 min) vorher. Für zwei Beispiele ist jeweils der Prognosepunkt der Meßreihe mit den dazugehörigen Vorhersagen verbunden worden (gestrichelt), so daß zum Prognosezeitpunkt alle links von der parabelförmigen Abgrenzung befindlichen Daten bekannt sind.

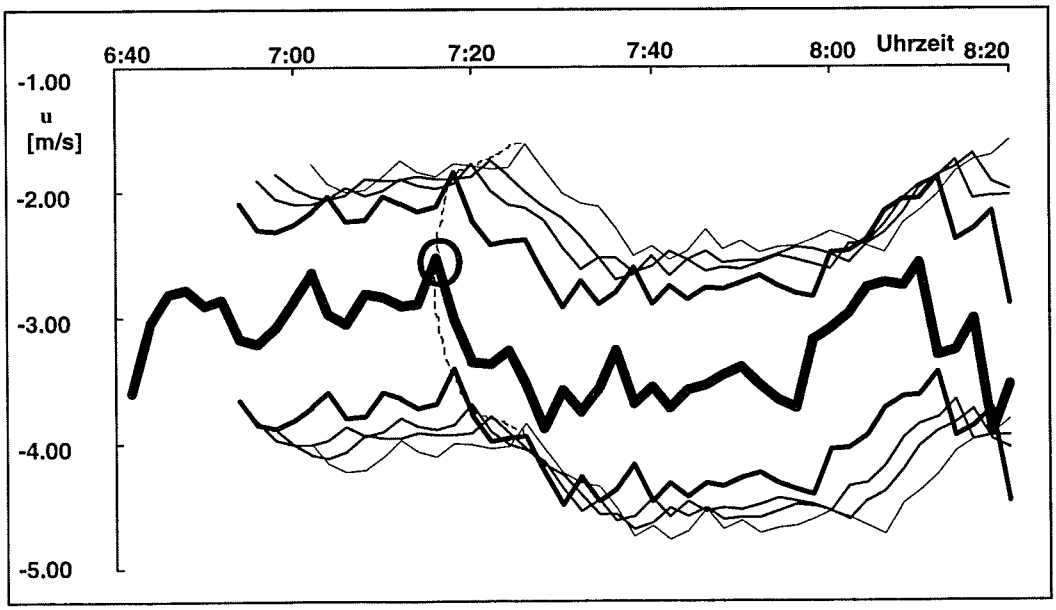

Abb. 5: AR(5)-Vorhersage von Querwindgeschwindigkeiten des ersten Meßtages: Messung (fett) und Konfidenzbereiche der Prognosen über 2, 4, 6 und 10 min (dünne Linien von innen nach außen).

Methodenvergleich

Von Franke (1995) wurde für die Querwindkomponente u eine Vorhersagemethode vorgeschlagen, die mit zwei klassierten Stabilitätskenngrößen und einem davon abhängigen Weibull-verteilten Sicherheitszuschlag arbeitet. Dieses Verfahren geht jedoch lediglich vom letzten Meßwert des Querwindes aus, kann also als Persistenz- verfahren bezeichnet werden. Informationen aus der Vergangenheit sind nur in den Stabilitätskenngrößen enthalten und gehen so in den Sicherheitszuschlag ein.

Die Leistungsfähigkeit des hier entwickelten AR-Prognoseansatzes soll nun mit der des Persistenz-Vorhersagesystems verglichen werden. Zu diesem Zweck wurde der Mittelwert der für die Tage 1 bis 3 geschätzten AR-Modellparameter (vgl. Tab. 1) zur Querwindprognose des nächsten Tages verwendet.

In Abb. 6 sind für den 4. Meßtag der reale Verlauf der Meßreihe (mittlere fette Kur- ve) sowie der über 5 Zeitschritte (= 10 Minuten) mit der AR-Prognose vorhergesagte Vertrauensbereich angegeben. Dieser Vertrauensbereich ist auf eine statistische Sicherheit von 95% eingestellt. Die in 5% der Fälle auftretenden Fehlprognosen des Querwindes zeigen sich an den Zeitpunkten, an denen die realen Meßwerte (fette Kurve) außerhalb des Bereiches zwischen den Prognosegrenzen liegen.

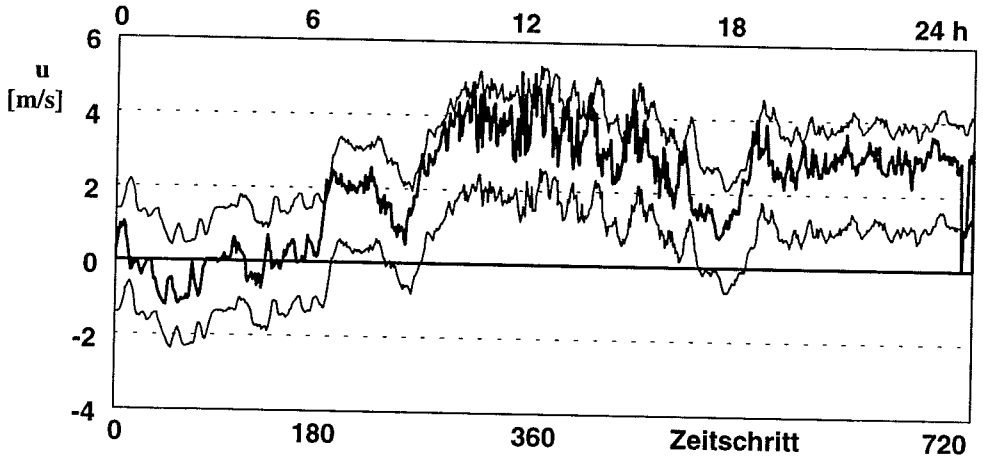

Abb. 6: Am 4. Meßtag registrierte Querwindgeschwindigkeit und Prognosebereich bei AR(5)-Vorhersage über 10 Zeitschritte (95% statist. Sicherheit, zweiseitig).

Bei der zum Vergleich in Abb. 7 gezeigten Prognose nach dem Persistenzverfahren wurde der Sicherheitszuschlag ebenfalls auf eine statistische Sicherheit von 95% eingestellt. Visuell läßt sich erkennen, daß dabei ein breiterer Prognosebereich, als in Abb. 6 entsteht. Die Vorhersage mit dem Persistenzverfahren ist also ungenauer, als die AR(5)-Prognose.

Um die beim Persistenzverfahren eingestellte Breite des Prognosebereiches im weiteren zu verwenden, kann man im AR(5)-Verfahren die statistische Sicherheit auf 97.5% erhöhen.

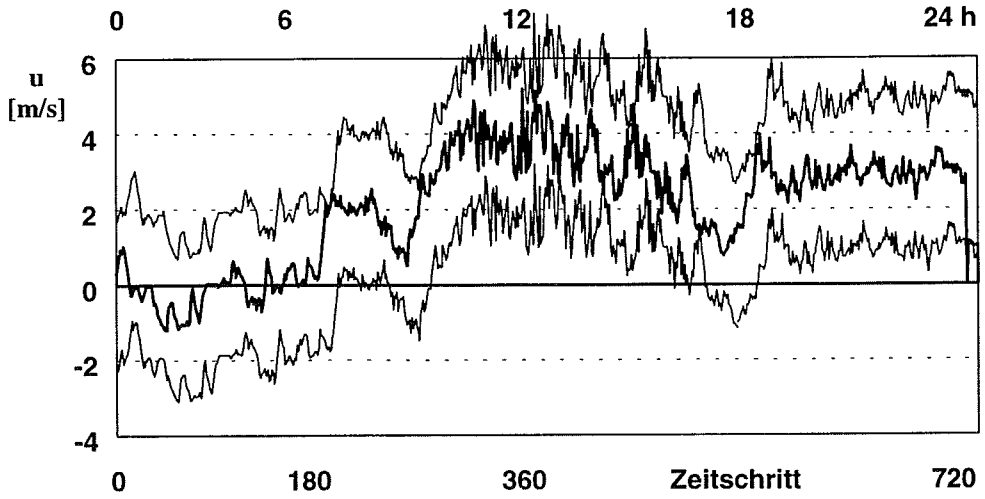

Abb. 7: Am 4. Meßtag registrierte Querwindgeschwindigkeit und Prognosebereich bei Persistenz-Vorhersage über 10 Zeitschritte (95% statistische Sicherheit).

Eine beim Persistenzverfahren auftretende Problematik waren Sprünge in der vorhergesagten Nutzungszeit ohne Wirbelschleppengefährdung (als kritische Prognosezusammenbrüche bezeichnet). Diese Sprünge sind auf plötzliche Änderungen in der vorhergesagten Querwindgeschwindigkeit zurückzuführen. Der systematische Tagesgang der Sprunghäufigkeit (Ahlbrecht et al., 1995) mit einem Maximum am Mittag läßt sich mit der zu dieser Zeit erhöhten Varianz der Meßreihe (siehe Abb. 7), die durch konvektive Vorgänge verursacht wird, erklären.

Wie ein Vergleich der Abbildungen 6 und 7 zeigt, liefert das AR(5)-Verfahren eine ausgeglichenere Querwindvorhersage. Starke Variationen der Vorhersage, wie sie beim Persistenzverfahren auftreten, gibt es hier nicht.

Ein endgültiger Modellvergleich soll nun anhand der Prognoseergebnisse für die letztlich genutzte Zielgröße, die Nutzungszeit ohne Wirbelschleppengefährdung τ_{frei} vorgenommen werden. Diese Zeitspanne τ_{frei} wird über Gleichungen zur Wirbellebensdauer und Wirbeleigengeschwindigkeit (vgl. Franke, 1995) aus der vorhergesagten Querwindgeschwindigkeit berechnet. Tabelle 4 stellt die von beiden Prognosealgorithmen angegebenen Zeiten τ_{frei} gegenüber.

Die erwähnten Sprünge in τ_{frei} bei der Persistenzvorhersage zeigen sich in Tabelle 4 beispielsweise für t=18->19, t=83->84, t=143->144, ... Bei der AR(5)-Vorhersage von τ_{frei} treten diese Sprünge nicht auf.

Tabelle 4: Von beiden Prognosealgorithmen angegebene Zeiten τ_{frei}.

Zeitschritt Nr.	10	11	12	13	14	15	16	17	18	19	20	21	22	23	24	25	26	27	28	29
Peristenz-Progn.	10	6	8	16	12	16	8	8	16	6	4	4	2	2	0	0	0	2	4	6
AR(5)-Prognose	20	20	20	20	20	20	20	20	20	20	20	18	14	8	8	4	4	4	8	10

Zeitschritt Nr.	30	31	32	33	34	35	36	37	38	39	40	41	42	43	44	45	46	47	48	49
Peristenz-Progn.	10	14	8	8	12	12	14	16	12	4	2	2	4	10	12	14	14	14	14	8
AR(5)-Prognose	14	20	20	20	20	20	20	20	20	20	20	18	20	20	20	20	20	20	20	20

Zeitschritt Nr.	50	51	52	53	54	55	56	57	58	59	60	61	62	63	64	65	66	67	68	69
Peristenz-Progn.	4	2	4	4	2	2	2	2	2	0	0	0	2	4	4	6	6	2	2	2
AR(5)-Prognose	20	18	16	14	10	8	6	4	2	2	2	2	2	4	10	12	14	10	8	6

Zeitschritt Nr.	70	71	72	73	74	75	76	77	78	79	80	81	82	83	84	85	86	87	88	89
Peristenz-Progn.	0	0	0	2	2	2	2	2	2	2	0	4	8	12	2	4	2	2	2	2
AR(5)-Prognose	4	2	2	2	2	2	2	2	2	2	2	4	12	16	18	16	12	10	6	4

Zeitschritt Nr.	90	91	92	93	94	95	96	97	98	99	100	101	102	103	104	105	106	107	108	109
Peristenz-Progn.	4	6	10	12	16	14	14	14	14	14	14	14	14	14	14	16	14	14	12	10
AR(5)-Prognose	8	12	16	20	20	20	20	20	20	20	20	20	20	20	20	20	20	20	20	20

Zeitschritt Nr.	110	111	112	113	114	115	116	117	118	119	120	121	122	123	124	125	126	127	128	129
Peristenz-Progn.	12	12	12	14	14	8	4	4	4	8	6	6	6	8	8	12	12	12	6	4
AR(5)-Prognose	20	20	20	20	20	20	18	14	14	16	16	16	18	18	20	20	20	20	20	18

Zeitschritt Nr.	130	131	132	133	134	135	136	137	138	139	140	141	142	143	144	145	146	147	148	149
Peristenz-Progn.	6	6	6	4	4	6	4	2	6	6	2	4	8	14	6	4	4	8	8	10
AR(5)-Prognose	16	16	16	14	14	16	12	14	16	14	12	14	16	20	20	18	16	16	18	20

Zeitschritt Nr.	150	151	152	153	154	155	156	157	158	159	160	161	162	163	164	165	166	167	168	169
Peristenz-Progn.	10	12	14	14	14	10	8	14	8	8	12	8	6	2	6	4	4	4	8	14
AR(5)-Prognose	20	20	20	20	20	20	20	20	20	20	20	20	18	18	16	14	12	12	16	20

Zeitschritt Nr.	170	171	172	173	174	175	176	177	178	179	180	181	182	183	184	185	186	187	188	189
Peristenz-Progn.	14	16	16	14	12	12	14	4	2	4	4	4	6	8	10	8	12	10	2	4
AR(5)-Prognose	20	20	20	20	20	20	20	20	16	14	14	12	14	18	20	20	20	20	16	14

Zeitschritt Nr.	190	191	192	193	194	195	196	197	198	199	200
Peristenz-Progn.	2	0	0	0	0	0	0	0	0	0	0
AR(5)-Prognose	8	4	0	0	0	0	0	0	0	0	0

Schlußfolgerungen

Die Zeitserienanalyse hat ergeben, daß die Autokorreliertheit ein wesentliches Charakteristikum der in Form von 2-Minuten-Mittelwerten gegebenen Winddaten ist. Daraus resultierte die Möglichkeit der Modellierung mit einem linearen autoregressi- ven AR(5)-Modell nach Box & Jenkins (1976). Neben den autokorrelativen bildet dieses Modell auch die spektralen Verhältnisse der Datenserien ab. In Anwendung des AR(5)-Modells läßt sich eine Vorhersagemethode angeben, die jeweils die letzten 5 Meßwerte mit in die Prognose der künftigen Windgeschwindigkeit und ihres Vertrauensbereiches einbezieht. Dadurch finden in der Vergangenheit erfolgte trendartige und zyklische Variationen des Querwindes in der Vorhersage Berücksichtigung. Das AR(5)-Prognoseverfahren stellt gegenüber dem Persistenzverfahren eine Verbesserung dar. Das wurde an folgenden Sachverhalten deutlich:

Das AR(5)-Verfahren liefert eine genauere Vorhersage, so daß sich hier mit einer statistischen Sicherheit von 97.5%, gegenüber 95% beim Persistenzverfahren, ar- beiten läßt. Würde man jedoch 95% Sicherheit verwenden, so ließe die AR(5)-Vor- hersage eine insgesamt größere wirbelschleppengefährdungsfreie Nutzungszeit zu. Die Parameter der AR-Prognose sind also stets so zu wählen, daß sich ein praktikabler Kompromiß zwischen Sicherheit und Nutzungs-

zeit ergibt. Durch die glättende Wirkung des AR(5)-Modells werden die bei der Persistenzvorhersage auftretenden Sprünge von τ_{frei} vermieden. Diese Eigenschaft trägt wesentlich zur Erhöhung der Akzeptanz des Prognosesystems beim Nutzer (Fluglotsen) bei. Außerdem scheint sie (wie Tab. 4 zeigt) allgemein eine Erhöhung der Nutzungszeit zu bewirken.

Weitere Verbesserungsmöglichkeiten bestehen in einer kontinuierlichen Schätzung der Modellparameter. Dadurch würde sich das Modell stets der aktuellen Situation anpassen. Das bedeutet einerseits, daß veränderte spektrale und autokorrelative Eigenschaften stets neu vom Modell adaptiert werden. Andererseits fließt aber auch ein verändertes Signal-Rausch-Verhältnis in den aktualisierten Parameter σ^2_ε ein und verändert darüber die Breite des vorhergesagten Konfidenzintervalls.

Literatur

Box, GEP und Jenkins, GM (1976): „Time series analysis - forecasting and control", Revised Edition, Prentice Hall, Englewood Cliffs, New Jersey.

Ding Y, Jiang Z (1996): „Study on canonical autoregressive prediction of meteorological ememente fields", Acta Meteorologica Sinica, 10(1), 41-51.

Otruba J, Ostrozlik M, Krnác P (1988): „Harmonische Komponenten des Tagesganges der Windgeschwindigkeit unter verschiedenen orografischen Bedingungen", Contributions of the Geophysical Institute of the Slovak Academy of Sciences. Series of Meteorology, 8, 54-79.

Gordon N (1992): „A new verification scheme for aerodrome forecasts", Proceedings of the WMO Technical Conference on Tropical Aeronautical Meteorology (TECTAM-92), Geneva, 169-172.

Franke, J-M (1995): "Untersuchungen zur Dynamik von Wirbelschleppen in der atmosphärischen Grenzschicht", Berichte des Instituts für Meteorologie und Klimatologie der Universität Hannover, Band 46.

Ahlbrecht M, Franke J-M, Gurke T, Pertzsch B, Tetzlaff G, Schlink U (1995): „Zwischenbericht zur Fortentwicklung des Prognoseverfahrens des Wirbelschleppen-Warnsystems", Deutsche Flugsicherung GmbH.

Slutzky, E (1927): „The summation of random causes as the source of cyclic processes", Econometrica, 5, 105.

Yule, G U (1927): „On a method of investigating periodicities in disturbed series, with special references to Wolfer's sunspot numbers", Phil. Trans. A., 226, 267.

Korrespondenz bitte an:

Prof. Dr. Gerd Tetzlaff
Institut für Meteorologie
Universität Leipzig
Stephanstraße 3
D-04103 Leipzig

Spektraler Extinktionsgang und Größenverteilung des Pinatubo-Aerosols

Wolfgang von Hoyningen-Huene, Peter Posse

Zusammenfassung:

Spektralradiometermessungen (spektrale optische Dicke und Himmelshelligkeitsfunktion) unter Hochgebirgsbedingungen (Zugspitze, 2965 m) wurden zur Bestimmung der klimarelevanten Aerosolparameter des stratosphärischen Vulkanaerosols (speziell des Pinatubo) verwendet. Die erhaltenen klimarelevanten Aerosolparameter aus den Meßkampagnen werden mit Angaben der Aerosolklimatologien verglichen und zur Abschätzung des kurzwelligen Strahlungsforcings durch das Pinatubo-Aerosol verwendet.

Summary:

Spectral radiometer measurements (spectral optical thickness and sky brightness function) under high mountain conditions (Zugspitze, 2965 m) have been used for the determination of climate-relevant aerosol parameters of the stratospheric volcanic aerosol (columnar size distribution, refractive index, phase function and asymmetry parameter - especially of the aerosol of the Pinatubo volcano eruption in 1991). The climate-relevant aerosol parameters of the measurement campaigns and their temporal change have been compared with data of the aerosol climatologies and have been used for the estimation of the short wave radiative forcing of the Pinatubo event.

1. Zielstellung

Die vorgestellten Ergebnisse sind Bestandteil des Ergebnisberichts zum BMBF Verbundprojekt 'Spurenstoffkreisläufe' und des darin geförderten Themas mit o.g. Bezeichnung.

Die wesentlichen Ziele des Teilprojekts waren:

- Messung des spektralen Verlaufs der optischen Dicke des vulkanischen Aerosols in der Stratosphäre (für den Ausbruch des Pinatubo) im Wellenlängenbereich von 0.35 - 1.1 µm mit einer spektralen Auflösung, die eine Ableitung der columnaren Aerosolgrößenverteilung mit den im CIRATRA-Ansatz enthaltenen Inversionsprogrammen ermöglicht.

- Durchführung von ergänzenden Messungen von Aureolen- und Himmelshelligkeitsstrahldichte im Almukantar (Sonnenhorizontal) zusammen mit den spektralen optischen Dicken, die die Grundlage für die Ermittlung der wesentlichen klimarelevanten optischen Aerosolparameter ermöglichen, die zur Abschätzung des kurzwelligen Strahlungsforcings durch das stratosphärische Aerosol, insbesondere des Beitrags des Pinatubo-Aerosols dienen.

- Bestimmung der wesentlichen klimarelevanten Aerosoleigenschaften für das Pinatubo-Aerosol

a) in Form der optischen Eigenschaften (spektrale optische Dicke und Phasenfunktion mit Asymmetrieparametern im solaren Einstrahlungsbereich, die
   1. die Grundlage für die Abschätzung des kurzwelligen Strahlungsforcings sind und
   2. den Vergleich zwischen verschiedenen Spektralbereichen (unterschiedliche LIDAR-Wellenlängen) gestatten,

a) in Form von Angaben über die optisch relevante Struktur und Zusammensetzung des Aerosols (columnare Größenverteilung, Angaben zur Teilchenform und komplexer Brechungsindex), die sowohl für die Bestimmung reaktiver Oberflächen, effektiver Radien und Modellierungen der Strahlungseigenschaften Verwendung finden.

- Abschätzung des kurzwelligen Strahlungsforcings durch den Impakt des starosphärischen Aerosols, insbesondere des Einflusses des vulkanischen Pinatubo-Aerosols.

2. Arbeitsbericht

Entsprechend der Antragstellung wurden folgende Arbeiten durchgeführt:

- Durchführung von zielgerichteten Meßkampagnen auf der Zugspitze, in denen Spektralradiometer zur Bestimmung der direkten Sonnenstrahlung und später auch der Himmelsstrahldichte zum Einsatz kamen. Für die Meßkampagnen auf der Zugspitze wurden verschiedenen Einrichtungen verwendet: Max-Planck-Hütte des MPI für Astrophysik, Meßeinrichtung des IFU auf dem Zugspitzgipfel, Umweltforschungsstation 'Schneefernerhaus'.

- Die Messungen auf der Zugspitze (oberhalb der Grundschicht) begrenzen den Meßeffekt auf das atmosphärische Aerosol der Stratosphäre und der freien Troposphäre, wovon der dominierende Effekt durch das vulkanische Aerosol des Pinatubo hervorgerufen wird. Die Einbeziehung von vor dem Projekt vorgenommenen Kalibrierungsmessungen gestattete die Erfassung der spektralen optischen Aerosoleigenschaften der Stratosphäre und der freien Troposphäre seit 1990. Ebenso wurden noch Daten vom Herbst 1996 hinzugefügt, die den Zustand einer unbelasteten Stratosphäre und freien Troposphäre zeigen. Damit ist eine Charakterisierung der Verhältnisse vor und nach dem Pinatubo-Ausbruch möglich.

- Die Weiterentwicklung der eingesetzten Inversionsprozeduren und der Meßtechnik für die Bestimmung der columnaren Aerosolgrößenverteilung, speziell Erweiterungen zur Untersuchung auch größerer Aerosolpartikeln der Supermicron-Fraktion. Hierzu gehört die zusätzliche Berücksichtigung von Daten der winkelabhängigen Aureolenhelligkeit zusammen mit der spektralen optischen Dicke in der zufallsgesteuerten nichtlinearen Inversionsprozedur. Sie ermöglichte eine Reduzierung des Inversionsfehlers im Radienbereich bis ca. 4 µm. In die gleiche Richtung führte die Umrüstung eines Spektrafotometers für Messungen im IR-Bereich für die Wellenlängen von 1.1 - 2.19 µm.

- Versuche zur Messung von spektralen optischen Dicken im IR-Bereich von 1.1 - 2.19 µm. Dazu wurde ein Versuchsaufbau eines Radiometers mit einer PbS-Diode realisiert auf der Basis der bisher eingesetzten Spektralradiometer mit Si-Diode. Der Versuchsaufbau hatte 5 Kanäle im angegebenen Wellenlängenbereich, die sich auf 'Aerosol'-Kanäle (gasabsorberfreie Spektralbereiche) beziehen. Die Versuche zeigten, daß für eine Messung so niedriger optischer Dicke, wie sie Ende 1995 und 1996 auf der Zugspitze vorlagen, die

Temperaturstabilisierung unzureichend war und der Effekt sich nicht signifikant aus dem Background-Signal abhob. Erst Ende 1996 mit einer verbesserten Temperaturstabilisierung konnten erste Ergebnisse auch unter diesen Bedingungen erhalten werden, so daß speziell für die optischen Eigenschaften der Pinatubo-Aerosols für diesen Wellenlängenbereich keine Ergebnisse mehr gewonnen werden konnten. Ungeachtet dessen konnte das Gerät schon für Bedingungen mit hohen optischen Dicken zum Einsatz kommen (z.B. 1995 in Senegal (Desert- Aerosol) und 1997 bei ACE-2 (Marine-Boundary-Layer Aerosol).

- Bestimmung von columnaren Aerosolgrößenverteilungen mit Hilfe der entwickelten Inversionsprozeduren und Anpassung von multimodalen logarithmischen Normalverteilungen, wie sie in den einschlägigen Aerosolmodellen (d'Almeida et al., 1991, GADS, 1997) Verwendung finden (r_0 , σ_0, N_0). Auf dieser Basis wurde die columnare Aerosolmasse und Oberfläche der Moden abgeschätzt. Die Einbeziehung von Aureolendaten reduzierte die Überbetonung von Moden im Supermicronbereich ($r \geq 1$ µm) und machte eine Überarbeitung früher bestimmter Aerosolgrößenverteilungen erforderlich.

- Anwendung des gekoppelten Inversions-Strahlungstransfer-Programms CIRATRA (Coupled Inversion RAdiantion TRAnsfer, Wendisch & von Hoyningen-Huene, 1992, 1994) auf kombinierte Messungen von spektraler optischer Dicke und Himmelshelligkeit bei völlig wolkenfreiem Himmel zur zusätzlichen Bestimmung von Phasenfunktion, Asymmetriefaktor und Brechungsindex. Damit liegen bis auf die Single Scattering Albedo alle wesentlichen klimarelevanten Aerosolparameter für das stratosphärische Vulkanaerosol vor, die zur Berechnung des Strahlungstransfers benötigt werden.

- Entsprechend der Fortführung des Antrags wurden, vor allem im letzten Jahr der Laufzeit, Berechnungen von auf- und abwärtsgerichteten kurzwelligen Strahlungsflüssen vorgenommen, die eine Abschätzung der Änderung der kurzwelligen Strahlungsbilanz am Oberrand der Atmosphäre gestatteten. Dazu wurde ein spektrales Strahlungsflußmodell auf der Basis des Strahlungskodes von Nakajima & Tanaka, 1988 verwendet, das anhand experimenteller abwärtsgerichteter Strahlungsflüsse validiert ist.

3. Erzielte Ergebnisse

3.1 Zeitlicher Verlauf der spektralen optischen Dicke und Größenverteilung des Pinatubo-Aerosols

Das direkt erhaltene Ergebnis der Messungen auf der Zugspitze ist der Spektralverlauf der optischen Dicke. Die Messungen erfolgten mit den Spektralradiometern ASP (Atmosphären-Spektral-Photometer) die in der Arbeitsgruppe des Projektleiters entwickelt worden sind. Von den 90 verfügbaren Spektralkanälen verfügten 80 über eine zuverlässige Kalibrierung, so daß die optische Dicke mit dieser Auflösung im Wellenlängenbereich von 0.35 - 1.1 µm gemessen werden konnte. Die Bandbreite der Kanäle variierte zwischen 8 und 15 nm.

Im Rahmen dieses Berichts wird vor allem auf den spektralen Verlauf der optischen Dicke und ihre zeitliche Änderung eingegangen, da eine zeitliche Darstellung von nichtspektralen Daten wesentlich häufiger und besser im Rahmen der beteiligten LIDAR-Projekte vorgenommen ist (Ansmann et al, 1997). Die spektrale Information allerdings für die Inversion von columnaren Größenverteilungen, für die Berechnung von Strahlungsflüssen und für die Vergleichbarkeit

und Homogenisierung von verschiedenen LIDAR-Datensätzen (unterschiedliche Wellenlängen) benötigt wird.

Die erhaltenen spektralen optischen Dicken der einzelnen durchgeführten Kampagnen seit 1990 bis 1996 sind in Abb. 1 als mittlere spektrale Verlaufe dargestellt. Die Darstellung zeigt deutlich, daß sich die optische Dicke sowohl der Größe nach als auch bezüglich des spektralen Verlaufs durch den Impakt des vulkanischen Pinatubo-Aerosols in der Stratosphäre während dieser Episode änderte.

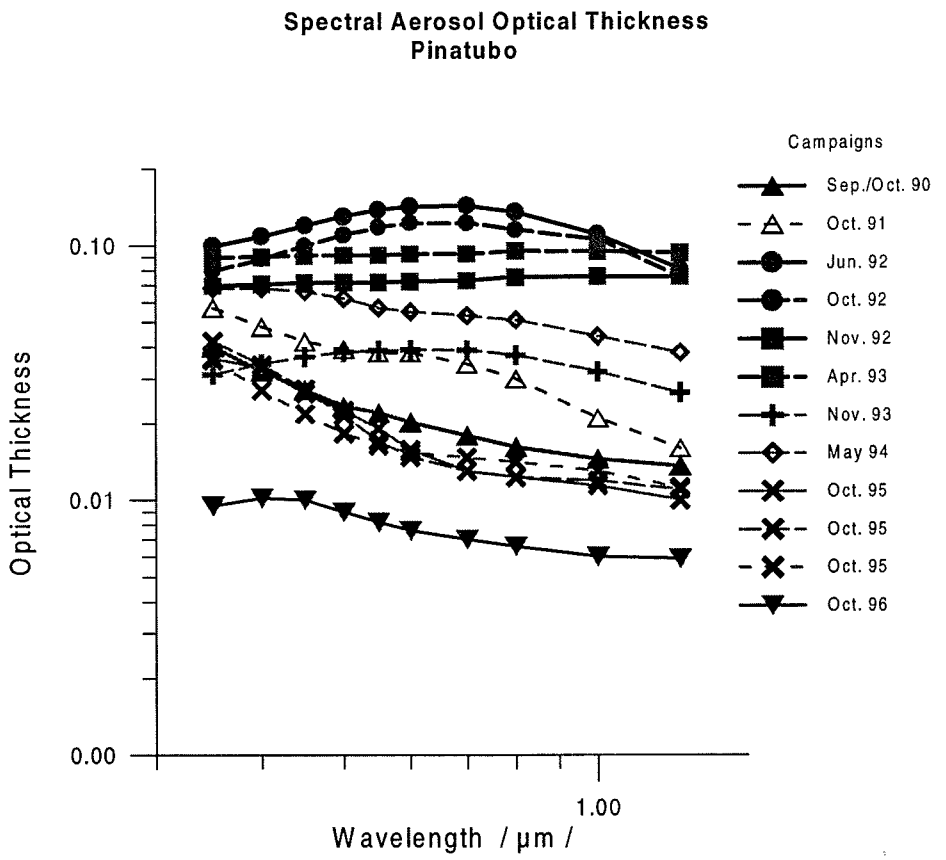

Abb. 1: Spektralverlaufe der optischen Dicke für die Meßkampagnen auf der Zugspitze (2965 m) mit dem optischen Einfluß von Stratosphäre und freier Troposphäre. Als Backgound Verhältnisse können die Daten vom Oktober 1996 dienen.

Um den Beitrag des Pinatubo-Aerosols vom natürlichen Background-Aerosol in der freien Troposphäre und unter normalen Stratosphärenbedingungen zu unterscheiden, hatten wir ursprünglich den Zustand vom September 1990 als ungestörten stratosphärischen Zustand betrachtet, zumal er in der selben Größenordung und einen ähnlichen Spektralverlauf hatte, wie die Daten von Oktober 1995. Jedoch die Messungen vom Oktober 1996 zeigten eine noch erheblich demgegenüber reduzierte optische Dicke. Den Daten ist auch zu vertrauen, da von mehreren verschiedenen Radiometern während der ACE-2 Radiometer-Kalibrierungskampagne RAD-I-CAL 96 das gleiche Ergebnis erhalten wurde. Daher ist offensichtlich der Background-Zustand der stratosphärischen Aerosolbelastung niedriger als ursprünglich angenommen. Das trifft sich ebenfalls mit Ergebnissen von Jaeger, 1997, der ebenfalls eine erheblich kleinere Rückstreuung in den LIDAR-Daten des IFU-LIDAR's fand.

Daß der Zustand von 1990 nicht der Background-Zustand sein konnte, zeigte sich während der Abklingphase ab November 1993 als der kurzwellige Teil (< 0,45 µm), die Werte von 1990 erreichte, während im sichtbaren bzw. im nahen IR immer noch deutlich höhere Werte der optischen Dicke gemessen wurden. Offensichtlich hatte das Pinatubo-Aerosol einen erheblichen Teil von Partikeln mit Radien unter 0.1 µm durch Koagulation in größere Teilchen inkorporiert. Erst zum Herbst 1995 wurde der Zustand von 1990 wieder erreicht. Damit hat sich die im Zwischenbericht von 1995 angegebene Halbwertszeit von 10 Monaten bestätigt, die aus dem Trend der exponentiellen Abnahme der optischen Dicke für das Pinatubo-Aerosol ergab.

Der Spektralverlauf zeigt in den verschiedenen Phasen in der Regel von einem Potenzverlauf abweichende Kurven. Dennoch wurde für die Parametrisierung des Spektralverlaufs die Form eines Potenzgesetzes verwendet, wobei es auf verschiedene Spektralbereiche angewendet wurde, um den unterschiedliche Krümmungsverläufen Rechnung tragen zu können.: a) gesamter Spektralbereich 0.35 - 1.1 µm, b) reduzierter Spektralbereich 0.35- 0.6 µm. Mit diesen Parametrisierungen sind Vergleichbetrachtungen zwischen unterschiedlichen LIDAR-Wellenlängen durchführbar, die von den beteiligten Gruppen auch zur Homogenisierung der unterschiedlichen LIDAR-Datensätze verwendet werden.

$$\delta_A(\lambda_2) = \delta_A(\lambda_1)\ (\lambda_2 / \lambda_1)^{-\alpha^*}$$

λ_1 und λ_2 sind die unterschiedlichen Wellenlängen, α^* der Spektralabfall des reduzierten Spektralbereichs , für den die Parametrisierung gültig sein soll. Im Fall des Angström'schen Potenzgesetzes ist λ_1 = 1.0 µm und α der Spektralabfall für den gesamten gemessenen Spektralbereich von 0.35 -1.1 µm. Die entsprechenden Parameter, die für die einzelnen Kampagnen gewonnen wurden sind in Tabelle 1 enthalten. Die entsprechende optische Dicke für 0.5 µm Wellenlänge ist zusammen mit Ergebnissen aus SAGE-II und AVHRR Satellitendaten in Abb. 2 dargestellt.
Die Satellitendaten liefern schon für das Jahr 1993 wesentlich niedrigere optische Dicken als die bodengestützten Radiometer und die LIDAR-Geräte. Für das Jahr 1994 werden keine Ergebnisse mehr für das Pinatubo-Aerosol angegeben. Offensichtlich sind sie nicht mehr in der Lage, die Aerosolwolke im unteren Teil der Stratosphäre vollständig zu erfassen.

Wie schon in den Zwischenberichten erwähnt, zeigt das Pinatubo-Aerosol in der Hauptphase Frühjahr 1992 bis Frühjahr 1993 einen flachen Spektralverlauf. Auch darüber hinaus bleibt der flache Spektralverlauf bis zum Herbst 1993 erhalten. Erst im Frühjahr 1994 stellt sich wieder eine Abfalltendenz im Spektralverlauf ein, die sich in der Folgezeit weiter verstärkt. Die entsprechenden Trübungsparameter für die Parametrisierungen sind in Tabelle 1 für alle Kampagnen, dic in diesem Zeitraum stattfanden enthalten. Die Daten der eigenen Meßkampagnen wurden noch durch Daten ergänzt, die vom DWD, Observatorium Lindenberg gemessen wurden.

Die Daten zeigen deutlich einen Jahresgang mit einem Maximum im Frühjahr und einem Minimum im Herbst. Ursache für den Jahresgang können jahreszeitliche Zirkulationsprozesse in der Stratosphäre sein, die jeweils im Frühjahr Aerosol aus anderen Breiten oder durch Tropopausenfaltungen in die Stratosphäre bringen.

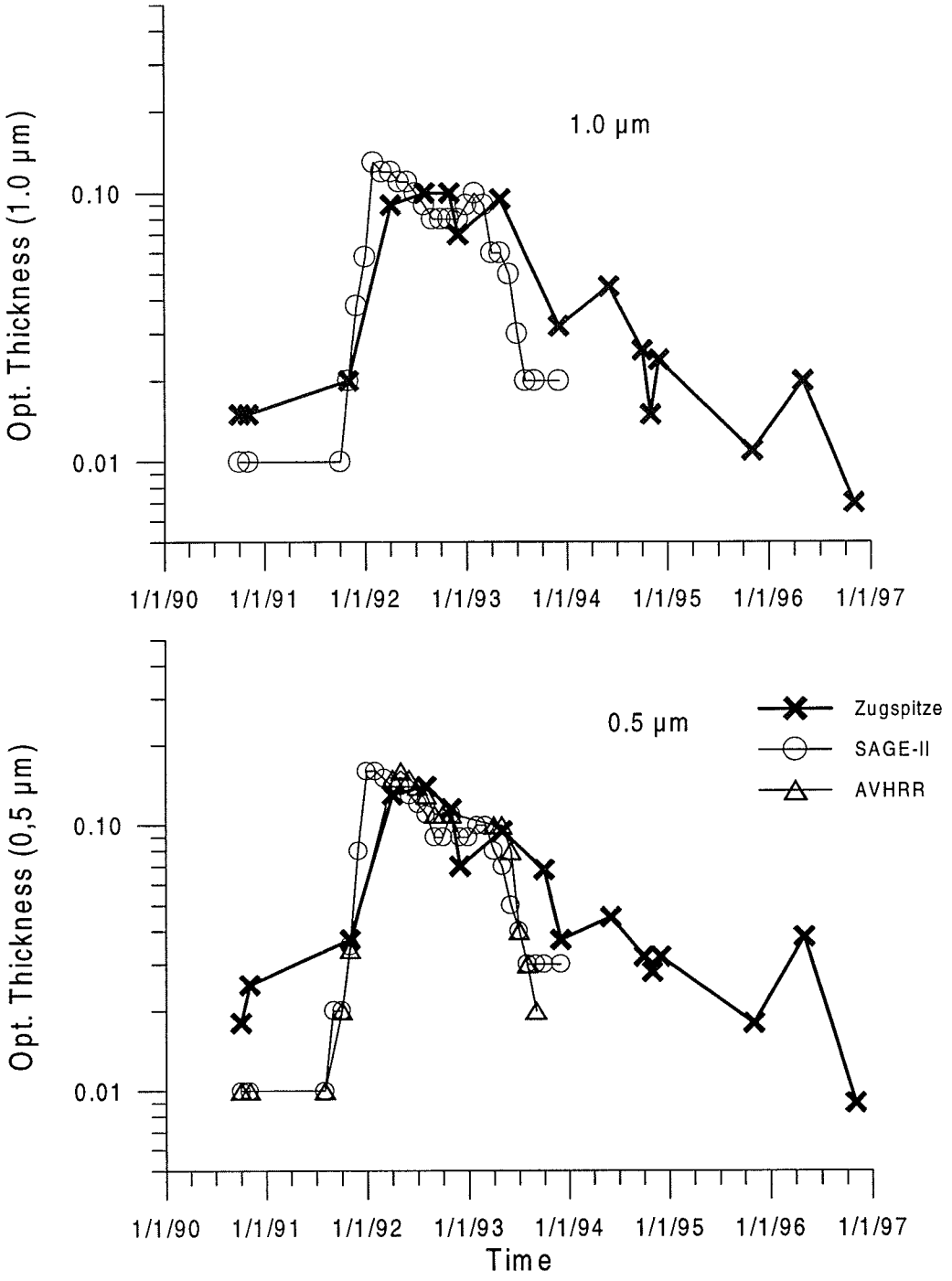

Abb. 2: Vergleich optischer Dicken der Messungen auf der Zugspitze und Retrievals von SAGE-II und AVHRR für 50°N für 0.5 µm und 1.0 µm Wellenlänge.

Die spektralen optischen Dicken des Pinatubo-Aerosols dieser Meßkampagnen sind von Ansmann et al., 1998 mit den Ergebnissen der LIDAR-Messungen (Raman-LIDAR der GKSS) verglichen worden. Dabei zeigten sich in den meisten Fällen Übereinstimmungen bei den Wellenlängen 1.064 und 0.532 µm. Während der Hauptphase des Pinatubo-Einflusses gab es auch Übereinstimmungen bei 0.355 µm.

Tabelle 1: Übersicht über die Trübungsparameter α und $\beta = \delta_A(1{,}0\ \mu m)$ des Angström'schen Potenzgesetzes für den gesamten Spektralbereich von 0.35 - 1,1 µm und α^* für den reduzierten Spektralbereich von 0.35 - 0.6 µm, sowie die optische Dicke des Aerosols $\delta_A(0{,}5\ \mu m)$ für eine Wellenlänge von 0.5 µm.

Zeitraum	α	β	α^*	$\delta_A(0{,}5\ \mu m)$
Sept. 1990	1.0	0.015	1.4	0.018
Okt. 1990	1.0	0.015	1.0	0.025
Okt. 1991	1.0	0.020	0.9	0.037
März 1992	0.2	0.090	-0.2	0.130
Juni 1992	0.3	0.100	0.0	0.140
Okt. 1992	0.2	0.100	0.1	0.115
Nov. 1992	-0.1	0.070	-0.1	0.070
April 1993	0.0	0.095	-0.1	0.095
Nov. 1993	0.0	0.032	-0.1	0.037
Mai 1994	0.4	0.045	0.4	0.045
Sept. 1994	1.0	0.026	1.4	0.032
Nov. 1994	1.1	0.024	1.4	0.032
Okt. 1995	1.1	0.011	1.5	0.018
Okt. 1996	0.8	0.007	0.8	0.009

Jedoch ab Ende 1994, als die größeren Spektralverläufe wieder auftraten, wurden vor allem bei der Wellenlänge 0.355 µm höhere optische Dicken als mit dem LIDAR erhalten. Daher sehen wir in dem stärkeren Spektralabfall, der sich auf den Wellenlängenbereich 0.35 - 0.6 µm beschränkt, vor allem einen Einfluß der freien Troposphäre, während ab 0.6 µm und mehr der Einfluß des vulkanischen Aerosols in der Stratosphäre noch erkennbar ist.

3.2. Himmelshelligkeitsfunktion

Ab 1993 wurde versucht, zusätzlich zur optischen Dicke die normierte Himmelshelligkeitsfunktion im Almukantar als weiteres optisches Charakteristikum der unbewölkten Atmosphäre zu ermitteln. Die normierte Himmelshelligkeitsfunktion wurde in zwei Wellenlängen (λ = 0.556 und 0.870 µm) gemessen. Sie ergibt sich als

$$p_{Sky}(\theta, \lambda) = L_{Sky}(\theta, \lambda) / \int_0^{180} L_{Sky}(\theta, \lambda) \sin\theta \, d\theta$$

mit

$$L_{Sky}(\theta, \lambda) = 1/M \quad i_{Sky}(\theta, \lambda) / (i_0(\lambda) \exp(-\delta(\lambda) M)),$$

der unnormierten Himmelshelligkeitsverteilung im Almukantar, wobei $i_{Sky}(\theta, \lambda)$ die gemessenen Werte für die Himmelshelligkeit zu den einzelnen Streuwinkeln

$$\theta = \arccos(\sin 2h + \cos 2h \cos\varphi)$$

ist. M ist die relativ durchstrahlte Luftmasse zur Sonnenhöhe h, φ ist der Azimuthwinkel relativ zur Sonnenposition und $i_0(\lambda)$ ist der Kalbrierwert für das 'extraterrestrische' Gerätesignal,

das durch die Langley-Plot-Kalibrierung gewonnen wird, jedoch hebt sich der Einfluß durch die Verwendung der normierten Himmelshelligkeitsunktion, wie auch der des Sonnenstandes wieder heraus.

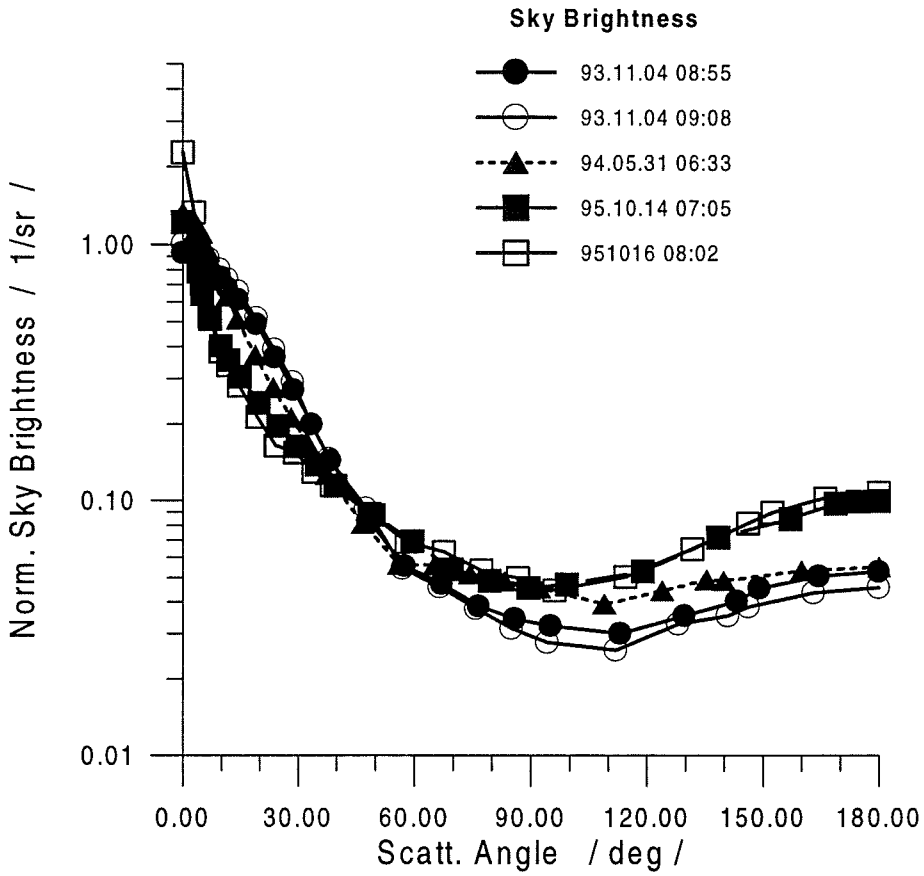

Abb. 3: normierte Himmelhelligkeitsverteilungen von Kampagnen auf der Zugspitze für die Wellenlänge von 870 nm.

Die normierte Himmelshelligkeitfunktion ist eine für eine Trübungssituation charakteristische Helligkeitverteilung in Abhängigkeit vom Streuwinkel im Sinne einer Phasenfunktion, allerdings noch mit dem Einfluß der Mehrfachstreuung behaftet. Die Aerosolphasenfunktion wird daraus durch Abtrennen der Mehrfachstreuung mit Hilfe des CIRATRA-Ansatzes ermittelt, vgl. 3.4.. Dennoch ist der Anteil der Mehrfachstreuung unter Zugspitzbedingungen gering und im wesentlichen auf die Rayleighstreuung beschränkt. Daher lassen sich in Spektralkanälen, in denen der Einfluß der Rayleighstreuung gering ist (z.B. bei $\lambda = 0.87\ \mu m$) deutlich die Veränderungen in der Phasenfunktion der Atmosphäre durch Änderung der columnaren Aerosolmenge und Größenverteilung erkennen, Abb. 3.

Da normierte Himmelshellgkeitsverteilungen erst ab November 1993 vorlagen (die Kampagnen vor Beginn des Projekts sahen solche Messungen nicht vor), konnten nur noch die Daten vom November 1993 den flachen Spektralverläufen der optischen Dicke (α um 0) zugeordnet werden, die als typisch für das vulkanische Aerosol angesehen werden. Begrenzt sind auch noch die Daten vom Mai 1994 verwendbar. Bei allen späteren Kampagnen waren größere Spektralabfälle charakteristisch.

3.3. Aerosolgrößenverteilung

Die spektralen optischen Dicken und die Hellgkeitsverteilung in der Sonnenaureole im Streuwinkelbereich von 3 - 12 Grad dienen als Eingangsdaten für die Inversion der columnaren Aerosolgrößenverteilung. Mit Hilfe eines zufallsgesteuerten nichtlinearen iterativen Inversionsansatzes werden Aerosolgrößenverteilungen in Form einer sektionalen Darstellung im Radienbereich von 0.08 - etwa 4 µm
erhalten, Die Inversionsrechung benötigt als weiteren Eingabeparameter den mittleren Berchungsindex für das Aerosol, der aus der Auswertung der kombinierten Messungen von spektraler optischer Dicke und Himmelshelligkeisfunktion mit Hilfe des CIRATRA-Ansatzes erhalten wurde, vgl. Abschnitt 3.3.

Beispiele invertierter Größenverteilungen zeigt Abb. 4. Durch die Anpassung von mehrmodalen logarithmischen Normalverteilungen an die sektionale Größenverteilung sind die Modenparameter (r_0, σ_0, N_0) für die einzelnen gefundenen Moden I, II, III ermittelt worden, die zum Vergleich mit den in der Literatur verwendeten Aerosolmodellen dienen. Ebenso gestattet die Modendarstellung eine einfache Bestimmung integraler Größen, wie Gesamtmasse oder relative Oberfläche in der durchstrahlten Säule, vgl. Tab. 2.
Für die Bestimmung der Säulenmasse wurde eine Dichte von 1.64 g/cm³ zugrundegelegt. Die Angaben der Säulenmasse und des Säulenvolumens sind etwas kleiner als die Angaben, die aus den LIDAR-Messungen, vgl. Ansmann et al., 1997. Das liegt daran, daß dort der effektive Radius einer monomodalen Verteilung für alle Abschätzungen zugrundegelegt wurde, während für die Berechnungen dieses Projekts multimodale Verteilungen mit den Parametern der Tabelle 2 Verwendung fanden.

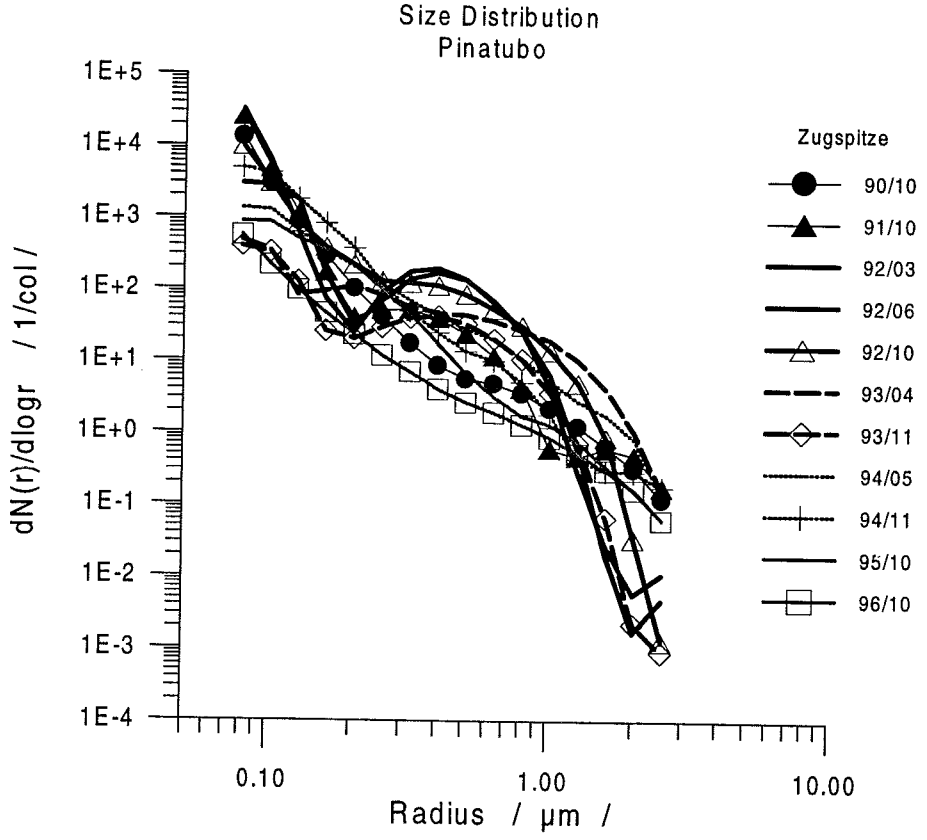

Abb. 4: Invertierte columnare Aerosolgrößenverteilungen zu den Meßkampagnen auf der Zugspitze (Gesamteffekt).

Unsere Erfahrungen zeigten, daß der sehr oft verwendete effektive Radius kein geeigneter Parameter ist, um die klima-relevanten optischen Eigenschaften des Aerosols zu beschreiben, weder der spektrale Gang der optischen Dicke noch die Phasenfunktion lassen sich mit dem effektiven Radius ausreichend gut darstellen, so daß vor allem Aussagen zu spektralen Strahldichten und Strahlungsflußdichten, die damit gewonnen wurden, fehlerhaft sind. Für die Modellierung des Strahlungsfelds werden multimodale Verteilungen oder die optischen Parameter direkt benötigt.
Während Mode II und III im Bereich geringer Inversionsfehler liegen, liegt die Mode I am Rande des invertierbaren Größenbereichs. Das Vorhandensein sehr kleiner Partikeln (Mode I) kann durch die verwendete Inversionsprozedur noch ermittelt werden, jedoch der Hauptteil der Mode liegt außerhalb des invertierbaren Bereichs, so daß vor allem die integralen Größen, wie Masse und Oberfläche nicht überbewertet werden dürfen. Deutlich ist das Verschwinden des stratosphärischen Background-Aerosols in Mode I mit der Zunahme der Hauptmode des vulkanischen Aerosols (Mode III).

Tabelle 2: Modenparameter der Aerosolgrößenverteilungen für logarthmische Normalverteilungen zu den einzelnen Meßkampagnen.

Zeit	Mode Nr.	Radius r_0 µm	σ_0	N_0	Säulen-masse mg/m²	Säulen-oberfläche m²/m²
Sept. 1990	I	0.049	1.46	6050.89	7.13	0.2466
	III	0.659	1.51	2.19	6.95	0.0168
Okt. 1990	I	0.042	1.55	6565.46	6.31	0.2226
	II	0.139	1.80	28.41	1.87	0.0138
	III	0.637	1.60	1.53	5.51	0.021
Okt. 1991	I	0.046	1.95	1737.11	6.59	0.1140
	III	0.339	1.56	8.78	4.31	0.0189
März 1992	II	0.260	1.39	83.13	12.38	0.0883
	III	0.549	1.28	17.73	20.34	0.0795
Juni 1992	II	0.216	1.42	136.01	12.33	0.1023
	III	0.479	1.35	27.87	23.73	0.0963
Okt. 1992	II	0.131	1.53	246.01	6.48	0.0766
	III	0.497	1.46	27.96	33.87	0.1159
Nov. 1992	II	0.218	1.72	56.15	11.39	0.0608
	III	0.771	1.38	4.82	18.20	0.0444
April 1993	II	0.210	1.36	37.89	2.80	0.0256
	III	0.553	1.48	22.46	39.21	0.1176
Nov. 1993	II	0.273	1.44	18.38	3.53	0.0225
	III	0.622	1.39	4.89	8.23	0.0243
Mai 1994	II	0.119	1.77	216.07	8.23	0.0744
	III	0.525	1.53	4.87	8.23	0.0243
Sept. 1994	I	0.041	1.60	10288	10.16	0.3449
	II	0.165	1.52	46.31	2.38	0.0226
	III	0.657	1.45	3.27	8.93	0.0234
Nov. 1994	I	0.037	1.72	9937.53	9.98	0.3132
	II	0.211	1.52	21.26	2.27	0.0169
	III	0.870	1.39	1.71	9.46	0.0202
Okt. 1995	I	0.050	1.47	6683,12	7.48	0.2588
	III	0.643	1.52	1.54	5.61	0.0123
Okt. 1996	I	0.078	1.43	832.87	5.37	0.1857
	III	0.636	1.52	1.14	4.14	0.0100

Das normale stratosphärische Background-Aerosol scheint durch Koagulation im vulkanischen Aerosol integriert zu werden. Erst ab September 1994 ist wieder eine Ausbildung einer stratosphärischen Background Mode zu beobachten.
Auf eine Anpassung einer Mode für Teilchen größer 1 µm Radius wurde verzichtet, da vor allem für die Meßkampagnen vor November 1993 keine Himmelshelligkeitsmessungen (speziell der winkelabhängigen Aureolenhelligkeit vorlagen) und dann die Bestimmung großer Teilchen unsicher ist.
Die Mode II ist sehr variabel mit Mode-Radien um 0.2 µm. Sie umfaßt die kleineren Partikel des Pinatubo-Aerosols
Die Hauptmode des stratosphärischen Aerosols ist die Mode III, deren Modenradius r_0 von ca. 0.3 µm im Oktober 1991 bis auf 0.7 µm gegen Ende 1994 anwächst, vgl. Abb. 5. Es ist anzunehmen, daß die Mode III in den Ergebnissen von 1990 ein Rest gealterten vulkanischen Aerosols aus vorangegangenen Vulkanausbrüchen (El Chichon) ist. Auch 1996 ist diese Mode, wenn auch sehr schwach, noch erkennbar.

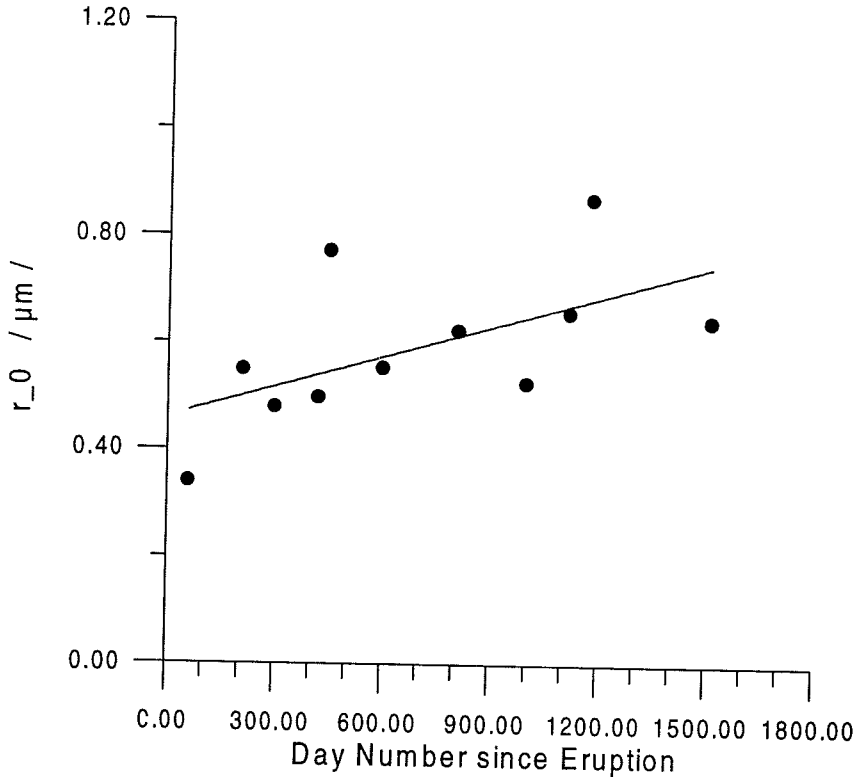

Abb. 5: Mode Radius r_0 für Mode III, der optischen Hauptmode des stratosphärischen Vulkanaerosols.

Unsere Ergebnisse zeigen eine signifikante Tendenz zum Anwachsen des Modenradius der Mode III, die in Form folgender Parameterbeziehung für den Moderadius mit der Zeit t in Tagen seit dem Ausbruch angegeben werden kann:

$$r_0\,(t) = 0.000187 * t\,[d] + 0.469.$$

Vergleichen wir die erhaltene Modenstruktur, so ist sie in keiner Weise vergleichbar mit den Annahmen, die in den Aerosolmodellen (WCP 55, 1983 und d'Almeida et al, 1991) getroffen werden. Dort wird zwar eine Mode für H_2SO_4-dropletts bei $r_0 = 0.069$ µm angegeben, die mit der Mode I Übereinstimmungen zeigt, die Mode III fehlt in den Modellangaben völlig. Mode III bestimmt jedoch im wesentlichen die optischen Eigenschaften des Pinatubo-Events und ist

mit den Ergebnissen für den effektiven Radius vergleichbar. Dagegen wird in den Modellen eine Mode bei $r_0 = 0.217$ angenommen, die in den vorliegenden Ergebnissen aus den Meßkampagnen (Mode II) nur untergordnete Bedeutung hat oder nur für nicht gealtertes vulkanisches Aerosol zutreffen kann.
Die Hauptmode, die in unseren Meßkampagnen gefunden werden konnte, ist nicht in den Aerosolmodellen erwähnt. Andererseits, experimentelle Ergebnisse zu Untersuchungen der Modenstruktur des El-Chichon-Aerosols (Pueschel et al. 1988, Jeager & Hoffman, 1991) zeigen eine ähnliche Modenstruktur, wie sie aus den Inversionsrechnungen zu den Meßkampagnen erhalten wurde.

3.4. Brechungsindex und Phasenfunktion

Ab November 1993 konnten auf der Zugspitze kombinierte Messungen von spektraler optischer Dicke und Himmelshelligkeitfunktion im Almukantar durchgeführt werden (vgl. 3.1. und 3.2.). Diese bilden die Eingangsdaten für das gekoppelte Inversions-Strahlungstransfer-Programm CIRATRA (Coupled Inversion Radiation TRAnsfer), Wendisch & von Hoyningen-Huene, 1992, 1994, zur Bestimmung von Brechungsindex, Phasenfunktion, Asymmetrieparameter und Angaben zur Teilchenform. Dieser Schließungsansatz zwischen spektraler optischer Dicke, Aureolenhelligkeitsverteilung und Himmelshelligkeitsverteilung gestattet die genannten Größen als columnare Werte zu ermitteln.

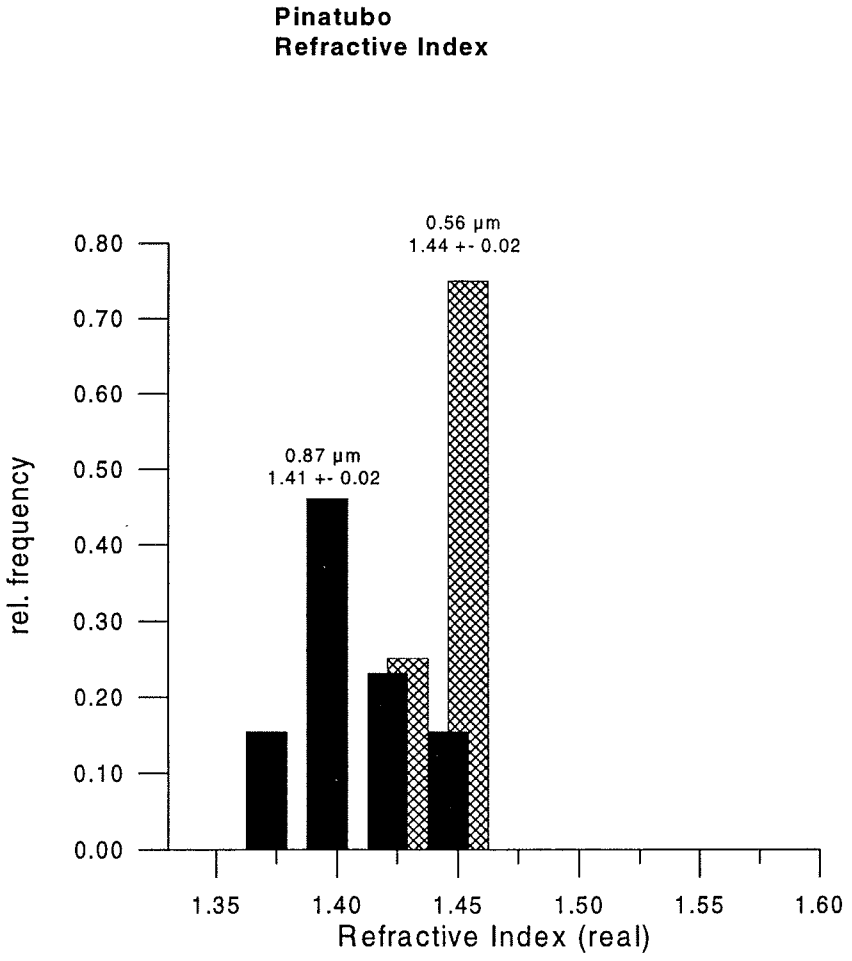

Abb. 6: Relative Häufigkeiten der erhaltenen Brechungsindizes (Realteil) für die Wellenlängen 556 und 870 nm.

Generell kann festgestellt werden, daß alle kombinierten Messungen, die den Einfluß des Pinatubo-Aerosols enthielten, gut mit der Annahme der Mie-Theorie für die Lichtstreuung an den Aerosolteilchen zu lösen waren. Die RMSD Werte zwischen gemessener und berechneter Himmelshelligkeitsfunktion lagen in der Regel bei 4 ... 5 %. Daher kann die Kugelform für die streuenden Partikel bestätigt werden. Aufwendige Kalkulationen zur Anwendung anderer nichtsphärischer Streutheorien konnten entfallen.

In Abb. 6 sind die relativen Häufigkeiten der erhaltenen Werte für den Realteil des Brechungsindexes für die beiden verwendeten Wellenlängen (0.87 und 0.556 µm) und die Messungen der Kampagnen von November 1993 und Mai 1994 enthalten, in denen noch ein nennenswerter Einfluß des stratosphärischen Vulkanaerosols in den Spektralverläufen erkennbar war. Als Mittelwerte für den Realteil des Brechungsiondex wurden erhalten: m(0.87 µm) = 1.41 ± 0.02 und m(0.56 µm) = 1.44 ± 0.02. Inwieweit die Unterschiede Ausdruck eines spektralen Gangs sind, ist auf Grund der Fehler unsicher.
Die Aerosolmodelle nehmen für vulkanisches Aerosol H_2SO_4-dropletts an, mit Brechungsindices von m(0.87 µm) = 1.425 und m(0.55 µm) = 1.43. Diesbezüglich besteht Übereinstimmung im Rahmen der Inversionsfehler.
Abb. 7 zeigt die Phasenfunktionen für die Wellenlänge 0.87 µm für das Pinatubo-Aerosol, von den Tagen mit guten Meßbedingungen. Daraus ergeben sich folgende Asymmetrieparameter:

λ / µm	0.87	0,56
g	0,76 ± 0,011	0.72 ± 0,012

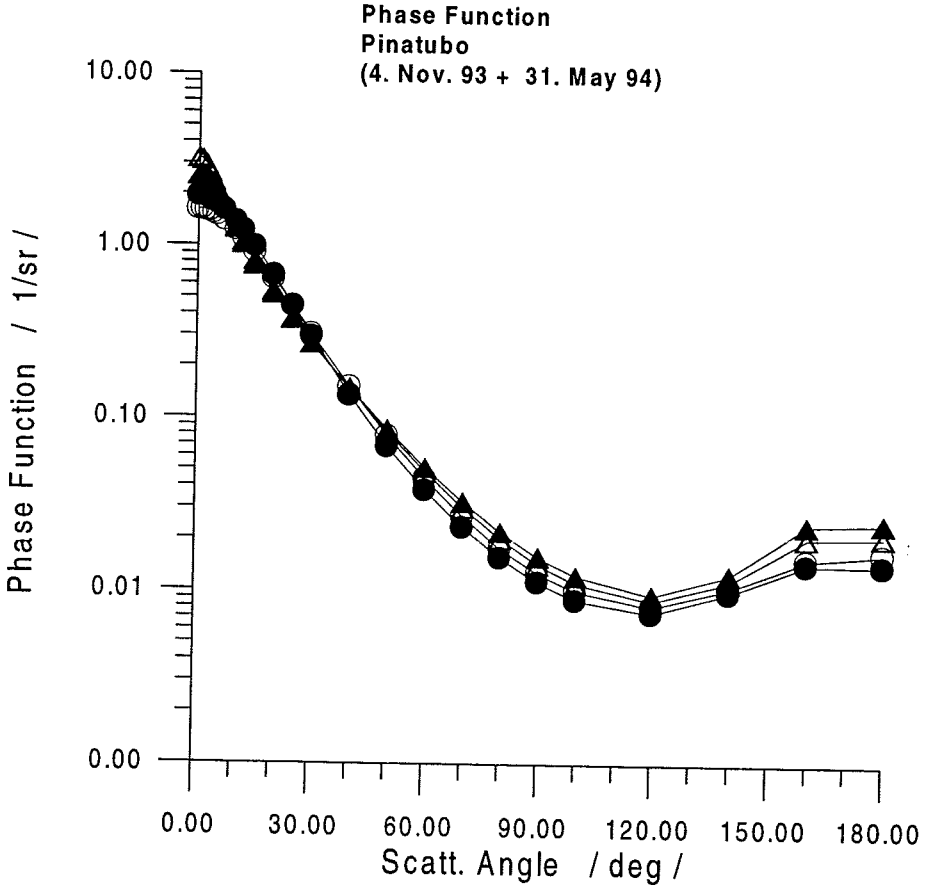

Abb. 7: Aerosolphasenfunktion aus CIRATRA für 870 nm Wellenlänge zu den Messungen vom November 1993 und Mai 1994.

Damit liegen aus indirekten Strahlungsmessungen alle wesentlichen klimarelevanten optischen Aerosolparameter vor. Ausnahme bildet die Single Scattering Albedo, für die zum Zeitpunkt der Messungen der erweiterte Schließungsansatz noch nicht fertig entwickelt war.

4. Abschätzungen zum kurzwelligen Strahlungsforcing durch das stratosphärische Vulkanaerosol

Mit dem Vorliegen aller wesentlichen klimarelevanten optischen Aerosolparameter (spektrale optische Dicke und Phasenfunktion bzw. Asymmetrieparameter) ist eine Abschätzung des kurzwelligen Strahlungsforcings, d.h. die Bestimmung der Strahlungsbilanzänderung am Oberrand der Atmosphäre, durch das Pinatubo Aerosol möglich. Dazu wurde ein spektrales kurzwelliges Strahlungsflußmodell erstellt, das für die gegebenen optischen Aerosolparameter die auf- und abwärtsgerichteten Strahlungsflüsse in 512 Spektralkanälen im Wellenlängenbereich von 0.3 - 3.9 µm monochromatisch für jede mögliche Sonnenhöhe berechnet. Die notwendigen spektralen Eingangsdaten werden durch Extrapolation der gemessenen Größen gewonnen. Die Integration über die Spektralkanäle liefert die kurzwelligen ab- und aufwärtsgerichteten Flüsse am Unterrand und Oberrand der Atmosphäre. Die Wichtung dieser Ergebnisse mit der Häufigkeitsverteilung der verschiedenen Sonnenstände und der Bezug auf eine reine Molekülatmosphäre liefert globale und zonale Mittelwerte für das kurzwellige Strahlungsforcing durch das Aerosol.

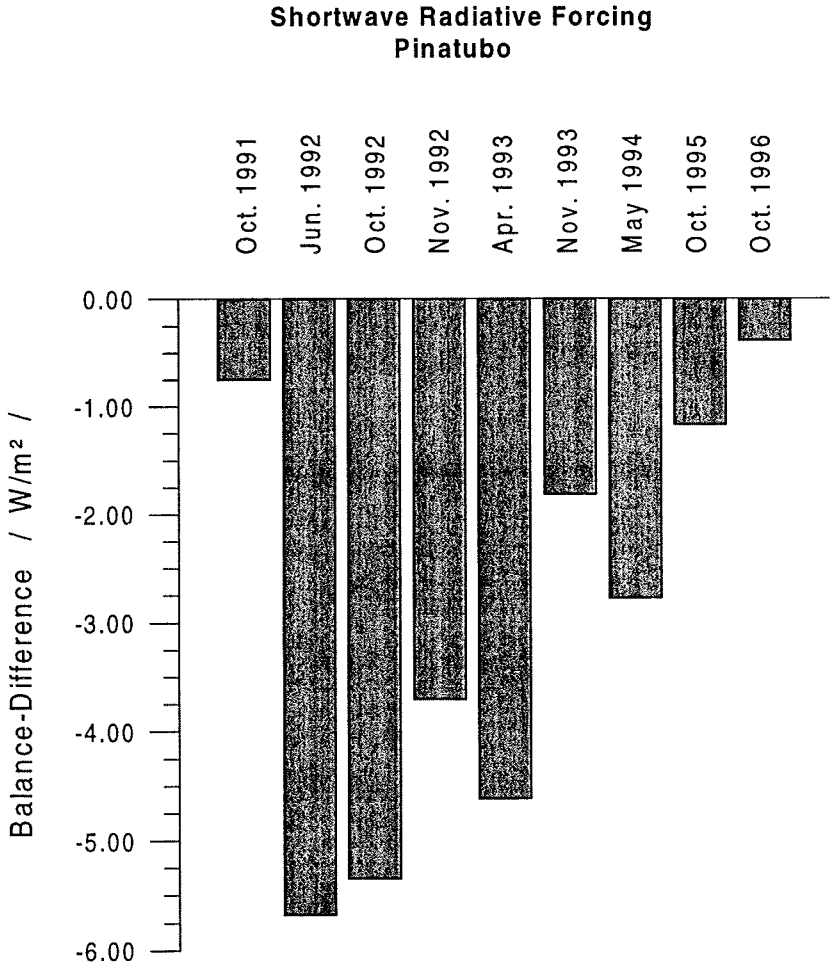

Abb. 8: Kurzwelliges Strahlungsforcing des Pinatobo-Aerosol am Oberrand der Atmosphäre (bezogen auf eine reine Rayleigh-Atmosphäre).

Die Ergebnisse für das kurzwellige Strahlungsforcing durch das Pinatubo Aerosol zum Zeitpunkt der Meßkampagnen enthält Abb. 8. Im Maximum des Pinatubo-Einflusses wurde eine Verringerung der Strahlungsbilanz um - 5.7 W/m² erreicht. Der unbelastete Zustand von Ende 1996 gab zusammen für Stratopshäre und freie Troposphäre einen Wert von - 0.39 W/m². Das Ergebnis steht in Einklang mit Angaben von ERBE. Auch in den Folgejahren (bis in das Jahr 1995 hinein) hat der Pinatubo durch Erhöhung der planetaren Albedo zu einer Absenkung der Strahlungsbilanz beigetragen. Erst mit den Daten vom Herbst 1996 wurde der Zustand von 1990 und 1991 unterschritten, so daß sich wieder so gut wie unbelastete Bedingungen in der Stratosphäre eingestellt hatten.

5. Zusammenfassung

Die im Rahmen des Projekts gewonnenen optischen Charakteristika gestatteten Parameter abzuleiten, die die Strahlungseigenschaften des Pinatubo Aerosols beschreiben. Auf der Basis der gewonnenen Daten konnte optisch relevante columnare Größenverteilung mit ihrer Modenstruktur erhalten werden und dem Aerosolmodell 'volcanic' der Aerosolklimatologie gegenübergestellt werden. Während im dort angenommenen Brechungsindex kein signifikanter Widerspruch zu den Ergebnissen diese Projekts auftrat, fehlte im 'volcanic' Modell die optische Hauptmode des Pinatubo-Aerosols. Es konnten weiterhin Angaben zum Anwachsen des Modenradius und der Alterung der Mode mit der Zeit in Form einer Regressionsbeziehung abgeleitet werden, die in ein neues Modell für vulkanische Aerosole in der Stratophäre einfließen sollen. Wesentlich für die Abschätzung des kurzwelligen Strahlungsforcings ist die Bestimmung der Phasenfunktion und des Asymmetrieparameters für das Pinatubo-Aerosol. Mit den im Projekt ermittelten klimarelevanten optischen Aerosolparametern für das Pinatubo Aerosol ist das kurzwellige Strahlungsforcing durch den vulkanischen Impakt abgeschätzt worden.

Danksagung

An dieser Stelle möchte ich dem BMBF und dem Koordinator des Verbundprojekts 'Spurenstoffkreisläufe' für die Förderung und Unterstützung danken.

Da die Datengewinnung schon lange vor dem Projekt begonnen hatte, haben an den hier dargestellten Arbeiten, die sich mit der Untersuchung des Pinatubo-Aerosols befaßten, unterschiedliche Projekte, die Rahmen der ehemaligen Arbeitsgruppe an der Universität Leipzig bearbeitet wurden und die damit befaßte Mitarbeiter unterschiedlichen Anteil:

1. SANA:	Michael Stettler, Torsten Plaul
2. BayFORKLIM:	
3. dieses Projekt:	Peter Posse
4. DFG 'Nichtsphärizität'	Karin Wenzel
5. ACE-2	Torsten Schmidt

Allen sei an dieser Stelle für ihre Beiträge gedankt.

Literatur:

d'Almeida G. A., Koepke, P., Shettle, E.P.: Atmospheric aerosol. Global climatology and radiative characteristics. Deepak Publ., Hampton 1991.

Ansmann, A. Mattis, I. Wandinger, U. Wagner, F., Reichhardt, J., Deshler, T.: Evoution of the Pinatubo Aerosol: Raman Lidar Observations of Particle Optical Depth, Effective Radius, Mass, and Surface Area over Central Europe at 53.4°N. J. Atmos. Sci 54 (1997) 2630-2641.

Ansmann, A., Mattis, I., Jäger, H., Wandinger, U.: Stratospheric Aerosol Monitoring With Lidar: Conventional Backscatter versus Raman Lidar Observations of Pinatubo Aerosol. Contr. Atm. Phys. (1998) (submitted 1997).

GADS, 1997: Koepke, P., Hess, M., Schult, I., Shettle, E.P.: Global aerosol Data set. Theoretical and Applied Climatology, (submitted, 1997).

Jeager, H., Hoffman, D.: Midlatitude lidar backscatter to mass, area, and extinction conversion model based on in situ aerosol measurements from 1980 to 1987. Applied Optics 30 (1991) 127-138.

Jaeger, 1997, personal communication

Nakajima, T., Tanaka, M.: Algorithms for radiative intensity calculations in moderately thick atmospheres using a truncation approximation. J. Quant. Spectrosc. Radiat. Transfer 40 (1988) 51-69.

Posse, P., von Hoyningen-Huene, W.: Climate-relevant parameters of stratospheric aerosol under consideration of Pinatubo event. Contr. Phys. Atmos. (1998) (submitted 1997).

Pueschel, R.F., Snetsinger, K.G., Livingston, J. M.: Effects of El-Chichon volcanic effluents on stratospheric aeroslo dynamics. In: P.E. Wagner, G. Vali (Eds) Lecture Notes in Physics (309) 'Atmospheric Aerosols and Nucleation' -Proceedings of the 12 Int. Conference on Atmospheric Aerosol and Nucleation, Vienna 22-27. Aug. 1988 221-223. Springer 1989.

WCP 55: A. Deepak and H. Gerber (Eds): Report of the expert meeting on aerosols and their climatic effects, WMO-Publ. Genf WCP-55 (1983).

Wendisch M. and von Hoyningen-Huene, W.: Optically equivalent refractive index of atmospheric aerosol particles, Beitr. Phys. Atmosph. \rm \bf 65, \rm 293-309 (1992).

Wendisch, M., von Hoyningen-Huene, W.: Possibility of refractive index determination of atmospheric aerosol particles by ground based solar extinction and scattering measurements. Atmos. Environment 28 (1994) 785-795.

Korrespondenz bitte an:

Dr. habil. Wolfgang von Hoyningen-Huene
Universidate de Evora
Dept. Fisica
R. Romero Ramalha 59
P-7000 Evora
Portugal

Zur Grobabschätzung von Schwebstaubkonzentrationen aus Sichtweitenbeobachtungen

Wolfgang von Hoyningen-Huene

Zusammenfassung:

Ein Weg zur Abschätzung von Schwebstaubkonzentrationen aus Sichtweitenbeobachtungen in einer belasteten Atmosphäre auf der Basis der Sichtweitentheorie nach Koschmieder, 1925 unter Berücksichtigung der Feuchtigkeit wird beschrieben.

Summary:

An approach for the estimation of concentrations of particulate matter in a polluted atmosphere has been described basing on the view range by the Koschmieder formula under consideration of the relative humidity.

1. Einführung

In manchen Fällen, wenn keine oder keine zuverlässigen Meßgeräte zur Verfügung stehen oder wenn Zweifel an angegebenen Meßwerten bestehen, kann die Sichtweite zu einer Grobabschätzung von Schwebstaubkonzentrationen und zur groben Bewertung von Belastungssituationen herangezogen werden. Dabei sollte man sich im Klaren sein, daß die Sichtweite selbst eine subjektive Größe ist, wenn sie aus einer visuellen Beobachtung stammt. Ebenso ist die Sichtweite Ausdruck des Feuchteeinflusses auf das atmosphärische Aerosol.

Eine solche Situation tritt dann auf, wenn z.B., wie in den Waldbrandgebieten Südostasiens, Bewertungen der Umweltsituation anzufertigen sind, jedoch keine oder nur unvollkommene Meßdaten verfügbar sind, bzw. es auch nicht möglich ist, entsprechende Meßgeräte an Ort und Stelle zu bringen.

Die hier vorgestellte Methode zur Grobeinschätzung von Schwebstaubkonzentrationen setzt sich aus verschiedenen Teilschritten zusammen, die zu einer Gesamtaussage vereint worden sind:

1. Sichtweitentheorie nach KOSCHMIEDER, 1925 und der darauf aufbauenden Bestimmung des aktuellen Extinktionskoeffizienten der Luft,
2. Korrektur des Feuchteeinflusses auf den Extinktionskoeffizienten, d.h. Berechnung eines feuchtenormierten Extinktionskoeffizienten,
3. Anwendung von empirischen Korrelationsbeziehungen zwischen feuchtenormierten Extinktionskoeffizienten und Schwebstaubkonzentrationen.

Während für unsere Untersuchungen im Rahmen des SANA-Projekts (SANA = Wissenschaftliches Begleitprogramm zur Sanierung der Atmosphäre über den neuen Bundesländern) der Extinktionskoeffizient mit Hilfe einer LASER-Transmissionsstrecke in Leipzig bestimmt wurde und damit eine objektivere Grundlage hatte als eine Sichtweitenbeobachtung, ist aber generell

das Vorgehen analog, vgl. UHLIG & von HOYNINGEN-HUENE, 1993, UHLIG et al., 1994, von HOYNINGEN-HUENE, 1996, STETTLER & von HOYNINGEN-HUENE, 1994. Ein ähnliches Vorgehen ist auch zu empfehlen, wenn Daten eines Sichtweitenmeßgeräts z.B. an einem Flughafen zur Verfügung stehen, die gerade wenn geringe Sichtweiten vorliegen zuverlässiger sind als die visuelle Beobachtung.

2. Darstellung der Methodik

Im folgenden sollen die 3 Teilschritte dargestellt und kommentiert werden, damit eine individuelle Einschätzung der Toleranzbereiche für die Gesamtaussage möglich wird.

a) Bestimmung des Extinktionskoeffizienten der Luft aus der Sichtweite

Entsprechend der Sichtweitentheorie nach KOSCHMIEDER, 1925 ergibt sich der Extinktionskoeffizient der Luft a_{ext} aus der Horizontalsichtweite VV als:

$$a_{ext}\,[1/km] = 3{,}912 / VV\,[km]. \qquad (1)$$

Dabei ist der Faktor 3,912 von Koschmieder für eine Kontrastschwelle des menschlichen Auges von 0,02 ermittelt worden. Koschmieder definierte die Sicht als die Entfernung in der ein schwarzes Objekt mit der angegebenen Kontrastschwelle gerade noch vom grauen Hintergrund des Himmelslichts (am Horizont) sichtbar ist. Da man aber im Bereich der Technik (vor allem im Luft- und Straßenverkehr) eine größere Sicherheit bei der individuellen Erkennbarkeit von Objekten bevorzugt (ILO-Standard), wird für diese Zwecke eine Kontrastschwelle von 0.05 verwendet und die Beziehung von Koschmieder modifiziert sich zu

$$a_{ext}\,[1/km] = 2{,}97 / VV\,[km]. \qquad (2)$$

Die Beziehung (2) liefert kleinere Extinktionskoeffizienten, die aber besser mit denen unserer Laser-Transmissionsstrecke in Leipzig übereinstimmten und auch mit den Angaben von Sichtweitenmeßgeräten konform gehen sollten, da diese auch den ILO-Standard verwenden.

Dieser Extinktionskoeffizient bezieht sich auf die aktuelle relative Feuchte und ist daher sehr variabel. Um den Extinktionskoeffizienten des Aerosols zu erhalten müßte, theoretisch von diesem Wert der Extinktionskoeffizient der Luftmoleküle (Rayleighstreuung) abgezogen werden. Dieser Wert ist für Normaldruck und eine Wellenlänge von 550 nm

$$a_{ext\text{-}Rayleigh} = 0{,}012\ [1/km]$$

und ist daher nur bei großen Sichtweiten zu berücksichtigen.

$$a_{ext\_Aersol} = a_{ext} - a_{ext\_Rayleigh} \qquad (3)$$

b) Bestimmung des feuchtenormierten Extinktionskoeffizienten

Um den gemessenen oder aus Beobachtungen abgeleiteten Extinktionskoeffzienten vom variablen Einfluß der relativen Feuchte f zu befreien, wurden von uns erfolgreich die Beziehungen von HÄNEL, 1976, 1984 für den Feuchteeinfluß verwendet. Vor allem die Parametrisierungen für 'urban' Aerosol in der Arbeit von 1984 ließen den Feuchteeinfluß in den Meßreihen aus

Leipzig nahezu verschwinden und waren daher für eine Feuchtekorrektur in Leipzig geeignet, vgl. UHLIG et al. 1994. Der feuchtenormierte Extinktionskoeffizient für das 'urban' Modell ergibt sich nach HÄNEL als

$$a_{ext}\,(f = 0) \;=\; B\;(1 - f)^{-A}\;\; a_{ext\_Aerosol} \qquad (4\,a)$$

für relative Feuchten $0{,}7 < f < 0{,}99$. Dabei sind für das 'urban' Modell folgende Koeffizienten für A und B angegeben worden: A = 0,7585, B = 0,6648. Diese Potenzbeziehung beschreibt den starken nichtlinearen Anstieg der Extinktion mit der Feuchte bei hohen Luftfeuchtigkeiten.

Für relative Feuchten $f < 0{,}7$ wird die folgende Beziehung verwendet:

$$a_{ext}\,(f = 0) \;=\; D\,(1 - f)^{-C} \;*\; a_{ext\_Aerosol}. \qquad (4\,b)$$

Der Koeffizient C ergibt sich aus A und B als $C = A - \ln(B/0{,}3)$. D ist nicht in den Modellen von HÄNEL enthalten und ist aus unseren empirischen Befunden und aus Kontinuitätsgründen bei der Feuchte $f = 0{,}7$ bestimmt worden: D = 1,735.

Mit dieser Feuchtekorrektur ließen sich Extinktionskoeffizienten von der Laser-Transmissionsstrecke und von Aerosol-Filterproben vergleichen und gestatteten dann Beziehungen zwischen Schwebstaubkonzentrationen und Extinktionskoeffizienten abzuleiten.

c) Schwebstaubkonzentration und Extinktionskoeffizient

Eine theoretische Ableitung einer solchen Beziehung zwischen Extinktionskoeffizient und Schwebstaubkonzentration M ist prinzipiell über die Zugrundelegung der Lichtstreutheoerie (Mie-Theorie) bei Kenntnis der Aerosolgrößenverteilung und des mittleren effektiven Brechungsindexes durch Lösung der Fredholm'schen Integralgleichung möglich. Jedoch in Fällen, wie sie in der Einführung beschrieben sind, fehlen die benötigten Angaben. Daher sind empirisch aus Experimenten abgeleitetet Korrelationsbeziehungen günstiger, wenn auch sie sich auf bestimmte Aerosoltypen beziehen, unter denen die Experimente durchgeführt wurden.
M ist hier als Total Particulate Matter TPM zu verstehen.

Eine solche Beziehung ist z.B. von GRIGGS, 1975, 1979 für marines Aerosol für die Bestimmung von Aerosolkonzentrationen aus Satellitendaten über dem Ozean aus Konzentrationsmessungen und den optischen Dicken abgeleitet worden. Dabei wurde das Aerosolmodell 'maritime' von ELTERMANN, 1970 verwendet:

$$M\;[\mu g/m^3] \;= 420\;[(\mu g * km)/\,m^3] * a_{ext}\,(f = 0)\;[1/km]. \qquad (5a)$$

Generell ist der Proportionalitätsfaktor zwischen Extinktionskoeffizient und Aerosolmasse der Kehrwert der spezifischen Extinktion E.

$$M\;[\mu g/m^3] \;=\; a_{ext}\,(f = 0)\;[1/km] \,/\, E\;[m^3 / (\mu g * km)]. \qquad (5)$$

Für eine adäquate Verwendung dieser Beziehung ist die zutreffende spezifische Extinktion E für den vorherrschenden Belastungsfall erforderlich. Da die Beziehung von GRIGGS in erster Linie für maritimes Aerosol entwickelt wurde und daher die spezifische Extinktion für diesen Fall verwendet, ist sie nicht unbedingt die günstigste für den Fall des Waldbrand-Haze.

Bei den experimentellen Untersuchungen mit Hilfe der Laser-Transmissionsstrecke in Leipzig wurden direkt Korrelationsbeziehungen zwischen Schwebstaubkonzentrationen als TPM und dem feuchtenormierten Extinktionskoeffzienten in einer belasteten Atmosphäre abgeleitet. Die TPM-Werte stammten dort aus ß-Absorptionsmessungen, die vom Umweltfachamt Leipzig durchgeführt wurden, die feuchtenormierten Extinktionskoeffizienten von der Laser-Transmissionsstrecke, die während des SANA-Projekts in Leipzig betrieben wurde.

Dabei konnte eine Veränderung der spezifischen Extinktion im Zeitraum von 1991 bis 1995 beobachtet werden. 1995 hatte sich die Situation an Verhältnisse angenähert, wie sie z.B. in Berlin-Dahlem gemessen wurden, 1991 und 1992 waren signifikant kleinere Werte vorherrschend.

Aus den Leipziger Messungen ergaben sich folgende spezifische Extinktionen E bez. Proportionalitätsfaktoren 1/E:

Tabelle 1: Zeitliche Entwicklung der spezifischen Extinktion und des daraus resultierenden Proportionalitätsfaktors zwischen feuchtenormiertem Extinktionskoeffizienten und der Schwebstaubkonzentration

Jahr	E $[m^2/g]$	1/E $[\mu g*km / m^3]$
1991	3,33	300
1992	3,50	285
1993	2,37	422
1994	2,81	356
1995	2,42	413
Berlin	2,35	425

Die Ergebnisse dieser Untersuchungen zeigen, daß große spezifische Extinktionen (kleine Proportionalitätsfaktoren) für solche Gebiete gefunden wurden, in denen ein hoher Rußanteil im Aerosol vorhanden ist, wie in den neuen Bundesländern in den Jahren 1991 und 1992. Ähnliches wird auch in den Arbeiten von TRIER & HORVATH, 1993 bestätigt. Daher ist die Beziehung von GRIGGS (5a) mehr für remote conditions zutreffend und nicht für den Waldbrand-Haze. Hierfür sind Werte aus den Leipziger Messungen der Jahre 1991 und 1992 besser geeignet, da sie für höhere Trübungszustände und auch für einen höheren Rußgehalt im Aerosol zutreffend sind.

Daher wird für die Abschätzung von Schwebstaubkonzentrationen aus dem Waldbrand-Haze die folgende Relation vorgeschlagen:

$$M\ [\mu g/m^3] = 300\ a_{ext}\ (f = 0)\ [1/km]. \qquad (5b)$$

Die Daten des Jahres 1992 weisen darauf hin, daß noch kleinere Proportionalitätsfaktoren gefunden wurden. Leider liegen keine verläßlichen mittleren Angaben zur spezifischen Extinktion für den Zeitraum vor 1991 vor, so daß vorgeschlagen wird, den Wert von 300 zu verwenden anstatt der 420, wie in der GRIGGS'schen Beziehung, sofern keine bessere Datenbasis zur Verfügung steht.

3. Zusammengefaßte Schwebstaubabschätzung aus der Sichtweite unter Berücksichtigung des Feuchteinflusses

Fassen wir die Betrachtungen von 2 a - c zusammen, so erhält man folgende Relation, die den Feuchteinfluß in Rechnung stellt:

$$M = 300 * 2.97 / VV / (B * (1 - f)^{-A}) \quad \text{für } 0{,}99 > f > 0{,}7 \qquad (6a)$$

und

$$M = 300 * 2.97 / VV / (D * (1 - f)^{-C}) \quad \text{für } f < 0{,}7. \qquad (6b)$$

Die Einheiten sind, wenn die Koeffizienten wie vorstehend verwendet werden, M - die Aerosolmasse in $\mu g/m^3$, VV - die Sichtweite in km und f - die relative Feuchte als Mischungsverhältnis (< 1).

4. Diskussion von Ergebnissen

Die folgenden Ergebnisse sind Berechnungen für die resultierende Schwebstaubkonzentration bei verschiedenen relativen Feuchten f und für verschiedene Sichtweite VV. Sie zeigen, daß der Feuchteeinfluß einen großen Einfluß hat und eine ungenügende Kenntnis der Feuchte, vor allem im Bereich f > 0,8 zu erheblichen Fehlern von mehr als 100 % für die abzuschätzende Schwebstaubkonzentration führt. Dieser Effekt setzt sich fort für Feuchten f > 0,98.

Eine Erweiterung für noch kleinere Sichtweiten ist formal möglich. Dann sollte aber die Sichtweite mit einem Sichtweitenmeßgerät bestimmt werden, weil die subjektive Bewertung zu großen Unterschieden in der angegebenen Sichtweite mit Konsequenzen für die Konzentrationsabschätzung führt.

Tabelle 2: Berechnete Schwebstaubkonzentrationen für gegebene Sichtweiten und verschiedene relative Feuchten unter Zugrundelegung von Gleichung 6a und 6b.

	M [µg/m³]								
f =	0,0	0,5	0,6	0,7	0,8	0,85	0,9	0,95	0,98
VV[km]									
10	51	53	53	54	40	32	23	14	7
5	103	106	107	108	79	64	47	28	14
4	129	132	133	134	99	80	58	35	17
3	172	176	177	179	132	106	78	46	23
2,5	206	211	213	215	158	127	94	55	28
2	257	269	266	269	198	159	116	69	35
1,5	343	352	355	359	264	212	156	92	46
1	514	528	532	538	395	318	234	138	69
0,7	735	754	760	768	565	454	334	197	99
0,5	1.029	1.056	1.065	1.076	791	636	467	276	138
0,4	1.286	1.320	1.331	1.344	989	795	584	345	172
0,3	1.715	1.760	1.774	1.793	1.318	1.060	779	461	230
0,2	2.572	2.639	2.661	2.689	1.977	1.589	1.169	691	345
0,1	5.144	5.279	5.323	5.378	3.954	3.179	2.337	1.382	690
0,05	10.289	10.558	10.646	10.755	7.908	6.357	4.674	2.763	1.379

Immerhin werden aus den direkt betroffenen Stationen Jambi und Palangkaraya auf Sumatra und Borneo Schwebstaubkonzenrationen von 2000 bis 4000 $\mu g/m^3$ gemeldet, die nach den angestellten Betrachtungen im Zusammenhang mit Sichtweitenbewertung auch über diesen Weg zu realistischeren Grobabschätzungen führen können.

Ein Fehler in der Sichtweitenbestimmung von 10 m bei einer Sichtweite von 50 m liefert ungefähr 30 % Abweichung im Resultat bezüglich der Schwebstaubkonzentration. Noch größer ist die Abweichung bei der relativen Feuchte im Bereich hoher Feuchten. Ein Fehler von 0,01 in der relativen Feuchte bringt bei f = 0,98 35 % Abweichung in der Schwebstaubkonzentration. Daher ist gerade im Fall geringer Sichtweiten und hoher relativer Feuchten mit einem Gesamtfehler von nahezu 100 % zu rechnen. Dieser Fehler nimmt ab mit zunehmender Sichtweite und sinkender relativer Feuchte.

Weiterhin ist es denkbar, daß in den Waldbrandgebieten von Indonesien noch größere spezifische Extinktionen (kleinere Proportionalitätsfaktoren) anzusetzen sind, als sie sich aus den Leipziger Untersuchungen mit der Laser-Transmissionsstrecke ergeben haben. Selbst hier ist in Leipzig 1992 ein Mittelwert von E = 3,50 m^2/g (285 $\mu g*km/m^3$) gefunden worden. Jedoch sind die 5 % derzeit nicht der Hauptfehler. Ein Weg zu Präzisierung der spezifischen Extinktion wären simultane Messungen von Schwebstabkonzentrationen und spektraler Transmission in der atmosphärischen Grundschicht, die der experimentellen Bestimmung des Extinktionskoeffizienten dient, analog der in Leipzig bei SANA praktizierte Herangehensweise.

Dank

Dem BMBF und den Mitarbeitern der Deutschen Botschaften von Kuala Lumpur und Jakarta möchte ich für die schnelle Unterstützung bei der Realisierung der ad-hoc Effect-Finding Mission in Südostasien danken, den Mitarbeitern der GTZ Jakarta, insbesondere Herrn Auge, Frau Ellen Kramer, Herrn Dieterle und Herrn H. Hanke für die Diskussion und Anregung, eine solche Problemstellung anzugehen.

Literatur:

Eltermann, L.: Vertival Attenuation Model with eight surface meteorological ranges 2 to 13 kilometers. AFCRL-70-0200, AD 70 7088, 1970.

Griggs, M. Measurements of atmospheric aerosol optical thickness over water using ERTS-1 data. Air Pollution Control Ass. Journal 25 (1975) 622-626.

Griggs, M.: Satellite observations of atmospheric aerosols during the EOMET cruise. Amosph. Sci. 36 (1979) 695-698.

Hänel, G.: The properties of atmospheric aerosol particles as functions of relative humidity at thermodynamic equilibrium with the surrounding moist air. Adv. Geophys. 19 (1976) 73-188.

Hänel, G.: Parametrization of the influence of relative humidity on optical aerosol properties. In: Aerosols and their climatic effects. A. Deepak Publ. Hampton 1984, 117-122.

Koschmieder, H.: Theorie der horizontalen Sichtweite. Beitr. Phys. Atmosph. 12 (1925) 33-557.

Settler, M., von Hoyningen-Huene, W.: Three years of aerosol extinction measurements with a He-Ne-Laser in the urban boundary layer of Leipzig, Germany. Beitr. Phys. Atmosph. 67 (1994) 169-180.

Trier, A., Horvath, H.: A study of the aerosol of Santiago de Chile. - 2. Mass extinction coefficients, visibilities and Angström exponents. Atmospheric Environment 27A (1993) 385-395.

Uhlig, E.-M., von Hoyningen-Huene, W.: Correlation of atmospheric extinction coefficient with the concentration of particulate matter in a polluted urban area. Atmospheric Research 30 (1993) 181-195.

Uhlig, E.-M., Stettler M., von Hoyningen-Huene, W.: Experimental studies on the variability of the extinktion coeffizient by different air masses. Atmospheric Environment 28 (1994) 811-814.

von Hoyningen-Huene, W.: Erfassung des atmosphärischen Trübungszustands und seiner zeitlichen Veränderung infolge von Emissionsabnahmen auf Grund sich vollziehender Strukturänderungen in Mitteldeutschland. (Abschlußbericht zum SANA-Teilprojekt B 1.6) In: Wissenschaftliches Begleitprogramm zur Sanierung der Atmosphäre über den neuen Bundesländern - Abschlußbericht - Band , BMBF - GSF PT Umwelt und Klima 1996.

Korrespondenz bitte an:

Dr. habil. Wolfgang von Hoyningen-Huene
Universidate de Evora
Dept. Fisica
R. Romero Ramalha 59
P-7000 Evora
Portugal

On the influence of the geostrophic wind direction on the atmospheric response to landuse changes

Nicole Mölders

Summary:

Simulations alternatively assuming a landscape with and without urbanization plus open-cast mining were performed with a non-hydrostatic model. It is examined whether the atmospheric response to landuse changes is sensitive to the direction of the geostrophic wind. The results of simulations with the same geostrophic wind direction show that except for the cloud and precipitating particles the daily domain-averages of the variables of state hardly differ for the different landscapes. Nevertheless, the local weather may be affected appreciably over and downwind of the altered surfaces. The significant differences in the cloud and precipitating particles, however, are not bound to the environs of the landuse changes. Generally, the most significant differences occur for the cloud and precipitation particles, the soil wetness factors and the vertical component of the wind vector. The latter changes strongly influence the cloud and precipitation formation by the interaction cloud microphysics-dynamics. The results also indicate that for most of the quantities the local magnitude of the atmospheric response changes for the various directions of the geostrophic wind. However, the differences of the domain-averaged 24h-accumulated evapotranspiration are similar for all geostrophic wind directions.

Zusammenfassung:

Um zu untersuchen, ob die atmosphärische Antwort auf Landnutzungsänderungen sensitiv zur Richtung des geostrophischen Windes ist, wurden Simulationen durchgeführt, bei denen alternativ eine Landschaft mit und ohne Urbanisierung plus Tagebauten angenommen wurde. Die Simulationsergebnisse zeigen, daß - außer für Wolken- und Niederschlagspartikel - die täglichen Gebietsmittelwerte der Zustandsvariablen sich kaum für die beiden Landschaften unterscheiden. Trotzdem kann das lokale Wetter merklich über und im Lee der Oberflächen mit veränderter Landnutzung beeinflußt werden. Die signifikanten Differenzen in den Wolken- und Niederschlagspartikeln sind jedoch nicht an die unmittelbare Nähe der Landnutzungsänderungen gebunden. Generell treten die signifikanten Unterschiede bei den Wolken- und Niederschlagspartikeln, der Bodenfeuchte und der Vertikalkomponente des Windvektors auf. Letztere beeinflussen stark die Wolken- und Niederschlagsbildung durch die Wechselwirkung Wolkenmikrophysik-Dynamik. Die Ergebnisse zeigen außerdem, daß lokal der Grad der atmosphärischen Reaktion für die meisten Größen bei unterschiedlicher Richtung des geostrophischen Windes anders ausfällt. Die Differenzen der Gebietsmittelwerte der 24h-akkumulierten Evapotranspiration gleichen sich jedoch für alle Richtungen des geostrophischen Windes.

1. Introduction

Since human began to grow crop and to build settlements, the land cover was modified. Different landuse types and slopes yield different fluxes of momentum, moisture and heat due to variations in water availability, surface temperature, plant and soil parameters (e.g., Avissar and Pielke, 1989). These differences also affect evapotranspiration, cloud and precipitation formation (e.g., Anthes, 1984; Chen and Avissar, 1994) as well as runoff by complicate nonlinear feedback mechanisms. Recent studies investigated the effect of anthropogenic or natural landuse changes on the local (e.g., Groß, 1988; 1989), regional (e.g., Anthes, 1984; Charney, 1975; Savenije, 1995; Xue, 1996), continental wide (Copeland et al., 1996) or global climate

(e.g., Dickinson, 1992; Zheng et al., 1996; Zhang et al., 1996; Sud et al., 1996). The most important aspects of different landuse types are (1) changes in the partitioning of energy into sensible and latent heat fluxes (e.g., Kerschgens and Drauschke, 1986; Cotton and Pielke, 1995), (2) the changes in the fraction of solar radiation reflected back to space (e.g., Cotton and Pielke, 1995), (3) changes in the structure of the atmospheric boundary layer (ABL; e.g., Pielke et al. 1990), and (4) changes in cloudiness and precipitation (e.g., Anthes, 1984; Changnon and Huff, 1986; Brubaker et al., 1993; Otterman et al., 1990). Hence, the landuse changes may affect the local atmospheric energy and water cycle under calm wind conditions. Under such conditions the cloud and precipitation formation is mainly forced by the underlying surface and the recycling of water within a region.

The previous studies of the effect of landuse changes on the local scale usually investigated the atmospheric response for the main direction of the near-surface wind because they were undertaken as planing studies (e.g., Gross, 1988; 1989). The global studies, however, examined the potential effect of landuse changes for longer time scales. Herein, of course, different directions of wind occur. Nevertheless, no evaluation was carried out whether the atmospheric response to the landuse changes is sensitive to the direction of the geostrophic wind. This question is addressed in this paper. In doing so, simulations are performed with the non-hydrostatic meso-β-scale meteorological model GESIMA (Kapitza and Eppel, 1992; Eppel et al., 1995) in its Leipzig's version. Four different directions of the geostrophic wind are assumed in a landscape with and without urbanization and open-cast mining.

2. Brief description of the model

The dynamical part of GESIMA is based on the anelastic equations (Kapitza and Eppel, 1992; Eppel et al., 1995). The prognostic equations are solved with a predictor/corrector scheme. Advection of momentum and potential temperature is determined with a MacCormack scheme modified for the applications to incompressible flow. The transport of passive quantities is formulated according to Smolarkiewicz (1984).

Tab. 1. Parameters (from Deardorff 1978, Eppel et al. 1995, Wilson et al. 1987) as used for the different landuse types. The letters k_s, c_i, ε, α, z_0, w_k, α_c, and g_l are the thermal conductivity of the soil, the heat capacity, the emissivity, the albedo, the roughness length, the field capacity, the capillarity, and the maximal evaporative conductivity, respectively. The quantities indicated by * are calculated by the model.

Landuse type	k_s	c_i	ε	α	z_0	w_k	α_c	g_l
	$10^{-6}m^2/s$	$10^6J/(m^3K)$			m	m	$10^{-3}kg/(m^3s)$	m/s
Water	0.15	4.2	0.94	*	*	1.0	1000	-.-
Open-cast mining	0.84	2.1	0.90	0.30	0.0004	0.002	0.9	-.-
Grassland	0.56	2.1	0.95	0.25	0.02	0.010	8.0	0.04
Agriculture	0.74	2.9	0.95	0.18	0.04	0.003	3.0	0.04
Deciduous forest	0.70	2.5	0.97	0.20	0.8	0.010	8.0	0.023
Mixed forest	0.70	2.5	0.975	0.175	0.9	0.010	8.0	0.023
Coniferous forest	0.70	2.5	0.98	0.15	1.0	0.010	8.0	0.023
Suburb/village	1.0	2.0	0.90	0.20	0.8	0.003	1.0	-.-
City	1.0	2.0	0.95	0.15	1.0	0.002	0.9	-.-

Cloud processes are considered by a parameterization of bulk-microphysics. It takes into account the condensation and deposition of water vapor, the rainwater formation by autoconversion, coalescence, and melting of both ice and graupel, the riming of ice and graupel by cloud water, the homogeneous freezing of cloud water and rainwater, the evaporation of cloud water and rainwater, the sublimation of ice and graupel, the sedimentation of rainwater, ice

and graupel (Mölders et al., 1997). A simplified two-stream method calculates the radiative transfer (Eppel et al., 1995).

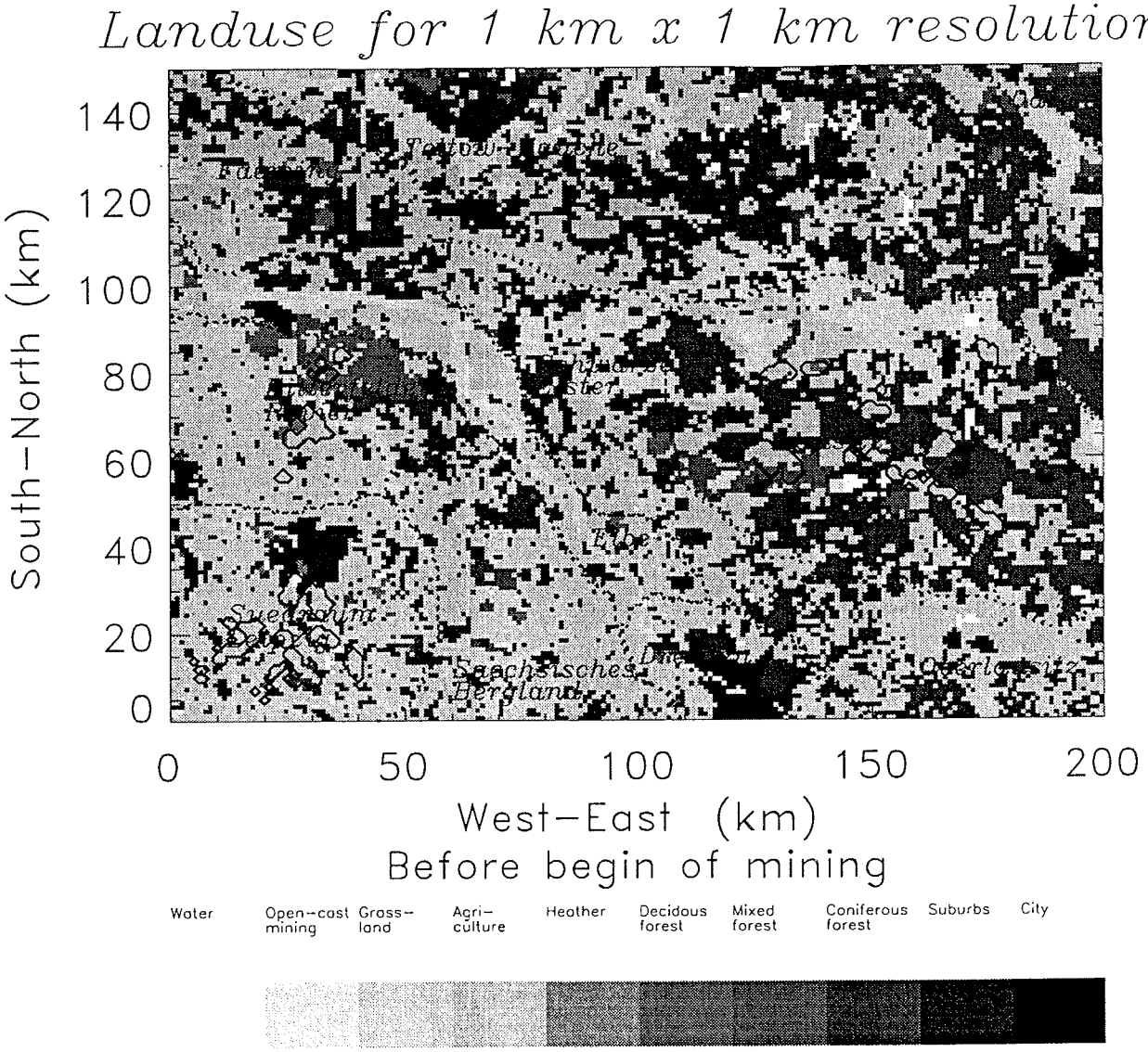

Fig. 1. Distribution of plant and soil characteristics according to Tab. 1 for REF. The thick contour lines indicate the *open-cast mining* in MINURB. The thin lines represent the boundaries of the districts discussed further in the text.

At the surface the calculation of the fluxes is based on a bulk-parameterization. Soil wetness is determined with a force-restore-method. The transpiration of plants is considered by a Jarvis-approach (1976). The soil heat flux and soil temperature are calculated by a diffusion equation (see also Eppel et al., 1995). The surface stress and the near-surface fluxes of heat and water vapor are expressed in terms of dimensionless drag and transfer coefficients with the parametric model of Kramm et al. (1995) that is based on the Monin-Obukhov similarity theory. Above the atmospheric surface layer a one-and-a-half-order closure scheme determines the turbulent fluxes of momentum.

The anthropogenic landuse changes are considered on a subgrid with a resolution of 1 x 1 km^2 using an explicit subgrid scheme (Seth et al., 1994; Mölders et al., 1996). This scheme determines the water and energy fluxes, soil wetness factor, soil and surface temperature on a finer grid resolution (1 x 1 km^2) than that used in the model (5 x 5 km^2). This modeling strategy means that in the domain-average the total change of land surface cover may be small, but when considering the local scale the landuse change is large.

The model encompasses the troposphere over southern Brandenburg and northern Saxonia (Fig. 1) from the surface to 10.5 km height. In the reference landscape, denoted as REF hereafter, the fractional coverage of *water*, *grassland*, *agriculture*, *deciduous forest*, *mixed forest*, *coniferous forest*, *suburbs/village*, and *city* amounts 266, 3238, 13677, 296, 959, 9121, 2305, and 138 km^2, respectively. In the landscape with open-cast mining and urbanization, called MINURB hereafter, these landuse types cover 260, 3191, 12857, 292, 973, 9074, 2798, and 138 km^2. In addition 417 km^2 of *open-cast mining* exist (Fig. 1). *Open-cast mining* occur in the Lausitz, in the Bitterfelder Revier, and the Südraum Leipzig. Since mining practice is to quarry on one side of the open-cast mining and to deposit the mining debris on the other side, only a small strip of coal (about 100 m width) is in contact to the atmosphere. Hence, the main part of an open-cast mining consists of tertiary and quatiary sands of different colors. Therefore, the soil characteristics of *sand* are taken for *open-cast mining* (Tab. 1). In the orographic data set of MINURB the average depth of each 1 x 1 km^2 area is applied as the terrain height of the open-cast mining.

The vertical resolution of the model varies from 20 m close to the ground to 1 km in 10 km height. Eight levels are located below 2 km and 8 above that height.

3. Initialization and design of the study

After describing the meteorological situations (section 4) the atmospheric response to the landuse changes will be separately investigated for four directions, namely, from 10°, 100°, 190° and 280°, respectively (section 5). In section 6 it will be examined whether the atmospheric response to the landuse changes is sensitive to the geostrophic wind direction. The notation of the simulation is that of the landscapes plus the direction of the geostrophic wind, i.e., REFxxx and MINURBxxx where xxx =10, 100, 190, and 280, respectively. Note that xxx will only be appended when the results of the simulations with the different geostrophic wind directions are discussed simultaneously.

Fractional differences, $\Delta = (\chi_i - \chi_j)/(\chi_i + \chi_j)$ of the predicted quantities, χ, are determined to obtain a measure how the sensitivity of the atmospheric response to the landuse changes varies with the direction of the geostrophic wind. Here, i and j represent REF and MINURB, respectively. This measure ranges from -1 to 1, with negative and positive values indicating larger values for MINURB and REF, respectively. If both simulations predict the same, Δ will be zero. A factor of 1.1 or 2 in agreement, for instance, results in a Δ of ± 0.05 and ± 0.33, respectively. Moreover, significance tests were performed for the pairs of the different landscapes but of the same wind directions.

In nature the rawins profiles would slightly differ in the ABL if they were measured over the different landscapes. Usually the synoptic conditions of different geostrophic wind directions are associated with different pressure, temperature and humidity regimes. Nevertheless, to avoid additional degrees of freedom and for comparability here all the simulations are initialized with the same profiles of humidity, air and soil temperature as well as the same speed of the geostrophic wind of 7.5 m/s. These profiles are adjusted to homogeneous terrain by a 1D-simulation of GESIMA. A surface pressure of 1003 hPa was assumed. In the radiation simulation the 122nd Julian day is applied. The soil wetness factors were set equal to 0.5. Throughout the entire simulation the water surface temperatures and the soil temperature in 1 m depth were hold constant at 285 K and 282.6 K, respectively. Analyzing Gerstengarbe's and Werner's (1993) weather regime data geostrophic winds around 100° (HNFA, SEZ, SA, TM, SEA), 190° (SWA, SWZ, TRM, HM), 280° (WA, NWA, BM) and 10° (NEA) existed in 9.4 %, 18.1%, 17.1 % and 2.4 % of the time from 1881 to 1992 in the domain of interest. Note that the local recycling of water is of minor importance when fronts pass the domain because then precipitation is mainly advected. Since the main focus is on the effect of the landuse changes on the local water cycle, the investigations are restricted to synoptic situations without frontal activities in the domain of interest.

4. The meteorological situations for the different directions of the geostrophic wind

4.1. Situation for a geostrophic wind from 10°

The surface temperatures are more sensitive to the cloud distribution than to that of landuse. The cities do not develop a worth mentioning heat island effect. At noon the near surface air temperatures increase from 8°C in the west to 11 °C in the eastern part of the model domain except for the area between Wittenberg and Leipzig, the Oberlausitz and the eastern Sächsisches Bergland. In the first mentioned area the temperatures exceed 10°C while in the latter two areas the temperatures are 1 °C cooler than in their surroundings. During the nighttime the temperatures vary among 5 °C in the Sächsisches Bergland and values higher than 7 °C along a line Leipzig-Torgau-Luckenwalde.

Evapotranspiration is slightly lower in areas of thick cloudiness than in the adjacent cloudfree areas of the same landuse type. Note that this is true in all the simulations. In xxx10 the distribution of evapotranspiration is more similar to that of the clouds than to that of the landuse types. During the daytime the humidity of the ABL is about 1 g/kg higher in the north of Leipzig, over the Fläming as well as north and over the Lausitz than in the other parts of the domain. In the nighttime the humidity exceeds 5.4 g/kg in the middle of the domain. It is less than 4.8 g/kg in the east and the west.

During the daytime cloud bands form along a line from the Fläming over Leipzig to the Sächsisches Bergland and in the eastern part of the model domain. Except for the orographically induced clouds over the Sächsisches Bergland the cloud fields form along convergence lines of the wind field. In their upper part they are strongly iced. During the nighttime two north-south-orientated partly iced cloud bands form which provide precipitation.

4.2. Situation for a geostrophic wind from 100°

In contrast to a geostrophic wind from 10° the distribution of surface temperatures is governed by the distribution of the prevailing landuse for a geostrophic wind from 100°. Since the heat capacities and the thermal conductivity of the soil assumed for *agriculture* and *settlements* exceed those of *grassland* or *forest*, the former areas heat more strongly than the latter. Hence, in the south-western part of the model domain slightly higher surface temperatures are achieved due to the larger fractional coverage by *settlements* and *agriculture* than in the north-eastern part. During the daytime, for instance, surface temperatures range from 14 °C in the immediate vicinity of *waters* and 34°C in Dresden and Leipzig.

In the diurnal course air temperatures vary between 4° and 15°C within the near surface layer. Here, low air temperatures occur in the Sächsisches Bergland, the Fläming and downwind of largely extended *grassland*. Over the cities of Dresden and Leipzig the air is slightly warmer during the nighttime than in their environs.

During the daytime the humidity of the near surface layer is strongly related to that of evapotranspiration and the prevailing landuse (about 4.4 g/kg for *agriculture* and *settlements*, more than 5 g/kg for *grassland*, and intermediate values for *forest*). The areas dominated by *forest* or *grassland* evapotranspirate more strongly than those dominated by *agriculture* or *settlements* because of the higher field capacity and capillarity of the former than of the latter. Therefore, more water is restored from the ground water, and, despite the stronger evapotranspiration, the soils of *forest* and *grassland* are moister than those of *agriculture*. During the nighttime humidity slightly depends on topography. High values occur in the upper ABL of areas with low terrain elevation.

At the top of the ABL relatively flat clouds form over the Lausitz, the Sächsisches Bergland and the Südraum Leipzig during the daytime. In the early evening and the nighttime cloudiness decreases within the domain (Fig. 2). Downwind of Leipzig great amounts of cloud and precipitating particles occur. Here, intense precipitation reached the ground in the early

evening. Moreover, intense precipitation occurs over and downwind of Dessau. Precipitation bands exist in the northern Niederlausitz and the Oberlausitz.

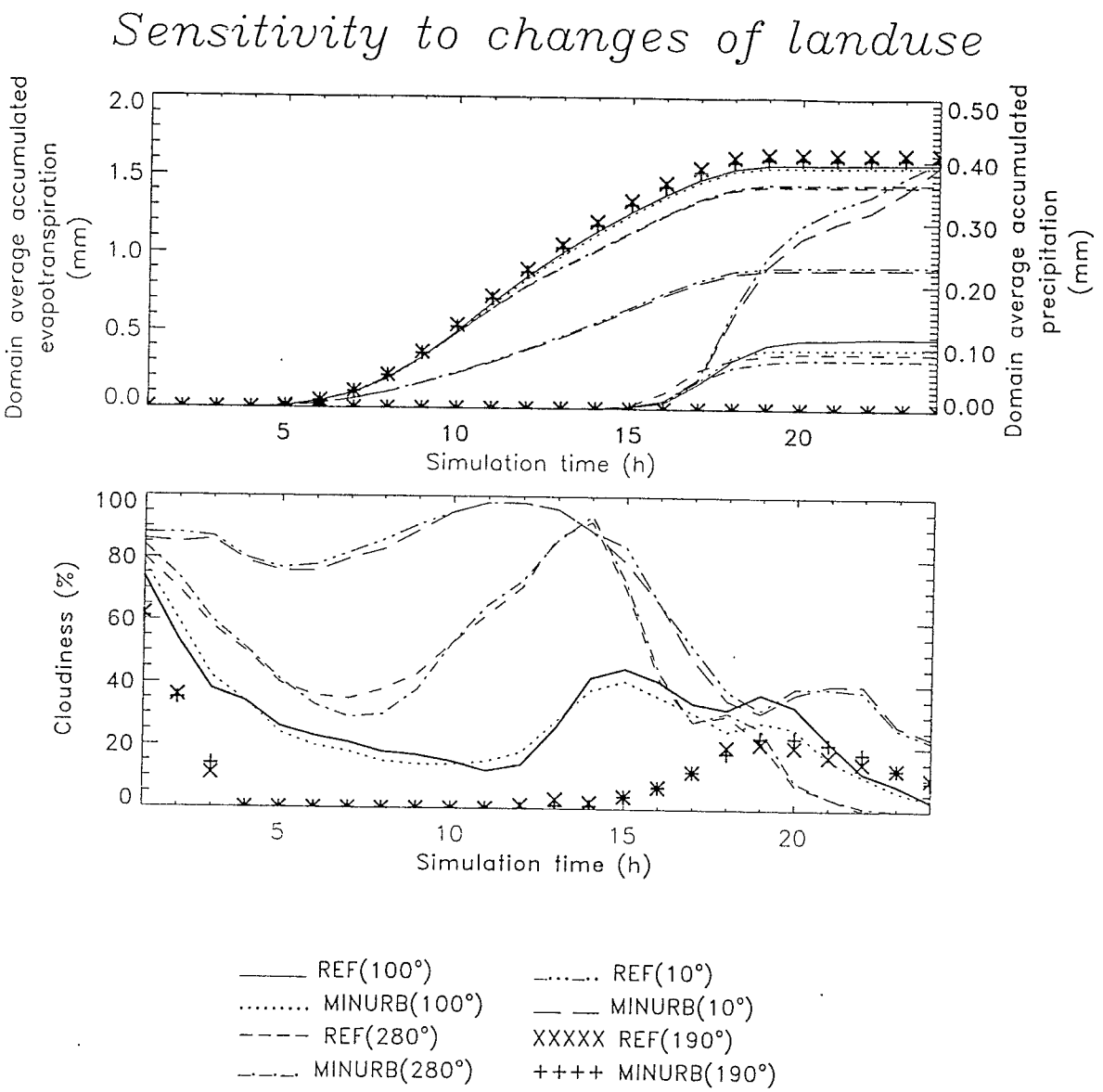

Fig. 2. Temporal development of the domain-averaged accumulated evapotranspiration and precipitation (upper part) as well as cloudiness (lower part) for different directions of the geostrophic wind.

4.3. Geostrophic wind from 190°

Like for a geostrophic wind from 100°, the distribution of surface temperatures is strongly related to that of the prevailing landuse for a geostrophic wind from 190°. In the ABL the temperatures are higher in the flat terrain of the northern part (about 13 °C at noon) than in the mountainous southern part of the model domain (lower than 10 °C). During the nighttime temperatures vary between 11 °C (Halle-Leipzig-Bitterfeld-area and along the river Elbe) and 8 °C (Sächsisches Bergland). There is a slight inversion of temperature below 100 m above ground.

Like for a geostrophic wind from 100°, evapotranspiration and, hence, the humidity of the lower ABL clearly depend on the distribution of the prevailing landuse during the daytime (5 g/kg and more over *forest* and *grassland*, about 4 g/kg for *agriculture* and large cities). During the nighttime the humidity does not exceed 3.4 g/kg in the Ober- and Niederlausitz. Values of more than 3.8 g/kg occur west of Leipzig and in the water meadows of the Odra.

During the daytime clouds only exist over the Oberlausitz. During the nighttime stratiform clouds form over and south of the Fläming. Their most southern boundaries reach the South of Halle. A further cloud field builds between Luckenwalde and Lindenberg. Both cloud fields are partly iced. Although some rainwater develops, no precipitation reaches the ground during the entire simulation time (Fig. 2).

4.4. Situation for a geostrophic wind from 280°

During the daytime the surface temperatures are related to the distribution of landuse only in the cloudfree southern part. Here, surface temperatures reach up to 33.1 °C at Dresden, for example. At noon the near surface air temperatures range from less than 10 °C in the Sächsisches Bergland and the Fläming to more than 13 °C at the Polish boarder. During the nighttime they range from less than 7 °C in the Sächsisches Bergland to more than 9 °C at Leipzig, Dresden and in the western part of the model domain.

During the daytime the distribution of humidity is strongly related to the landuse of the underlying surface. Values of humidity lower than 4.4 g/kg occur in the areas dominated by *agriculture* and about 4.8 g/kg in areas prevailingly covered by *forests* and *grassland*. Humidity is up to 0.2 g/kg lower over the larger cities (e.g., Leipzig, Wittenberg, Dresden, Cottbus) than over the adjacent vegetated land. At noon, for instance, humidity is slightly lower between Luckenwalde and Lindenberg than in the other areas prevailingly covered by *forest* and *grassland*. During the nighttime humidity exceeds 4.4 g/kg south of a line Halle-Torgau-Cottbus. Values less than 4.0 g/kg are achieved in the Fläming.

In the daytime broken stratus cloud fields form at the top of the ABL. At noon, for instance, cloudfree areas exist between Leipzig-Riesa-Meißen and in some parts of the Lausitz. Except for some locations over the Sächsisches Bergland no clouds exist during the nighttime (see also Fig. 2).

In the late afternoon and early evening precipitation occurs (e.g., Fig. 2) along a line Halle-Bautzen and in the Sächsisches Bergland. In the lee of Leipzig and Riesa precipitation is enhanced as compared to the other areas with precipitation. A third precipitation field exists east of the Lausitz.

5. The atmospheric response to the landuse changes for different geostrophic wind directions

Settlements as well as *open-cast mining* have similar thermal (thermal conductivity of the soil, heat capacity) and hydrologic (field capacity, capillarity) characteristics. The main differences are in the albedo and in the roughness length (Tab. 1). This means that the two landuse changes have similar effects except for dynamics and radiation. It is well known that dry, sandy areas evapotranspirate significantly less and heat more strongly the atmosphere than the vegetated areas. The expected drying and warming effect of the atmosphere occurs in the immediate vicinity of the landuse conversions for MINURBxxx. This, on average, leads to a slightly warmer and drier atmosphere for MINUBxxx than for REFxxx. Moreover, recent studies showed that urban areas increase convection (e.g., Landsberg, 1970) and precipitation in and downwind of a large city (e.g., Changnon and Huff, 1986). This effect is sometimes found for larger cities, too.

For all directions of the geostrophic wind the variability of wind, temperature and humidity grows in the areas of the landuse changes when approaching the Earth's surface. Generally, the landuse changes do not influence the predicted quantities of state above the ABL in all the simulations. In most of the cases the predicted variables of state as well as the water and energy fluxes differ over and downwind of the landuse changes. Because of the higher energetic input during the daytime, then the fluxes predicted for the various landscapes differ more strongly than during the nighttime. As compared to REFxxx in MINURBxxx the w-component of the wind vector significantly changes (Tab. 2) over the converted areas due

to the stronger heating than the formerly vegetated land. This is due to the aforementioned different thermal behavior of *sand* and *settlements* on the one hand side and that of vegetated land on the other (see Tab. 1). Significant differences occur in the cloud and precipitating particles, the vertical component of the wind vector, the soil wetness factors, and evapotranspiration for all the directions of the geostrophic wind (Tab. 2).

In the case of the same geostrophic wind direction the domain-averaged daily values of the surface and air temperatures as well as humidity of REF and MINURB hardly differ. Nevertheless, for all the directions of the geostrophic wind there exists a larger variance of the humidity of the lower ABL in MINURB than for REF. For geostrophic winds from 190° or 10° the variance is higher for most of the quantities and fluxes in REF than in MINURB. The opposite is true for geostrophic winds from 100° or 280°. For all geostrophic wind directions the cloud and precipitating particles significantly change after the landuse conversions. These differences are not bound to the location of the altered landuse. The soil wetness factors of REF and MINURB significantly differ (Tab. 2) because of the dry up by the urbanization and the mining activities. In the case of xxx = 10, 100, 280 also the significantly different precipitation distributions and intensities play a role. This again affects evapotranspiration. If precipitation occurs, the domain-averaged 24h-accumulated precipitation will be reduced by the occurrence of *open-cast mining* and urbanization (Fig. 2).

Tab. 2. Comparison of maximum significance, s, and area, A, (km^2) for which the landuse changes cause significant differences (90 % confidence and higher) in the predicted quantities for the various directions of the geostrophic wind. Bold numbers emphasize the changes that are at least 95 % significant. Note that no precipitation reached the ground in REF190 and MINURB190, respectively.

Geostrophic wind from	10°		100°		190°		280°	
Significance/area size (km^2)	s	A	s	A	s	A	s	A
Ice	**99.99**	3750	**99.99**	6925	**99.99**	5925	**99.99**	10850
Rainwater	**99.99**	3250	**99.99**	4725	**99.99**	5675	**99.99**	11775
Cloud water	**99.99**	350	**99.99**	2000	**99.99**	7350	**99.99**	3775
Total liquid and solid water	**99.99**	750	**99.99**	2125	**99.99**	4025	**99.99**	5275
w-component of wind vector	**99.99**	1950	**99.99**	1725	**99.99**	3425	**99.99**	2650
Soil wetness factor	**99.99**	675	**99.99**	1325	**99.99**	675	**99.99**	2525
Graupel	**99.99**	1200	**99.99**	4250	**99.99**	350	**95**	350
Precipitation	**99.99**	1950	**99.99**	5450	-.-	-.-	**99.99**	19000
Evapotranspiration	**95**	350	**99**	300	**95**	300	**99.99**	650
Temperature	**99.99**	1300	90	75	68	0	**99.7**	225
Surface temperature	68	0	**95**	25	**95**	25	68	0
u-component of wind vector	45	0	68	0	45	0	90	75
Humidity	45	0	45	0	90	75	68	0
Sensible heat fluxes	68	0	68	0	45	0	90	25
v-component of wind vector	45	0	45	0	68	0	90	25

5.1. The atmospheric response to the landuse changes for a geostrophic wind from 10°

As compared to the reference landscape the soil heat fluxes rise appreciably in the open-cast mining and in the grown conurbation. Consequently, in these areas the surface temperatures of MINURB exceed those of REF. The predicted air temperatures of MINURB significantly grow in the western Bitterfelder Revier, the northern Lausitz, the Südraum Leipzig, and over Leipzig.

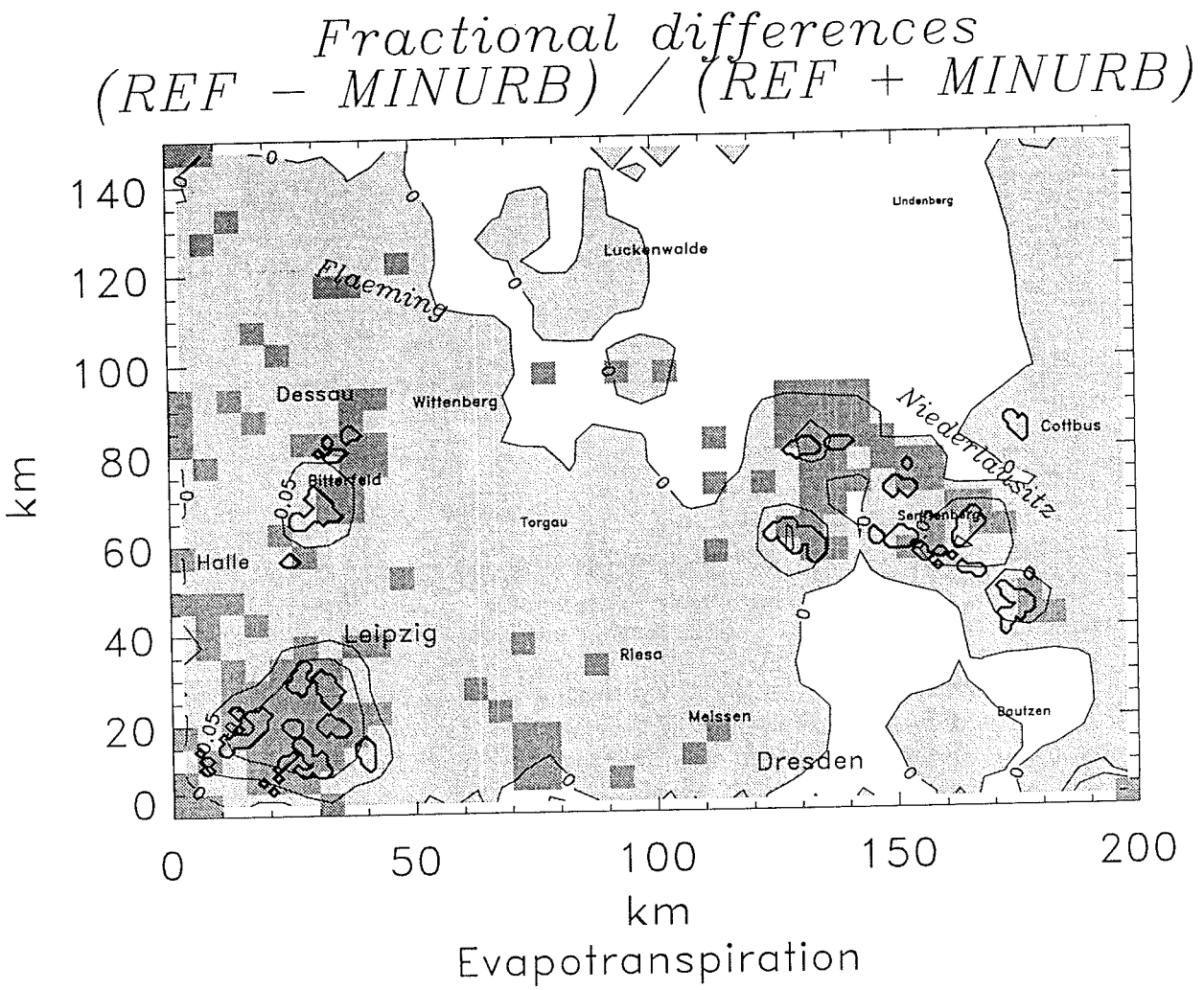

Fig. 3. Fractional differences of evapotranspiration at noon for a geostrophic wind from 10°. Grey shaded and white areas stand for positive and negative values, respectively. The dark grey boxes indicate grid cells for which at least one of the following quantities, namely, air temperature, evapotranspiration, the vertical component of the wind vector or soil wetness, differ at 90 % or better statistical significance level due to the landuse changes (Tab. 2).

In addition to the ABL over all the open-cast mining, the vertical component of the wind vector also significantly changes (e.g., Tab. 2) in the Sächsisches Bergland. Due to the grown conurbation evapotranspiration and soil wetness factors are appreciably reduced around Torgau, Riesa, Meißen, and Cottbus (e.g., Fig. 3). They are significantly reduced in the grown conurbation of Dresden, in the open-cast mining of the Südraum Leipzig and the Lausitz. In the latter region the extension of the area with significantly lower soil wetness factors are less than in the Südraum Leipzig. Nevertheless, significantly less water evapotranspirates only in the Südraum Leipzig and the southern Lausitz (e.g., Fig. 3). Consequently, on average, the air is slightly drier over and in the lee of the open-cast mining districts in MINURB than in REF. The drying effect of the sandy open-cast mining is greater in the lee of the Bitterfelder Revier and the Südraum Leipzig than in the lee of the Lausitz (e.g., Fig. 3). This may be partly due to the concurrently occurring urbanization that is greater in the former than in the latter region. Furthermore, in the lee of the open-cast mining the slightly enhanced near surface air temperatures may increase more strongly the evapotranspiration in the adjacent *forest* and *grassland* of the Lausitz than in the adjacent *agriculture* of the Südraum Leipzig and the Bitterfelder Revier (e.g., Fig. 3).

Tab. 3. Maximum hourly precipitation (mm) in the districts as obtained for the simulation REFxxx and the respective differences, Δ = REF - MINURBxxx. Areas that achieved both landuse changes, namely, urbanization and open-cast mining are given in bold letters.

Geostrophic wind direction	10°		100°		280°	
District as indicated in Fig. 1	REF	Δ	REF	Δ	REF	Δ
Fläming	0.0	0.0	0.1	0.0	0.0	-0.1
Teltow-Zauche	1.5	0.1	1.0	0.0	0.0	-0.1
Elbe	1.3	-0.6	0.3	-0.2	0.7	-0.5
Bitterfelder Revier	**0.0**	**0.0**	**0.8**	**-0.1**	**0.1**	**-0.4**
Leipzig-Südraum Leipzig	**0.1**	**0.0**	**0.7**	**-0.2**	**0.9**	**-0.2**
Sächs. B.-Dübener Heide	1.4	-0.5	0.7	0.1	0.9	-0.2
Schwarze Elster	0.7	-0.1	0.4	0.0	0.8	-0.7
Oberlausitz	2.6	0.3	0.0	0.0	0.7	0.2
Lausitz	**2.3**	**0.1**	**1.1**	**0.0**	**0.6**	**-0.5**
Conurbation of Dresden	1.5	-0.6	0.1	0.0	0.1	0.0
Odra	0.0	-1.6	0.3	0.3	0.0	0.0

Over the Bitterfelder Revier the cloud mixing ratio are significantly affected by the landuse changes. Here and over the valley of the river Elbe rainwater formation significantly changes due to the landuse conversion. Note that the latter leads to significant differences of the precipitation over the Elbe from Dresden to Torgau. In contrast to the liquid phase, the ice mixing ratios are significantly modified for all cloud fields. Nevertheless, the mixing ratios of the total cloud and precipitating particles are significantly influenced by the landuse changes (e.g., Tab. 2) only over the Bitterfelder Revier and the conurbation of Dresden. Precipitation is appreciably enhanced in the lee of Meißen. The hourly district-maximum precipitation rates grow in the area of the Elbe, the Odra, Dresden and the Sächsiches Bergland (Tab. 3).

On summarizing, in addition to the significant changes common to all directions of the geostrophic wind, the landuse changes significantly affect air temperature and evapotranspiration for a geostrophic wind from 10°.

5.2. Geostrophic wind from 100°

Only in the Lausitz surface temperatures significantly increase (e.g., Tab. 2) about 0.7 K for the change from REF to MINURB. The ABL is slightly warmer in MINURB than in REF, especially, over the open-cast mining (up to 0.3 K) and the conurbation (up to 0.2 K). Positive differences in air temperature go along with regions prevailingly covered by high vegetation (e.g., south of Bitterfeld, north of Senftenberg) while negative values arise in connection with a dominance of low vegetation (e.g., south of Leipzig, south of Cottbus). This substantiates that the landuse adjacent to the accumulated landuse changes, i.e., the simultaneous occurrence of two landuse changes within a small area, also strongly influences the kind of change in the temperature of the ABL.

In the ABL the vertical component of the wind vector will significantly change over the Lausitz, the Bitterfelder Revier, the Südraum Leipzig and some locations of the Fläming and the Sächsisches Bergland if the origin landscape changes to a landscape with *open-cast mining* and increased *settlements*.

In MINURB the humidity decreases more than 0.3 g/kg over and south of Leipzig, the Lausitz (especially around Cottbus) and the Bitterfelder Revier. Here, both the effects the drying up by urbanization and the low water holding capacity of the *open-cast mining* contribute to the significantly lower water supply to the atmosphere as compared to the formerly vegetated land (Fig. 4). On the contrary, in the conurbation of Dresden the humidity appreciably goes down by the urbanization alone. Here, the effect of urbanization on the distribu-

tion of water vapor is nearly as strong as the effect due to urbanization and *open-cast mining* around and in the Südraum Leipzig. There are several reasons. In the conurbation of Dresden a lot of smaller cities exist (Fig. 1) that all grow. Here, *grassland* changes to *settlement* while around Leipzig *agriculture* converts to *open-cast mining* or *settlement*. Consequently, in the former the surface characteristics change more strongly than in the latter area (e.g., Tab. 1). In the areas around Luckenwalde and Lindenberg urbanization is also the only landuse change. Due to the low density of *settlements* in this area the effective urbanization rate is low, too. Hence, the urbanization marginally reduces evapotranspiration (e.g., Fig. 4) and humidity in MINURB as compared to REF. This indicates that the local urbanization rate is also decisive for the magnitude of the atmospheric response.

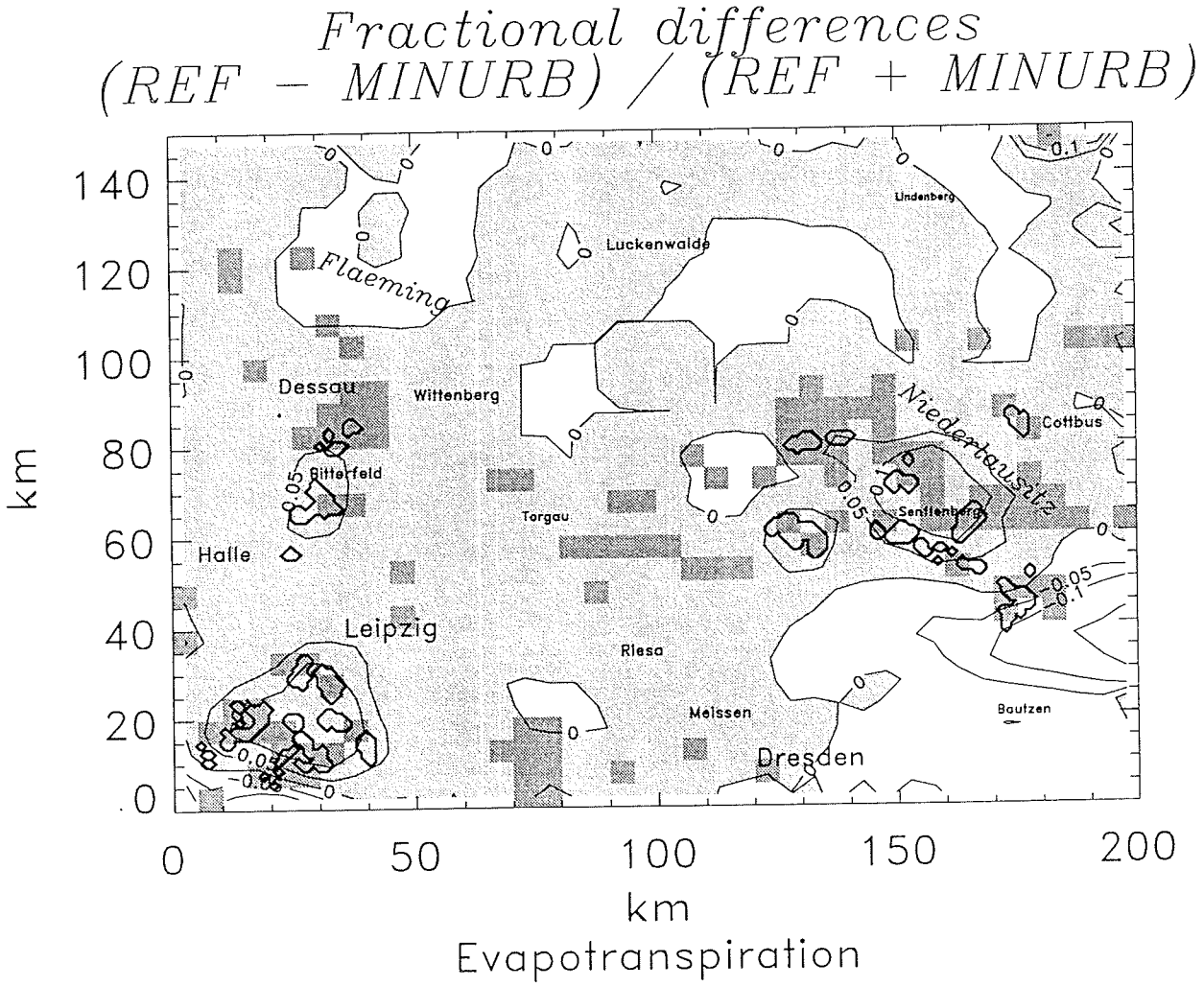

Fig. 4. As Fig. 3 but for a geostrophic wind from 100°. The dark grey boxes indicate grid cells for which at least one of the following quantities, namely, air and surface temperature, evapotranspiration, the vertical component of the wind vector or soil wetness, differ at 90 % or better statistical significance level due to the landuse changes (Tab. 2).

During the daytime the cloudiness predicted by MINURB increases over the Sächsisches Bergland, the river Neiße as well as over the Fläming while it is reduced over the Lausitz. Cloudiness significantly decreases downwind of Dresden, the Südraum Leipzig, the Bitterfelder Revier and the Lausitz. The assumed accumulated landuse changes result in a lower cloud coverage during the nighttime (Fig. 2).

During the nighttime the mixing ratios of cloud water and ice are significantly greater in the lee of Leipzig in MINURB than in REF. Consequently, MINURB provides significantly more rainfall downwind of Leipzig than REF. The extensions of the precipitation fields are

reduced in MINURB. The domain-averaged 24h-accumulated rainfall of MINURB does not reach that of REF (Fig. 2), but MINURB achieves a higher maximum of the 24h-accumulated rainfall (1.4 mm) than REF (1.3 mm). The hourly maximum precipitation increases in the Bitterfelder Revier, along the Elbe and in the Südraum Leipzig (Tab. 3). While REF predicts rainfall in the Odra-district, here no rainfall occurs in MINURB (Tab. 3).

On summarizing, in addition to the significant differences, which are common for all directions of the geostrophic wind, the surface and air temperatures significantly differ. In the lee side of Leipzig the modified moisture convergence results to higher local rainfall maxima in the late afternoon and early evening.

5.3. The atmospheric response to the landuse changes for a geostrophic wind from 190°

Surface temperatures are significantly enhanced (e.g., Tab. 2) in the open-cast mining of the Lausitz. During the nighttime the air is slightly warmer over and in the lee of the grown cities (e.g., Halle, Bitterfeld, Leipzig, Dresden) as well as in the northern part of the Lausitz. The fluxes of sensible heat only slightly differ while the soil heat fluxes differ more strongly (e.g., Tab. 2).

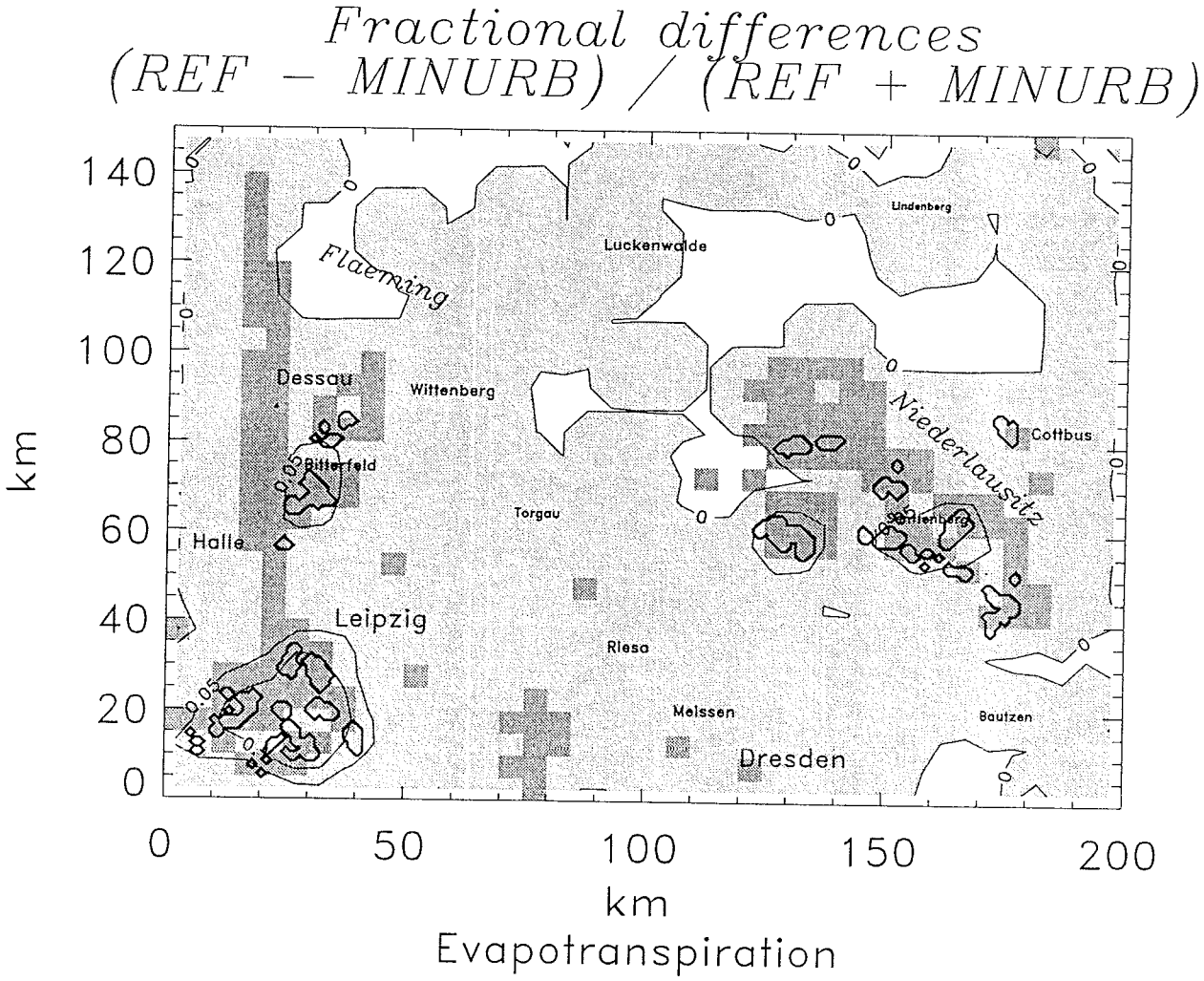

Fig. 5. As Fig 3 but for a geostrophic wind from 190°. The dark grey boxes indicate grid cells for which at least one of the following quantities, namely, surface temperature, evapotranspiration, humidity at reference height, the vertical component of the wind vector or soil wetness, differ at 90 % or better statistical significance level due to the landuse changes (Tab. 2).

Due to the different heating of vegetation and *open-cast mining* or of vegetation and *settlements* the vertical component of the wind vector is significantly modified by the landuse changes over all open-cast mining districts as well as the western part of the Sächsisches Bergland.

In MINURB evapotranspiration and soil wetness factors significantly decrease in the Südraum Leipzig. They are appreciably reduced in the grown conurbation (e.g., Fig. 5; see also Tab. 2). Note that the horizontal extension of the areas with a significantly reduced evapotranspiration is greater in the Südraum Leipzig than in the Lausitz (e.g., Fig. 5). In the former region humidity even decreases significantly (e.g., Tab. 2). In the nighttime the humidity of MINURB is still appreciably lower (about 0.2 g/kg) over and in the lee of the open-cast mining and the grown cities than in REF. As compared to REF the soil wetness factors significantly decrease (e.g., Tab. 2) in the Südraum Leipzig, the Bitterfelder Revier, the Lausitz as well as in the grown conurbation of Leipzig and Dresden in MINURB.

The cloud water and rainwater of REF and MINURB significantly differ (e.g., Tab. 2) over the Sächsisches Bergland, in the lee of the Fläming and in the lee of the Lausitz. On the contrary, the amount of ice is significantly affected by the landuse changes (e.g., Tab. 2) north of the Lausitz. The total condensed and frozen water, however, is significantly influenced (e.g., Tab. 2) in the lee of the Lausitz, in the Oberlausitz, over Leipzig, and over the Südraum Leipzig. This means that the paths of the cloud and precipitation formation are appreciably modified due to the atmospheric responses to the landuse changes. During the nighttime cloudiness increases in the lee of Dessau, Bitterfeld and Leipzig due to the growing of the cities. The mixed phase cloud field that builds between Luckenwalde and Lindenberg in REF becomes totally iced in MINURB. Furthermore, during the nighttime the mixing ratios of the cloud and precipitating particles of those cloud fields, which are predicted in both the simulations, are, on average, lower in MINURB than in REF. No precipitation reaches the ground in both the simulations (e.g., Fig. 2, Tab. 2).

On summarizing, in addition to the significant changes which occur for all directions of the geostrophic wind, the humidity, the surface and air temperatures of MINURB significantly differ form that of REF (Tab. 2).

5.4. The atmospheric response to the landuse changes for a geostrophic wind from 280°

Surface temperatures appreciably increase in the grown conurbation and the larger one of the open-cast mining. They decrease where thicker clouds form in MINURB than in REF or where the clouds exists over a longer time in MINURB than in REF so that insolation is appreciably reduced. In the Bitterfelder Revier the soil heat fluxes significantly change (Tab. 2). The turbulent fluxes of sensible heat provided by MINURB and REF differ up to 50 W/m^2 in the lee of the open-cast mining. At noon, for instance, the sensible heat fluxes decrease more than a factor of 2 in the Lausitz, the lee of the Bitterfelder Revier (e.g., Fig. 6). They increase more than a factor of 1.1 in the Südraum Leipzig, in the water meadows of the river Elbe between Riesa and Meißen, and south-west of the Fläming (e.g., Fig. 6). It seems that whether an increase or decrease is obtained mainly depends on the prevailing landuse of the patches adjacent to the land use conversion, namely, low and high vegetation for an increase and decrease, respectively. In Leipzig the sensible heat fluxes even significantly increase due to the urbanization (e.g., Fig. 6). Nevertheless, significant increases in air temperatures (Tab. 2) are only found over the open-cast mining of the Lausitz. As compared to REF the air temperatures of MINURB slightly increase in the lee of the open-cast mining during the daytime. During the nighttime the air is appreciably warmer in the conurbation of Leipzig, Dresden, Riesa, Meißen and Cottbus.

The horizontal wind field is hardly affected by the modified roughness and the changed terrain elevation except for the Lausitz where the predicted u- and v-components of the wind vector significantly differ (e.g., Tab. 2). On the contrary, the vertical component of

the wind vector significantly changes over all the open-cast mining due to the stronger heating of the latter than the vegetated land (e.g., Tab. 2).

Since in the open-cast mining as well as in the urbanized areas the soils are significantly drier than the formerly vegetated land of REF (e.g., Tab. 2), evapotranspiration is significantly reduced (e.g., Fig. 7). Therefore, over and in the lee of the open-cast mining as well as over and in the lee of the grown conurbation of Dresden and Leipzig the water vapor decreases about 0.2 g/kg in the lower ABL. As pointed out already in the Leipzig area the urbanization rate is high and *open-cast mining* occurs simultaneously. Here, the effects of the landuse changes enhance each other and provide a larger response towards lower humidity than in the other open-cast mining districts or areas with high urbanization rates (e.g., Fig. 7). During the nighttime the humidity of the air is appreciably reduced in the Südraum Leipzig and along the Elbe north of Dresden in MINURB. The former is due to the *open-cast mining* and urbanization while the latter results from urbanization alone. As aforementioned, here, the old and the new thermal, hydrologic and dynamic characteristics extremely differ (Tab. 1).

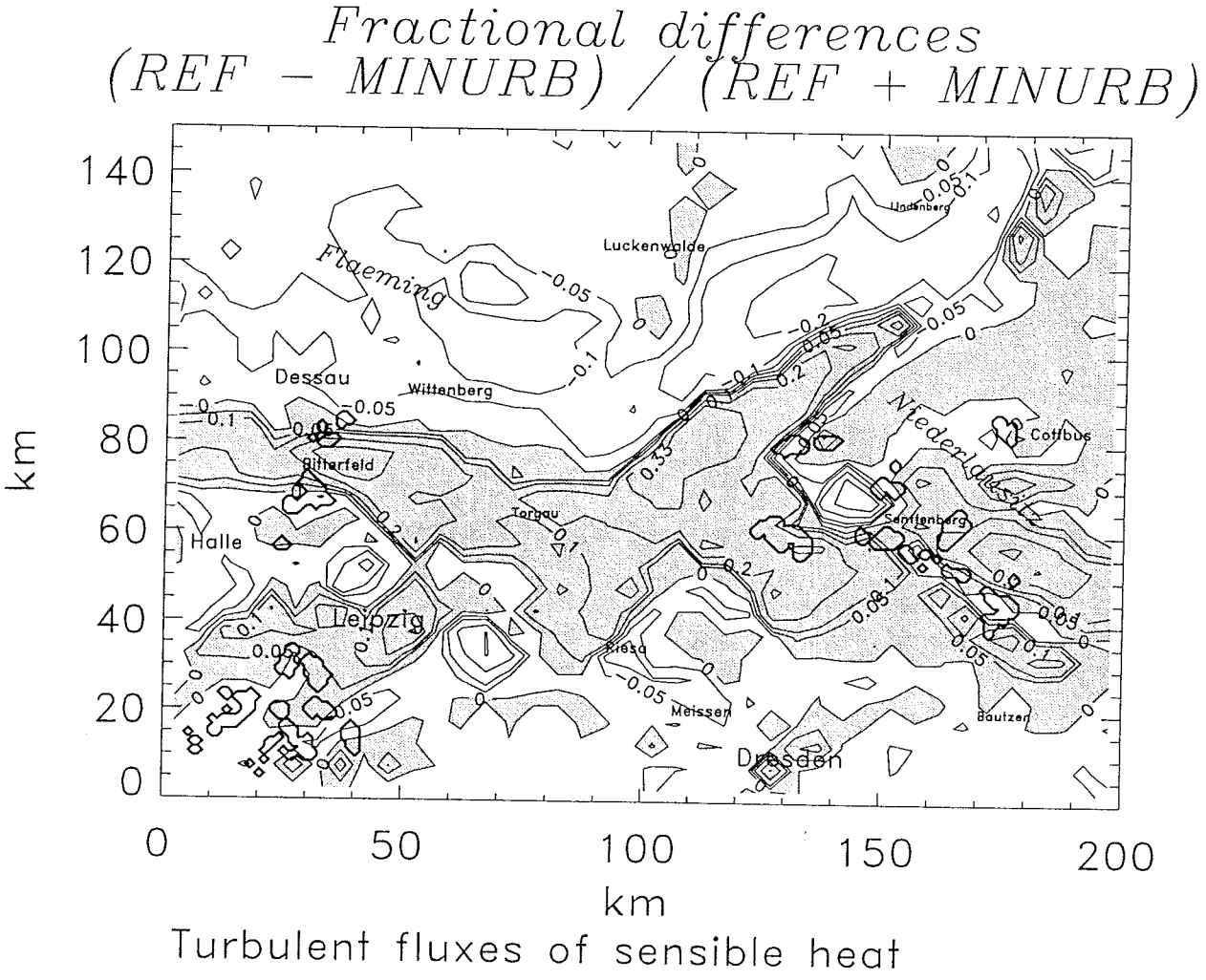

Fig. 6. Fractional differences of the fluxes of sensible heat at noon for a geostrophic wind from 280°. The dark grey boxes indicate grid cells for which at least one of the following quantities, namely, air temperature, evapotranspiration, the sensible heat fluxes, the w-, u- and v-component of the wind vector or soil wetness, differ at 90 % or better statistical significance level due to the landuse changes (Tab. 2).

On average, cloudiness decreases in the landscape with *open-cast mining* and urbanization (Fig. 2). During the daytime less rainwater forms in the lee of Leipzig, the Südraum Leipzig and the Lausitz while more rainwater is built over the water meadows of the river Elbe. Here,

the higher air temperature caused by the urbanization enhances evapotranspiration and hence, the cloud and rainwater formation. In the lee of the open-cast mining as well as over and in the lee of Leipzig the amount of ice is greater in MINURB than in REF due to the changed vertical motion and moisture convergence. During the nighttime there exists a higher degree of icing in MINURB than in REF. The district-maximum hourly precipitation increases in the Lausitz as well as in the districts adjacent East or West of the Elbe (Tab. 3).

On summarizing, in the lee of larger cities the vertical lifting and the moisture convergence grow by urbanization. This may locally enhance cloudiness. While evapotranspiration is reduced the most significantly in the Südraum Leipzig, air temperature significantly increases in the Lausitz only. This may be related to the adjacent dominating landuse. Besides the significant differences, which occur for all directions of the geostrophic wind, the landuse changes also significantly affect the u- and v-component of the wind vector, the sensible heat fluxes, the air and surface temperatures.

6. The sensitivity of the differences between REF and MINURB to the directions of the geostrophic wind

The landuse changes modify the heating, the vertical mixing, and the stability resulting in appreciable, and at some locations significant, differences between the cloud and precipitating particles of REF and MINURB. The significant changes occur in different regions for the different directions of the geostrophic wind (see also Tab. 3). Moreover, it depends on the geostrophic wind direction which quantities or fluxes significantly change (Tab. 2).

The results substantiate an obvious relationship among the distributions of surface cover and water vapor for geostrophic wind from 100°, 190°, and 280°. This is due to the water availability, the hydrologic behavior of the underlying surface (e.g., field capacity, capillarity), and hence, evapotranspiration and soil wetness factors. In REF10, however, the atmosphere becomes more cloudy than for the aforementioned synoptic situations. Therefore, the reduced insolation lessens evapotranspiration and heating. Note that in xxx10 in reference height the domain-averaged air temperatures are about 2 K lower than for the other wind directions.

6.1. The Fluxes

Net radiation is hardly affected by the landuse changes for all directions of the geostrophic wind. Generally, the *open-cast mining* and the grown *settlements* heat more strongly. They hold longer the heat than the vegetated areas occurring in REF at the same place. The most sensitive component of the energy budget to the landuse changes is the latent heat flux, followed by the sensible and soil heat fluxes (Tab. 2). Note that significant changes of the fluxes of sensible heat only occur for a geostrophic wind from 280° (Tab. 2).

Of course, the domain-averaged 24h-accumulated evapotranspiration depends on the direction of the geostrophic wind. It is the greatest for REF190 and the lowest for MINURB10 for which evapotranspiration does not exceed 2/3 of that provided by REF190 (Fig. 2). In the domain-average, slightly less water evapotranspirates in the simulations with a geostrophic wind direction of 100° and 280° than in that of 190°. On average, less water evapotranspirates in MINURBxxx than in REFxxx for all directions of the geostrophic wind. There is a higher significance that the changes in evapotranspiration are due to the landuse changes for geostrophic winds from 100° and 280° than for the other directions (Tab. 2). The fact that the differences in the domain-averaged evapotranspiration are similar and the fact that a lower correlation between the landuse changes and the differences in evapotranspiration is yield for geostrophic wind directions from 280° and 100° means that evapotranspiration is more strongly modified in the lee of the landuse changes for these two geostrophic wind directions than for the other geostrophic wind directions.

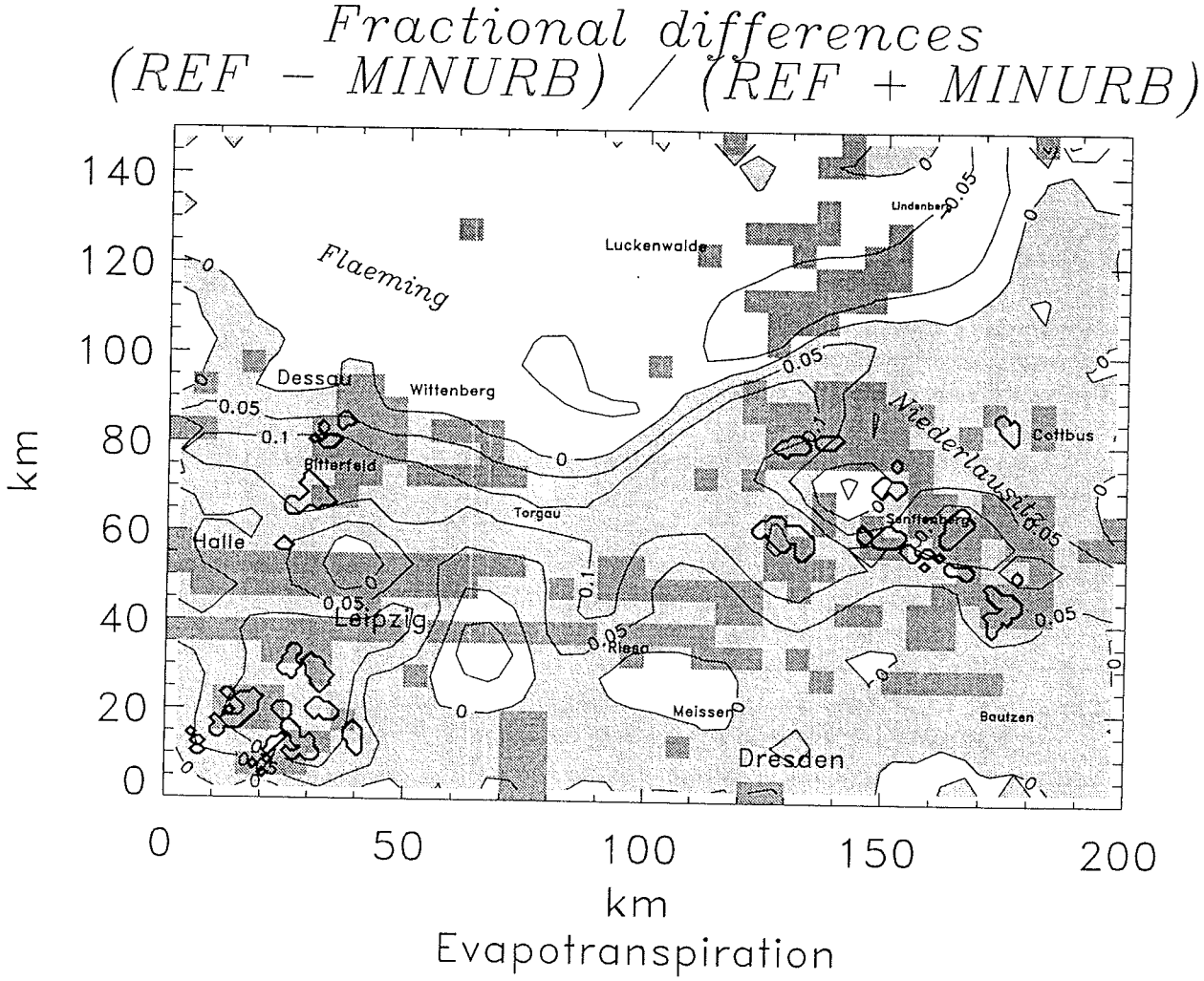

Fig. 7. As Fig 3 but for a geostrophic wind from 280°. The dark grey boxes indicate grid cells for which at least one of the following quantities, namely, air temperature, evapotranspiration, the sensible heat fluxes, the w-, u- and v-component of the wind vector or soil wetness, differ at 90 % or better statistical significance level due to the landuse changes.

Generally, the domain-averaged 24h-accumulated precipitation is greater for REF than for MINURB for all directions of the geostrophic wind except for a geostrophic wind from 190°. As pointed out already in xxx190 no precipitation reaches the ground (Fig. 2). In MINURBxxx the horizontal extension of the precipitation pattern is less than in REFxxx. Although the domain-averaged precipitation decreases, when urbanization and *open-cast mining* take place, the local 24h-accumulated maxima of MINURBxxx exceed those of REFxxx in the lee of larger cities. This means that in MINURBxxx more intense precipitation falls (e.g., Tab. 3) at fewer places than in REFxxx.

The differences in the 24h-accumulated precipitation do not correspond to that in the 24h-accumulated evapotranspiration for all directions of the geostrophic wind (Fig. 2). This means that the differences in the local water cycle which are caused by the landuse changes strongly depend on the geostrophic wind direction and the related orographically or roughness induced modification of the wind field. For a geostrophic wind from 10° the landuse changes affect the domain-averaged 24h-accumulated precipitation as well as the temporal development of the precipitation the greatest of all wind directions investigated here (Fig. 2).

On summarizing, for all directions of the geostrophic wind the landuse changes significantly affect evapotranspiration. Evapotranspiration is noticeably enhanced or reduced when the near surface wind passes both the landuse types immediately one after the other. The

tendency of an increased moisture convergence in the lee of the grown, conurbation as well as the difference between REF and MINURB in the domain-averaged evapotranspiration seem to be independent of the geostrophic wind direction.

6.2. The variables of state

Comparison of the fractional differences shows that the air temperatures are the most sensitive to the landuse changes for a geostrophic wind from 10° and 100° and the less sensitive for 190°. Nevertheless, the greatest correlation between the landuse changes and the resulting differences in air or surface temperature is obtained for a geostrophic wind from 190°. This indicates that there exists only a slight, but continuous, change in temperature over the entire area of landuse conversion. Surface temperatures, however, significantly alter for the landuse changes under a geostrophic wind from 190° (Tab. 2). Note that for a geostrophic wind from 100° the landuse changes significantly influence both air and surface temperature (Tab. 2).

Due to the stronger heating of the grown conurbation and the open-cast mining the vertical mixing is significantly enhanced for all directions of the geostrophic wind at these locations (Tab. 2). Nevertheless, these significant changes occur in different regions for the different geostrophic wind directions.

In contrast to a geostrophic wind from 100° and 280° the near surface horizontal wind field is strongly determined by the underlying surface for a geostrophic wind direction of 10° and 190°, respectively. Here, convergence occurs because the flow is directed by orography. Note that for a geostrophic wind direction of 10° and 190° cloud formation mainly occurs along these convergence lines. The landuse changes significantly influence the v- and the u-component of the wind vector only for geostrophic wind from 280° (Tab. 2).

If REF or MINURB provides the larger cloud coverage can not be generalized (Fig. 2). The cloudiness of REF and MINURB differs the largest for a geostrophic wind from 280° in the morning and for a geostrophic wind from 100° in the late afternoon and early evening (Fig. 2). In REF10 the cloud coverage exceeds that of all simulations (Fig. 2). The increased cloudiness of REF10 results from the higher evapotranspiration than in MINURB10. The larger cloudiness of xxx10 may be due to the enhanced vertical motion by the convergence of the wind field and the orographically induced cloud formation at the Sächsisches Bergland. In all simulations with urbanization (MINURBxxx) there exists a tendency for increased humidity and an initiation of cloud formation or even an increased cloud formation in the lee of larger cities.

On summarizing, a stronger sensitivity of the local water cycle to landuse changes was detected for geostrophic wind directions from 100° and 280° than for the other geostrophic wind directions examined here (e.g., Tab. 2). This may be partly explained by the nearly orthogonal orientation of the near surface wind field towards the landuse pattern and the *open-cast mining*. The orographically directed flow and the more or less parallel flow to the stripes of the prevailing landuse seem to lessen the effects of the landuse changes for the two other directions of the geostrophic wind.

7. Conclusions

The study investigates the effect of *open-cast mining* and urbanization on the local and mesoscale weather for various directions of the geostrophic wind. It was motivated by the actual landuse changes occurring in large areas of eastern Germany. Eight 24h-simulations were performed with the Leipzig's version of GESIMA by assuming a landscape with and without urbanization and *open-cast mining* under four directions of the geostrophic wind. Significance test were performed to evaluate the sensitivity of the atmospheric response to the landuse changes. Moreover, the fractional differences of REF and MINURB were determined. The results substantiate the following:

- The landuse changes significantly influence soil wetness factors, the vertical component of the wind vector, cloud and precipitating particles as well as evapotranspiration for all directions of the geostrophic wind.
- The domain-averaged evapotranspiration and, if precipitation occurs, also the domain-averaged precipitation are always lower in MINURB than in REF.
- Independent of the direction of the geostrophic wind direction urbanization leads to an enlarged moisture convergence over and in the lee of larger cities. This may enhance cloudiness and rainfall in their lee side.
- The magnitude and location of the changes as well as, whether the other variables of state and/or the other fluxes are affected by the landuse changes, varies for the different geostrophic wind directions.
- Whether the effects of the accumulated landuse changes enhance each other or counteract, depends on their location to each other along the surface wind direction and on the prevailingly adjacent landuse.
- For a geostrophic wind direction from 280° the landuse changes significantly influence the most quantities all the wind directions investigated here. Moreover, the areas that achieve significant changes are larger for a geostrophic wind direction from 280° than for the other directions.

Considering these findings it may be concluded that the atmospheric response to the local landuse changes is sensitive to the direction of the geostrophic wind. The stronger sensitivity of the local weather to landuse changes for geostrophic winds from 100° and 280° seems to depend on the specific constellation of the landscape investigated (flatter terrain in the north than in the south, preference for *forests* and *grassland* in the north-eastern part and for *agriculture* in the south-western part, a higher urbanization rate in the south-western part than in the north-eastern part; Fig. 1). Therefore, future studies should examine if the higher sensitivity of the local weather to landuse changes that was detected for geostrophic winds from 100° and 280° can be found for other mid-latitude landscapes, too. It has to be expected that in very complex terrain mountain circulation will prevail. Hence, here the influence of the geostrophic wind direction on the atmospheric response to the landuse changes will depend on whether the geostrophic wind directions leads to another wind regime in the valley or not.

Acknowledgments

I would like to express my thanks to the Deutsche Forschungsgemeinschaft (DFG) for the support of this study under contracts Mo770/1-1 and Mo770/1-2. Thanks also to K. Friedrich who provided the landuse and topography data. I also wish to thank A. Ziemann, G. Kramm and K.E. Erdmann for fruitful discussions as well as B. Beckmann for providing the digitized 'Großwetterlagen'.

References

Anthes, R.A., 1984: Enhancement of convective precipitation by mesoscale variations in vegetative covering in semiarid regions. *J. Clim. Appl. Met.*, **23**, 541-554.

Avissar, R., Pielke, R.A., 1989: A parameterization of heterogeneous land surface for atmospheric numerical models and its impact on regional meteorology. *Mon. Wea. Rev.*, **117**, 2113-2136.

Brubaker, K.L., Entekhabi, A., Eagleson, P.S., 1993: Estimation of continental precipitation recycling. *J. Clim.*, **6**, 1077-1089.

Changnon, S.A., Huff, F.A., 1986: The urban-related nocturnal rainfall anomaly at St. Louis. *J. Clim. Appl. Meteor.*, **25**, 1985-1995.

Charney, J., 1975: Dynamics of desert and droughts in the Sahel. *Q. J. R. Meteorol. Soc.*, **101**, 193-202.

Chen, F., Avissar, R., 1994: Impact of land-surface variability on local shallow convective cumulus and precipitation in large-scale models. *J. Appl. Met.*, **33**, 1382-1401.

Copeland, J.H., Pielke, R.A., Kittel, T.G.F., 1996: Potential climatic impacts of vegetation change: A regional modeling study. *J. Geophys. Res.*, **101D**, 7409-7418.

Cotton, W.R., Pielke, R.A., 1995: *Human impacts on climate*. Cambridge University Press.

Deardorff, J.W., 1978: Efficient prediction of ground surface temperature and moisture, with inclusion of a layer of vegetation. *J. Geophys. Res.*, **84C**, 1889-1903.

Dickinson, R.E., 1992: Change in landuse. *Climate System Modeling*, K.E. Trenberth (ed.), Cambridge Press, 689-701.

Eppel, D.P., Kapitza, H., Claussen, M., Jacob, D., Koch, W., Levkov, L., Mengelkamp, H.-T., Werrmann, N., 1995: The non-hydrostatic mesoscale model GESIMA. Part II: Parameterizations and applications. *Contrib. Atmos. Phys.*, **68**, 15-41.

Gerstengarbe, F.-W., Werner, P.C., 1993. Katalog der Großwetterlagen Europas nach Paul Hess and Helmuth Brezowsky 1981-1992. *Ber. DWD* **113**.

Groß, G., 1988: A numerical estimation of the deforestation effects on local climate in the area of the Frankfurt International Airport. *Contrib. Atmos. Phys.*, **61**, 219-231.

Groß, G., 1989: Anwendungsmöglichkeiten mesoskaliger Simulationsmodelle dargestellt am Beispiel Darmstadt Teil I: Wind- und Temperaturfelder. *Meteorolo. Rdsch.*, **43**, 97-112.

Jarvis, P.G., 1976: The interpretation of the variation in leaf water potentail and stomatal conductance found in canopies in the field. *Phil. Trans. R. Soc. Lond.*, B., **273**, 593-610.

Kapitza, H., Eppel, D.P., 1992: The non-hydrostatic mesoscale model GESIMA. Part I: Dynamical equations and tests. *Contr. Phys. Atmos.*, **65**, 129-146.

Kerschgens, M., Drauschke, R.L., 1986: On the energy budget of a wintry mid-latitude city atmosphere. *Contrib. Atmos. Phys.*, **59**, 115-125.

Kramm, G., Dlugi, R., Dollard, G.J., Foken, T., Mölders, N., Müller, H., Seiler, W., Sievering, H., 1995: On the dry deposition of ozone and reactive nitrogen compounds. *Atmos. Environ.*, **29**, 3209-3231.

Landsberg, H.E., 1970: Man-made climatic changes. *Science*, **170**, 1265-1274.

Mölders, N., Raabe, A., Tetzlaff, G., 1996: A comparison of two strategies on land surface heterogeneity used in a mesoscale β meteorological model. *Tellus*, **48A**, 733-749.

Mölders, N., Kramm, G., Laube, M., Raabe, A., 1997: On the influence of bulk-parameterization schemes of cloud microphysics on the predicted water-cycle relevant quantities - a case study. *Met. Zeitschr.*, **6**, 21-32.

Otterman, J., Manes, A., rubin, S., Alpert, P., O'Starr, D.C., 1990: An increase of early rains in southern Isreal following land-use change? *Bound.-Layer Meteor.* **53**, 333-351.

Pielke, R.A., Dalu, G., Snook, J.S., Lee, T.J., Kittel, T.G.F., 1990: Non-linear influence of mesoscale landuse on waether and climate. *J. Clim.*, **4**, 1053-1069.

Savenije, H.H.G., 1995: New definitions for moisture recycling and the relationship with land-use changes in the Sahel. *J. Hydrol.*, **167**, 57-78.

Smolarkiewicz, P.K., 1984: A fully multidimensional positive definite advection transport alogorithm with small implicit diffusion. *J. Comp. Phys.*, **54**, 325-362.

Seth, A., Giorgi, F., Dickinson, R.E., 1994: Simulating fluxes from heterogeneous land surfaces: explicit subgrid method employing the biosphere-atmosphere transfer scheme (BATS). *J. Geophys. Res.*, **99D**, 18651-18667.

Sud, Y.C., Yang, R., Walker, G.K., 1996: Impact of in situ deforestation in Amazonia on the regional climate: General circulation model simulation study. *J. Geophys. Res.*, **101D**, 7095-7109.

Wilson, M.F., Henderson-Sellers, A., Dickinson, R.E., Kennedy, P.J., 1987: Sensitivity of the biosphere-atmosphere transfer scheme (BATS) to the inclusion of variable soil characteristics. *J. Clim. Appl. Met.*, **26**, 341-362.

Xue, Y., 1996: The impact of desertification in the Mongolian and the inner Mongolian grassland dson the regional climate. *J. Climate*, **9**, 2173-2189.

Zhang, H., Henderson-Sellers, A., McGuffie, K., 1996: Impacts of tropical deforestation. Part I: Process analysis of local climate change. *J. Clim.*, **9**, 1497-1517.

Zheng, N., Dickinson, R.E., Zheng, X., 1996: Climatic Impact of Amazon deforestation - A mechanistic model study. *J. Clim.*, **9**, 859-883.

Address of the author:
LIM - Institut für Meteorologie
Universität Leipzig
Stephanstr. 3
04103 Leipzig
Germany
gppnm@hpmet180.meteo.uni-leipzig.de

A Numerical Case Study on the Sensitivity of the Water and Energy Fluxes to the Heterogeneity of the Distribution of Land Use

Katja Friedrich and Nicole Mölders

Summary:

Numerical experiments assuming land-use distributions of different heterogeneity of wet and dry surfaces were performed on a cloudy day in spring with a calm wind to examine their influences on the domain-averaged fluxes as well as on the distribution of the fluxes within the domain. The results substantiate that, for large heterogeneity, i.e., small patches, the distribution of the patches plays no role in the magnitude of the atmospheric fluxes. For larger patches, however, the domain-averaged latent heat-fluxes depend appreciably on both the heterogeneity as well as on the fractional coverage by the land-use types. On the average, for heterogeneous conditions, the prevailing land-use type governs the fluxes. Nevertheless, no exact linearity between the fractionally coverage of the two land-use types and the resulting fluxes exists. Discontinuities in the fluxes which lead to the non-linear behaviour of the domain-averaged fluxes occur at the border between two larger areas of extremely different characteristics, namely, *grass* (wet, cool) and *sand* (dry, warm). Three different patterns of behaviour are found for the temporal development of the differences in the domain-averaged fluxes which depend on both the heterogeneity and the pattern of the land use.

Zusammenfassung:

Numerische Experimente, bei denen unterschiedlich heterogene Landnutzungsverteilungen trockener und feuchte Flächen angenommen werden, wurden für einen wolkigen Schwachwindtag im Frühjahr durchgeführt. Die Ergebnisse belegen, daß bei großer Heterogenität, d.h. kleinen Flächen, deren Anordnung keine Rolle spielt. Bei großen Flächen jedoch hängen die Gebietsmittelwerte der latenten Wärmeflüsse merklich sowohl von der Heterogenität als auch von dem Flächenanteil der Landnutzung ab. Im Mittel beherrscht der vorherrschende Landnutzungstyp die Flüsse. Dennoch ist kein exaktes lineares Verhalten zwischen dem Flächenanteil der Landnutzung und den resultierenden Flüssen vorhanden. Diskontinuitäten in der Verteilung der Flüsse, die letztendlich zu der Nichtlinearität der Gebietsmittelwerte der Flüsse führen, treten an den Grenzen der größeren Flächen unterschiedlicher Oberflächencharakteristika auf, in dieser Studie Gras (feucht, kühl) und Sand (trocken, warm). Drei unterschiedliche Verhaltensweisen im zeitlichen Verlauf der Differenzen der Gebietsmittelwerte der Flüsse wurden gefunden, die vom Muster und der Heterogenität der Landnutzung abhängen.

1. Introduction

Flying over a landscape in mid-latitudes on a day with calm winds presents a fantastic view over patchy domains of various surfaces and sizes. Recently, observational, theoretical and numerical studies illustrated the impact of surface characteristics and discontinuities on the atmospheric boundary layer (ABL; e.g., Anthes 1984, Avissar and Pielke 1989, Mahrt et al. 1994). This impact is exacerbated by the moistening of the low-level atmosphere through transpiration, the rising of the resulting lighter, moist air (as compared to dry), and the additional ascending motion induced by surface thermal heterogeneity. The ascent and descent of air induced by surface heterogeneity tend to disappear, however, when surface wind speeds exceed 4 m/s due to turbulence (Shen and Leclerc 1994).

The horizontal grid resolution of meteorological models is much coarser than that required by hydrological studies. Moreover, a grid element of a meso-β-scale meteorological model encompasses several square kilometers for which often the dominant land-use type is assumed to be the representative one to determine the water and energy fluxes at the earth's surface. Since landscapes are often heterogeneous over the resolvable scales considered in meteorological models of that mesoscale, it has to be expected that the practice frequently applied to calculate the water and energy fluxes on the basis of dominant land-use types may be inadequate to represent the surface forcing because different land surfaces and slopes yield different fluxes of momentum, moisture, and heat (due to differences in water availability) as well as insulation, plant, and soil parameters (e.g., Avissar and Pielke 1989). Recently, several authors examined the behaviour of fluxes under heterogeneous surface conditions. Using different horizontal grid resolutions and assuming the dominant land-use type within a grid box as the representative surface type for the entire grid element, Mölders and Raabe (1996) showed that the grid resolution may strongly affect the calculated water and energy fluxes because a land-use type (being of subgrid-scale on a coarse grid and here of minor importance) may be dominant on a finer grid.

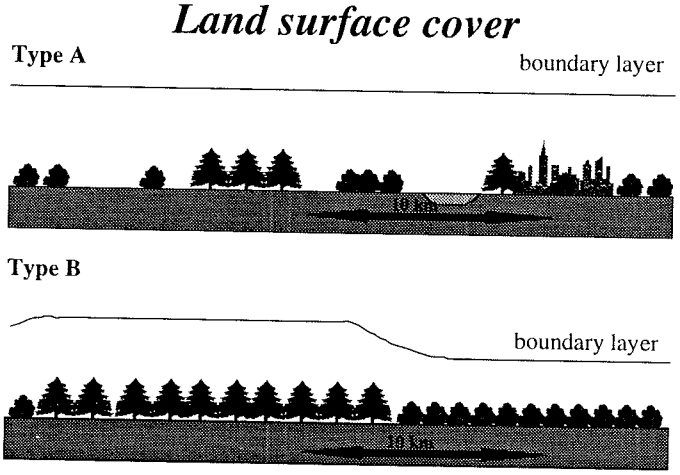

Fig. 1. Schematic view of the atmospheric response to the underlying surface for land-use type A and B (modified after Shuttleworth (1991)).

Recently, Shuttleworth (1988) proposed two distinct scales of land-cover influence: a 'disorganised' land surface (type A land-surface cover; Fig. 1), whose characteristic horizontal scales are less than 10 km, and an 'organised' land surface of characteristic length > 10 km (type B land-surface cover; Fig. 1). He theorised that only larger organised heterogeneity allows the atmosphere to develop a coherent response to land cover as substantiated by the formation of clouds and precipitation because the convective fluxes are aggregated over larger horizontal and vertical scales. It appears that there are two scales that need to be examined, i.e., the scale of about 100 km for homogeneous land-cover types, and the scale of 10 km or so, for heterogeneous land-cover types (O'Neal 1996). The emphasis of the present study is on investigating the role that the degree of heterogeneity of land use plays on the 'disorganised' modulation of the water and energy fluxes. In doing so, results provided by numerical simulations with different patterns of surface heterogeneity (Fig. 2) are compared and evaluated.

2. Model Description and Initialisation

The Leipzig version of the non-hydrostatic meteorological model GESIMA (Geesthacht's Simulation Model of the Atmosphere; Kapitza and Eppel 1992, Eppel et al. 1995) was used to investigate the response of the water and energy fluxes to the heterogeneity of the underlying

surface. Its dynamical part is based on the anelastic equations. The model's physical features are as follows: A five water-classes cloud-parameterisation scheme was applied (Mölders et al. 1997). The treatment of the soil/vegetation/atmosphere interaction follows Deardorff (1978, see also Eppel et al. 1995), assuming homogeneous soil and land-surface characteristics within a grid cell. The surface stress and the near-surface fluxes of heat and water vapour are expressed in terms of dimensionless drag and transfer coefficients applying the parametric model of Kramm et al. (1995). Radiation transfer is calculated by a simplified two-stream method (Eppel et al. 1995).

A homogeneous flat terrain was assumed for all simulations. The model was initiated using profiles of air temperature and humidity typical for a cloudy atmosphere in spring. A geostrophic wind of 8 m/s from the west was assumed. The simulations were integrated for 24 hours where the first six hours serve as the adjusting phase. The whole test domain has a size of 75 x 75 km^2 with a horizontal resolution of 5 x 5 km^2. The vertical resolution varies from 20 m close to the ground to 1.5 km at the top. The model whole domain has a hight of 10.5 km. Eight levels are located below the 2-km height and 7 are above.

3. Design of the Numerical Experiments

The investigations are performed for different patches of a *sand /grass* mixture which differ not only in the amount but also in the heterogeneity. Sixteen simulations with heterogeneous land-surface conditions are performed and two with homogeneous. In the two simulations assuming homogeneous surface conditions, the entire domain is covered by *grass* and *sand*. These runs will be addressed as HOMG and HOMS hereafter. Eight simulations assuming heterogeneous land-surface conditions are performed with altering *sand* and *grass* strips equal in width to 25 km and 5 km, respectively. The strips are once orientated in NS-direction perpendicular to the direction of the geostrophic wind and once in EW-direction parallel to the geostrophic wind (Fig. 2). These runs are referred to as GSGP25, SGSP25, GSGR25, SGSR25, GSGR5, SGSR5, GSGP5, SGSP5, where G stands for *grass*, and S for *sand*, respectively. The letters P and R represent the orientation of the strips to the wind direction, namely, *parallel* and *perpendicular*. Furthermore, six simulations are carried out using a chessboard for which the squares have a length of 25 km, 10 km and 5 km (Fig. 2). These runs are referred to as GSGC25, SGSC25, GSGC10, SGSC10 (where the last east and the last south row have a 10 x 15 km^2 resolution), GSGC5, GSGC5, where G and S represent the *grass* and *sand* land use as mentioned above, and C stands for *chessboard*, respectively. Two further simulations are performed with a north-south- and east-west-orientated cross which consists of five homogeneous 25 x 25 km^2 patches in the centre and four alternating 25 x 25 km^2 *sand* or *grass* patches on each corner (Fig. 2). These simulations are denoted as GSGX25 and SGSX25, respectively, where X stands for *cross*.

On summarising, the name of a simulation consists of six letters: the first three represent the land use (GSG, SGS) while the last three letters stand for the patch size and the patch arrangement (Fig. 2). In the following discussion we use xxx representing all variations of land use for a specific arrangement (xxxC25) or for all arrangements with a specific variation of land use (SGSxxx).

The dependency of the energy budget on the heterogeneity of the underlying surface is examined as follows. First, the temporal development of the domain averages of the components of the energy budget (fluxes of latent and sensible heat, soil heat-flux, net radiation) was determined for each simulation on an hourly basis for the entire simulation time (Fig. 4, sect.4.1.). In addition, we use this directly to compare the energy budget of simulations with the same amount of *grass* and *sand* but different heterogeneity (Fig. 5, sect. 4.2.).The differences of the domain averages of the 'homogeneous' to the 'heterogeneous' simulations are investigated by subtracting the domain averages of the respective heterogeneous simulations from those of HOMG and HOMS (Fig. 6, sect.4.3.).

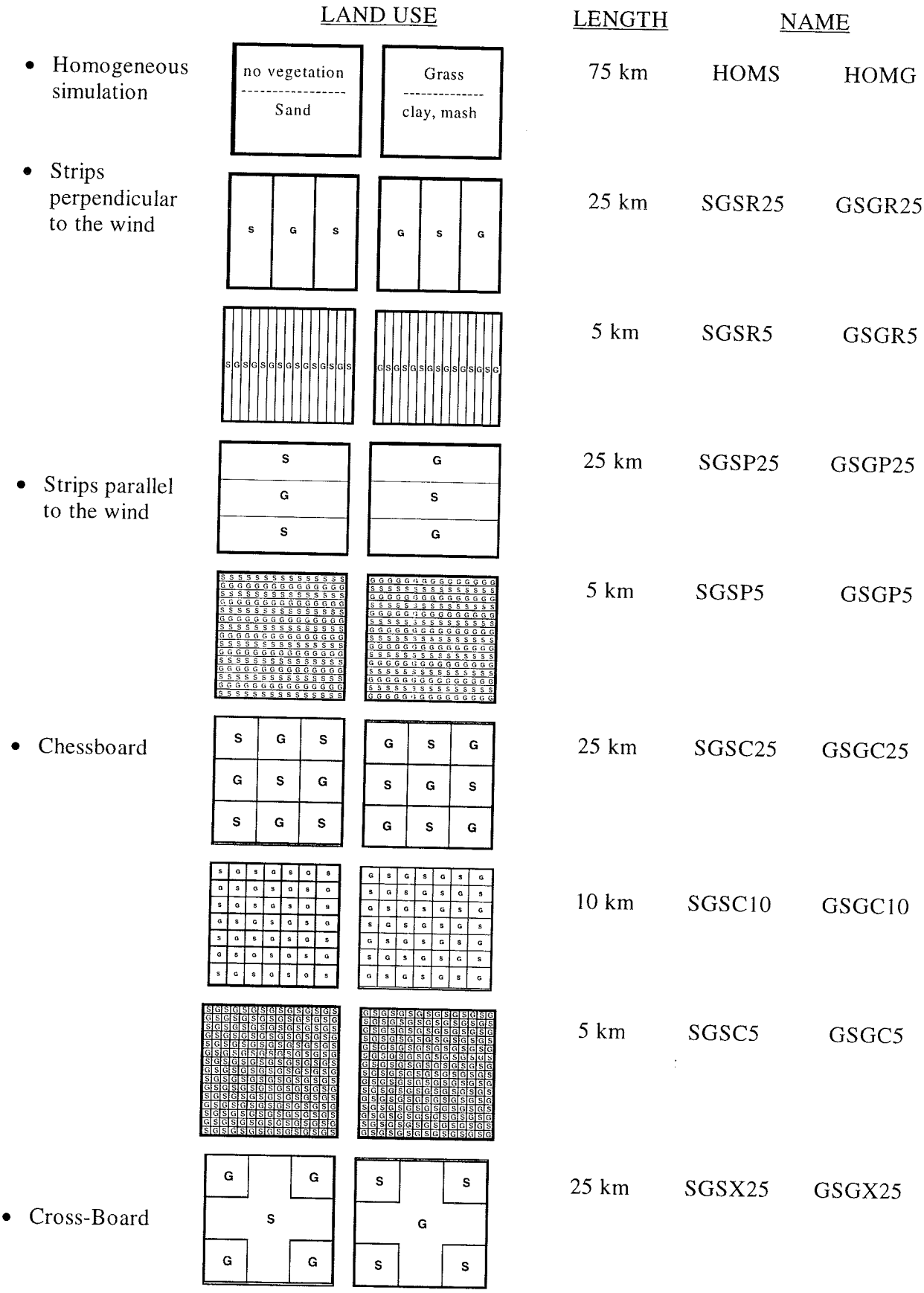

Fig. 2. Schematic view of the land-use distribution applied in the numerical experiments peformed for this study.

To investigate the contribution of a *grass*- and a *sand*-covered patches in the 'heterogeneous' simulations, the fractionally weighted domain averages of the homogeneous runs were subtracted from the domain averages of fluxes of the heterogeneous runs (Fig. 7, sec.4.4.). Herein, the area covered by the same land use in both runs determines the fractional weight (Eq. 1). For purposes of understanding factionally weighted land-use constribution we created the following equation:

$$F^K(HET) = \alpha F^K(HETi) + (1-\alpha) F^K(HETj) = \beta [\alpha F^K(HOMi) + (1-\alpha) F^K(HOMj)] \quad [1]$$
$$\text{with } i \neq j ,$$

where the index K stands for the fluxes of latent heat, Q_{lat}, sensible heat, Q_{sens}, soil heat, Q_{soil}, and net radiation, Q_{rad}, respectively. The idea behind this is as follows: If the contribution of the different patches add up linearly, then the differences (determined according to Eq. 1) will be the same as 1 minus the residuum of the fractional weight times the domain-averaged flux of the respective other homogeneous run. In the linear case, β would be equal to 1. By comparing these results, we can quantify the effect of the heterogeneity. Finally, a grid-point-by-grid-point comparison of the fluxes provided by the different simulations was performed to investigate where potential non-linear behaviour existed (Fig. 8).

The aim of these experimental designs is (1) to show the amount and the time of deviation (Figs. 6, 7) and (2) to investigate how the heterogeneous simulations average between the response to *grass* and *sand*, respectively (Fig. 8).

4. Results and Discussions

4.1. Impact of heterogeneity on energy budget

On the average, net radiation and the sensible heat-flux hardly differ for the different underlying surfaces. Generally, the increase of the soil heat-flux is at the expense of the sensible and latent heat-flux for a *grass*-dominated land surface, as compared to that obtained in the case of homogeneous coverage by *grass*. While for a *sand*-dominated land surface the soil heat-flux enhances by reducing the latent heat-flux. Therefore, in most parts of the article the latent heat- fluxes are discussed exemplarily.

By comparing each flux, similar results as illustrated in Fig. 3 are found. Although no great differences of fluxes will be expected at a latitude of 51° north, we found some differences in time of maximum of the fluxes and amount of fluxes (e.g., Figs. 2, 3, 4, Tabs. 4, 5). The more often *sand* occurs in the domain, the more the fluxes behave like *sand*. Therefore a maximum of *grass* and a minimum of *sand* occur for the sensible and latent heat- flux and a maximum of *grass* and a minimum of *sand* are found for the soil heat-flux and the net radiation.

If there were a linear response of the fluxes to the fractionally coverage by a certain land- use type, we should expect the magnitude of the domain-averaged fluxes to arrange themselves as given in Tab. 1.

NUMBER	NAME	AMOUNT OF *GRASS* IN 225TH
1	HOMG	225
2	GSGP25	150
3	GSGR25	150
4	GSGX25	125
5	GSGC25	125
6	GSGR5	120
7	GSGP5	120
8	GSGC10	117
9	GSGC5	113

NUMBER	NAME	AMOUNT OF *GRASS* IN 225TH
10	SGSC5	112
11	SGSC10	108
12	SGSR5	105
13	SGSP5	105
14	SGSC25	100
15	SGSX25	100
16	SGSP25	75
17	SGSR25	75
18	HOMS	0

Tab. 1. Arrangement of the simulations as expected for a linear response of the fluxes according to the fractionally coverage of *grass*.

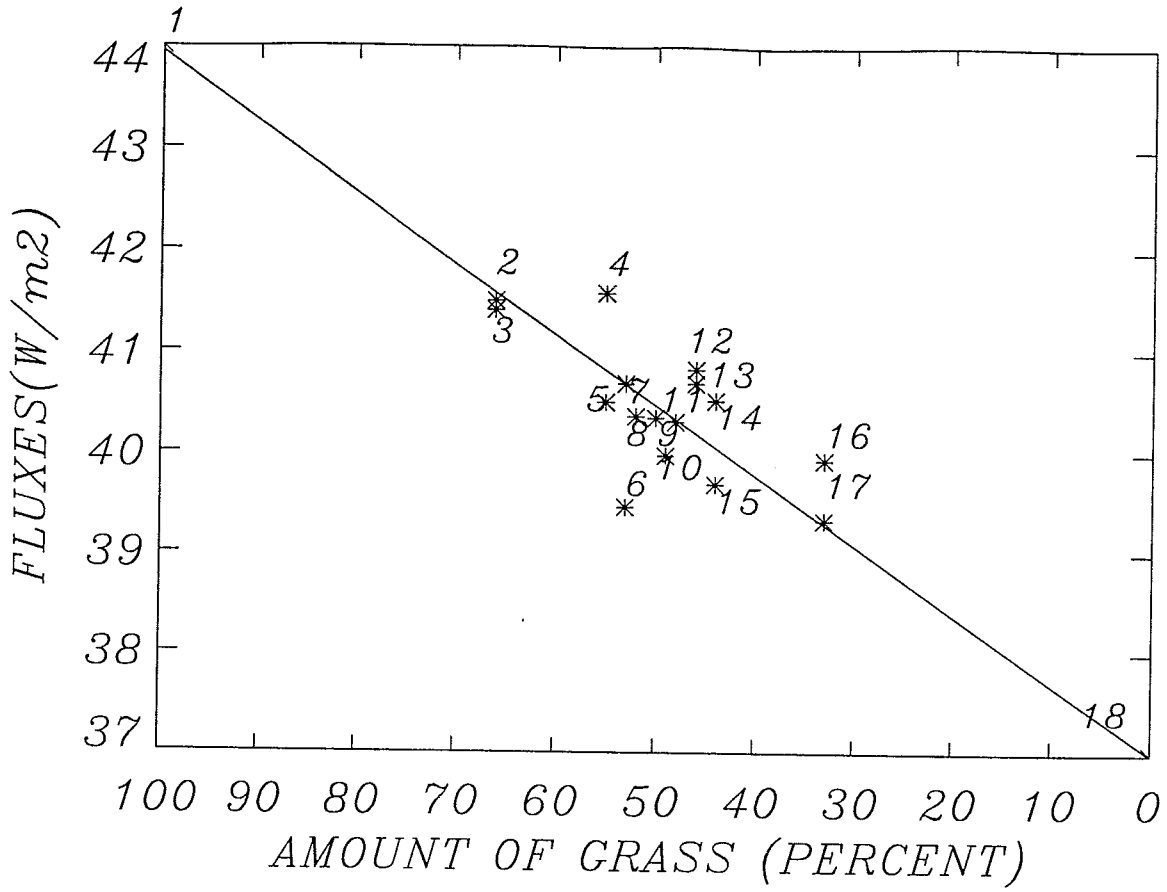

Fig. 3. Sensitivity of the domain averaged latent heat-fluxes for different fractional coverage of *grass* and *sand*, respectively, as well as for different patch arrangements at 1200LT. The numbers code the simulations as explained in Tab. 1.

The tendency of each simulation is exemplarily demonstrated in Fig. 3 for the flux of latent heat at 1200 LT. Obviously there are deviations from linearity, especially for fractional coverage around 50 %.

In the following chapter we compare all domain-averaged fluxes obtained for the different heterogeneous simulations to each other. For better comprehension of the correlation between increasing heterogeneity and the behaviour of the latent heat-flux, we use the following subjective way of arranging the simulations after heterogeneity (Tab. 2):

Ranging	Simulation name	Size of the largest patch
1	HOMx	75 x75 km (5625 km²)
2	xxxX25	5x25x25 km (3125 km²)
3	xxxP25	25x75 km (1875 km²)
4	xxxR25	25x75 km (1875 km²)
5	xxxC25	25x25 km (625 km²)
6	xxxP5	5x75 km (375 km²)
7	xxxR5	5x75 km (375 km²)
8	xxxC10	10x15 km (150 km²)
9	xxxC5	5x5 km (25 km²)

Tab. 2. Illustration of the heterogeneity according to the extension of the largest patch. Here it is assumed that the parallel strips have fewer effects on the energy budget than the perpendicular strips because the wind blows from the west and gets less affected by parallel strips than by perpendicular ones. The xxx stands for the subsequent combination of either SGS or GSG, and x represents *grass*, G, and *sand*, S.

Due to the different distributions of the surface energy budget of a mainly *grass*- or *sand*-covered surface (latent heat-flux for *grass* is larger than for *sand*), we divided the comparison of energy budget in *grass*-dominated land surface and *sand*-dominated land surface. As a result of the different thermal and hydrologic behaviour of *grass* and *sand,* the greatest deviations from the linearity occur for the latent heat-flux and the soil heat-flux.

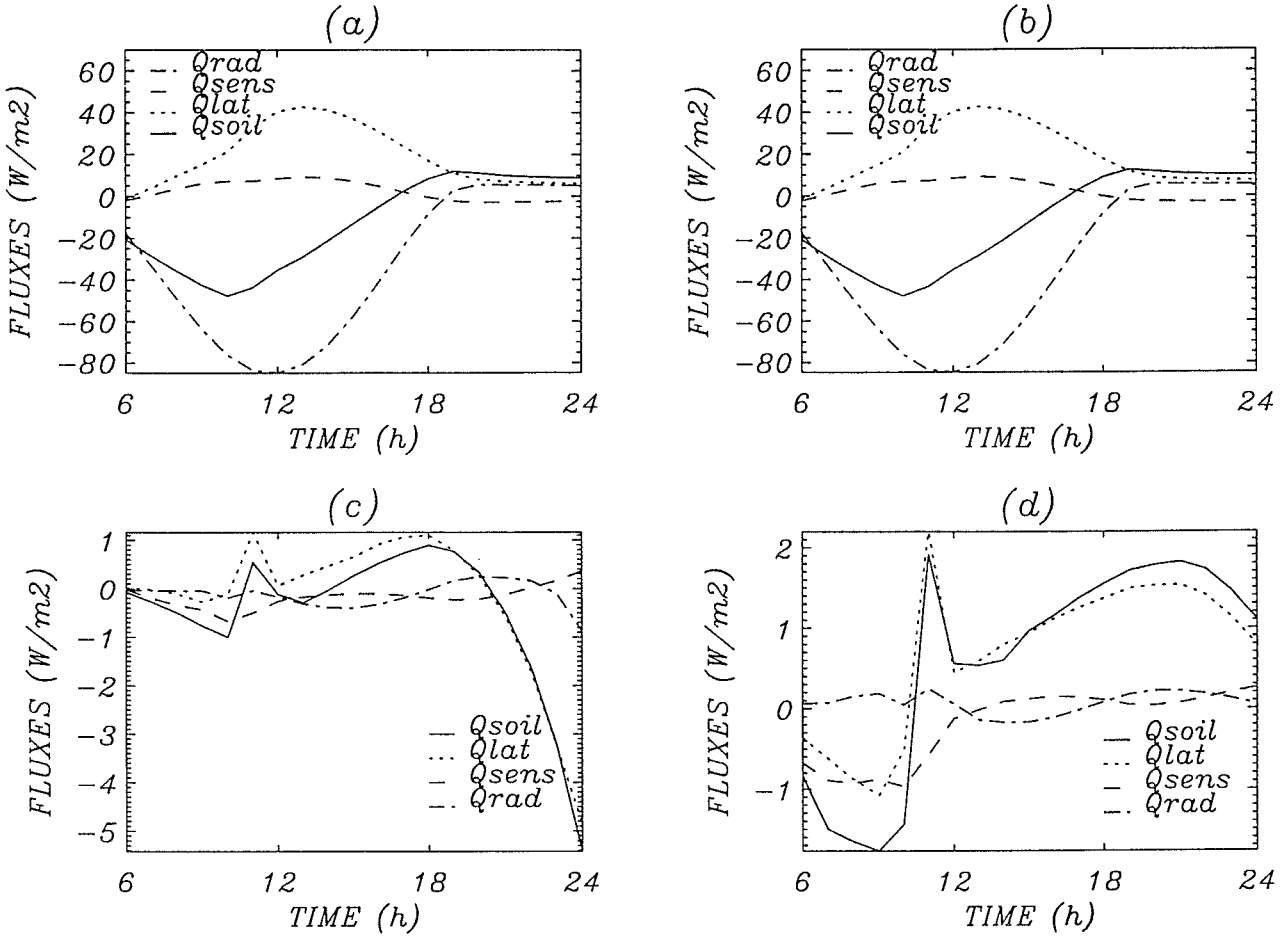

Fig. 4. Energy budgets arranged according to the degree of heterogeneity for simulations: (a) GSGC10 (b) GSGC5, (c) GSGC10-SGSC10, (d) GSGC5-SGSC5. Notice that further results of energy budget are shown in Fig. 6 under the condition of same amount of land use but different heterogeneity. All fluxes are domain averages.

4.1.1. Domain-averaged latent heat-fluxes of simulations with *grass* as the dominant land use

In the following two subsections we drop the extension GSG when addressing the simulations. When comparing all simulations in which *grass* is the dominant underlying surface, the domain- averaged latent heat-flux differs during the whole simulation time from 0800 to 2400 LT (Figs. 4 a and 4b). The maximum of the latent heat-flux occurs in all simulations at about 1300 LT with a value of 40-44 W/m². The maximum of the latent heat-flux for simulation HOMG is about 4 W/m² larger than for the most heterogeneous simulation (C5 - Fig. 4b). When comparing the least heterogeneous simulation (X25) with the most heterogeneous simulation (C5) (Tab. 2) deviations of about 2-4 W/m² less are obtained for the latter between 1000-1500 LT and deviations of about 7 W/m² less are found between 1700-2400 LT for C5 (Fig. 4b). If one looks for the degree of heterogeneity in more detail, one will usually find mostly no differences except in the juxtaposition of simulations P25 and R25. Compared to P25, simulation R25 has a decrease of 2-4 W/m² and a reduction of 4-5 W/m² in

the morning and after sunset. Furthermore, an exception is found for the juxtaposition of simulations R5 and C10 as well as for the juxtaposition of simulations C10 and C5 (Figs. 4a and 4b). Here, the latent heat-fluxes increase 1-2 W/m² for the more heterogeneous simulation.

4.1.2. Domain-averaged soil heat-fluxes of simulations with *grass* as the dominant land use

If the domain is mainly covered by *grass*, in the morning the temporal development of the behaviour of the domain-averaged soil heat-flux will hardly differ from that of the latent heat-fluxes for the simulations with the *grass*-dominated land cover. Between 0700-1300 LT we find a slight increase (1-2 W/m²) of soil heat-flux in the juxtaposition of simulations P25 and R25 as well as for simulations X2 and C5 (Fig. 4b). A more obvious difference between the domain-averaged soil heat-flux and the domain-averaged latent heat-flux occur after sunset. Generally, the increase ranges from 2-10 W/m² for the more heterogeneous surfaces (Tab. 2). For example, in comparing the domain-averaged soil heat-flux: simulations P25 and R25 have a difference of 8 W/m², simulations R25 and R5 differ about 4 W/m², and for simulations X25 and C5 (Fig. 4b) have a 10 W/m² difference. An exception is found for the comparison of the domain-averaged soil heat-fluxes of R5 to C10 as well as for the juxtaposition of C10 and C5 (Figs. 4a and 4b), where the more heterogeneous simulations (Tab. 2) have a stronger (about 1-3 W/m²) soil heat-flux than the less heterogeneous ones. A small differentiation is found for some simulations between 1900 and 2000 LT. Finally, the soil heat-flux of HOMG gets an increase of 3 W/m² towards the most heterogeneous simulation.

4.1.3. Domain-averaged latent heat-fluxes of simulations with *sand* as the dominant land use

For purposes of simplicity, we drop the extension SGS in the following two subsections when addressing the simulations. In the simulations in which the underlying surface is mostly covered by *sand* (Figs. 4c and 4d) there is obviously no linear increase of latent heat-flux or soil heat-flux from the most heterogeneous to the homogeneous, as was found for the simulations in which the underlying surface was mainly dominated by *grass* (Figs. 4a and 4b).

A slight enlargement of the latent heat-flux maximum from 40 W/m² for HOMS to 42 W/m² is found for the most heterogeneous simulation (C5). Before and after the maximum which occurs between 1200-1500 LT, we find a slight increase of 1-4 W/m² for the more heterogeneous simulations, especially for the comparison of X25 with P25 and R25 with R5. Generally, there is a reduction of latent heat-flux for *sand*-dominated land use of about 4 W/m² after sunset when comparing the least heterogeneous simulation (X25) with the most heterogeneous simulation (C5 - Fig. 4d). In juxtapozing the less heterogeneous with the next more heterogeneous simulation (Tab. 2), we do not get a linear increase as expected. Instead, an increase is investigated for the more heterogeneous simulations of 1-5 W/m² for simulations X25 and P25, R25 and R5 and for simulations R5 and C10 (Fig. 4c), as well as for simulations R5 and C5 (Fig. 4d). A reduction of 1-5 W/m² for the more heterogeneous simulation is observed for simulations P25 and R25 as well as for simulations C10 and C5 (Figs. 4c and 4d). A comparison of the results (obtained by the simulation assuming those strips perpendicular and parallel to the geostrophic wind) showed that the latent heat-flux in the case of strips parallel to the geostrophic wind is about 4-6 W/m² higher than the latent heat-flux of strips perpendicular to the geostrophic wind.

4.1.4. Domain-averaged soil heat-fluxes of simulations with *sand* as the dominant land use

Like the domain-averaged soil heat-fluxes, obtained from the simulations in which the underlying surface is dominated by *grass* (Figs. 4a and 4b), the domain-averaged soil heat-flux shows a different temporal behaviour and sensitivity than the domain-averaged latent heat-flux. We find no general tendency between the results of the homogeneous and the most heterogeneous simulations and the dependency of the soil heat-flux on increasing heterogeneity (Tab. 2). Only in the morning the domain-averaged soil heat-flux increases slightly for 1-3 W/m² between 1000-1400 LT in the case of the more heterogeneous surfaces when comparing simulations P25 with R25, simulations R5 with C10 as well as simulations C10 with C5 (Figs. 4c and 4d). On the other hand, by comparing simulations R25 with R5, the domain-averaged soil heat-flux decreases for about 1-3 W/m² for the more heterogeneous cases (Tab. 2). After 1800 LT, the domain-averaged soil heat-flux rises by 4 W/m² when comparing HOMS with C5. By juxtapozing the results of the heterogeneous with the next heterogeneous simulations (Tab. 2), we observe a decrease for simulations X25 and P25 (1-8 W/m²), R25 and R5 (1-3 W/m²), R5 and C10 (1-3 W/m²), while there is an enlargement of 1-8 W/m² for the pairs P5 and R5, as well as for the pairs C10 and C5 (Figs. 4c and 4d).

4.2. Net radiation-flux, soil heat-flux, sensible heat-flux and latent heat-flux in simulations with the same amount of land use but different heterogeneity

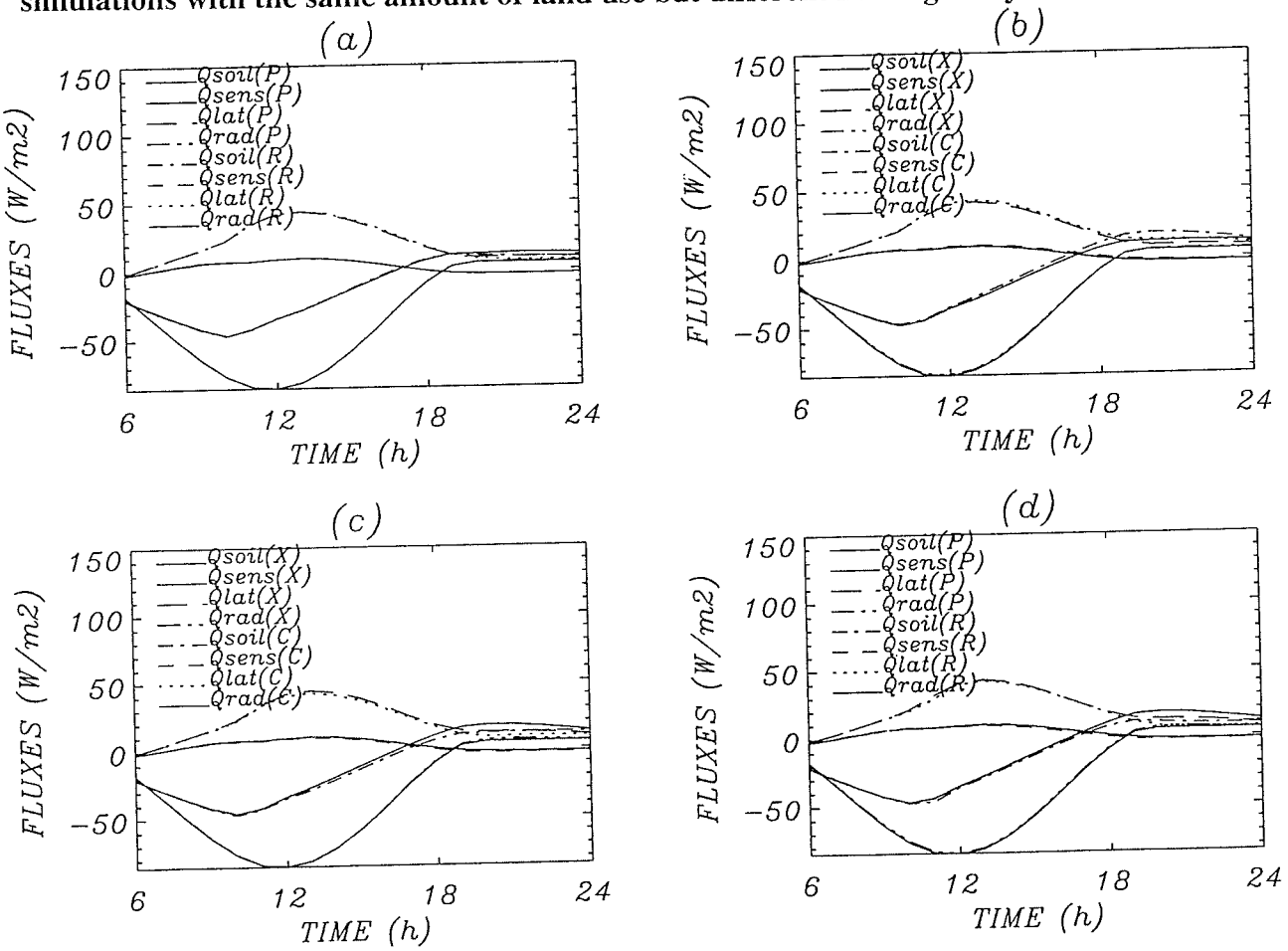

Fig. 5. Comparison of domain averaged energy budget of simulations with the same amount of *grass* and *sand* but different heterogeneity for (a) 66,7 % (GSGR25/P25) (b) 55,6% (GSGC25/X25) (c) 44,4% (SGSC25/X25) and (d) 33,3% (SGSR25/P25) *grass*.

In the previous section, we discusse the energy budget of simulations with varying amounts of *sand* and *grass* land use (Tab. 1) and different heterogeneity (Tab. 2). In this section we will

focus on the energy budget of simulations with the same amount of *grass* or *sand* but different heterogeneity. Figure 5 illustrates the dependency of the energy budget on heterogeneity.

The impact of heterogeneity on the energy budget is investigated by the juxtaposition of the simulations xxxP5 and xxxR5 (while xxx stands for GSG and SGS, respectively), where the 5 km strips are orientated parallel and perpendicular to the wind, respectively. The results show that a patch size of 5 x 5 km^2 is too small for developing a different energy budget. This coincides well with Shuttleworth's hypothesis (1991).

In simulations with a strip length of 25 km (xxxR25/P25), the sensible heat-flux and the soil heat-flux start to increase about 1-2 W/m^2 after 1200 LT, while the greatest differences for the soil heat-flux achieve up to 10 W/m^2 LT after sunset (Fig. 5a and 5d). The differences between xxxX25 and xxxC25 increase about 2-3 W/m^2 before sunset and up to 6 W/m^2 afterwards (Figs. 5b and 5c).

4.3. Domain-averages of the latent heat-fluxes obtained by the simulations with homogeneous underlying surface compared to those without, i.e. heterogeneous

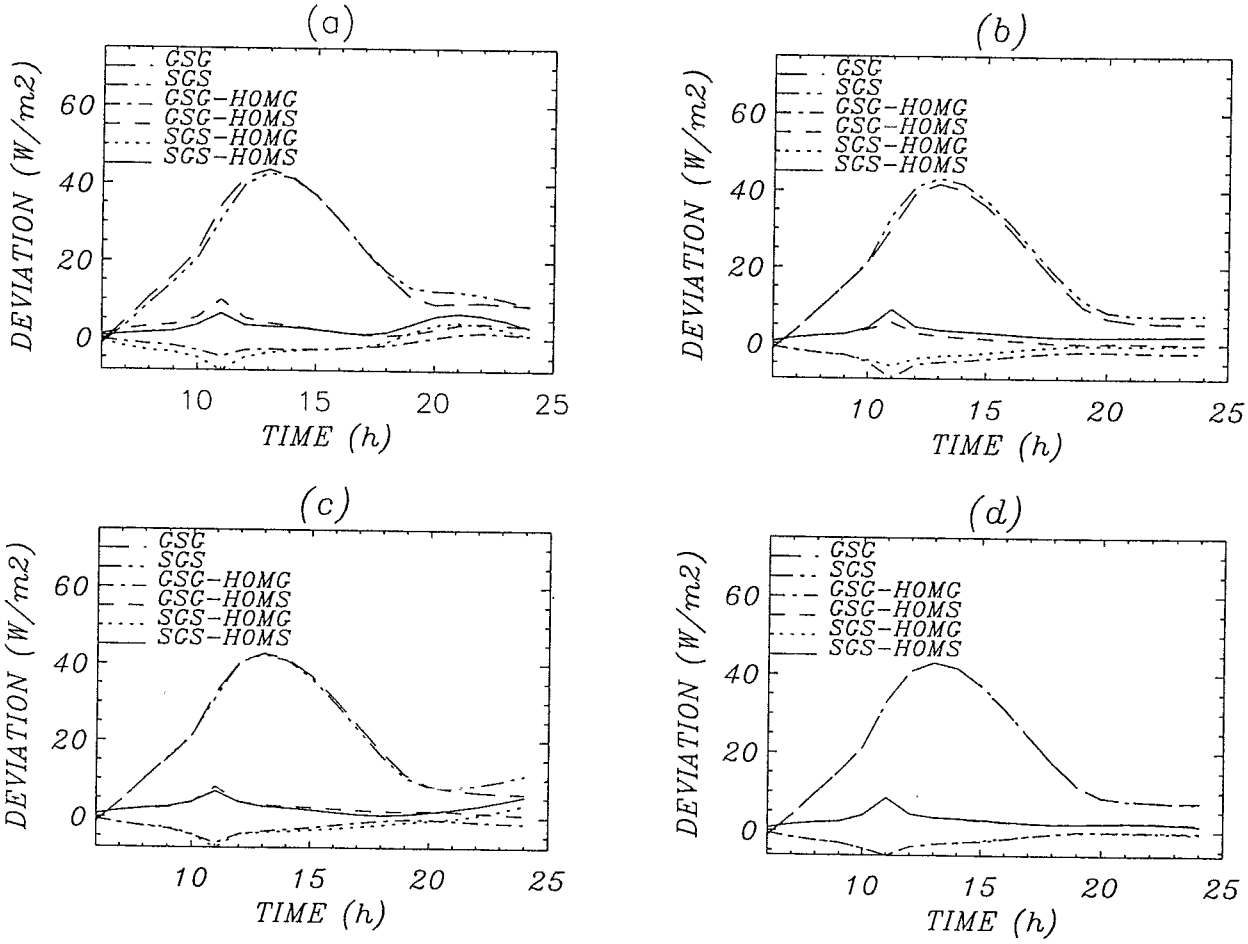

Fig. 6. Difference of domain averaged latent heat-flux for (a) xxxP25-HOMx representing the 3π-sinus curve (b) xxxR5-HOMx describing the π-sinus curve and (c) xxxC10-HOMx expressing the 5/2π-sinus and (d) xxxP5-HOMx. Note that xxx stands either for GSG or SGS and x represents *sand* or *grass*, respectively.

The domain averages of the simulations with heterogeneous land use (called HET hereafter) were subtracted from the results of the simulations with homogeneous *grass* as well as with homogeneous *sand* (Fig. 6). In the following description xxx stands for all possibilities: either all heterogeneous land use (GSG or SGS) or all patch-style contributions (R25, P5, etc.).

Notice HETxxx means all domain-averaged heat-fluxes of all heterogeneous simulations, while HETG = GSGxxx-HOMS = SGSxxx - HOMS and HETS = GSGxxx - HOMG = SGSxxx - HOMG. Be aware that the differences in chapter 4.4 are fractional-weighted latent heat-fluxes (Eq. 1), while here the contribution of the fractions of equal land use are compared.

The latent heat-flux is the most sensitive component of the energy budget with respect to changes in heterogeneity. Therefore, we will limit the discussion to this aspect. Generally, the differential HETxxx-HOMG of the latent heat-flux decreases till 1100 LT, followed by an increase till 1900 LT. After subtracting the latent heat-flux of HOMG from those of SGSxxx and GSGxxx (which leads to HETS), the differences provide a minimum at 1100 LT in all simulations ranging from -4 till -11 W/m² and a maximum in the afternoon and evening (1900-2400 LT) of -1 till 4 W/m² in some simulations. Two different patterns of behaviour were obtained after sunset for the results of HETS:

1. The first is a slight decrease with a tendency to stagnation between 1900-2400 LT in simulations with smaller patches like xxxC10-HOMG (Fig. 6c), xxxC5-HOMG, xxxP5-HOMG (Fig. 6d), xxxR25-HOMG .
2. The second is a maximum at 2100 LT and a decrease afterwards in simulations with coarser patches like xxxP25-HOMG (Fig. 6a), xxxX25-HOMG, xxxC25-HOMG.

Notice the same subtractions are done for HOMS and SGSxxx/GSGxxx (which leads to HETG). There the simulations again behave after special shapes (Tab. 3).

As pointed out before, assuming a linear behaviour between the increase/decrease in the latent heat-flux and the increase in the fractionally coverage of the model domain by *grass/sand* (under conditions without rain or dew), the greatest domain-averaged latent heat-flux is expected for homogeneous *grass* followed by the heterogeneous *grass*-dominated conditions, and finally by the heterogeneous *sand*-dominated conditions. However, some exceptions to the above assumption were observed. This is mainly visible when the domain-averaged latent heat-flux, provided by the simulation with the homogeneously *sand*-covered surface (HOMS), is subtracted from that provided by the simulations with the heterogeneous surfaces. The resulting values of latent heat-flux of the *grass*-covered fraction (SGSxxx-HOMS = HETG or GSGxxx-HOMS = HETG) become positive. On the other hand, the latent heat-fluxes provided by the simulation with homogeneous *grass* coverage, minus those with the heterogeneous coverage simulations (GSGxxx-HOMG = HETS or SGSxxx-HOMG = HETS), receive latent heat-fluxes which are directed to the ground. This deviation of the domain-averaged latent heat-fluxes from the linear assumption is as followes:

- xxxC25: 1200-2000 LT HOMG>SGSxxx>GSGxxx
  2000-2400 LT SGSxxx>GSGxxx>HOMG
- xxxP25 (Fig. 6a): 1700-2400 LT SGSxxx>GSGxxx>HOMG
- SGSC10 (Fig. 6c): 2100-2400 LT SGSxxx>HOMG>GSGxxx
- xxxX25: 0000-1900 LT HOMG>GSGxxx>HOMS
- xxxR5 (Fig. 6b): 0900-2400 LT HOMG>SGSxxx>GSGxxx

These effects only occur for the latent heat-fluxes resulting *grass* (HETxxx-HOMS), because the latent heat-flux of homogeneous *sand* does never exceed that of the simulations with a heterogeneous land cover. Only in simulations GSGC25 (0000-1200 LT), GSGP25 (1700-2400 LT), GSGC10 (2000-2400 LT) and GSGR5 (0900-2400 LT) the heterogeneous *sand* dominated land use exceeds the latent heat-flux of the heterogeneous *grass* dominated land use. As mentioned before, all these results are obvious in the energy budget in Fig. 4 as well.

There is no correlation between the onset of the irregularity and the amount of *sand* or *grass*. It seems that the starting depends on the arrangment of patches (Tab. 2), e.g., the starting point for xxxC25 is later than for xxxP25.

Finally, in the simulations assuming an underlying surface of 5 km wide strips parallel to the geostrophic wind, we find no differences between the latent heat-flux of SGSP5-HOMG (which represents the contribution of the *sand*-covered patches to the domain-

averaged flux) and GSGP5-HOMG (that also represents the contribution of the *sand* covered patches to the domain averaged flux !). Notice that both results from the subtraction lead to *sand* (HETS) but the amount of *sand* is different while the latent heat-flux is equal (Fig. 6d).

For the differentials of the results of HOMS minus those of all heterogeneous simulations (which leads to HETG) an opposite behaviour than that of the differences of HETS is expected. Nevertheless, this is only confirmed by the latent heat-flux of xxxR25-HOMS and xxxR5-HOMS (Figs. 6a and 6b). While the latter converge against each other for the whole simulation time, all other simulations converge against one another till 1700 LT (Fig. 6). Afterwards the temporal evolution of the domain-averaged fluxes is parallel to each other (from 1700-2400 LT). The maximum of the differentials of the latent heat-flux is found at 1100 LT with a value of about 6-9W/m².

Curve shape	**Time of the first maximum (value)**	**Time of the second maximum (value)**	**Time of the first minimum (value)**	**Simulations representing HETG**
3π sinus	1100 LT (6-10 W/m²)	21/2200 LT (3-7 W/m²)	1800 LT (0.5-2 W/m²)	xxxC25-HOMS xxxP25-HOMS xxxX25-HOMS
π sinus	1100 LT (6-11 W/m²)			xxxR25-HOMS GSGC10-HOMS GSGC5-HOMS xxxP5-HOMS xxxR5-HOMS
5/2π sinus	1100 LT (6-10 W/m²)	2400 LT (5 W/m²)	1800 LT (1-2 W/m²)	SGSC10-HOMS SGSC5-HOMS

Tab. 3. Classification of the effects of heterogeneity according to the temporal behaviour of the differences between the simulations assuming homogeneous land cover, HOMx, and those assuming heterogeneous land cover, namely HETxxx. Note that xxx stands for the patch style contribution, respectively.

We distinguishe between three different patterns of behaviour of the curve of the differentials, namely, a π-sinus, a 3π-sinus, and a 5/2π-sinus curve-like behaviour (Tab. 3). Notice that for the simulations with a curve like a 3π-sinus the greatest deviations are found for xxxX25-HOMS. The simulations refer to as xxxC25-HOMS and xxxP25-HOMS are similar in their behaviour with a greater difference of xxxP25-HOMS and an irregular behaviour after sunset. The greatest deviations from linearity as well as irregularity (which were discussed already in the context with xxxR25-HOMS) are found in the simulations providing a π-sinus curve of the differences.

An exception to the behaviour after 1900 LT is found in simulations xxxC10 (Fig. 6c), for which SGSC10-HOMS and SGSC10-HOMG increase. For the latter differences, two maxima of 5 and 3 W/m² occur at 2400 LT. The differentials GSGC10-HOMG and GSGC10-HOMS decrease after a maximum at 2000 LT till 2400 LT.

4.4. Comparison of fractionally weighted heterogeneous to fractionally weighted homogeneous simulation of latent heat-flux

The domain averages of fluxes obtained by the simulations with heterogeneous land use were subtracted from the fractionally weighted domain averages of the simulations with a homogeneous coverage by *sand* or *grass*, respectively.

By comparing the fractionally weighted latent heat-flux of the 'homogeneous' with that of the 'heterogeneous' simulation (by using Eq. 1), we get a closer look at how heterogeneity

effects the energy budget. The magnitude of the differences varies over a wide range from simulation to simulation, but the greatest differences are found in the evening after sunset.

To evaluate the temporal development and the magnitude of the non-linear behaviour of the latent heat-flux due to heterogeneity of land use, the differential of (1-α)HETS was compared to (1-α)HOMS and the differential of αHETG was compared to αHOMG, respectively (Fig. 7).

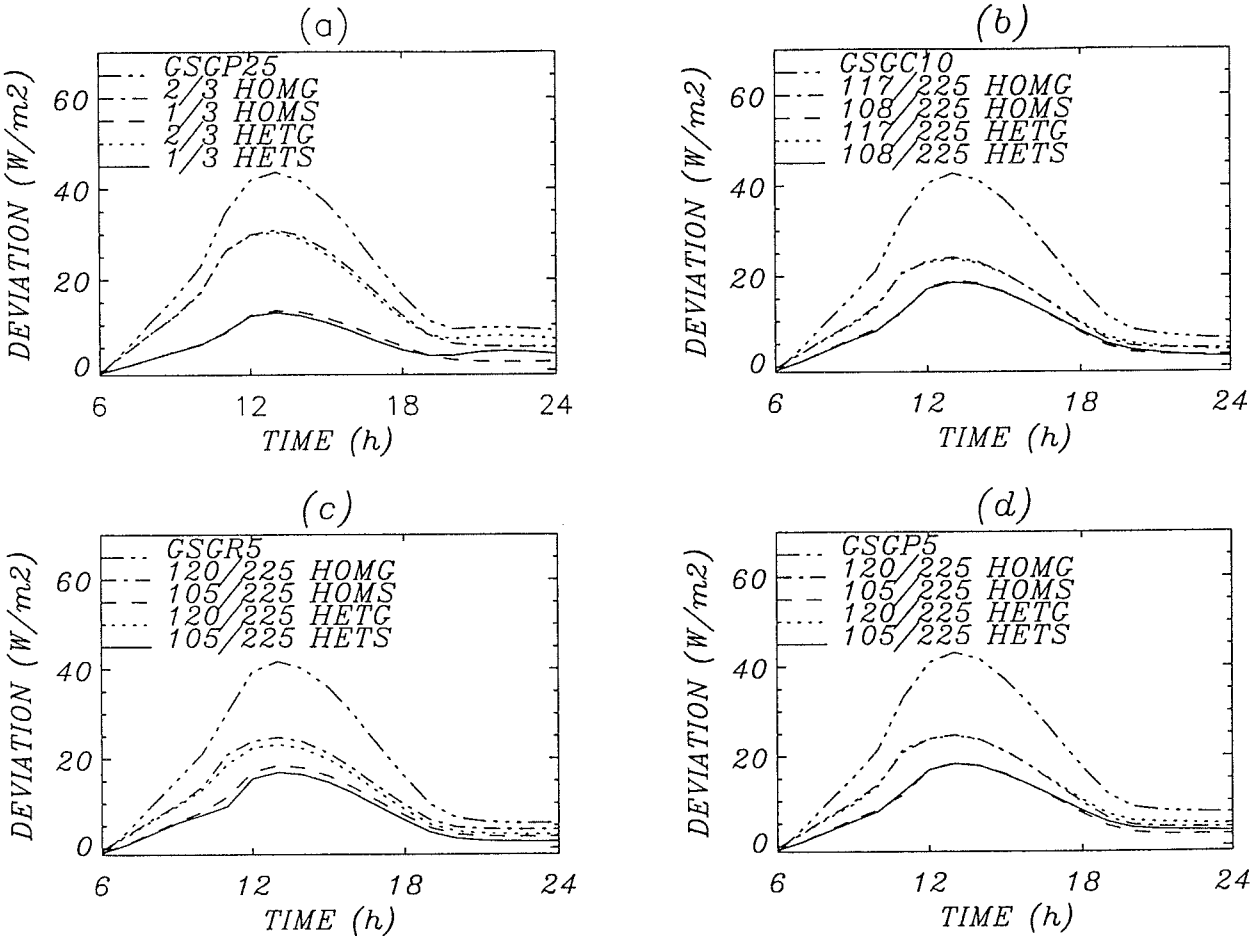

Fig. 7. Fractional weighted latent heat-flux representing the differences of heterogeneous simulations to homogeneous simulations of *grass* for (a) GSGP25, (b) GSGC10, (c) GSGR5 and (d) GSGP5. All fluxes are domain averages.

Time of greatest differences of (1-α)HETS and αHETG	**Simulation with the heterogeneous land cover**
1100	SGSR25 SGSR5
1300	GSGR25
after sunset	xxxC25 xxxP25 GSGC5 xxxX25 xxxP5
1300 and 2100	GSGR5

Tab. 4. Grouping of the simulations according to the magnitude of β. Here, xxx stands for GSG and SGS, respectively. Parameters are used as explained for Eq. 1.

Since the differences on the left-hand side of Eq. 1 are similar for *sand* and *grass* in magnitude and their temporal behaviour, the following comments are valid for both. We create four groups of simulations with an identical onset of great differences and, hence, a β which is not equal to 1 (Tab. 4).

Furthermore, we focuse on the magnitude of the comparison between the latent heat-flux of fractionally weighted homogeneous land use and fractionally weighted homogeneous when subtracting from fractionally weighted heterogeneous land use. We get a detailed view compared to Tab. 4 where the latent heat-flux is higher, either in the heterogeneous or in the homogeneous fraction according to Eq. 1. In doing so, we found the five kinds of similar behaviour as listed in Tab. 5.

In Tab. 5, the role of heterogeneity on the energy budget is obviously seen with a variation of higher and lower latent heat-fluxes for heterogeneous land use compared to homogeneous land use. Without consideration of the heterogeneity of land use, the value of latent heat-flux of a 'homogeneous (dominant) land use' will be mostly calculated too high, while after sunset it will be calculated too low.

No		Simulation name x=*sand* and *grass*	Time of difference	Magnitude of difference
1.	$(1-\alpha)$ HETS < $(1-\alpha)$ HOMS α HETG < α HOMG	GSGC25 GSGP25	1100-1900 LT	1-3 W/m²
	$(1-\alpha)$ HETS > $(1-\alpha)$ HOMS α HETG > α HOMG	SGSC5 GSGC5 GSGX25	1900-2400 LT	1-5 W/m²
2.	$(1-\alpha)$ HETS > $(1-\alpha)$ HOMS α HETG > α HOMG	SGSC25 SGSP25 SGSX25 SGSR5	1000-1500 LT 1800-2400 LT	1-3 W/m² 1-8 W/m²
3.	$(1-\alpha)$ HETS < $(1-\alpha)$ HOMS α HETG < α HOMG	SGSR5	1000-1200 LT	1 W/m²
		GSGR25	1200-1400 LT	1 W/m²
		SGSC5 GSGR5	1000-2400 LT	1-3 W/m²
4.	$(1-\alpha)$ HETS > $(1-\alpha)$ HOMS α HETG > α HOMG	GSGP5	1800-2400 LT	1-2 W/m²
5.	$(1-\alpha)$ HETS > $(1-\alpha)$ HOMS	GSGC10	1800-2200 LT	1 W/m²
	$(1-\alpha)$ HETS < $(1-\alpha)$ HOMS		1200-1400 LT 2200-2400 LT	1 W/m²

Tab. 5. Grouping of the simulations according to their temporal behaviour of non-linearity with respect to Eq. 1. Here, xxx stands for GSG and SGS. Parameters are used as explained for Eq. 1.

The maximum of latent heat-flux of the fractionally weighted homogeneous and heterogeneous simulations is achieved at 1300 LT (Fig. 7). The value of the greatest latent heat-flux of fractionally weighted homogeneous or heterogeneous land-use *grass* ranges between 16 and 31 W/m² depending on the amount of *grass*. While the maximum of fractionally weighted homogeneous or heterogeneous land-use *sand* strays from 12 to 27 W/m² correlating with the amount of *sand*. Despite some exceptions (Tab. 5, No.2) the fractionally weighted homogeneous maximum of latent heat-flux is usually a little higher (1-2 W/m²) than the fractionally weighted heterogeneous maximum at 1300 LT. Generally, during daytime, the latent heat-flux of the fractionally weighted homogeneous simulation has a slightly larger amount than the fractionally weighted heterogeneous simulation and has a slightly smaller amount after sunset.

The minimum of the latent heat-flux of the fractionally weighted heterogeneous and homogeneous simulations appears after sunset but in different shapes (Fig. 7): First, the minimum of (1-α)HETS and αHETG is located at 2400 LT when in Eq. 1 HETx stands for GSGR25, SGSC25, SGSP25 or SGSR25, respectively. Furthermore, the latent heat-flux shows no changes after 2100 LT or the minimum occurs at 2100 LT followed by an increase afterwards, e.g. in GSGR5, GSGC10 and GSGP5. The last shape builds up two minima one at 2000 LT and one at 2400 LT. The latter will appear mainly if, in the heterogeneous simulation, the amount of *grass* and *sand* is nearly the same (45-55 %).

Finally, large deviations in the fractionally weighted heterogeneous simulations compared to the fractionally weighted homogeneous simulations may occur if the heterogeneous simulations are xxxC25, xxxR5 and xxxP25, while small or negligible deviations are found for xxxR25, xxxC10, xxxP5, xxxC5 and xxxR5.

4.5. Grid-point-by-grid-point differences of latent heat-flux

In a grid-point-by-grid-point manner, the results of HOMG are alternatively subtracted from those of all heterogeneous simulations at 1200 LT. It has to be expected that the greatest differences occur at the boundary between the patches of *sand* and *grass* land use. The latent heat-flux for HOMS is about 36 W/m² and for HOMG has a value of 44 W/m² at 1200 LT. Furthermore, we expect values close to ground zero if the land use is the same (in this case *grass*), and positive values (around 8 W/m²) if the patches are covered differently (in this case *sand*), because a *grass*-covered surface usually provides greater latent heat-fluxes than a sandy surface under the same micrometerological conditions.

As pointed out already, the results substantiate that the differences do not behave linearly to the amount of *grass* or *sand*. The size and the arrangement of the *grass* and *sand* have a great impact on the horizontal distribution of the latent heat-flux. The distributions of the differences in the latent heat-flux show no interactions between the neighbouring *sand* and *grass* patches in simulations with a *grass/sand* patch size of 5 km and in the simulations with patches arranged parallel to the geostrophic wind like HOMG-xxxC5, HOMG-xxxR5, HOMG-xxxP5 and HOMG-GSGP25. This agrees entirely with Shuttleworth's (1991) hypothesis that a 'disorganised' land surface-cover (with a length < 10 km) has not a clearly proved influence on the energy budget.

In simulation HOMG-GSGP25, no effect of heterogeneity on the latent heat-flux is found at the interface between *sand* and *grass* patches. This missing effect could be explained as a tunnel-like flow with smooth *sand* in the middle surrounded by the high and rough *grass*. On the other hand for the differential of HOMG-SGSP25, appreciable effects were detected in the northern *sand* patch with higher latent heat-flux of approximatly 5 W/m² in SGSP25 than in HOMG. This can be explained by the flow from the higher and rougher *grass* patches towards the smoother *sand*, which leads to an acceleration of the flow and, hence, increased latent heat-flux.

For the distributions of the latent heat-flux small differences in xxxC10-HOMG are obtained for the *sand* patches and no differences are inquired for the *grass* patches. This might be partly an 'organised' and random influence.

Greater interactions between the neighbouring *sand* and *grass* patches are found in the distributions of the differentials HOMG-xxxX25, HOMG-xxxC25 and HOMG-xxxR25, respectively (Fig. 8). In the simulation GSGC25 (Fig. 8a), the interaction mainly occurs at the middle strip and the east strip. For the most part there is a jump in the latent heat-flux between -3 and 12 W/m² directly at the interface between *grass* and *sand,* and a decrease from *sand* to the *grass* patches, respectively. This means an increase of the latent heat-flux for the northern and southern *sand* patches and a decrease of the eastern and western *sand* patches as compared to the case of a homogeneously *grass*-covered domain. In the heterogeneous case, the latent heat-flux of the *grass* patches is greater at the edges and smaller in the middle, compared to the homogeneous latent heat-flux of *grass*.

(a)

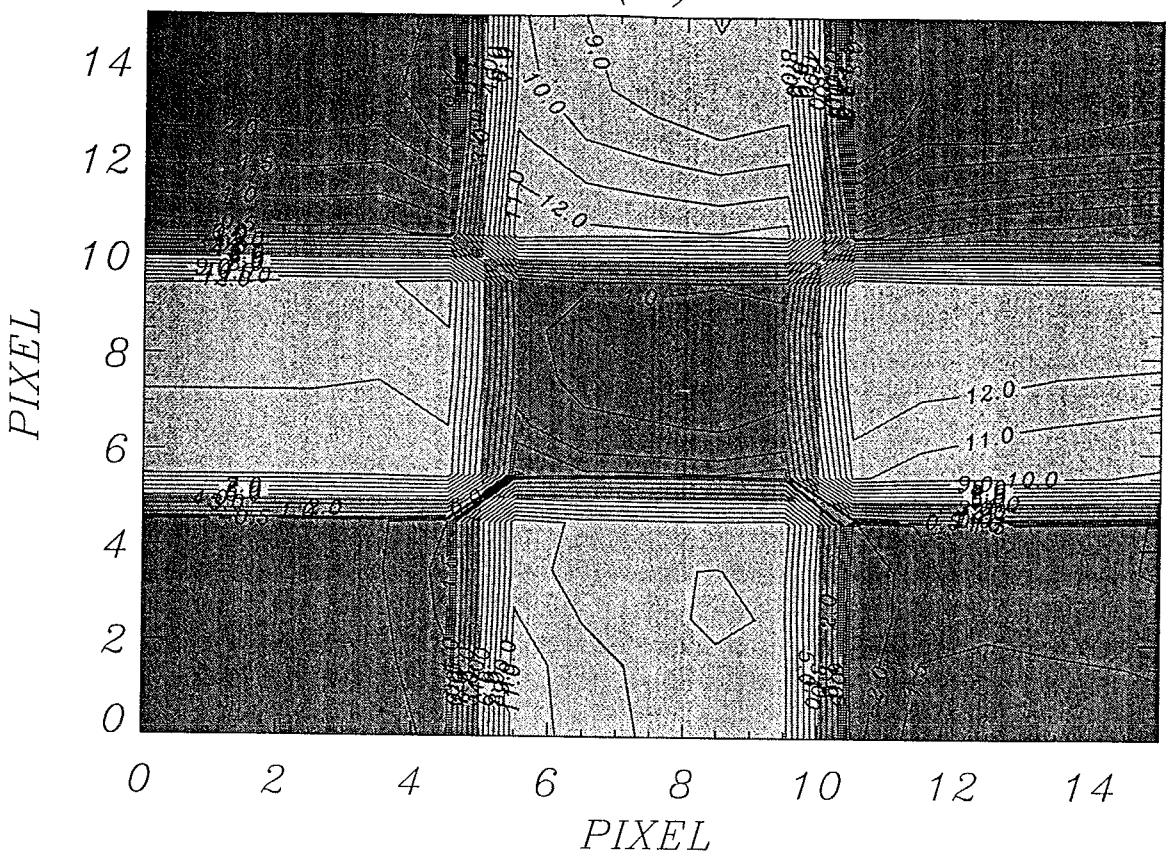
PIXEL
0
2
4
6
8
10
12
14
PIXEL
12.0
11.0
10.0

(b)

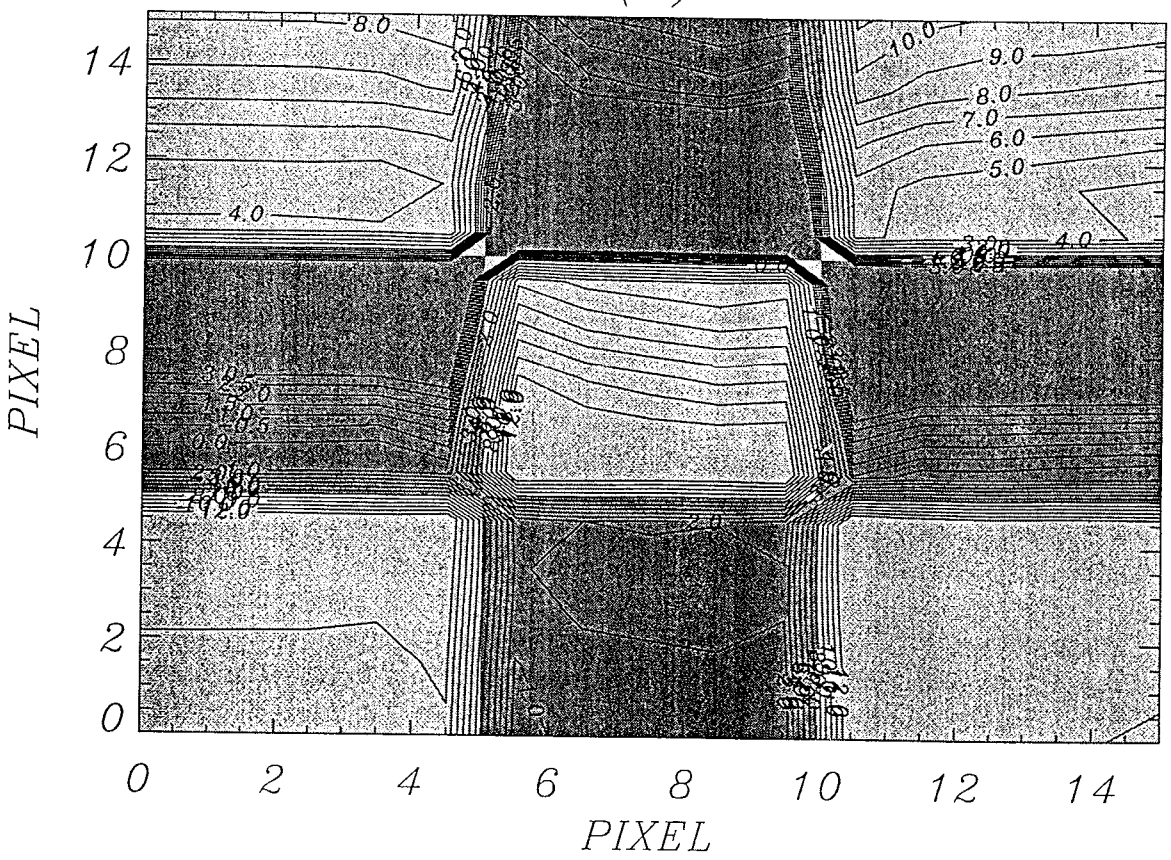
PIXEL
0
2
4
6
8
10
12
14
PIXEL
8.0
10.0
9.0
8.0
7.0
6.0
5.0
4.0
4.0

(c)

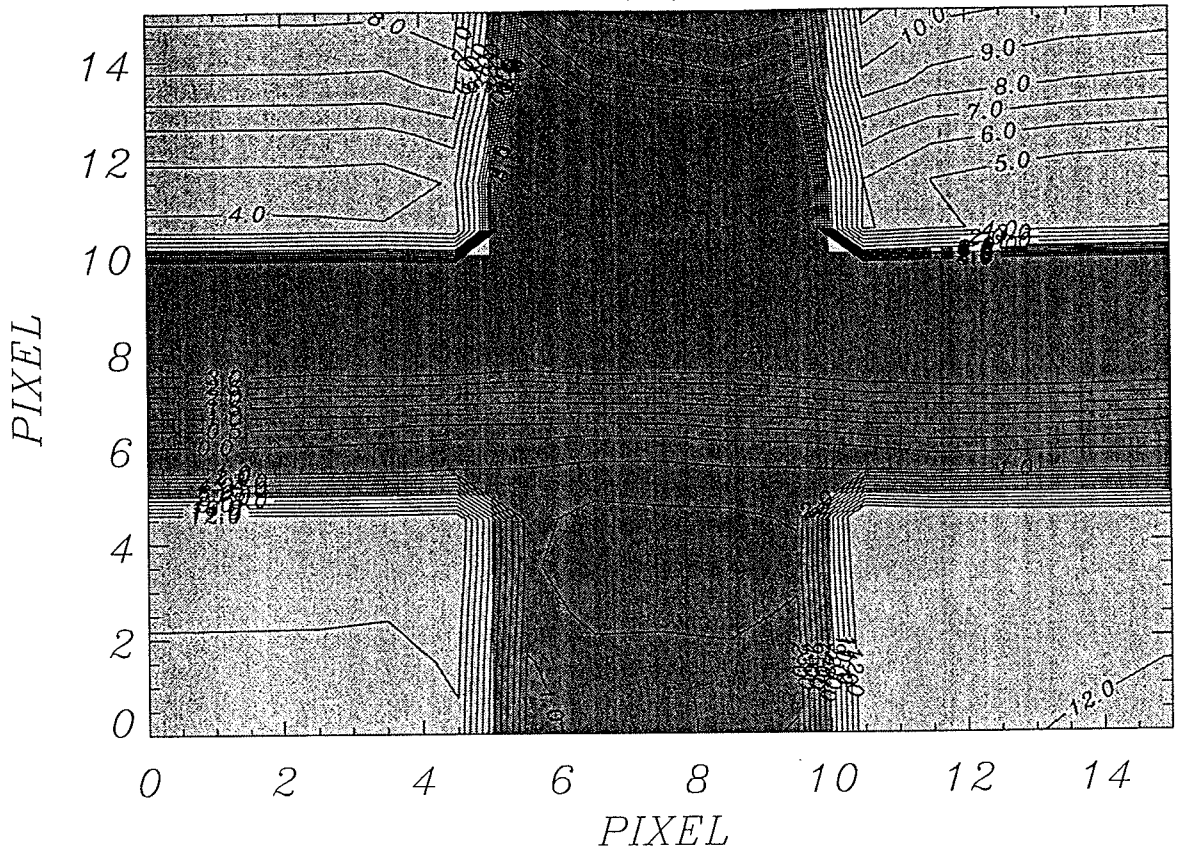
PIXEL
0
2
4
6
8
10
12
14
PIXEL
0
2
4
6
8
10
12
14
10.0
9.0
8.0
7.0
6.0
5.0
4.0
12.0

(d)

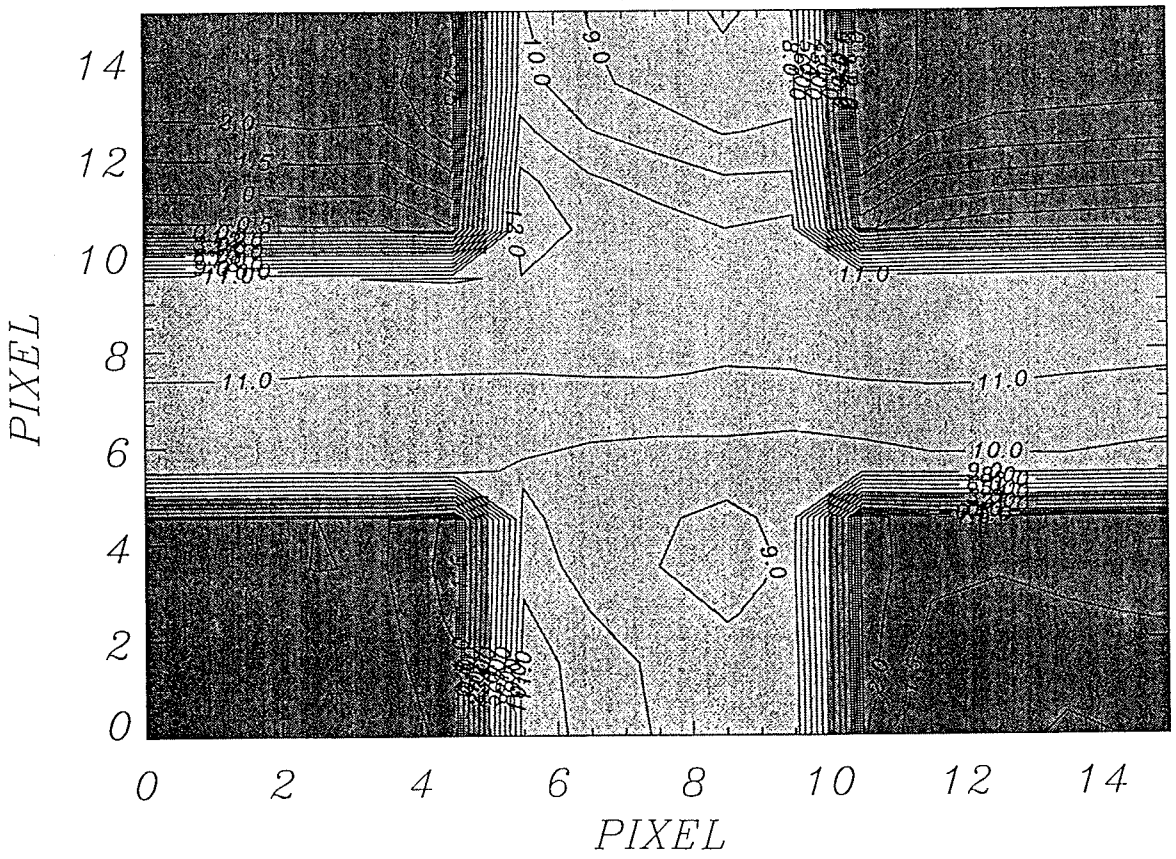
PIXEL
0
2
4
6
8
10
12
14
PIXEL
0
2
4
6
8
10
12
14
10.0
9.0
11.0
11.0
11.0
10.0
9.0

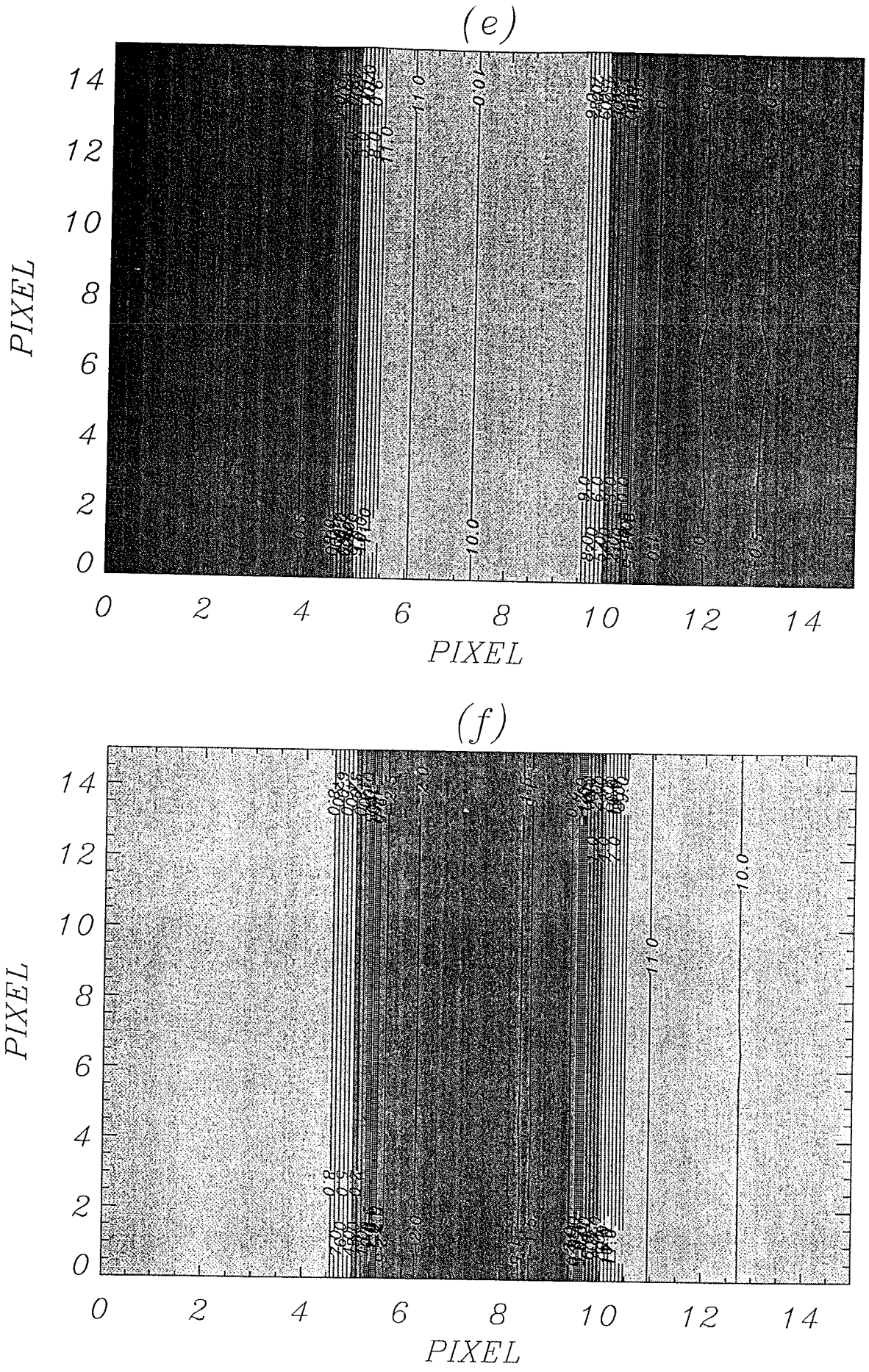

Fig. 8. Two-dimensional sections of latent heat-flux representing the difference of heterogeneous *grass* dominated simulations and HOMG and (a) GSGC25 (b) SGSC25 (c) GSGX25 (d) SGSX25 (e) GSGR25 (f) SGSR25 at 1200 LT. Grey patches indicate *grass* and light grey patches indicate *sand*, respectively.

In simulation refer to as SGSC25 (Fig. 8b), the latent heat-flux over *grass* patches are higher in the northeastern and the western part of the domain than in the simulation with a homogeneous *grass*-covered surface. The opposite is true for the southern part of the domain. In the northern *sand* patches and partial in the *sand* patch in the middle of the domain, the latent heat-flux (provided by the simulation with the heterogeneous surface) exceeds that of the simulation with a homogeneously covered *grass* surface. This indicates interactions in the northern part.

Similar differences result from the simulation called GSGX25 and SGSX25 (Fig. 8c and 8d). In simulation SGSX25 the latent heat-flux differs from those of HOMG in the northern and southern *sand* patches. No differences are found at the *grass* patches in the corners and between kilometres 5 to 10 in an east-west direction of the north-south-strip, where the wind flows without hitting obstacles.

Subtracting HOMG from GSGX25, we observed no differences in the southern part but strong interactions between neighbouring *sand* and *grass* patches in the northern part. These effects are visible till kilometre 8 in the south. Herein, the latent heat-flux of *sand* increases due to interaction with the adjacent *grass* patches.

5. Summary and Conclusions

First of all, we investigated how the degree of heterogeneity of a landscape can influence the energy and water fluxes. Although a difference of 2-4 W/m² in the morning and 2-7 W/m² in the afternoon, between the fluxes for a homogeneous and a heterogeneous surface, is very small and far beyond the accuracy of any measurements, the impact of heterogeneity on the latent heat-flux cannot be neglected. Even though the difference is just some W/m² per day, it has to be considered that a difference of 1 W/(m²•d) means an enlarged evapotranspiration of 12.6 mm/a. If we focus on the latent heat-flux of *sand* with an amount of 39.5 W/m² at 1300 LT on a day with a calm wind and a cloudy atmosphere in spring, a deviation of 2 to 8 W/m² means a difference of 5 to 20 % for *sand*. For the latent heat-flux of *grass*, this results in a difference of 4 % for 2 W/m² and 17 % for 8 W/m². Hence, the results indicate that changes in land use or simple heterogeneity do have a strong impact on the energy and water fluxes.

Nevertheless, the comparison of simulations with the same amount of land use and varying patch arrangements shows hardly any differences between simulations with a patch size of 5 km (cf. Fig. 7d). For simulations with a patch size of 25 km, however, the dependence of latent heat-flux on heterogeneity starts at 1200 LT and increases with time (Fig. 6). If we focus on simulations with same patch arrangements and varying amounts of land use (Fig. 5), the latent heat-flux approaches the value of the simulation with the homogeneous land use, that means, e.g., the more *grass* in the domain, the greater the latent heat-flux. Generally speaking, the maximum of the latent heat-flux decreases with increasing heterogeneity and increasing coverage by *grass*, except for the simulations xxxC25 and xxxP5. Nevertheless, this behaviour is not linear (cf. Fig. 3). The greatest deviations from the linearity are found around 1300 LT and after sunset.

The enlargement of latent heat-flux with increasing heterogeneity is at the expense of the sensible heat-fluxes and soil heat-fluxes. Therefore, with some exceptions, the soil heat-flux and the latent heat-flux decrease by increasing heterogeneity, while the sensible heat-flux increases. Note that these exceptions can result from the arrangement of simulations we used to classify the heterogeneity in Tab. 2.

When comparing the results from simulations with different heterogeneity, the simulations with a patch length < 10 km are found to have no influence on the daily or annual energy budget, i.e., patches with a length < 10 km give no apparent 'organised' response to the atmospheric boundary layer. The latent heat-fluxes of simulations with a larger patch size than 10 km clearly response to heterogeneity. This is manifested by the comparison of the latent heat-fluxes provided by simulations with same amount of land use but different heterogeneity.

For instance, the energy budget of xxxR25 and xxxP25 differs less than that of xxxX25. The same is true for the distributions of the differences xxxP5-HOMG and xxxC10-HOMG.

Based on these findings, we may conclude that changes in land use or simple heterogeneity may have a strong impact on the local water and energy fluxes and, therefore, on the variables of state and local meteorological processes taking place.

6. Acknowledgments

This study was financially supported by the DFG under contracts Mo770/1-1 and Mo770/1-2 and by the BMBF under contracts 521-4007-07 VWK 01 and LT2.D.2.

7. References

Anthes, R.A., 1984. Enhancement of convective precipitation by mesoscale variations in vegetative covering in semiarid regions. *J. Clim. and Appl. Met.* **23**, 541-554.

Avissar, R., R.A. Pielke, 1989. A parameterization of heterogeneous land surface for atmospheric numerical models and its impact on regional meteorology. *Mon. Wea. Rev.* **117**, 2113-2136.

Deardorff, J.W., 1978. Efficient prediction of ground surface temperature and moisture, with inclusion of a layer of vegetation. *J. Geophys. Res.* **84C**, 1889-1903.

Eppel, D.P., H. Kapitza, M. Claussen, D. Jacob, W. Koch, L. Levkov, H.-T. Mengelkamp, N. Werrmann, 1995. The non-hydrostatic mesoscale model GESIMA. Part II: Parameterizations and applications. *Contrib. Atmos. Phys.* **68**, 15-41.

Kapitza, H., D.P. Eppel, 1992. The non-hydrostatic mesoscale model GESIMA. Part I: Dynamical equations and tests. *Contr. Phys. Atmos.* **65**, 129-146.

Kramm, G., R. Dlugi, D.J. Dollard, T. Foken, N. Mölders, H. Müller, W. Seiler, H. Sievering, 1995. On the dry deposition of ozone and reactive nitrogen compounds. *Atmos. Environ.* **29**, 3209-3231.

Mahrt, L., J. Sun, D. Vickers, J.I. MacPherson, J.R. Pederson, 1994. Ozone fluxes over patchy cultivated surface. *J. Geophys. Res.* **100D**, 23125-23131.

Mölders, N., A. Raabe, 1996. Numerical investigations on the influence of subgrid-scale surface heterogeneity on evapotranspiration and cloud processes. *J. Appl. Meteor.* **35**, 782-795.

Mölders, N., G. Kramm, M. Laube, A. Raabe, 1997. On the influence of bulk parameterization schemes of cloud relevant microphysics on the predicted water cycle relevant quantities - a case study. *Meteorol. Zeischr.* **6**, 21-32.

O'Neal, 1996. Interactions between land cover and convective cloud cover over Midwestern North America detected from GOES satellite data. *Int. J. Remote Sensing* **17**, 1149-1181.

Shen, S., M.Y. Leclerc, 1994. Large eddy simulation of small-scale surface effects on the convective boundary layer. *Atmosphere-Ocean* **32**, 717-731.

Shuttleworth, W.J., 1988. Macrohydrology - the new challenge for process hydrology. *J. Hydrology* **100**, 31-56.

Shuttleworth, W.J., 1991. Insight from large-scale observational studies on land/atmosphere interactions. *Surveys in Geophysics* **12**, 3-30.

Address of the authors:

LIM - Institut für Meteorologie
Universität Leipzig
Stephanstraße 3
04103 Leipzig
Germany

Vergleich beobachteter und aus parametrisierten Beziehungen berechneter Windreibungskoeffizienten während eines Sturmes an der Ostseeküste

Armin Raabe, Katja Friedrich, Holger Fritsch

Zusammenfassung:

Beobachtete und über parametrisierte Beziehungen berechnete Windreibungs-koeffizienten werden für die Zeit eines Sturms, der in der Zeit zwischen dem 08.07.96 und 11.07.96 an der Ostseeküste tobte, verglichen. Die innerhalb der ufernahen Zone aus Windprofildaten ermittelten Reibungskoeffizienten lassen sich mit weniger als 20% Fehler auch über vorliegende parametrisierten Beziehungen aus einer standardisierten Windgeschwindigkeitsmessung berechnen.

Summary:

A comparison between observed and calculated wind drag coefficients were investigated during a storm with wind speeds up to 20 m/s at the Baltic Sea coast between 8th July, 1996 and 11th July, 1996.
The drag coefficient which was determined from observed wind speeds from wind profile measurements can also be predicted on behalf of parameterised relations with a random error less then 20%.

1. Einführung

In der Literatur sind eine Vielzahl von Experimenten beschrieben, die den Versuch unternehmen, den reibungsbedingten Impulsaustausch zwischen der bewegten Atmosphäre und einer beweglichen Unterlage (Wasser, Meer) zu parametrisieren. Eine Übersicht findet man z.B. bei Garrat, 1977 oder Panin, 1985. In letzter Zeit gelang es auch, Ergebnisse von Experimenten zu vereinheitlichen, die aus Satellitendaten entsprechende Beziehungen ableiten (Yelland u.a., 1996).
Im großen und ganzen herrscht heute Einigkeit darüber, in welchem Maße der aerodynamische Reibungskoeffizient sich verändert, wenn die Windgeschwindigkeit zunimmt. Einmal variiert dieser mit der Stabilität der Schichtung zwischen Unterlage und Atmosphäre, zum anderen beobachtet man aber auch eine Zunahme des Reibungskoeffizienten mit wachsender Windgeschwindigkeit bei nahezu neutralen Schichtungsverhältnissen (s. Hasse, 1993).

Auf der Grundlage solcher parametrisierter Beziehungen wurden beispielsweise großräumige Klimaatlanten, die regionale Angaben über die Wechselwirkung zwischen Meer und Atmosphäre vorstellen, erarbeitet (z.B. Isemer und Hasse, 1987). Numerische Modelle greifen auf diese Beziehungen zurück, um die windgeschwindigkeitsabhängigen turbulenten Flüsse über der Unterlage zu den verschiedenen Prognosezeitpunkten festzulegen.

Seltener gelang es jedoch während der kurzen Zeit eines Experimentes die gesamte Breite der in der Natur auftretenden Windgeschwindigkeiten in den Meßdaten wiederzufinden. Oft setzen sich die abgeleiteten Beziehungen aus Daten zusammen, die über Jahre hinweg zu verschiedenen Zeiten und in verschiedenen Gebieten gesammelt wurden. Das zeigt das Vertrauen auf die

zugrundeliegenden physikalischen Prozesse, die egal wo, unter vergleichbaren Bedingungen übereinstimmende Reibungsverhältnisse reproduzieren müssen.

2. Die Parametrisierung der Reibungskoeffizienten

Reibt die bewegte Luft an der Unterlage, so verliert diese an Geschwindigkeit. Der Geschwindigkeitsverlust äußert sich vertikal zur parallel zur Unterlage verlaufenden Strömung als ein Gradient der Windgeschwindigkeit. Demnach wird von unten nach oben der Luft Impuls entzogen. Dieser Impulsstrom τ $\left(kg \cdot m \cdot s^{-1}\right)/\left(m^{2} \cdot s\right)$ quer zur Strömungsrichtung entspricht einer Schubspannung $\left(N \cdot m^{-2}\right)$ und ist eine der wichtigsten Größen, die zur Beschreibung der reibungsbeeinflußten Bewegung einer Luftmasse unter turbulenten Strömungsverhältnissen benötigt werden. Bei Berücksichtigung der Luftdichte ρ $\left(kg/m^{3}\right)$ reduziert sich die Maßeinheit des auf die Dichte bezogen Impulsstromes τ/ρ zu $\left(m^{2}/s^{2}\right)$. Das suggeriert eine Beziehung zum Quadrat einer Geschwindigkeit $\left(u_{*}\right)^{2}$. Diese Geschwindigkeit u_{*} trägt die Bezeichnung Schubspannungsgeschwindigkeit. Es liegt nahe, nach einer Beziehung zwischen der Schubspannungsgeschwindigkeit u_{*} und der leicht zu beobachtenden Windgeschwindigkeit u_{10} (z.B. bezogen auf die Standardhöhe 10m über der Unterlage) zu fragen. Damit letztlich die Verbindung zum Impulsstrom bzw. Schubspannung τ sichtbar wird, ist es zweckmäßig, einen Koeffizienten C_{10}, der als Reibungskoeffizient (engl. Drag-coefficient) bezeichnet wird, in der folgenden Form einzuführen:

$$C_{10} = \left(\frac{u_{*}}{u_{10}}\right)^{2} = \frac{\tau}{\rho} \cdot u_{10}^{-2}$$

Der Reibungskoeffizient C_{10} charakterisiert die Reibung der bewegten Luft an einer bestimmten Unterlage. In erster Näherung sollte dieser Wert konstant sein. Das kann experimentell überprüft werden, wenn aus geeigneten Untersuchungen Windgeschwindigkeiten und Schubspannungsgeschwindigkeiten vorliegen. Experimentelle Untersuchungen zeigen dann dessen Variabilität mit der Stabilität der Luftschichtung über der entsprechenden Unterlage. Desweiteren gibt es feste und bewegliche Unterlagen. Über einer beweglichen Unterlage, Meer oder Wasser, variiert der Reibungskoeffizient selbst mit der Windgeschwindigkeit $C_{10}\left(u_{10}\right)$, was in Verbindung zur Entwicklung der Wasserwellen an der Grenze zwischen Wasser und Luft gesetzt werden kann.

Bei der Vielzahl der Parametrisierungen $C_{10}\left(u_{10}\right)$ ist es unmöglich zu entscheiden, welche man in welchem Zusammenhang verwenden sollte. Über die Güte der Parametrisierung entscheidet letztlich, wie gut es gelingt den Reibungskoeffizient abzuschätzen, wenn nur Windgeschwindigkeitsmessungen vorliegen.

Yelland u.a., 1996 stellen eine aus Satellitendaten abgeleitete Beziehung $C_{10}\left(u_{10}\right)$ vor, die mit bodengebundenen Beobachtungen von Smith, 1988 übereinstimmt und deshalb hier in der folgenden einfachen Form verwendet werden soll:

$$C_{10} = \left(0{,}57 + 0{,}066 \cdot u_{10}\right) \cdot 10^{-3} \qquad \text{im Bereich } 6\frac{m}{s} \le u_{10} \le 25\frac{m}{s} \qquad (1)$$

Für die ufernahe Zone des Meeres unterscheiden Hupfer und Raabe, 1994 zwischen niedrigen und hohen Windgeschwindigkeiten:

$$C_{10} = (0{,}8 + 0{,}08 \cdot u_{10}) \cdot 10^{-3} \qquad \text{im Bereich } 2\frac{m}{s} \le u_{10} < 7\frac{m}{s}$$

$$C_{10} = (0{,}5 + 0{,}08 \cdot u_{10}) \cdot 10^{-3} \qquad \text{im Bereich } 7\frac{m}{s} \le u_{10} \le 15\frac{m}{s} \qquad (2)$$

Diese Unterscheidung wird auf eine Änderung der Reibungsverhältnisse zurückgeführt, die letztlich mit der Transformation des Seegangs im Flachwasserbereich der ufernahen Zone zusammenhängt (s. Raabe, 1991). Basis für die Ableitung dieser Zusammenhänge bildeten experimentelle Untersuchungen im Bereich der ufernahen Zone der Ostsee bei Zingst. An dieser Stelle wurden auch die in dem hier vorgestellten Experiment bestimmten Reibungskoeffizienten aus Windprofilen abgeleitet.

3. Ein standardisiertes Experiment zur Bestimmung von Reibungskoeffizienten

Während eines Praktikums an der Ostseeküste nahe Zingst (54° 26,6' N; 12° 42,1' E) wurden unmittelbar am Ufer der Ostsee Windprofilmessungen durchgeführt. Aus den beobachteten Gradienten der Windgeschwindigkeit sollten auf der Grundlage üblicher Beziehungen die Reibungskoeffizienten der ufernahen Seeoberfläche bestimmt werden (Anwendung des logarithmischen Windgesetzes, Friedrich und Fritsch, 1996). Aufgrund des Standortes des Mastes repräsentieren die beobachteten Daten im Fall auflandiger und uferparalleler Windrichtungen Verhältnisse, wie sie für eine Wasserfläche typisch sind (s. Raabe u.a., 1987).

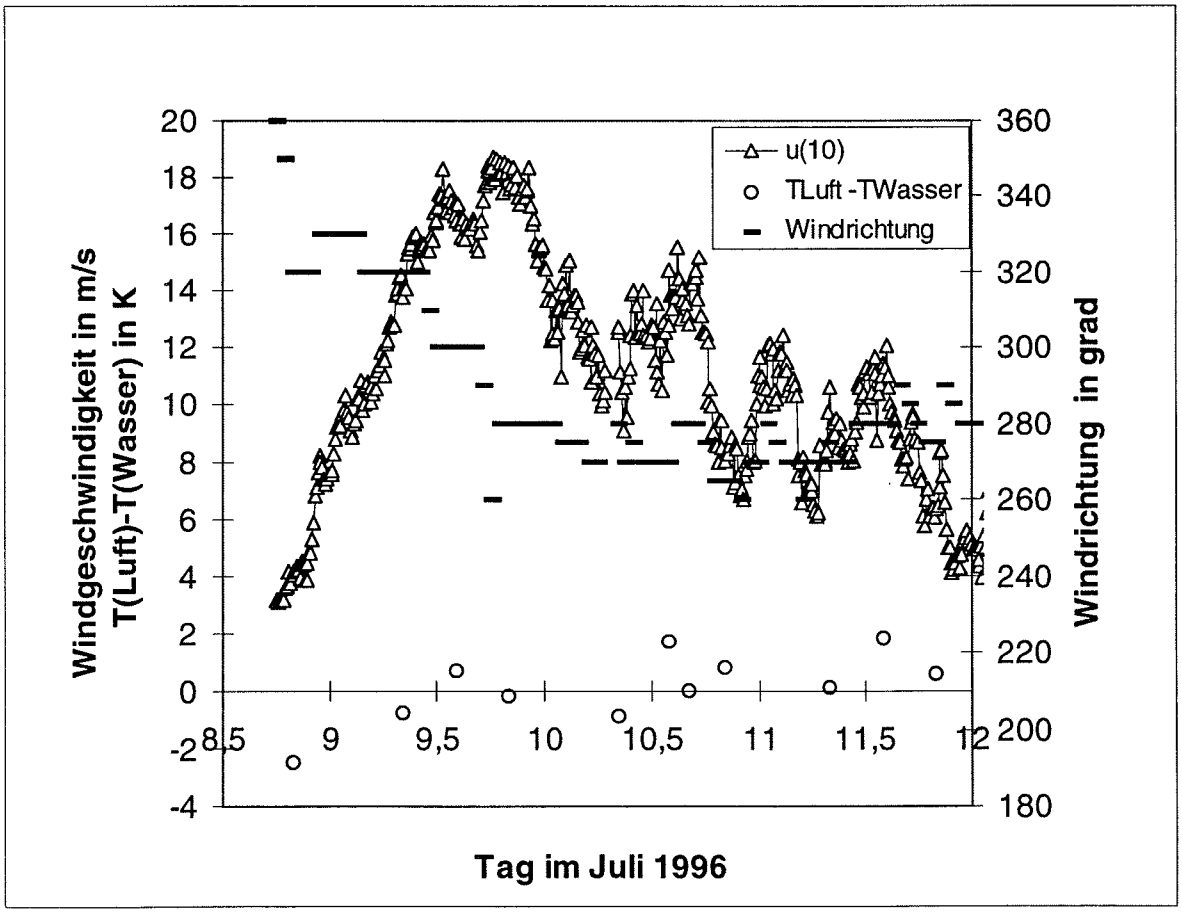

Abb. 1: Einige meteorologische Größen für die Zeit des Sturmes.

In der Zeit zwischen dem 08.07. und 12.07.96 wurde die Küste von Zingst von einem Sturm heimgesucht, der innerhalb weniger Stunden die Windgeschwindigkeit von 3m/s auf etwa 20m/s ansteigen ließ. Danach sanken die Windgeschwindigkeiten fast ebenso schnell wieder ab. Im Fall der Zunahme der Windgeschwindigkeit herrschten auflandige Windrichtungen vor (360° bis 280°), danach beim Abflauen drehte der Wind auf uferparallel (280° bis 260°, s. Abb.1).
Aus den Meßwerten der fünf zwischen einer Höhe von 1m bis 12m über Grund angeordneten Anemometer wurden zehn Minuten Mittelwerte der Windgeschwindigkeit gebildet. So ergab sich die seltene Gelegenheit, während des Sturmes einen Zusammenhang zwischen der Windgeschwindigkeit und dem Reibungskoeffizienten im Bereich von 3 bis 20m/s abzuleiten. Das bietet auch die Möglichkeit, verschiedene vorliegende parametrisierte Beziehungen mit dieser einen Realisierung zu vergleichen. Die Höhen der Anemometer wurden korrigiert bezüglich des aktuellen Pegelstandes des Meeresspiegels. Die Anemometer wurden in einem Windkanal im Bereich zwischen 1m/s und 18m/s vor und nach dem Experiment geeicht, wobei die absolute Genauigkeit der Eichgeschwindigkeit im Windkanal 0,05m/s erreichte.
Die Stabilität der Schichtung zwischen Atmosphäre und Wasser wurde durch einfache Beobachtung von Lufttemperatur (in 2m Höhe) und Wassertemperatur (in 0,5m Tiefe) zu den meteorologischen Haupt- und Nebenterminen kontrolliert. Während der gesamten Beobachtungszeit überstiegen die Temperaturdifferenzen zwischen Wasser und Luft nicht 2K (s. Abb. 1), was zusammen mit den hohen Windgeschwindigkeiten auf nahezu neutrale Schichtung schließen läßt.

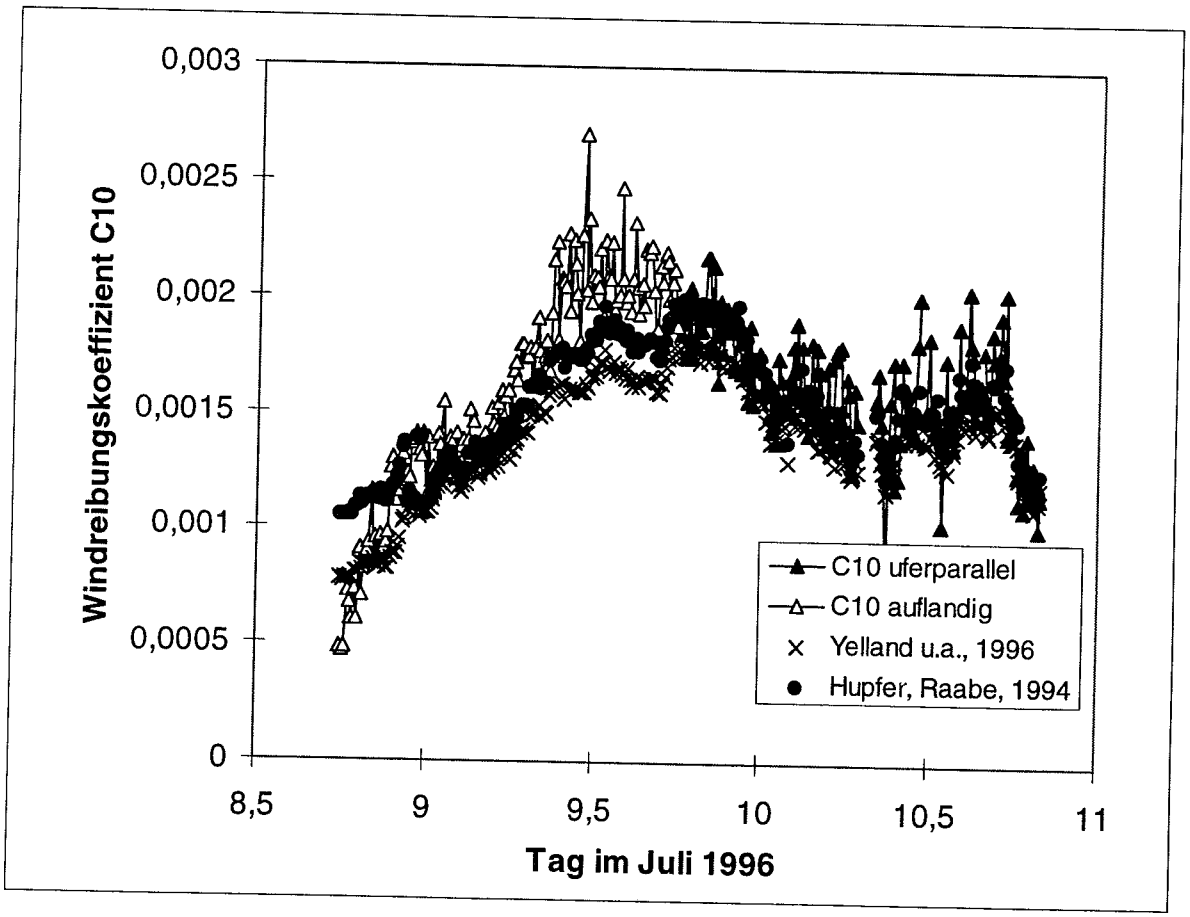

Abb.2: Experimentell bestimmte und über parametrisierte Beziehungen berechnete Reibungskoeffizienten während des Sturmes

4. Ergebnisse

Während des Sturmes nahm die Windgeschwindigkeit bei auflandiger Richtung vom Beginn der Beobachtungen an (18:00 am 08.07.96 MESZ) bis etwa 20:00 am 09.07.97 zu, danach drehte der Wind auf nahezu uferparallele Richtung und flaute bis zum Abend des 10.07.96 ab (Abb. 1).
Mißt man nur die Windgeschwindigkeiten und berechnet die Reibungskoeffizienten für diese Zeit über die parametrisierten Beziehungen Gl. (1) und (2), auch dann steht ein recht guter Wert für den Reibungskoeffizienten zur Verfügung (s. Abb. 2 und 3). Die Beziehung (1) nach Yelland u.a., 1996 stellt geringfügig geringere Reibungskoeffizienten bereit. Auffällig ist, daß selbst bei diesem einzelnen Sturm die Abnahme des Reibungskoeffizienten bei Übersteigen der Windgeschwindigkeit von etwa 7m/s beobachtet werden kann, wie das in den parametrisierten Beziehungen von Hupfer und Raabe,1994 zum Ausdruck kommt (Gl. (2), s. Abb.3). Die experimentell bestimmten Reibungsparameter weichen besonders bei hohen Windgeschwindigkeiten stärker von denen über die parametrisierten Beziehungen berechneten ab. Das ist auf die Gestalt der Küste vor Zingst zurückzuführen. Bei auflandigem Wind spielt der Rückstau der Luft an dem Küstenschutzwald eine Rolle, in dessen Vorfeld der Windprofilmast aufgebaut wurde. Dieser Einfluß täuscht höhere Reibungskoeffizienten vor. Der Einfluß des Rückstaus verschwindet natürlich bei uferparalleler Windrichtung. Deshalb liegen die Reibungskoeffizienten, die bei uferparallelem Wind beobachtet werden niedriger als bei auflandigem Wind. Die parametrisierte Beziehung (2) stellt natürlich einen Zusammenhang für vom Rückstau der Luft unbeeinflußte Luftströmungen dar.

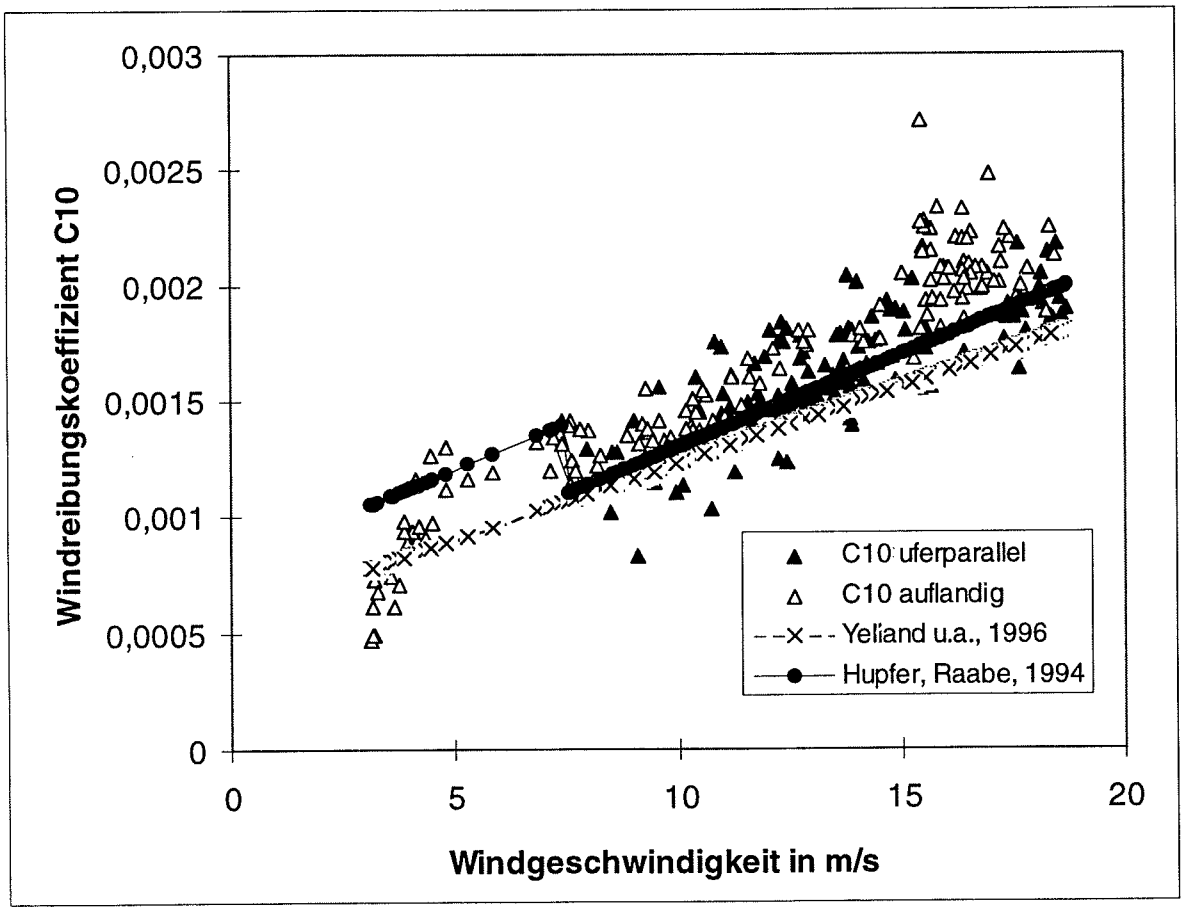

Abb.3: Die während des Strumes beobachteten Reibungskoeffizienten im Vergleich zu nach parametrisierten Beziehungen berechneten Reibungsoeffizienten.

Deshalb fallen die damit für uferparallele Windrichtungen berechneten Werte besser mit den beobachteten zusammen. Es sei denn, die im Fall des auflandigen Windes beobachteten Windgeschwindigkeiten würden vor der Berechnung der Reibungskoeffizienten korrigiert (s. Raabe u.a., 1987).
Im einzelnen ergeben sich in einem Windgeschwindigkeitsbereich zwischen 4m/s und 20m/s die in Tab. 1 zusammengestellten relativen Abweichungen zwischen den beobachteten und den über die parametrisieren Beziehungen berechneten Werten.

$\frac{C_{10,\text{auflandig beo.}}}{C_{10\text{parametrisiert}}}$ nach Hupfer, Raabe, 1994	$\frac{C_{10,\text{auflandig beo.}}}{C_{10\text{parametrisiert}}}$ nach Yelland u.a., 1996	$\frac{C_{10,\text{uferparallel beo.}}}{C_{10\text{parametrisiert}}}$ nach Hupfer Raabe, 1994	$\frac{C_{10,\text{uferparallel beo.}}}{C_{10\text{parametrisiert}}}$ nach Yelland u.a. 1996
1,09±0,09	1,20±0,05	1,03±0,04	1,10±0,02

Tab. 1.: Vergleich zwischen beobachteten und berechneten Reibungskoeffizienten unterschieden nach auflandiger und uferparalleler Windrichtung

5. Schlußfolgerung

Die hier vorgestellten Beobachtungen von Reibungskoeffizienten während eines Sturmes an der Küste der Ostsee ermöglichen eine Überprüfung vorliegender parametrisierter Beziehungen zur Bestimmung des Impulsaustausches. Während dieses Experimentes konnten innerhalb kürzester Zeit Reibungskoeffizienten im Bereich zwischen 4 und 20m/s Windgeschwindigkeit beobachtet werden. Der turbulente Impulsaustausch zwischen bewegter Luft und Unterlage ist eine Größe, die in prognostischen Atmosphärenmodellen immer auf bestimmte parametrisierte Beziehungen, d.h. ursprünglich experimentell abgeleitete Beziehungen, zurückgreift. Die heute für Wasserflächen verwendeten parametrisierten Beziehungen zwischen Windgeschwindigkeit und Reibungskoeffizient können mit weniger als 20% Abweichung die aktuellen Reibungskoeffizienten festlegen, auch wenn die parametrisierten Zusammenhänge nicht für eine spezielle Region abgeleitet wurden (Gl.(1)).
Im Fall der hier ausgewerteten Situation reduziert sich der Unterschied zwischen beobachteten und einer aus früheren Beobachtungen speziell für dieses Gebiet abgeleiteten parametrisierten Beziehung auf weniger als 10%.

Literatur:

Friedrich, K.; H. Fritsch, 1996: Praktikumsbericht Zingst Juli 1996, Inst. f. Meteorol. Univ. Leipzig 35S. (unveröff.).

Garrat, J.R., 1977: Review of Drag Coefficients over Oceans and Continents. Month. Weather Rev. 105, 915-929.

Hasse, L., 1993: Observation of air sea fluxes. In Raschke, E.; D. Jacob (eds.): Energy and Water Cycles in the Climate System. NATO ASI Series Dordrecht I,5, 263-293.

Hupfer, P.; A. Raabe, 1994: Meteorological transition between land and sea in the microscale. Meteorol. Zeitschr. N.F. 3, 100-103.

Isemer, H.J.; L. Hasse, 1987: The Bunker Climate atlas of the North Atlantic Ocean. Vol. 2: Air-sea interaction. Springer Verlag , Berlin 252p.

Panin, G.N., 1985: Heat and mass exchange between the water and the atmosphere in the nature. Moscow: Nauka, 206p. (in Russian).

Raabe, A., 1991: Zur Wechselwirkung von Atmosphäre und Meer sowie Atmosphäre und Land in unmittelbarer Nähe einer Küste. Geophys. Veröff. Univ. Leipzig, 4, 57-73

Raabe, A.; G.N.Panin, H.J.Schönfeldt; 1987: Die Variabilität des Windreibungskoeffizienten über der See in der Nähe einer Küste mit steil ansteigendem Ufer. Zeitschr. F. Meteorol. 37,3, 137-147.

Smith, S.D., 1988: Coefficients for sea surface wind stress. J. Geophys. Res. 93, 15467-15472.

Yelland, u.a., 1996: Zitiert nach: Annual Report 1996 of the South Hampton Oceangr. Centre, p.23.

Adresse der Autoren:

Dr. Armin Raabe, Katja Friedrich, Holger Fritsch
Universität Leipzig
Institut für Meteorologie
Stephanstr. 3
D-04103 Leipzig

Acoustic tomography in the atmospheric surface layer

Astrid Ziemann, Klaus Arnold, Armin Raabe

Zusammenfassung:

Die vorgestellte Methode der akustischen Tomographie (Simultane Iterative Rekonstruktionstechnik) und ein spezieller Auswertungsalgorithmus können flächengemittelte Werte meteorologischer Größen direkt bereitstellen. Somit werden zur Validierung numerischer mikroskaliger Atmosphärenmodelle weitgehend konsistente Daten geliefert.
Das Verfahren verwendet die horizontale Ausbreitung von Schallstrahlen in der atmosphärischen Bodenschicht. Um einen allgemeinen Überblick zur Schallausbreitung unter verschiedenen atmosphärischen Bedingungen zu erhalten, wird ein zweidimensionales Schallausbreitungsmodell genutzt.
Von Messungen der akustischen Laufzeit zwischen Sendern und Empfängern an verschiedenen Punkten in einem Meßfeld kann der Zustand der durchquerten Atmosphäre abgeschätzt werden. Die Ableitung flächengemittelter Werte für die Schallgeschwindigkeit und der daraus deduzierten Lufttemperatur resultiert aus der Inversion der Laufzeitwerte für alle möglichen Schallwege. Das angewandte zweidimensionale Tomographiemodell mit geradliniger Schallstrahlapproximation stellt dabei geringe Computeranforderungen und ist auch während des online-Betriebes einfach zu handhaben.

Summary:

The presented method of acoustic tomography (Simultaneous Iterative Reconstruction Technique) and a special algorithm of analysis can directly provide area averaged values of meteorological quantities. As a result rather consistent data will be delivered for validation of numerical atmospheric micro-scale models.
The procedure uses the horizontal propagation of sound waves in the atmospheric surface layer. To obtain a general overview of the sound propagation under various atmospheric conditions a two-dimensional ray-tracing model is used.
The state of the crossed atmosphere can be estimated from measurements of acoustic travel time between sources and receivers on different points in an tomographic array. Derivation of area averaged values of the sound speed and furthermore of air temperature results from the inversion of travel time values for all possible acoustic paths. Thereby, the applied straight-ray two-dimensional tomographic model is characterised as a method with small computational requirements and simple handling, especially, during online working.

1. Introduction

The development of micro-scale atmospheric and LES (Large Eddy Simulation) models which are applied for different questions in meteorology, forces their validation by means of accurate experimental data and so the derivation of area averaged meteorological quantities.
Spatial averaged data and so consistent data for model validation were conventionally provided by point measurements and a following interpolation technique. A relatively new way to get

such values directly is the transfer of tomographic methods to the atmospheric surface layer (see Spiesberger and Fristrup, 1990; Wilson and Thomson, 1994).
As an inverse technique tomography has been used routinely for instance in medicine, biology, geophysics and oceanography for many years (see, e.g., Munk et al., 1995).
There are various advances of tomographic measurements compared with conventional methods, e.g., the effect as spatial filter for turbulence below the micro-scale, the remote monitoring, because the test medium is not influenced by devices, the higher number of data per sensor in comparison to the traditional point measurements (Wilson and Thomson, 1994).
In our study we use a kind of acoustic travel time tomography, where the sound speed can be determined by measuring the travel time of a signal at a defined propagation path. Applying a suitable procedure measurements of the speed of sound can be used to reconstruct the spatially and temporally variable temperature and wind fields.
Wilson and Thomson (1994) demonstrated the applicability of acoustic tomography to the atmospheric boundary layer. The significant difference to the work presented here lies in the numerical algorithm used and in the kind of the output. We exert the tomographic technique SIRT (Simultaneous Iterative Reconstruction Technique) to provide from the measured line integrals, the travel time data, not only differences from a mean value, but also area averaged absolute values for the sound speed and the air temperature, respectively. Our measuring system, which can be used for a wide range of environmental and equipment situations, is introduced as a method to complete meteorological point measurements, especially, during experimental campaigns.
The following chapter describes some fundamentals of the sound propagation in the atmosphere. In chapter 3, a general review of the tomographic methods and, especially, of the SIRT used in our study is given. The next chapter deals with the implementation of the presented principles of geometric acoustics and tomography in numerical models, namely a two-dimensional ray-tracing model for a stratified atmosphere and a tomographic model according to a horizontal-slice scheme. In chapter 5, the experimental equipment and the processing of acoustic signals as well as the demanded accuracy of the travel time data are described. Finally, in chapters 6 and 7 results of our last experimental campaign MEPEX'97 in autumn 1997 and an outlook to necessary improvements are supplied.

2. Theoretical bases of the sound propagation in the atmosphere

In addition to the well-known reduction of the sound level with increasing distance from the sound source the damping due to the influence of inhomogeneities within the atmosphere, the structure of the ground and the air absorption play a role during the sound propagation through the atmosphere. If the sound propagation can be considered as spreading of small perturbations in an unbounded, frictionless and compressible fluid without external forces the wave equations

$$\frac{\partial^2 \rho'}{\partial t^2} = c^2 \Delta \rho' \text{ and } \frac{\partial^2 p'}{\partial t^2} = c^2 \Delta p' \qquad \left(\Delta = \nabla^2 \text{ as usual}\right) \tag{1}$$

can be obtained from the Euler equation and the continuity equation with the well-known relationship between the pressure, p, and the air density, ρ, fluctuations, $p' = c^2 \rho'$, and between the sound speed and the compressibility, $c^2 = \frac{dp}{d\rho}$ (see, e.g., Birkhoff, 1988; Pierce, 1989; Spiesberger and Fristrup, 1990).

If the dry air is considered as an ideal gas, Laplace's equation of sound speed can be used under adiabatic conditions:

$$c = \sqrt{\kappa R_a T}, \tag{2}$$

where T is the air temperature in Kelvin, R_a $\left(= 287.05 \text{ J kg}^{-1} \text{ K}^{-1}\right)$ is the dry adiabatic gaseous constant and κ $(= 1.4)$ is the compressibility.

Effects of air humidity (e.g., Spiesberger and Fristrup, 1990) or a modified air composition on sound velocity are neglected because typical changes are less than 0.05%.

Additionally to spatial (x, y, z) and temporal (t) alterations concerning changes of air temperature, also an influence in consequence of the wind field $\vec{v}(t,x,y,z)$ appends to the sound velocity and leads to an effective sound speed vector using the approximation of wave fronts from geometrical acoustics (see Pierce, 1989) with $\vec{n}$ as unit vector normal to the wave front:

$$\vec{c}_{eff}(T,\vec{v}) = c(T(t,x,y,z))\vec{n}(t,x,y,z) + \vec{v}(t,x,y,z) \tag{3}$$

Thereby, the conditions for sound propagation are changed and so a deviation from straightforward course between sound sources and receivers can be observed.

The sound propagation can be described with sound rays if the principles of the geometric acoustics, i.e., small acoustic refraction index gradient compared to the wave number of the sound wave (e.g., Klug, 1991), are applicable. This case often occurs under outdoor conditions except in the direct vicinity of the ground. Then sound rays represent lines whose tangents correspond to the propagation direction of the sound wave. Although the use of the sound ray theory, which is based on the principles of Fermat and Huygens, is associated with limitations, it offers, in comparison to wave models, the following advantages: (1) an easy visualisation of sound propagation inside the atmosphere and (2) a simple consideration of inhomogeneities inside the medium by application of the refraction law.

At the boundary between two parts of the atmosphere, which are characterised by different values of air temperature and wind vector the sound rays are refracted. This refraction is due to a variation in air temperature and wind vector depending on altitude in stratified fluids. According to Fasold et al. (1984) we used a general form of Snell's law for a moving and vertical inhomogeneous medium with the same frequency f in the two layers 1 and 2:

$$\sin\alpha_2 = \frac{k_1 \sin\alpha_1}{k_2 + (k_2|\vec{Ma}_1|\cos\varphi - k_1|\vec{Ma}_2|\cos\varphi)\sin\alpha_1} \tag{4}$$

$$\text{with} \quad |\vec{Ma}_1| = \frac{|\vec{v}_1|}{c_2}, \; |\vec{Ma}_2| = \frac{|\vec{v}_2|}{c_1}, \; k_1 = 2\cdot\pi\cdot\frac{f}{c_1}, \; k_2 = 2\cdot\pi\cdot\frac{f}{c_2}$$

Thereby, α_1 is the incident and α_2 is the refracting angle, φ is the angle between the wind direction and the undisturbed (without wind influence) sound velocity vector, Ma_1 and Ma_2 are the Mach numbers, k_1 and k_2 are the wave numbers. Note that the angles α_1 and α_2 are related to the wave normals in the layers 1 and 2, respectively.

According to numerous authors (Tatarskii, 1961; Kneser, 1961; Aubry et al., 1974; Daigle et al., 1978; Bass, 1981), other atmospheric influences, like the changes of the sound pressure level caused by scattering of the sound waves on temperature inhomogeneities and turbulence elements as well as the damping in consideration of air absorption, can be neglected for the frequency range used here, namely 1000 Hz, and source-receiver distances between 50 and 300 m.

However, the influence of the soil and the land cover can be much greater. After many authors (Embleton et al., 1976; Chessel, 1977; Bolen et al., 1981; Rasmussen, 1986; Klug, 1991; Salomons, 1994) a minimum in the transfer function, i.e., the sound pressure level related to undisturbed conditions of propagation, can occur near a frequency of about 500 Hz for grassland. Such damping due to sound wave interference increases with the distance between the source and the receiver and also with decreasing height of the experimental tools above the reflecting plane. According to Klug (1991), the described ground dip disappears by positive gradients of the sound velocity, by an increasing turbulent exchange or by use of a changed measuring geometry with device heights greater than 4 m as well as higher frequencies.

3. Travel time tomography

The theoretical basis of tomography lies on the Radon transformation (Radon, 1917) related to the projection of a two-dimensional scalar field and the transition from the measured value distribution to the projection field. According to Radon's law, it is possible to reconstruct a spatial distribution of parameters by inversion of line integral values, e.g., measured travel times. That means, that a continuously two-dimensional function can be derived from an infinite number of its continuously one-dimensional projections. The task is to determine the original distribution of parameter values from the measured projections. Thereby, the projection-slice scheme will be applied (e.g., Rüter and Gelbke, 1986).
The general principle of tomography (Greek 'tomos' means slice or section), as a certain image reconstruction technique and solving method for inversion problems, is to create a model of physical parameters in such a way that the projected data agree with the measured data.
Review of first applications of acoustic tomography is given by Wilson and Thomson (1994). The historical development, especially, in seismic applications of tomography is presented at Humphreys and Clayton (1988). Recently tomographic methods of the sound propagation in the atmosphere were applied by Spiesberger and Fristrup (1990) who described a method for passive localisation of calling animals and by Wilson and Thomson (1994) who primarily include the characterisation of the atmosphere. The main differences of these works to our study exist in the experimental design, the signal processing and the interpretation algorithm including the tomographic method. Both the studies, the presented here and the one from Wilson and Thomson (1994), use horizontal-slice schemes, i.e., a two-dimensional tomography. The advantages of our procedure are the small computational time and memory requirements. Only one ray is in the memory at one time. Therefore, it is possible to use the introduced model also for online interpretation of measuring results during experimental studies.
According to Worthington (1984), the procedures to solve tomographic problems can be divided into three main groups. Direct analytical solutions based on Fourier or inverse Radon transformation are usually employed for biological and medical applications with a homogenous ray covering of a high density. Alternative methods were developed, e.g., in geophysics and oceanography, where such ideal ray and angle covering usually does not occur.
One possible algorithm to solve the linear equation system with the desired parameter values as unknown variables is the matrix inversion method. Thereby, the generalised matrix inversion is the most important procedure if there are more unknowns than linearly independent equations (see Aki and Richards, 1980; Backus and Gilbert, 1968). Because of the very space- and time-consuming handling of large matrixes, which have to be inverted, the practical applicability of this method is limited. Furthermore, significant stability problems can occur during inversion (Krajewski et al., 1989). Consequently, methods referred to as row action (Trampert and

Leveque, 1990) or ART (Algebraic reconstruction Technique), in which the approximate solution is updated by successively processing the equations, are more attractive.
The large number of iterative reconstruction techniques (e.g., Peterson et al., 1985) can successfully be used for different measurement geometries with irregular sampling or limited projection angles with the additional advantage of simple handling and small computational requirements. The most prominent methods are the ART and the SIRT according to Gordon et al. (1970) and Gilbert (1972), respectively. A comprehensive review of to the mathematical background of ART-like methods is given by van der Sluis and van der Vorst (1987). Techniques, which update the approximate solution only after all equations have been processed, are called SIRT (Trampert and Leveque, 1990). In our study we apply a special form of this method.
Principally, an observed data set consists of line integrals along a specified path of the parameter to be imaged, e.g., acoustic travel time, which contains information about the physical quantities of the medium. Inhomogeneities of air temperature or in the wind field inside the tomographic array influence each measured travel time in an other way. Each measurement is ambiguous, only the inversion of every travel time measurement produces an image of the medium features radiated through with sound rays.
For a two-dimensional consideration the line integral for the travel time τ of a signal between a fixed acoustic source and receiver can be acquired

$$\tau = \int_{ray} \frac{dl}{\left|\vec{c}_{eff}\right|(t,x,y)} = \int_{ray} s(t,x,y)dl, \qquad (5)$$

where dl is the element of arc length along the propagation path and s symbolises the slowness, i.e., the reciprocal effective sound velocity.
Fundamental difficulties thereby are that the ray path itself depends on the unknown slowness distribution and that therefore the line integral becomes non-linear in slowness. Usually, a linearisation is applied to get some initial slowness model and to solve this problem. Thereby, straight lines connecting the sound source and the receiver are used to approximate the true ray path.
In the praxis only a limited number of measurements is available. Therefore, the searched two-dimensional function can only be reconstructed as a discrete parameter distribution, i.e., constant parameter values inside the grid cells. Various discretizations are possible. We use a tomographic array covered with square cells of constant size. The linearized set of equations in discrete form follows that of Rüter and Gelbke (1986) as

$$\tau_i = \sum_{j=1}^{J} s_j l_{ij} \qquad \text{with} \qquad s_j = \frac{1}{c_j}, \qquad (6)$$

where τ_i is the travel time of the i^{th} sound ray, s_j and c_j are the slowness and the effective sound speed in grid cell j, respectively, and l_{ij} is the length of the ray piece of the ray i in the j^{th} cell.
An image of diverse properties of the domain, which were radiated through from several angles of view, can be deduced by the following inversion technique. Thereby, the measuring field (260×200 m^2) of our experimental campaign MEPEX'97 was divided into small area elements (20×20 m^2) according to Fig. 1.
The dimension of the grid cells was chosen depending on the number of sound rays and the wished resolution. For each grid cell constant values of the slowness and the sound speed, respectively, were assumed.
In the mean travel time τ_i an information about the searched travel time and slowness in each grid cell j can be extracted using the known ray path l_{ij}. The aim of the following procedure is the reconstruction of the slowness s_j.

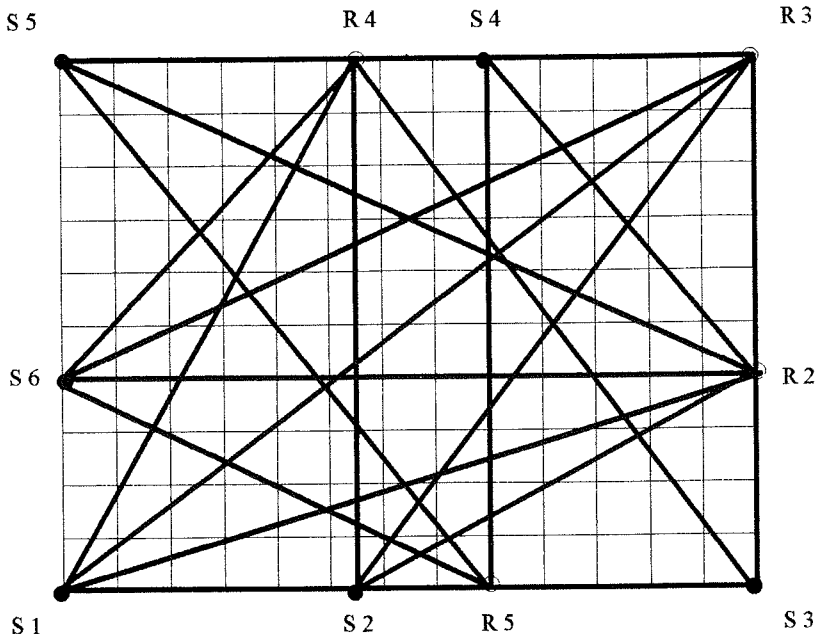

Fig. 1. Layout of the tomographic array (200 × 260 m²). The grid cells (20 × 20 m²) symbolise the solution of the tomographic model. The sources are labeled S1 to S6, the receivers are labeled R2 to R5. Note that R1 is the frequency generator.

In our study we applied a kind of straight ray tomography, the simplest ray tracing between sources and receivers. The error made by this approximation is investigated with a ray tracing model which requires high resolved vertical profiles of meteorological quantities. This model is described in chapter 2 and 4.

For every algebraic reconstruction technique a forward model has to be proposed in order to get the searched distribution by an iterative comparison process between calculated and experimental data. Starting with an initial guess of the slowness values, s_i^0, SIRT iterates on the difference between the experimental obtained travel time $\tau_i^{measure}$ and the last model prediction τ_i. After back projection of this difference and adding the resulting correction $\bar{k}_j$ to the present model an updated version of the simulated travel time follows. Thereby, corrections $\bar{k}_j$ are carried out to meet the condition:

$$\tau_i^{measure} = \sum_{j=1}^{J} (s_j + \bar{k}_j) x_{ij} \tag{7}$$

Among all grid cells an averaged value for correction $\bar{k}_j$ will be obtained from the distribution of the differences

$$\Delta\tau_i = \tau_i^{measure} - \tau_i \tag{8}$$

This corresponds to the minimum energy criterion, after multiplication with the corresponding ray length l_{ij} (according to Dines and Lytle, 1979; McMechan, 1983) as well as after the treatment of all rays which touch the respective cell N_j times:

$$k_j = \Delta\tau_i \frac{l_{ij}}{\sum_{j=1}^{J} l_{ij}^2} \quad \Rightarrow \quad \bar{k}_j = \frac{1}{N_j} \sum_{j=1}^{J} k_j \tag{9}$$

This process is continued until reaching of a convergence criterion. Thereby, SIRT converges to the least-squares solution (see Ivansson, 1983). The resulting set of area averaged values of slowness and sound velocities, respectively, is called tomogram.
According to Santamarina (1994) the fidelity and quality of inversions are conditioned by the nature of the analysed phenomenon, the quality of measured data and the applied inversion procedure. Errors in the data set can lead to a tomogram with artificial chess board pattern during the iteration cycle, especially, without an averaging process of the corrections k_j. A minimum difference between the measured and simulated data is only the necessary, but not a sufficient condition for the convergence to the correct model. For strongly erroneous data only a solution with a maximum entropy can be found. Furthermore, possible artefacts in the solution can be caused by badly sampled cells and non-ideal ray geometry, especially, for longer rays (Trampert and Leveque, 1990). The larger the distance between source and receiver, the larger is the measuring effect and the influence of the measurement to the tomographic solution. Therefore, the accuracy of the signal and data analyses as well as the positions of the sources and receivers are very important for a successful tomography.
In medical applications it is possible to produce an isotropic and homogeneous ray coverage. For an application in the atmosphere, however, usually both of these properties do not hold. The non-ideal ray distribution can lead to streaks that radiate from anomalous blocks along the direction taken by the rays traversing these blocks. By reducing the weight given rays aligned in common orientations this effect can be reduced (see Humphreys and Clayton, 1988). Only anomalies bordered and crossed by ray paths can accurately be reconstructed, otherwise a smearing of inhomogeneity can occur. Damping, slowness constraints or the use of other prior information effectively removes the possible problems due to the underdetermination of the system of equations (see Bregman et al., 1989; Krajewski et al., 1989). Therefore, we have also to deal with these topics to improve our tomographic results in the future.

4. Numerical modelling of the sound propagation and travel time tomography

Under special conditions, given in chapter 2, the sound propagation through the atmosphere can be described with a ray-tracing model. In the presented study a two-dimensional (x-z) ray-tracing model for a homogeneous atmosphere in the horizontal direction is applied to determine the principal characteristics of sound propagation in the atmosphere and the difference between a straight and curved ray according to actual conditions. It is assumed in our model that the sound propagation follows the x-direction (see Raabe et al., 1996) in a Cartesian coordinates system. The atmosphere is thereby divided into height levels with thickness, Δz. Equation (4) and the relations

$$\Delta s = \sqrt{\Delta x^2 + \Delta z^2}$$
$$\Delta x = \Delta z \cdot \tan\alpha_2 = \Delta z \frac{\sin\alpha_2}{\sqrt{1-\sin^2\alpha_2}} \qquad (10)$$

are used for the calculation of the ray path Δs inside the vertical and horizontal range Δz and Δx, respectively. Vertical temperature and wind profiles from a numerical atmospheric boundary layer model (see, e.g., Mix et al., 1994; Ziemann, 1998) with high resolution of a few centimetres in the lowest 20 m or from experiments, i.e., from a meteorological mast, are used as start values for the ray-tracing model.
The discrepancies between the actual calculated ray path, which is influenced by the angle of emission, and the exactly straight ray path between the source and the receiver amount to

about 0.20 m for a source-receiver-distance of about 200 m (see Figure 2). This value nearly agrees with the results obtained by Spiesberger and Fristrup (1990) for a linear profile of the sound speed under typical daytime conditions.

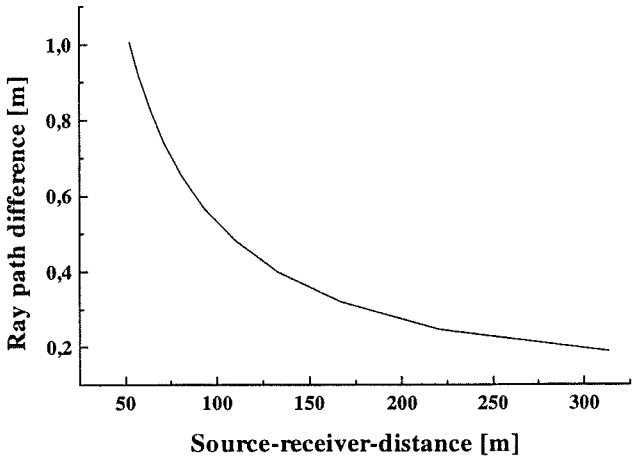

Fig. 2. Differences between the actually calculated ray path from the ray tracing model and the exactly straight ray path between the source and the receiver in dependence of the source-receiver distance using measured temperature and wind data from the 25th of October 1997, 10.00 MET (downwind conditions).

Up to now area averaged values can be considered by a straight ray two-dimensional (x-y) tomographic model. Therefore, the influence of the curved ray path in the vertical direction has to be estimated with the ray-tracing model. The basic set of equations used in the tomographic model was already explained in the previous chapter.

One disadvantage of the presented SIRT is that information about the resolution matrix, according to Backus and Gilbert (1968), is not available. A quantitative measure of the similarity of the reconstructed image and the model is defined by the Euclidic distance (ED) with the actual model-slowness, s_k, and the current estimate, s_k^n, from the n^{th} iteration cycle (see Krajewski et al., 1989)

$$ED = \frac{1}{K} \sum_{k=1}^{K} (s_k - s_k^n)^2 . \qquad (11)$$

It is obvious that the inversion result becomes better for smaller than for larger ED.

To avoid the divergence of the solution and the formation of artefacts due to erroneous data, the number of iterations should be limited corresponding to the optimal reconstruction result. Therefore, the sum of squared residuals (SSR) from equation (9) is a quantity describing the progress of the solution of the equation system. The optimal image will be achieved if the current decrease of SSR-values, averaged over five iteration cycles, diminishes to about 1% of the decrease during the first five steps (see Krajewski et al., 1989). In our study this value is reached not later than after 100 iterations taking a computational time of about one minute on a PC (Pentium 100 MHz).

The size of the grid cells (see Fig. 1) has to be chosen that on one hand area elements are crossed by a relatively great number of rays and on the other hand the wished resolution for searched distribution of meteorological parameters is achieved. The spatial resolution depends on the ray density, grid-spacing and travel time precision. The better the measured travel times and the greater the amount of the temperature inhomogeneity are, the smaller is the anomaly size which could be resolved. The size of the grid cells has to be chosen according to a Krajewski et al (1989) about one times the minimum dimension of resolvable anomaly.

Because of the actual measuring arrangement not all grid cells are passed through with a sufficiently high number of sound rays. The empty places are filled up with additional values for fictitious sources and receivers from geometrical relations between them. Thereby, two travel time measurements are the starting-points. Additional values are calculated for imaginary sources and receivers between the real ones using the averaged travel time data for fictional ray paths.

5. Experimental procedure and data analyses

The experimental studies should give an answer to the following questions:

(1) Which solution is attainable to estimate meteorological parameters and which additional information is necessary?

(2) Is there a possibility of producing absolute data (temperature and wind field) in contrast to Spiesberger and Fristrup (1990) and Wilson and Thomson (1994), or only fluctuations to a known initial state?

To obtain meteorological relevant data (temperature ± 0.3 K, wind velocity ± 0.5 ms^{-1}) a lot of requirements are obligatory.

The demanded accuracy for the travel time measurements can derived in similar manner like Spiesberger and Fristrup (1990). The travel time difference between the actual travel time τ_1 along ray path Γ_1 and the undisturbed, that means without wind influence, reference travel time τ_0 along the ray path Γ_0 is given by:

$$\tau_1 - \tau_0 = \int_{\Gamma_1} \frac{dl}{c_1(\Gamma_1) + \vec{u}(\Gamma_1)\cdot\vec{l}} - \int_{\Gamma_0} \frac{dl}{c_0(\Gamma_0)}, \tag{12}$$

where $\vec{u}$ is the wind vector, $\vec{l}$ is the unit vector along the ray path, dl is the differential length of the path and c_0 and c_1 are the sound velocities. Thereby, it will be assumed that $c_1 = c_0 + \delta c$. Assuming approximately equal ray paths leads to:

$$\tau_1 - \tau_0 = \int_{\Gamma_0} - \frac{dl(\delta c + \vec{u}\cdot\vec{l})}{c_0^2 + c_0\delta c + c_0(\vec{u}\circ\vec{l})}. \tag{13}$$

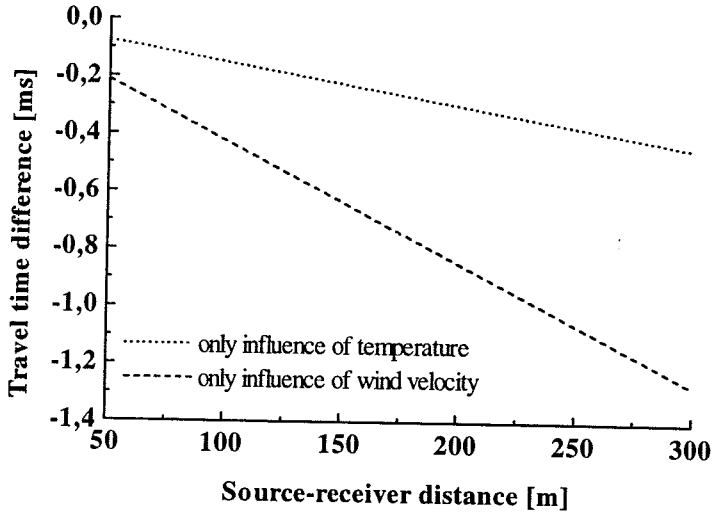

Fig. 3. Demanded travel time accuracy corresponding to only an influence of air temperature (air temperature: 15°C, wished accuracy: 0,3 K) and only a wind influence (wind velocity: 0,5 ms^{-1}, wished accuracy: 0,5 ms^{-1}) for source-receiver distances of the experimental campaign MEPEX'97.

Figure 3 illustrates the great influence of the source-receiver distance for the demanded travel time accuracy computed with equation (13) corresponding to temperature influence without wind on one side and with wind influence without temperature changes on the other side.
The travel time measurements have to be carried out with a high degree of accuracy. This includes, as pointed out already, the precise determination of the distance between source and receiver, the synchronisation of all connected instrumentation and the data processing. Additionally, the separation of different effects on travel time is necessary. A single travel time measurement contains mixed information on temperature and the component of wind along the path. With the rough approximation of a reciprocal sound propagation (straight rays) along the same path a separation of the two effects for a first view is possible.
In cooperation with the Instiute for Tropospheric Research (IfT) Leipzig an experimental campaign was carried out on a grassland site near Melpitz, 50 km north east of Leipzig. Besides several surface layer flux measurements, carried out by IfT, the essential aim for the field experiment was to check the acoustical system developed at our Institute for Meteorology.
Figure 2 shows the layout of the tomographic array of 260×200 m^2. Six sources, compression drivers and four receivers were positioned on tripods at a height of 2 m and 4.5 m, respectively (see Fig. 4 and 5).

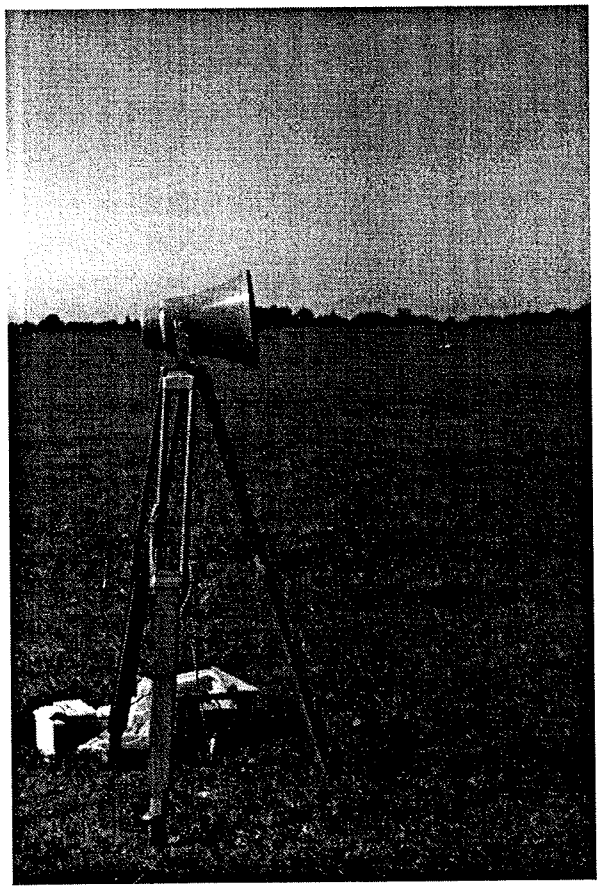

Fig. 4. The speaker system (compression driver, amplifier, portable battery supply).

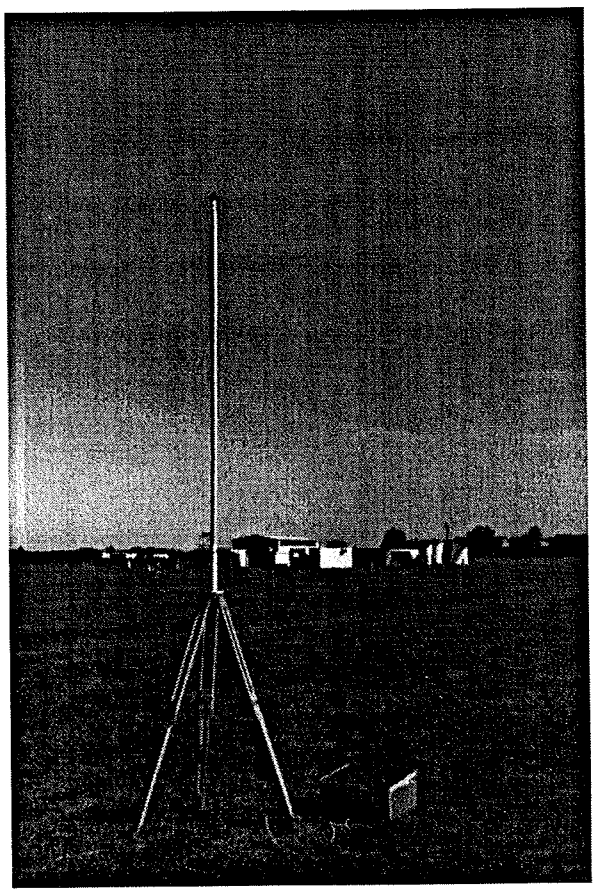

Fig. 5. One receiver set (microphone at a prolonged tripod and a data logger).

The positions of the transducers were determined using trigonometric measurements with an accuracy of 0.1 cm. The effects of the extension of the technical device (speaker: ± 10 cm, mi-

crophone ± 1 cm) can be neglected during the post processing calculations. In different short distances (between 3 m and 10 m) the transmitted signal was recorded and from the shift of a marked point the influence of the speaker extension can be estimated.
All sources simultaneously transmit an acoustic signal. The signal is a sine oscillation with a double peak with a duration in each case of 4 ms, however, the ringing of the compression driver prolongs the signal (see Fig. 6).

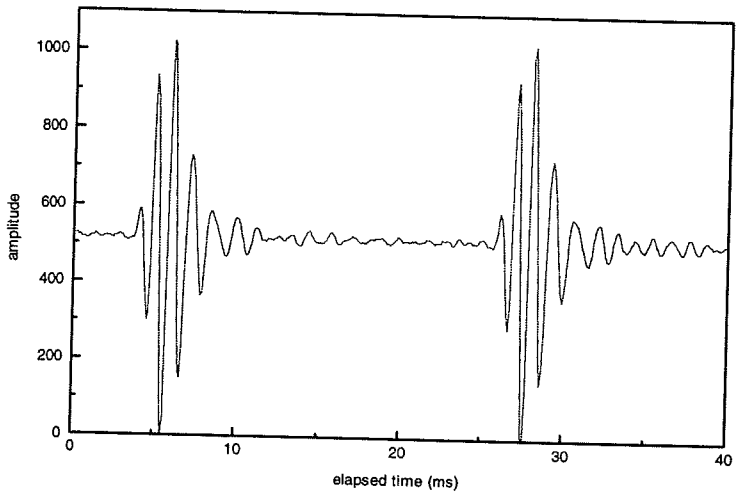

Fig. 6. Example of the transmitted signal: sine oscillation with a double peak (duration of 4 ms) with a constant frequency of 1000 Hz.

Using this special signature at unsatisfactory signal/noise ratios a clear identification of the transmitted signal is possible. The duration of the signal was chosen to be very short to prevent overlapping of different signals. Although the function generator can provide any frequency can be chosen, mostly a constant frequency of 1000 Hz was used. The function generator is additionally connected with all data loggers and gives the start signal for registration. So synchronisation of all devices is ensured.
A receiver set consists of an one inch microphone, a sound level meter and a data logger. The sound level meter is used for power supply and band-pass filtering. After amplifying the signals were sent to the A/D converter. The 10 Bit converter was capable of sampling at a rate of 10 kHz. The digitised data were immediately transferred in a circular system to a hard drive (laptop) that collects all recorded data. So an expensive solution with several memory cards is not necessary.
The travel time of each signal was estimated from the recorded data by cross correlation between the received (output) and the transmitted (input) signal. Each peak of the cross correlation is associated with a separate ray path. The delay time corresponds to the travel time of the transmitted signal. Using the input signal as an calibration signal all delays caused by the device can be eliminated. Figure 7 and Figure 8 show an example of the recorded signals and the cross correlation of the filtered signal with the reference signal. Figure 8 indicates the satisfying signal/noise ratio for all distances.

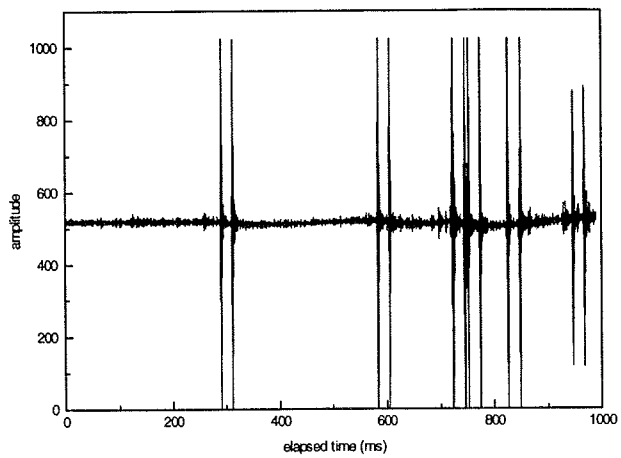

Fig. 7. Example of recorded signals (Receiver R3) after bandpass filtering during the tomography experiment on the 17th of September 1997, 13.02 MET.

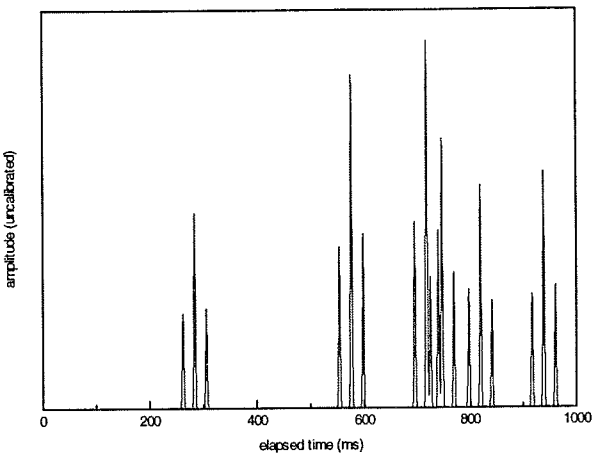

Fig. 8. Cross correlation of the filtered signal (Fig. 7) with the reference signal.

The assignment of each signal to the corresponding source is possible taking the tomographic array layout where all single rays have significantly different path lengths.
The effect of ground reflection can be roughly estimated from a simple geometrical travel time difference between the direct and the reflected sound ray according to Klug (1991). The larger the source-receiver distance is, the smaller the path and travel time difference will be. In this case the travel times can only be distinguished using an information about the amplitude which is smaller for the ground reflected ray over grassland than that without such reflection.
To simulate the actually sound propagation in the atmospheric surface layer the data from the meteorological mast at the Melpitz site were used as aforementioned. The mast (12 m high) is instrumentated with 8 cup anemometers, 8 temperature sensors and one wind-vane.
Additionally, measurements of wind and temperature, which are accomplished with two ultrasonic anemometers, were used for the validation of the tomographic model and to compare the area averaged data with point measurements.

6. First results

Area averages of the effective sound velocity, with one value for each grid cell, were calculated with the travel time data from the introduced experimental campaign (see Fig. 9).
Although the obtained values are not yet recalculated into meteorological parameters principal temperature trends are visible. The heating phase on the 25th of October, a so called 'golden day', is reproduced through increased values of the sound speed. Another interesting effect is the cold edge on the upper right side of Fig. 9 in both parts. It is presumable caused by the cooling power of a water ditch. This indicates that, it is possible to apply the presented tomographic method to detect inhomogeneities in the landscape, especially, during meteorological field experiments. In the future the area averaged values for sound speed can yield corresponding values for air temperature and wind velocity after a more detailed data analysis.

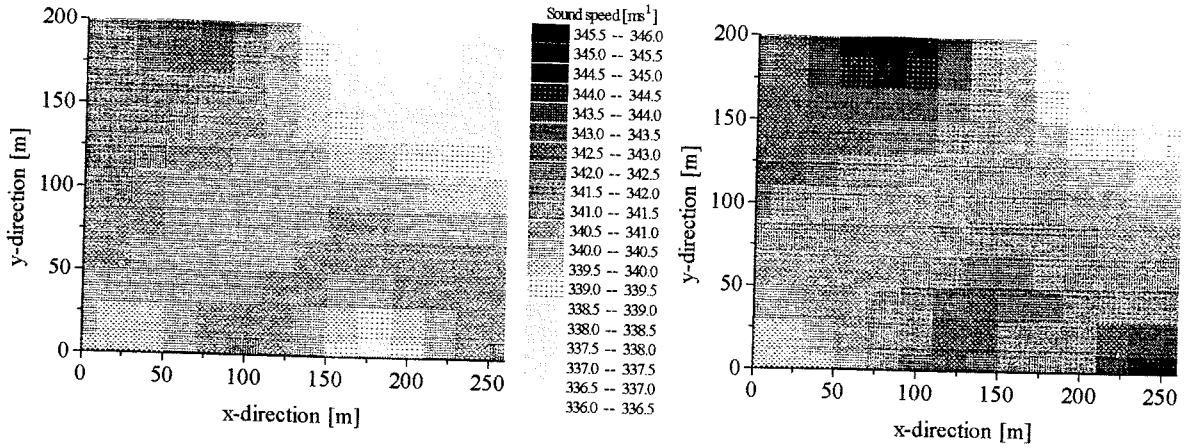

Fig. 9. Area averaged values (one constant for each grid cell) of the effective sound speed as derived from the acoustic travel time tomography for 25th of October 1997.
Left: 10.00 MET, Right: 13.00 MET

7. Conclusions and Outlook

The only small evaluation demonstrates the general applicability of the tomographic monitoring. Acoustic measurements alone are not sufficient for tomographic studies presented. Additional information about wind and temperature profiles are necessary to simulate the general sound propagation in the atmospheric surface layer under different meteorological conditions and to validate the tomographic data.
For meteorological relevant data a higher precision of the procedure is inevitable. Area averages of sound speed can be converted with sufficient accuracy into meteorological parameters, i.e., 0.3 K for temperature and 0.5 ms^{-1} for wind velocity. However, the following improvements are indispensable: a further upgrade of the measuring configuration, a possibility for the exact calculation of the wind influence on the travel time measurements, the use of more traces between receivers to increase the accuracy of travel time determination and also an enlarged number of sources and receivers to obtain a better area coverage.
Up to now only a straightforward sound propagation and area averaged values can be considered with a two-dimensional (x-y) tomographic model. Therefore, improvements with regard to an expansion in the vertical model direction have to be applied in order to get volume averaged values of meteorological parameters. Such volume averaged values are usually provided by microscale and LES models which are to be validated by the method developed here.

Acknowledgements

We would like to thank F. Weiße and M. Engelhorn for their support in the development and manufacturing of the measuring system. Furthermore, we, especially, acknowledge U. Teichmann and the staff of the test site Melpitz for the supply of the meteorological data during the field experiment MEPEX'97. We also wish to express our thanks to E. Danckwardt from the Institute of Geophysics at the University Leipzig for the support when adapting the tomographic model to the atmosphere. Thanks also to N. Mölders for fruitful discussions. We also thank the students from the Institute of Meteorology for their assistance during the experiment. This work was supported by the Deutsche Forschungsgemeinschaft under grant Ra 569/3-1.

References

Aki, K. and Richards, P.: 1980, Quantitative seismology-Theory and methods, Vol. II, W.H. Freeman & Co..

Aubry, M., Baudin, F., Weill, A. and Rainteau, P.:1974, Measurements of the total attenuation of acoustic waves in the turbulent atmosphere, J. Geophys. Res., 79, 5598-5606.

Backus, G. and Gilbert, F.: 1968, The resolving power of gross earth data, Geophys. J., 16, 169-205.

Bass H.E.: 1981, Absorption of sound in air: High temperature predictions, J. Acoust. Soc. Am, 69, 124-138.

Birkhoff, G.: 1988, The consistency of models of sound waves in fluids, In: Lee, D. Sternberg, R.L. and Schultz, M.H. (eds.)., Computational Acoustics, Wave propagation, Elsevier Science Publishers B.V., 117-156.

Bolen, L.N. and Bass, H.E.: 1981, Effects of ground cover on the propagation of sound through the atmosphere, J. Acoust. Soc. Am., 69, 950-955.

Bregman, N.D., Chapman, C.H. and Bailey, R.C.: 1989, Travel time and amplitude analysis in seismic tomography, J. Geophys. Res., 94, 7577-7587.

Chessel, C.I: 1977, Propagation of noise along a finite impedance boundary, J. Acoust. Soc. Am., 62, 825-834.

Daigle, G.A., Piercy, J.E. and Embleton, T.F.W.: 1978, Effects of atmospheric turbulence on the interference of sound waves near a hard boundary, J. Acoust. Soc. Am., 64.

Dines, K.A. and Lytle, R.J: 1979, Computerised geophysical tomography, Proceedings of IEEE, 67, 1065-1078.

Embleton, T.F.W., Piercy, J.E. and Olson, N.: 1976, Outdoor sound propagation over ground of finite impedance, J. Acoust. Soc. Am., 59, 267-277.

Fasold, W., Kraak, W. und Schirmer, W. (eds): 1984, Taschenbuch der Akustik, Teil 1, VEB Verlag Technik, Berlin.

Gilbert, P: 1972, Iterative methods for the three-dimensional reconstruction of an object from projections, J. Theor. Biol., 36, 105-117.

Gordon, R., Bender, R. and Herman, G.T.: 1970, Algebraic reconstruction techniques for three-dimensional electron microscopy and X-ray photography, J. Theor. Biol., 29, 471-481.

Humphreys, E. and Clayton, R.W.: 1988, Adaptation of back projection tomography to seismic travel time problems, J. Geophys. Res., 93, 1073-1085.

Ivansson, S.: 1983, Remark on earlier proposed iterative tomographic algorithm, Geophys. J., 75, 855-860.

Klug, H.: 1991, Sound-speed profiles determined from outdoor sound propagation measurements, J. Acoust. Soc. Am., 90, 475-481.

Kneser, H.O.: 1961, Schallabsorption und -dispersion in Gasen, 192-195, In: Handbuch der Physik, Band XI/1, Springer-Verlag, Berlin.

Krajewski, C., Dresen, L., Gelbke, C. and Rüter, H.: 1989, Iterative tomographic methods to locate seismic low-velocity anomalies: A model study, Geophys. Prosp., 37, 717-751.

McMechan, G.A.: 1983, Seismic tomography in boreholes, Geophys. J. R. astr. Soc., 74, 601-612.

Mix, W., Goldberg, V. and Bernhardt, K.-H.: 1994, Numerical experiments with different approaches for boundary layer modeling under large-area forest canopy conditions, Meteorol. Z., N.F. 3, 187-192.

Munk, W.H., Worcester, P. and Wunsch, C.: 1995, Ocean acoustic tomography, Cambridge University Press, New York.

Peterson, J.E., Paulsson, B.N.P. and McEvilly, T.V.: 1985, Applications of algebraic reconstruction techniques to crosshole seismic data, Geophysics, 50, 1566-1580.

Pierce, A.D.: 1989, Acoustics. An introduction to its physical principles and applications, Acoustic. Soc. Am., New York.

Raabe, A., Arnold, K. and Ziemann, A.: 1996, Akustische Tomographie im Bereich der Atmosphärischen Grenzschicht, Wiss. Mitt. Inst. für Meteorol. Univ. Leipzig und Inst. für Troposphärenforschg. Leipzig, 4, 113-123.

Radon, J.: 1917, Über die Bestimmung von Funktionen durch die Integralwerte längs gewisser Mannigfaltigkeiten, Berichte Sächs. Akademie der Wiss., 69, 262-277.

Rasmussen, K.B.: 1986, Outdoor sound propagation under the influence of wind and temperature gradients, J. Sound Vibr., 104, 321-335.

Rüter, H. and Gelbke, C.: 1986, Seismische Tomographie, In: Dresen, L., Fertig, J., Rüter, H. and Budach, W. (ed.): 6. Minitrop-Seminar. Seismik auf neuen Wegen. Ausgewählte Beispiele und Schwerpunkte, DVGI-Fachauschuß Geophysik Celle, 207-240.

Salomons, E.M.: 1994, Diffraction by a screen in downwind sound propagation, A parabolic-equation approach, J. Acoust. Soc. Am., 95, 3109.

Santamarina, J.C. and Reed, A.C.: 1994, Ray tomography: errors and error functions, J. Appl. Geophys., 32, 347-355.

van der Sluis, A. and van der Vorst, H.A.: 1987, Numerical solution of large, sparse linear algebraic systems arising from tomographic problems, In: Nolet, G. (ed.), Seismic tomography, D. Reidel, Dordrecht, 49-83.

Spiesberger, J.L. and Fristrup, K.M.: 1990, Passive localization of calling animals and sensing of their acoustic environment using acoustic tomography, Am. Natural., 135, 107-153.

Tatarskii, V.I.: 1961, Wave propagation in a turbulent medium, McGraw-Hill Book Company, New York.

Trampert, J. and Leveque, J.-J.: 1990, Simultaneous iterative reconstruction technique: Physical interpretation based on the generalized least squares solution, J. Geophys. Res., 95, 12553-12559.

Wilson, D.K. and Thomson, D.W.: 1994, Acoustic tomographic monitoring of the atmospheric surface layer, J. Atm. Ocean. Technol., 11, 751-768.

Worthington, M.H.: 1984, An introduction to geophysical tomography, First Break, 2, 20-26.

Ziemann, A., 1998: Numerical simulation of meteorological quantities in and above forest canopies, Meteorol. Z., accepted.

Address of Authors:

Astrid Ziemann, Klaus Arnold, Dr. Armin Raabe
Institut für Meteorologie
Universität Leipzig
Stephanstr. 3
D-04103 Leipzig

On the Correlation of the Mesopause Region Wind Field, the North Atlantic Oscillation and the Central Europe Winter Temperatures

B.-R. Beckmann and Ch. Jacobi

Summary:

The stratospheric and mesospheric wind field in winter is dominated by the stratospheric polar vortex, which reaches out up into the mesopause region and leads to strong westerlies there in winter. On the other hand, the tropospheric mean winter wind field is also connected with the polar vortex which thus can be considered as being extended from the surface up to the lower thermosphere. It is found that the winter mesopause region zonal winds, as measured at the Collm Observatory of the University of Leipzig, are closely connected with the North Atlantic Oscillation (NAO) being an integrated measure for the northern hemispheric mean circulation. The NAO itself is found to be a measure for Central Europe winter temperatures. Thus also the mesopause region winds are closely correlated to the Central European winter surface temperatures.

Zusammenfassung:

Das stratosphärische und mesosphärische Windfeld wird im Winter wesentlich vom stratosphärischen Polarwirbel bestimmt, der von der Stratosphäre bis in die Mesopausenregion reicht und dort zu starken Westwinden führt. Auf der anderen Seite ist die mittlere troposphärische Zirkulation ebenfalls mit dem stratosphärischen Wirbel korreliert, so daß letzterer als von der Erdoberfläche bis in die untere Thermosphäre reichend betrachtet werden kann. Aus diesem Grund sind die mittleren Zonalwinde, gemessen am Observatorium Collm der Universität Leipzig, mit der Nordatlantikoszillation (NAO) korreliert. Andererseits hat die NAO einen starken Einfluß auf mitteleuropäische Wintertemperaturen, und damit ist der Wind im Mesopausenbereich ebenfalls mit den Wintertemperaturen korreliert.

1. Introduction

The winter middle atmosphere circulation at midlatitudes is dominated by the stratospheric polar vortex and its extension into the mesosphere up to the lower thermosphere. Generally, the vortex consists of a very cold polar stratosphere with strong westerly winds. It has been found (Holton an Tan, 1980; 1982) that in general the stratospheric vortex is dependent on the equatorial quasi-biennial oscillation (QBO), and this is reflected in a weak dependence of the mesopause region circulation on the QBO (Jacobi et al., 1996, 1997a). But in some winters during major stratospheric warmings the vortex breaks up, and thus the zonal westerlies in midlatitudes are smaller. It was found that this is due to a correlation between the QBO, the stratospheric vortex and the 11-year solar cycle (e.g. Labitzke and van Loon, 1992, 1996). As it could be shown, the mesospheric wind are reacting on stratospheric warmings (Schminder and Kürschner, 1981; Greisiger et al., 1984; Muller et al., 1985; Jacobi et al., 1997b), so that generally the zonal prevailing wind is reduced or even easterlies prevail during the warming, which is due to the breakdown of the vortex then. It may be summarised that the mesopause region circulation follows the stratospheric dynamics in some way, so that part of the interan-

nual variability of the winter upper mesosphere/lower thermosphere can be explained by the stratospheric variability.

The large-scale tropospheric circulation in the middle latitudes may be described using the North Atlantic Oscillation (NAO), being defined as the pressure difference between the Azores and Iceland. As recently shown (Hurrell, 1995, 1996; Mahlberg and Bökens, 1997), the NAO can be correlated with winter temperatures in Central Europe, which is most reasonable since the NAO directly describes the strength of the westerly midlatitude tropospheric circulation and European winter temperatures are higher when westerly winds are prevailing. On the other hand, the winter midlatitude westerlies can be regarded as the flow around the tropospheric polar vortex, and thus we are interested in the connection between the stratospheric and tropospheric polar vortex, since this would provide a direct link from the mesopause region down to the lower troposphere. Such a link then could be useful in the detection of long-term variability, since mesospheric processes are much less influenced by local effects than this is the case in the troposphere. Therefore in the following we consider mesopause zonal winds and their correlation with the NAO, as well as their connection to Central Europe winter temperatures.

2. Data

The wind field of the upper mesopause region (about 95 km height) is observed by daily wind measurements at the Collm Observatory of the University of Leipzig. (Schminder and Kürschner, 1992, 1994; Schminder, 1995), using the ionospherically reflected sky wave from three commercial radio transmitters. The data are combined to half-hourly zonal and meridional mean wind values that refer to a reflection point at 52°N, 15°E. Since during the day the absorption of the sky wave is too large, the daily measuring period is in summer restricted to night and twilight, while in winter partly measurements are possible during the whole day. Since thus the measurements are inhomogeneously distributed in time and height, a direct estimation of the horizontal prevailing winds and the tidal components is not possible, and a multiple regression analysis is used to determine the daily prevailing wind as well as the tidal wind field components using the half-hourly mean values of the measured zonal and meridional wind components. The spectral selectivity of the separation of prevailing and tidal wind was improved through assuming clockwise circularly polarized tidal wind components (Kürschner, 1991). The model can be expressed by the following two equations:

$$\begin{aligned} v_z &= a_z + b\ \sin(\omega t) + c\ \cos(\omega t)\ , \\ v_m &= a_m + b\ \cos(\omega t) - c\ \sin(\omega t)\ , \end{aligned} \tag{1}$$

where v_z and v_m are the horizontal wind components and $\omega = 2\pi/12\text{h}$ the angular frequency of the semidiurnal tide. Note that in this kind of investigation the height is not used, although since 1982 it can be measured (Kürschner et al, 1987) and the regression delivers more reliable results then using height-dependent coefficients. However, to avoid artefacts due to different data evaluation we use the monthly mean half-hourly wind values in Eq. (1) that are measured since 1979. The coefficients a, b and c are determined by a least square fit of modelled and measured values. The zonal and meridional prevailing winds are simply

$$v_{oz} = a_z, \qquad v_{om} = a_m\ . \tag{2}$$

The semidiurnal tidal amplitude and phase are not used in this investigation.

For the NAO we used indices that were contributed by the NCAR (National Center for Atmospheric Research, Boulder) Climate Analysis Section. The monthly index of the NAO is based on the difference of normalised sea level pressures (SLP) between Ponta Delgada, Azores and Stykkisholmur, Iceland. The SLP anomalies at each station were normalised by division of each monthly pressure by the long-term (1865 to 1984) standard deviation.

Estimates of stratospheric winds v_{30} at the 30 hPa pressure level can be calculated from monthly mean geopotential heights as given by the Berlin stratospheric analyses (e.g. Pawson et al., 1993) by assuming geostrophic equilibrium. We used zonally averages mean values, thus the meridional component vanishes, and we obtain:

$$v_{30} = \frac{g}{2\Omega a \sin\varphi}\overline{\left(\frac{\Delta z}{\Delta \varphi}\right)} \quad , \tag{3}$$

with z as the height of the 30 hPa level, φ as the latitude, g the acceleration due to gravity, Ω the rotation rate and a the radius of the earth. The bar indicates that v_{30} consists of a zonal mean value of the geostrophic winds.

3. The mesopause and the NAO

In Figure 1 the mean winter zonal prevailing winds are shown, together with the three-monthly mean NAO index. The data are calculated from monthly means each. The analysis shows that the mesopause region winds follow the NAO index very closely, with the exception of only the years 1983 and 1984 (see Figure 1). The correlation between v_{oz} and NAO index is shown in Figure 2. The correlation coefficient is 0.61, with 99% significance.

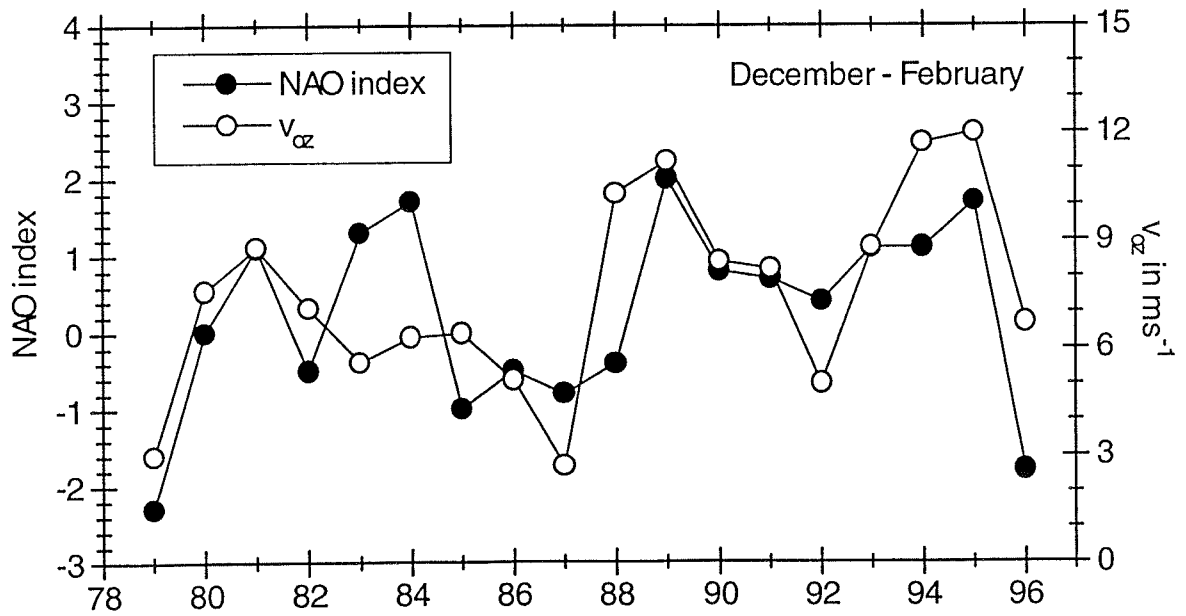

Figure 1: *Time series of the winter (December - February) mean values of the NAO index and the zonal prevailing wind v_{oz} at Collm.*

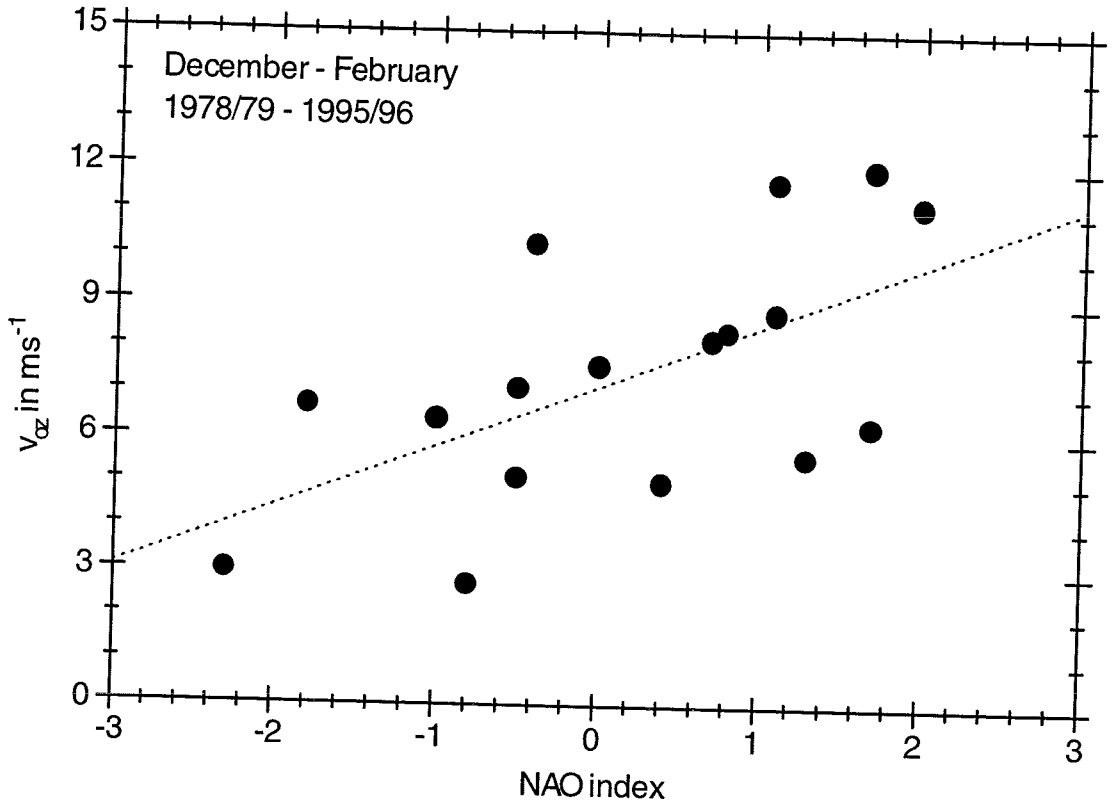

Figure 2: *Mean winter mesopause region zonal prevailing wind v_{oz} in dependence of the NAO index.*

Figures 1 and 2 show that obviously the winter polar vortex acts as one uniform system. This is also visible if the stratospheric winds are regarded. These are shown, together with the NAO index, in Figure 3. It can be seen, that the interannual stratospheric variations, this means the sign of the differences from year to year, generally seem to follow those of the NAO index, with the exception of the winter of 1995/1996, which was extremely cold in the stratosphere, which is not reflected neither in the NAO index nor in the mesopause region wind in Figure 1. There is no direct correlation between NAO index and v_{30}, but if we regard their year-to year differences ΔNAO and Δv_{30} in Figure 4, we find that these parameters are correlated with a regression coefficient of 0.29, which enlarges to 0.69 if we omit the difference between 1995 and 1996. Since, however, we have no plausible reason to do so, we may conclude that obviously there is a link between the NAO and the stratospheric winds, but there must be other effects that in some cases superpose this connection.

In winter the polar vortex is directly coupled to the troposphere as well as to the lower thermosphere. This is not the case in summer, and thus then a dependence of the mesopause region winds on the tropospheric circulation cannot be expected. This is shown in Figure 5, where time series of June - August mean values of v_{oz} and the NAO index are shown. It can be seen, that there is obviously no correlation. The correlation coefficient for each month separately, using the following regression analyses

$$v_{oz} = v_{oz,0} + \Delta \cdot \mathrm{NAO} \qquad (4)$$

is shown in Figure 6 together with the coefficient Δ. The two dotted lines denote the values of r that are due to 95% and 99% significance. It can be established that a statistically significant dependence is only found for January and February. The strongest correlation is found in January, while the coefficient is largest in February.

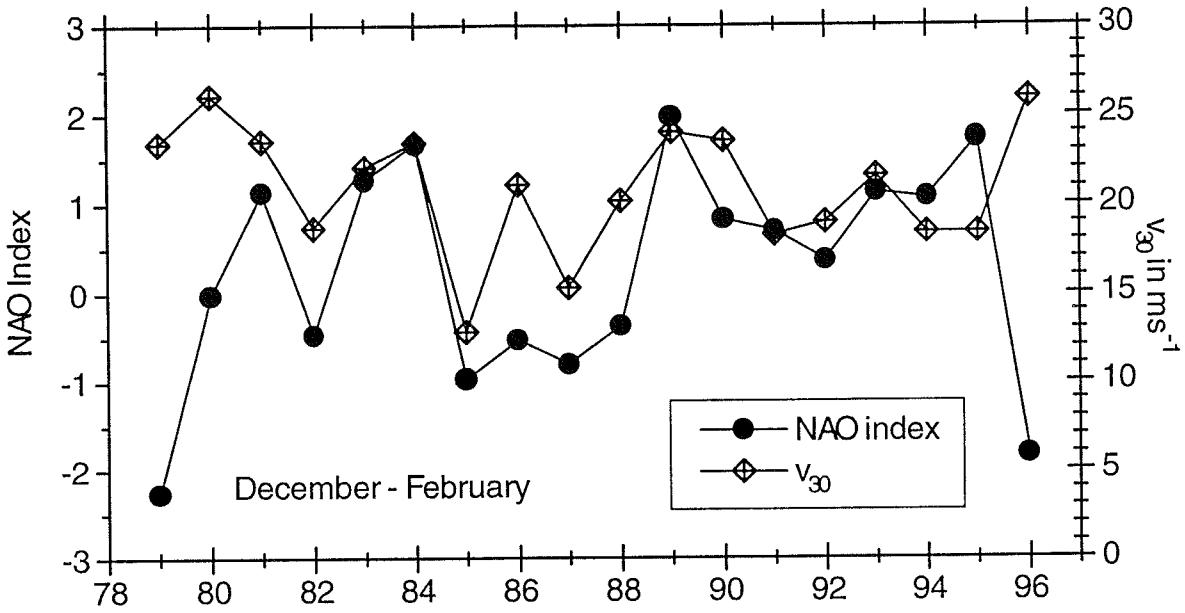

Figure 3: *Time series of winter (December - February) mean NAO indices and zonal mean geostrophic winds v_{30} at the 30 hPa level at 50°N.*

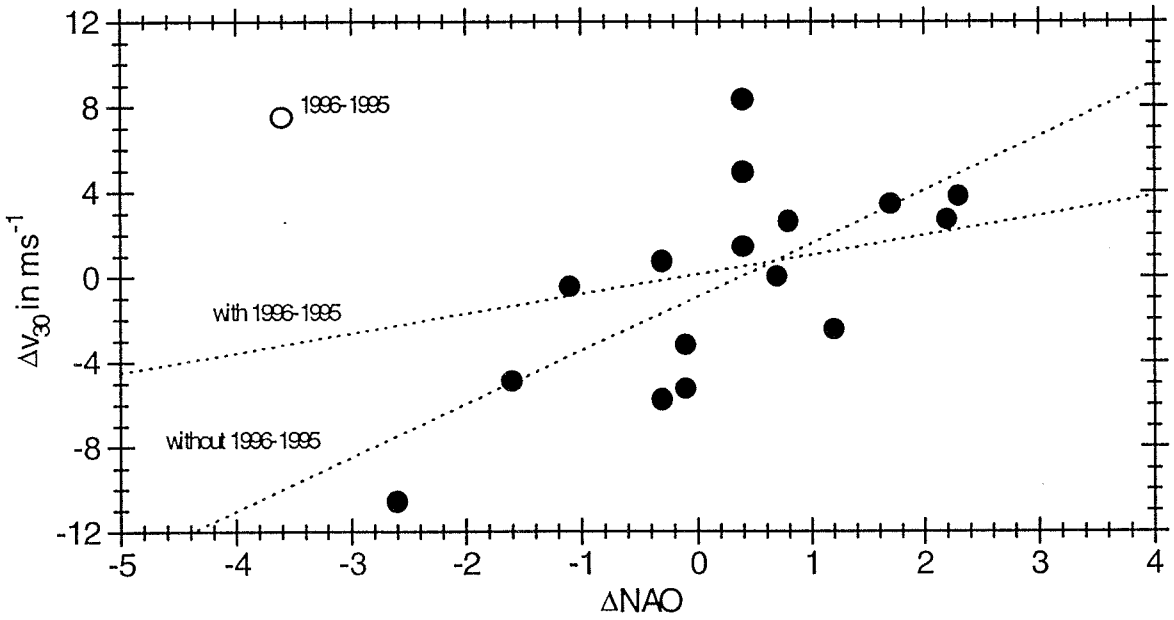

Figure 4: *Year-to-year difference Δv30 of the zonal mean geostrophic wind at 30 hPa in dependence of the year-to-year difference of the NAO index. The two dotted lines are regression lines that are constructed using all data or omitting the difference between 1996 and 1995, respectively.*

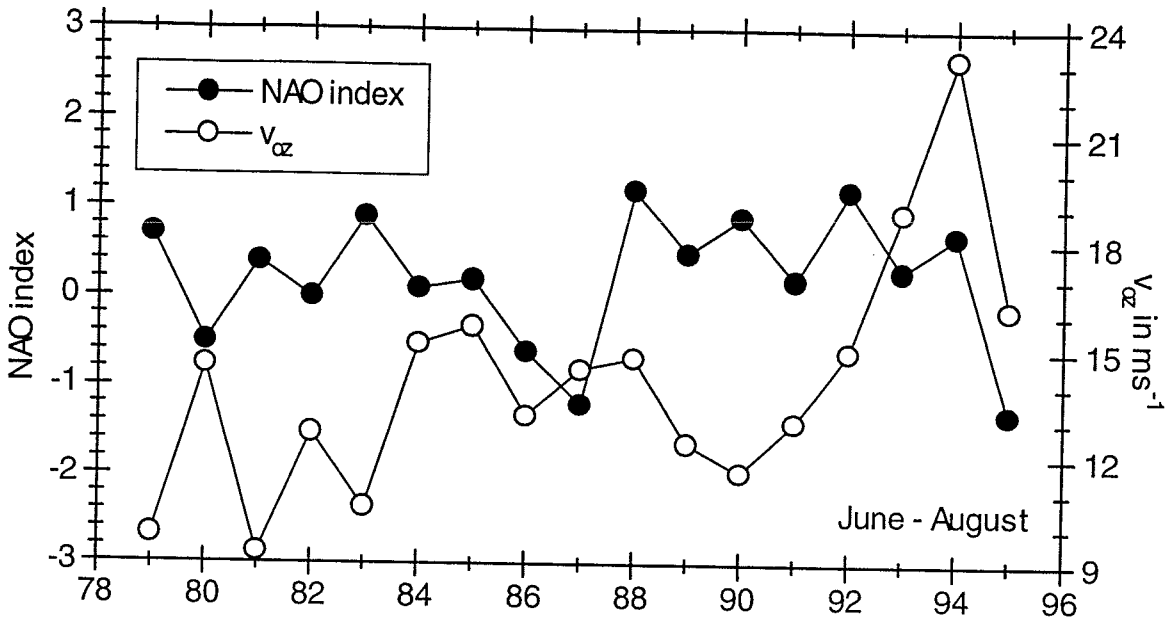

Figure 5: *Time series of the summer (June - August) mean values of the NAO index and the zonal prevailing wind v_{oz} at Collm.*

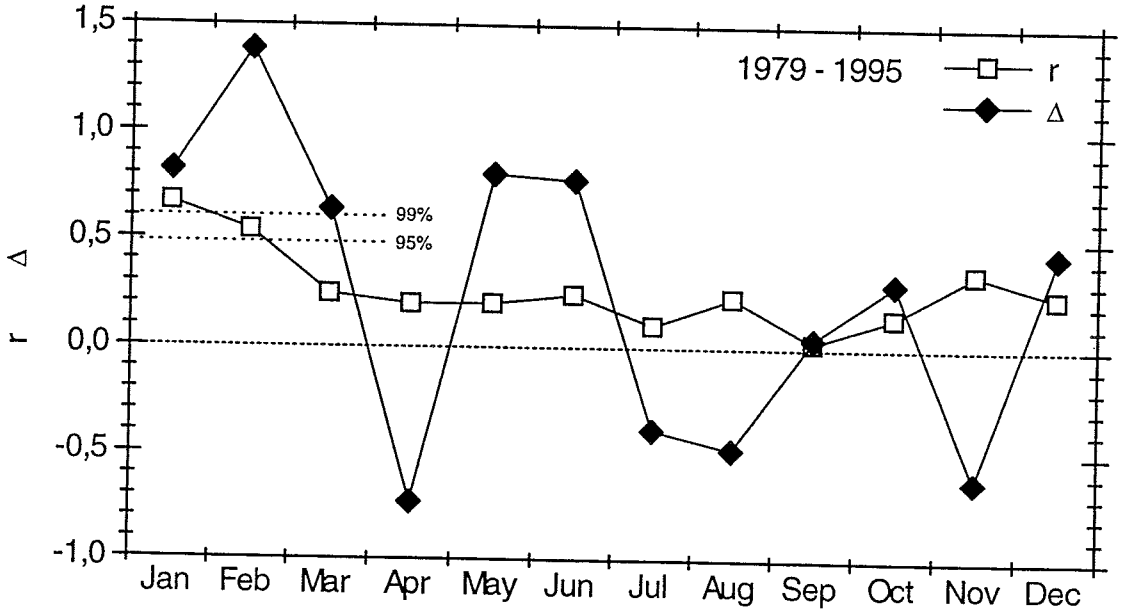

Figure 6: *Trend coefficient Δ, calculated after Eq. (4) for each month of the year. The regression coefficient r is added. The two dotted lines denote the values of r that are due to a significance of 95% or 99%, respectively.*

4. Winter temperatures and the mesopause wind field

It could be shown in the previous section that the winter mesopause wind field strongly correlates with the NAO index, which can be explained by a direct coupling of the troposphere-stratosphere-mesosphere-lower thermosphere system through a polar vortex that is uniformly

varying from year to year. From this it becomes evident that such a correlation cannot be expected in summer, since then the middle atmosphere is much more uncoupled from the lower atmosphere than it is the case in winter.

As it was recently shown by Mahlberg and Bökens (1997), the NAO index is strongly correlated to temperatures at Berlin in winter. Thus it can be expected, that the zonal mesopause region winds are correlated to Central Europe temperatures in winter as well. As an example, the mean winter v_{oz} values are shown in dependence of the temperatures at Hannover-Langenhagen. The correlation coefficient amounts to 0.66, and the correlation is significant at the 99% level. Since from Figure 6 it can be seen that the correlation between NAO and v_{oz} is strongest in January, one can expect an even stronger correlation between voz and temperature for this month regarded separately as well. This is really the case, the correlation coefficient, considering only January data, amounts to 0.72 then.

The correlation between v_{oz} and winter temperatures is found for other sites, too. In Table 1 the correlation coefficients are listed for 4 stations in Germany. In all cases a high correlation coefficient is found, and in all cases these are statistically significant at the 99% level.

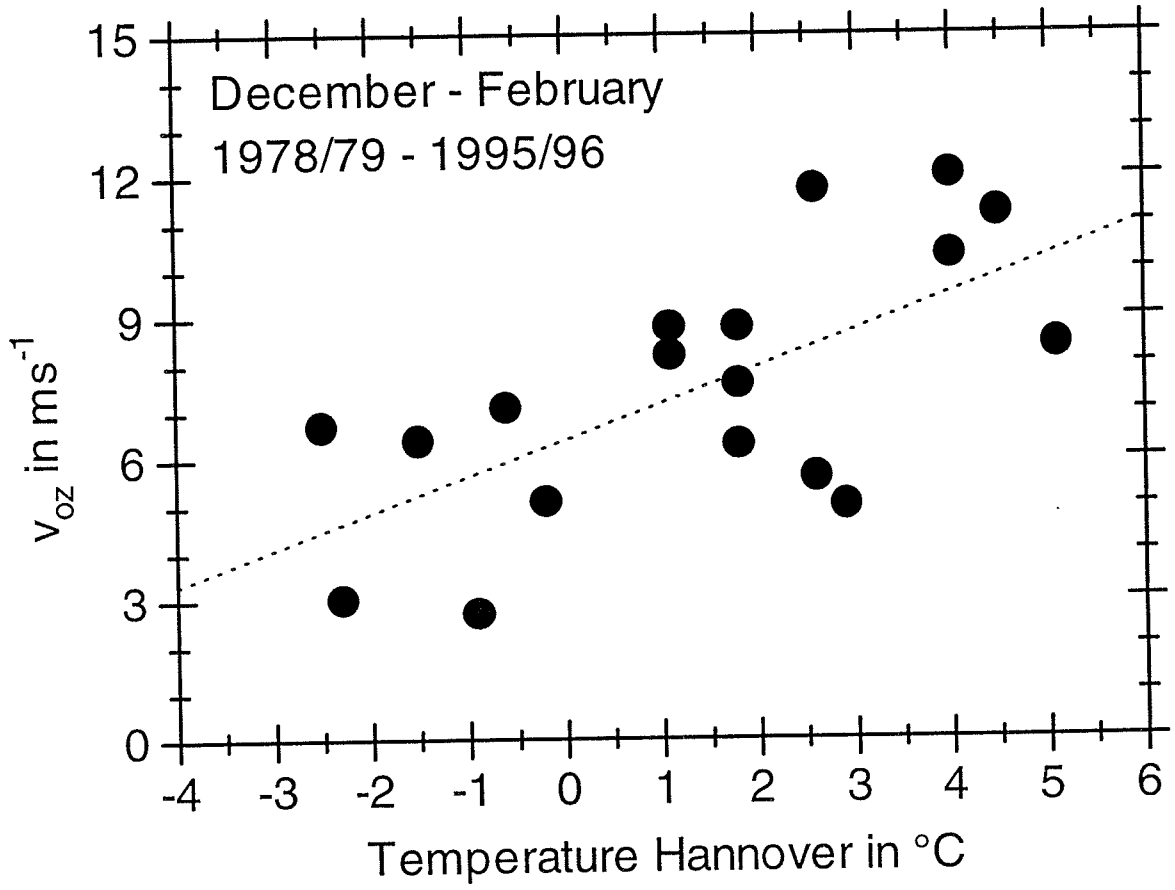

Figure 7: *Mean winter (December - February) mesopause region zonal prevailing wind in dependence of the mean winter temperatures at Hannover-Langenhagen.*

	January	December - February
Hannover-Langenhagen	0.72	0.66
Berlin-Tempelhof	0.71	0.62
Stuttgart-Schnarrenberg	0.71	0.69
München-Riem	0.61	0.62

Table 1: *Correlation coefficient between the mesopause region zonal prevailing wind at Collm and winter temperatures at 4 measuring sites for January alone (2nd column) and for December - February means (3rd column). The data were calculated from the winters 1978/79 through 1995/96.*

5. Conclusions

It is found from comparison of mesopause region zonal winds and NAO indices as well as Central Europe temperatures, that in winter both the temperatures and the NAO indices are closely correlated to the mesopause dynamics. This shows that in winter the polar stratospheric vortex acts as one dynamical unity and thus provides a physical link from the surface layer up to the lower thermosphere. Considering the strong dependence of lower tropospheric meteorological parameters on local effects, the interannual variability of the entire atmospheric system can be monitored using upper middle atmosphere measurements, which are much less affected by regional or local variations. However, the correlation between winter temperatures and mesopause region dynamics, although statistically significant, is not strong enough to calculate one from the other, and thus the mesopause winds can be used only as an indicator for Central Europe mean winter conditions.

Acknowledgements

This research was supported by the "Deutsche Forschungsgemeinschaft" (German Science Foundation) under contract Schm 981/2-2 and by the BMBF under contract 01 LK 9321/7. The authors wish to thank Dr. R. Schminder and Dr. D. Kürschner, Collm, for providing the Collm wind data, as well as the Institute for Meteorology of the FU Berlin for contributing the stratospheric data. The NAO indices were contributed by the NCAR Climate Analysis Section. The monthly mean winter temperatures were taken from the European Weather Reports of the German Weather Service.

References

Greisiger, K.M., Portnyagin, Yu.I., and Lysenko, I.A., 1984: Large-scale winter-time disturbances in meteor winds over Central and Eastern Europe and their connection with processes in the stratosphere. *J. Atmos. Terr. Phys.* **46**, 389 - 394.

Holton, J.R., and H.-C. Tan, 1980: The influence of the equatorial quasi-biennial oscillation on the global circulation at 50 mb. *J. Atmos. Sci.* **37**, 2200 - 2208.

Holton, J.R., and H.-C. Tan, 1982: The quasi-biennial oscillation in the northern hemisphere lower stratosphere. *J. Meteor. Soc. Japan* **60**, 140 - 147.

Hurrell, J.W., 1995: Decadal trends in the North Atlantic Oscillation: Regional temperatures and precipitation. *Science* **269**, 676-679.

Hurrell, J.W., 1996: Influence of variations in extratropical wintertime teleconnections on Northern Hemisphere temperature. *Geophys. Res. Lett.* **23**, 665 - 668.

Jacobi, Ch., R. Schminder, and Kürschner, D., 1996: On the influence of the stratospheric quasi-biennial oscillation on the mesopause zonal wind over Central Europe. *Meteorol. Zeitschrift N.F.* **5**, 218 - 223.

Jacobi, Ch., R. Schminder, and Kürschner, D., 1997a: Measurements of mesopause region winds over Central Europe from 1983 through 1995 at Collm, Germany. *Beitr. Phys. Atmosph.* **70**, 189 - 200.

Jacobi, Ch., R. Schminder, and Kürschner, D., 1997b: The winter mesopause wind field over Central Europe and its response to stratospheric warmings as measured by D1 LF wind measurements at Collm, Germany. *Adv. Space Res.* **20**, 1223 - 1226.

Kürschner, D., 1991: Ein Beitrag zur statistischen Analyse hochatmosphärischer Winddaten aus bodengebundenen Messungen, *Z. Meteorol.* **41**, 262 - 266.

Kürschner, D., Schminder, R., Singer, W., and Bremer, J., 1987: Ein neues Verfahren zur Realisierung absoluter Reflexionshöhenmessungen an Raumwellen amplitudenmodulierter Rundfunksender bei Schrägeinfall im Langwellenbereich als Hilfsmittel zur Ableitung von Windprofilen in der oberen Mesopausenregion, *Z. Meteorol.* **37**, 322 - 332.

Labitzke, K., and van Loon, H., 1992: On the association between the QBO and the extratropical stratosphere. *J. Atmos. Terr. Phys.* **54**, 1453 - 1463.

Labitzke, K., and van Loon, H., 1996: On the stratosphere, the QBO, and the sun: the winter of 1995-1996. *Meteorol. Zeitschrift, N.F.* **5**, 166 - 169.

Muller, H.G., Whitehurst, G.A., and O´Neill, A., 1985: Stratospheric warmings and their effect on the winds in the upper atmosphere during the winter of MAP/WINE 1983 - 1984. *J. Atmos. Terr. Phys.* **47**, 1143 - 1147.

Pawson, S., Labitzke, K., Lenschow, R., Naujokat, B., Rajewski, B., Wiesner, M., and Wohlfart, R.-C., 1993: Climatology of the northern hemisphere stratosphere derived from Berlin analyses. Part 1: Monthly means. *Meteorol. Abh. des Inst. f. Meteorol. d. FU Berlin, N.F., Ser. A*, **7**(3).

Schminder, R., 1995: Die Entwicklung des Arbeitsgebietes Physik der Hochatmosphäre am Geophysikalischen Observatorium Collm. In: Meteorologische Arbeiten aus Leipzig, *Wiss. Mitt. des LIM und des IFT*, Leipzig **1**, 1 - 21.

Schminder, R., and Kürschner, D., 1981: Wind field anomalies in the upper mesopause region over Central Europe and the major stratospheric warming in February 1981. *J. Atmos. Terr. Phys.* **43**, 735 - 736.

Schminder, R., and Kürschner, D., 1992: Höhen-Zeit-Schnitte der Windfelder (Grund- und Gezeitenwind) zwischen 85 und 105 km Höhe über Mitteleuropa für 1990 aus funktechnischen D1-Windmessungen am Observatorium Collm, *Kleinheubacher Berichte* **35**, 137 - 145.

Schminder, R., and Kürschner, D., 1994: Permanent monitoring of the upper mesosphere and lower thermosphere wind fields (prevailing and semidiurnal tidal components) obtained from LF D1 measurements in 1991 at the Collm Geophysical Observatory, *J. Atmos. Terr. Phys.* **56**, 1263 - 1269.

Addresses of Authors:

Dr. B.-R. Beckmann and Dr. Ch. Jacobi
Institut für Meteorologie, Universität Leipzig
Stephanstr. 3, 4103 Leipzig

Solar Cycle Dependence of Winds and Planetary Waves as Seen From Midlatitude Mesopause Region Wind Measurements at Collm - Evidence for Forcing From Below

Christoph Jacobi

Zusammenfassung:

Windmessungen im Mesopausenbereich über Mitteleuropa (Collm, 52°N, 15°E) werden im Hinblick auf Langzeittrends und eine eventuelle Abhängigkeit vom 11-jährigen Sonnenfleckenzyklus hin untersucht. Der Einfluß der solaren Variabilität ist jahreszeitenabhängig; nur in Frühjahr und Sommer wird eine signifikante Korrelation gefunden. Im Sommer ist diese Abhängigkeit mit stärkeren vertikalen Gradienten des mittleren zonalen Grundwindes im solaren Maximum verbunden. Dies weist auf einen Ursprung dieser Abhängigkeit in der Stratosphäre/Mesosphäre sowie auf Koppelungsmechanismen zwischen Stratosphäre, Mesosphäre und unteren Thermosphäre hin. Da die 2-Tage-Welle vom Gradienten abhängt, führt dies zu einer positiven Korrelation zwischen der Amplitude der 2-Tage-Welle und der Sonnenfleckenrelativzahl.

Summary:

Mesopause winds over Central Europe (Collm, 52°N, 15°E) are analysed with respect to long-term trends and 11-year solar cycle dependencies. The response of the prevailing wind to the solar cycle differs throughout the year. While in winter no significant correlation between the zonal prevailing wind and the solar activity is found, in spring and summer a negative correlation between solar activity and zonal prevailing wind can be seen from the measurements. This is connected with stronger vertical gradients of the zonal prevailing wind during solar maximum than during solar minimum. This hints to a forcing of the mesopause region dynamical reaction on solar activity from the stratosphere/mesosphere and to coupling processes in the stratosphere-mesosphere-lower thermosphere system. Since the amplitude of the quasi two-day wave is dependent on the zonal mean wind gradient, this is connected with a positive correlation between solar activity and quasi two-day wave activity.

1. Background

One of the first investigations of the solar cycle dependence on the mesopause winds was done by Sprenger and Schminder (1969). From D1 LF measurements they found an increase of both zonal and meridional prevailing wind with solar activity, and a decrease of the semidiurnal tidal amplitude with the solar radio flux. A similar study was carried out by Dartt et al. (1983), who confirmed their results concerning the solar cycle dependence of the winter prevailing wind. Additionally they found a negative correlation of the zonal prevailing wind and a positive correlation of the spring and early summer meridional prevailing wind with the solar activity. Greisiger et al. (1987), however, found negative correlation of solar flux and zonal prevailing wind, although they could confirm the negative correlation of solar flux and semidiurnal tide. Namboothiri et al. (1993) found a positive correlation of the zonal prevailing wind in winter, but a negative one in summer. A tendency of negative correlation of the meridional wind in winter and positive correlation in summer was also found. Recently, Bremer et al. (1997) reported positive correlation of the zonal as well as of the meridional wind and the solar flux in winter,

and negative correlation in summer. Jacobi et al. (1997a) found no solar cycle dependence of the semidiurnal tidal amplitude, but confirmed the negative correlation between the zonal prevailing wind and solar activity in summer.

It may be summarized, that so far the results concerning the dependence of the mesopause wind parameters on the solar cycle are not very conclusive and partially contradicting. At least for the case of the semidiurnal tidal amplitude this may be due to an oscillation at very long time scales that is obviously of non-solar origin (Jacobi et al., 1997a). On the other hand, there is evidence for an influence of the solar variability, especially of the 11-year solar cycle, on the stratosphere (e.g. van Loon and Labitzke, 1994, Labitzke and van Loon, 1992, 1996), and recently Svensmark and Friis-Cristensen (1997) proposed a link between cosmic ray flux and tropospheric climate variability. Thus it appears reasonable to explain any solar cycle dependence of mesopause region dynamics in terms of a forcing from below, i.e. in the first place from the stratosphere and mesosphere, rather than through an in situ effect as different ionization or absorption processes, for instance. In this connection, in the following mesopause wind data measured at the Collm Observatory of the University of Leipzig are investigated with respect to a possible solar cycle dependence and with emphasis of a possible connection to processes in the mesosphere below. The investigation will restrict on the zonal prevailing wind and the quasi 2-day wave, since these parameters in the past have been found to be the ones that are most influenced by solar variability (Jacobi et al., 1997a,b).

2. Description of measurements and data analysis

The wind field of the upper mesopause region is continuously observed by daily D1 (total reflection) wind measurements in the LF (low-frequency) radio wave range, using the ionospherically reflected sky wave of three commercial radio transmitters on 177, 225 and 270 kHz. The measurements are carried out according to the closely-spaced receiver technique. A modified form of the similar-fade method is used to interpret the wind measurements automatically since 1973 (Kürschner, 1975). Since in summer during the day the absorption of the sky wave is too strong, the daily measuring period is restricted to night and twilight then.

Since the measurements are inhomogeneously distributed in time, a multiple regression analysis is used to determine the monthly prevailing wind and the semidiurnal tidal wind components using the half-hourly mean values of the measured zonal and meridional wind components. The spectral selectivity of the separation of prevailing and tidal wind is improved through fitting the measured values for the two horizontal wind components as a vector, assuming clockwise circularly polarized tidal wind components:

$$\begin{aligned} v_z &= v_{oz} + b\ \sin(\omega t) + c\ \cos(\omega t), \\ v_m &= v_{om} + b\ \cos(\omega t) - c\ \sin(\omega t), \end{aligned} \tag{1}$$

with $\omega = 2\pi/12h$, where v_z and v_m are the zonal and meridional horizontal wind components, respectively, and v_{om} and v_{oz} are the components of the horizontal prevailing wind, while the semidiurnal phase (T_{2z}) and amplitude (v_{2z}) can be calculated from the coefficients b and c. The diurnal tidal components are not taken into account, because the daily, quasi-regularly distributed data gaps would lead to a large error in the calculation of these (Kürschner, 1991). Thus an error of the prevailing wind can occur when only nighttime measurements are performed. However, at midlatitudes the diurnal tide is a much less dominant feature than the semidiurnal tide (e.g. Manson et al., 1989), and comparison of calculations of the zonal prevailing wind calculated with and without including the diurnal tide into the regression analysis led to an error of less than 4 ms^{-1} in each month that is due to omitting the diurnal period in Eq. (1).

Since September 1982 the reflection height is measured on 177 kHz, using travel time differences of corresponding modulation bursts between the ground wave and the reflected sky wave in the 1.8 kHz modulation range (Kürschner et al., 1987). To avoid apparent wind variations due to reflection height variations in the presence of vertical gradients of the mean wind, only these times of the night are used for the regression analysis after Eq. (1), when the long-term mean reflection height, obtained from the measurements after 1982, is found to vary only slightly around the mean height of about 95 km (e.g. Jacobi et al., 1996a).

3. Results of monthly mean zonal winds

In Figure 1 time series of the winter (December - February) and summer (June - August) mean zonal prevailing wind are shown. Some variability at time scales of 2 - 5 years can be seen. Additionally Jacobi et al., (1996b) found a weak dependence of the winter zonal prevailing wind on the equatorial QBO, but a connection between QBO, solar activity and winter midlatitude circulation, as it was found for the stratosphere (e.g. Labitzke and van Loon, 1992, 1996), cannot be found from the Collm measurements, which is probably due to the strongly variable reaction of the mesopause circulation to sudden stratospheric warmings. However, in summer there is some evidence for a negative solar cycle dependence of v_{oz}. This is indicated by the two heavy arrows in Figure 1 that point to relative minimum values of the smoothed summer zonal prevailing wind.

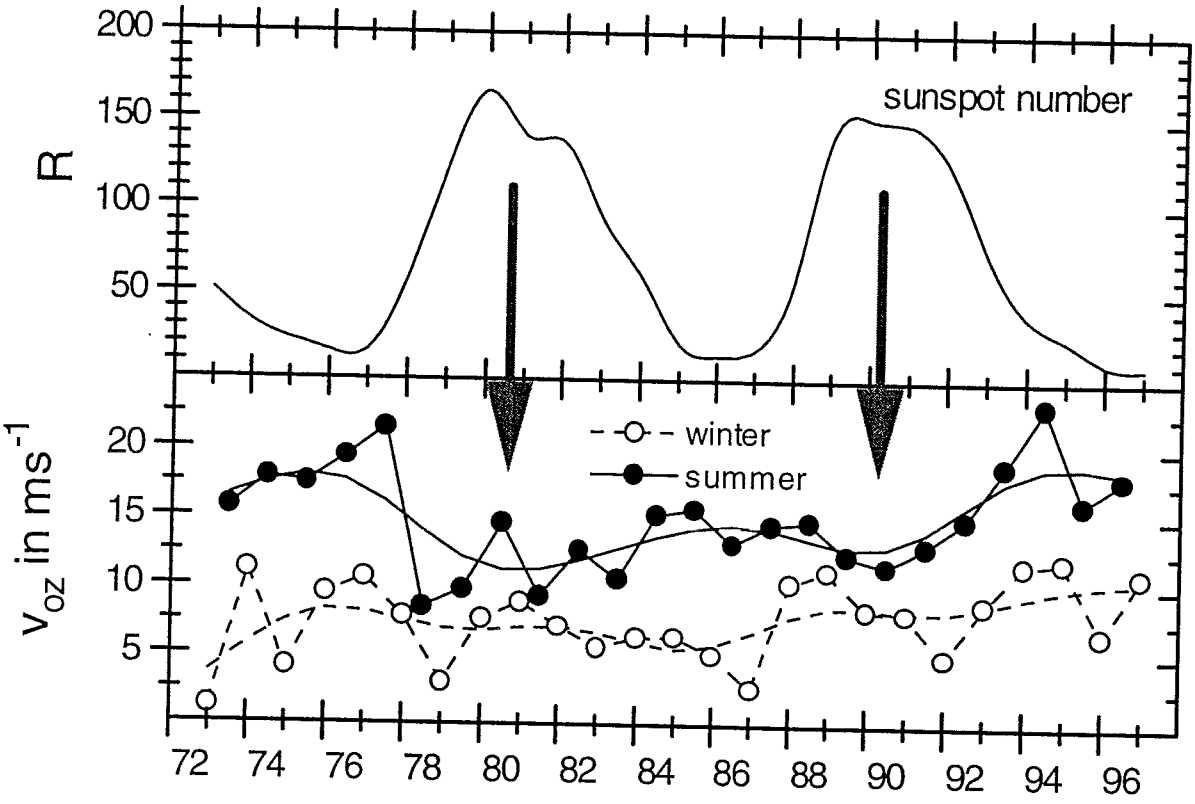

Figure 1: Time series of winter (December - February) and summer (June - August) mean values of the Collm zonal prevailing wind v_{oz} near 95 km. In the upper panel the 13-monthly smoothed sunspot number R is added (after Jacobi et al., 1997a, updated).

It can be seen from Figure 1 that the long-term variability of the wind parameters is different for summer and winter. To take this into account, the time series of the wind parameters in every month are investigated with respect to a long-term trend and a solar cycle dependence using a multiple regression analysis after

$$v_{oz} = a + b \bullet \text{year} + c \bullet R \ , \qquad (2)$$

where R is the 13-monthly smoothed sunspot number. The results for each month are shown in Figure 2. A significant long-term trend cannot be detected. The solar cycle dependency is shown in the lower panel. The most striking point is the negative solar cycle dependence of the zonal prevailing wind in spring and early summer that has already been found by other authors (e.g. Bremer at al., 1997, Jacobi et al., 1997a). In winter no solar cycle dependence of the zonal prevailing wind is found. Results presented by Roper and Xiao (1990) showed a negative solar cycle dependence of the winter upper mesosphere vertical wind shear that is modulated by the phase of the QBO, but their results refer to a height below 90 km, and recently Arnold and Robinson (1998) presented results from numerical simulation that indicate a strong solar cycle dependence of the mesospheric circulation, which, however, is rapidly decreasing for heights above about 80 km, so that the results of Roper and Xiao (1990) and those presented here do not contradict each other.

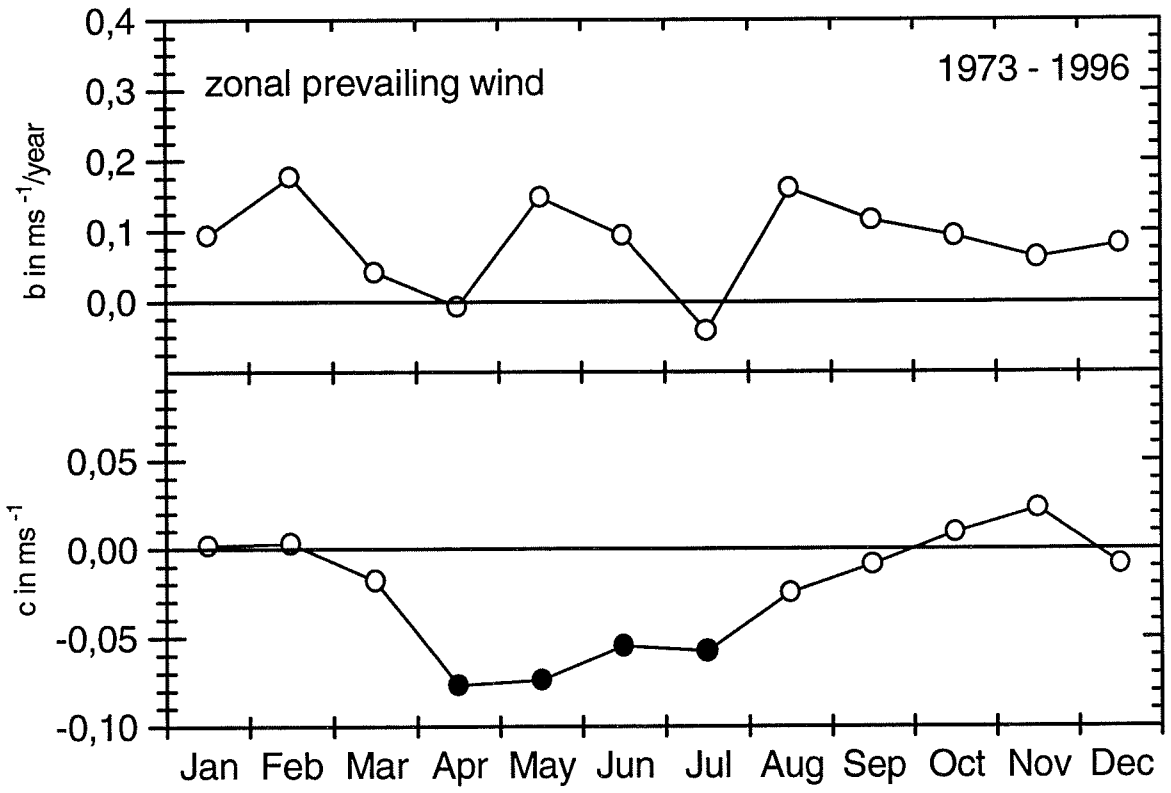

Figure 2: Coefficients b (trend) and c (solar cycle dependence) for the zonal prevailing wind, calculated after Eq. (2) for each month. Solid symbols denote a significant dependence on the 95%-level (after Jacobi et al., 1997a, updated).

In summer, around 95 km height the westerly mesopause jet is situated. However, the interannual variability of this jet reflects the behaviour of the mesosphere below as well. To visualise this, in Figure 3 summer mean profiles of the zonal prevailing wind, calculated from joint analyses (Schminder et al., 1994, 1997) of Collm D1 LF and Juliusruh medium frequency (MF) radar data are shown. The MF radar data were provided by the Institute of Atmospheric Physics at Kühlungsborn, Germany. It can be seen, that the stronger westerly winds in the mesopause region around 95 km in 1995 compared to 1990 are connected with weaker easterlies in the mesosphere below. Furthermore, the interannual variations appear to be stronger in the mesosphere at about 80 km altitude, which can already be seen from the results of Schminder et al. (1997, their Figure 2). This gives a hint to a stronger vertical zonal wind gradient during solar maximum.

The interannual variability of this gradient itself can be seen from the Collm wind data of the years 1983 - 1996, calculated using a modified form of Eq. (1) with height dependent coefficients:

$$v_z = \sum_{k=0}^{2} h^k a_{0k,z} + \sum_{k=0}^{2} b_k h^k \sin\omega t + \sum_{k=0}^{2} c_k h^k \cos\omega t \ ,$$
$$v_m = \sum_{k=0}^{2} h^k a_{0k,m} + \sum_{k=0}^{2} b_k h^k \cos\omega t - \sum_{k=0}^{2} b_k h^k \sin\omega t \ , \qquad (3)$$

again with the angular frequency being $\omega = 2\pi/12h$. Time series of the June - August mean vertical zonal prevailing wind gradients, calculated for a height of 90 km, are shown in Figure 4. The 13-monthly smoothed sunspot number is also added. Besides a long-term trend of the vertical gradient a solar cycle dependence is also indicated. This is well visible in Figure 5, showing the detrended summer vertical zonal wind gradients in dependence of the sunspot number R. The correlation is significant at the 95%-level (t-test).

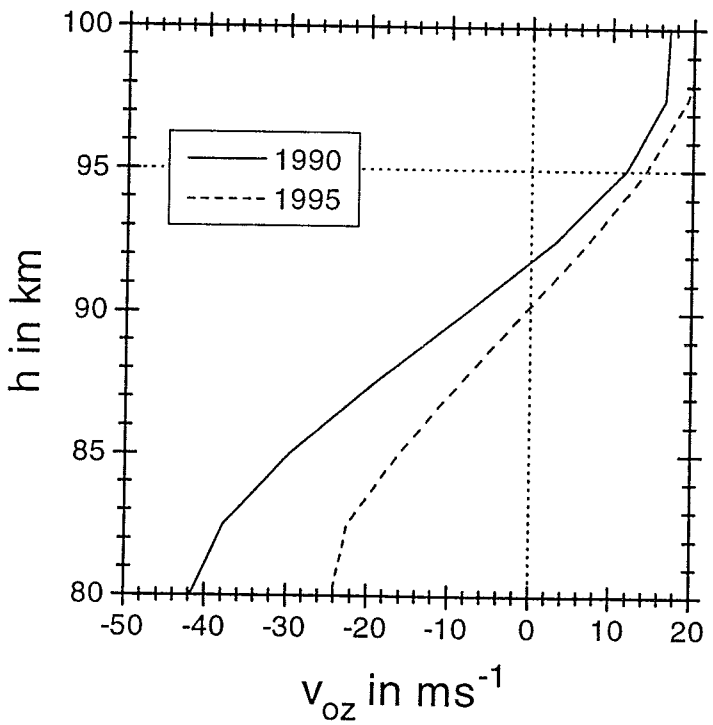

Figure 3: June - August mean profiles of mesosphere/lower thermosphere zonal prevailing winds for high (1990, R = 151) and low (1995, R = 15) solar activity. The data are taken from joint analyses of Collm LF D1 and Kühlungsborn MF radar data (after Schminder et al., 1994, 1997).

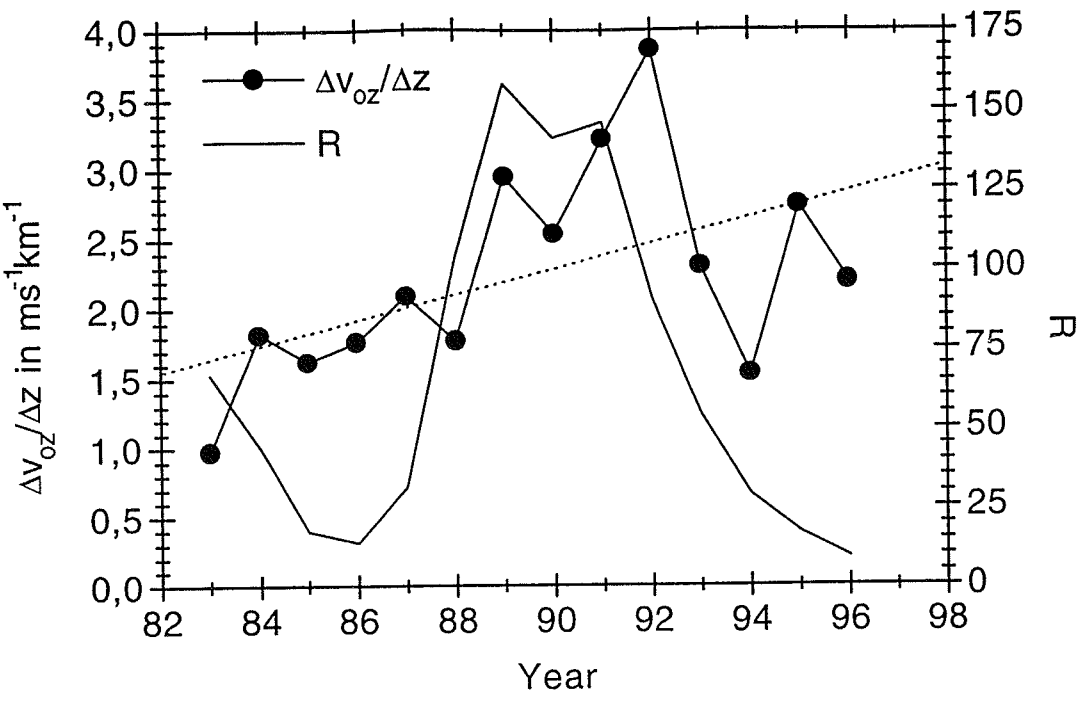

Figure 4: Time series of Collm summer (June - August) mean vertical gradients of the mesopause zonal prevailing wind at 90 km. The 13-monthly smoothed sunspot number is added.

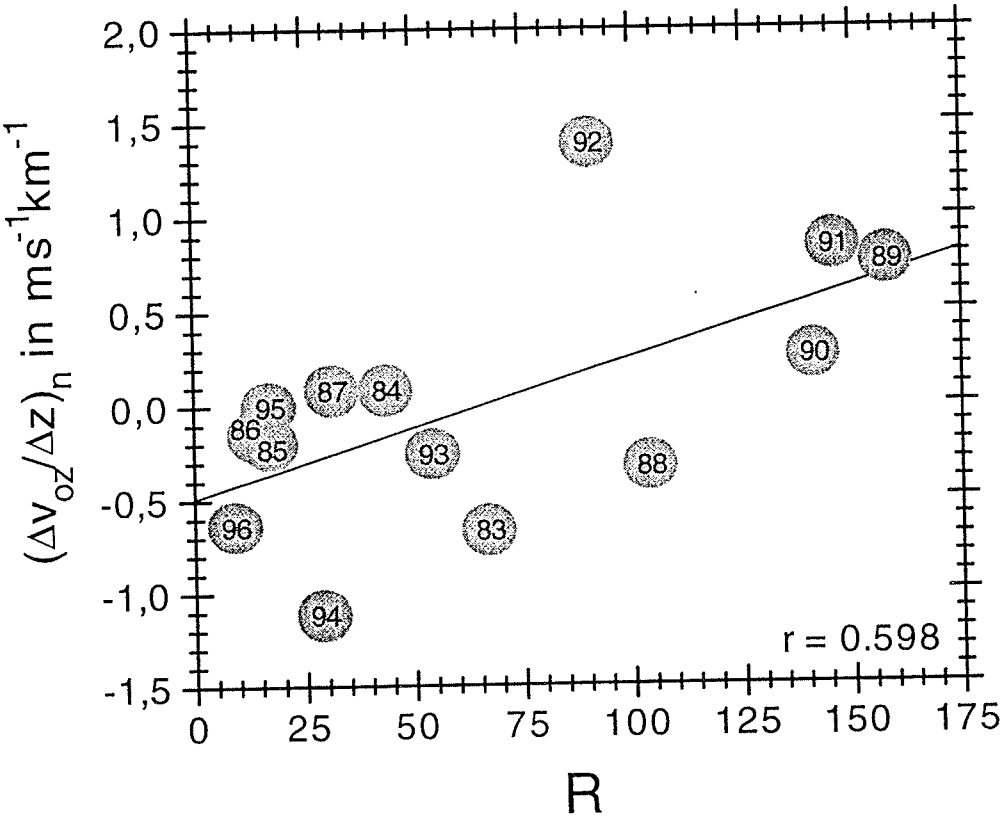

Figure 5: Detrended Collm mean summer (June - August) vertical gradient of the zonal prevailing wind at 90 km height, plotted in dependence of the 13-monthly smoothed sunspot number R.

4. Interannual variability of the quasi 2-day wave

One of the most prominent patterns in summer mesopause dynamics is the quasi 2-day wave that is known since the early 70s (Muller, 1972; Babadshanov et al., 1973). It very regularly appears around solstice and has been identified as a planetary wave of zonal wavenumber 3. Two mechanisms of the development of the wave are discussed: Salby (1981a,b) proposes, that the quasi two-day wave is a resonant amplification of the antisymmetric (3,3)-normal mode. Plumb (1983), however, suggests that the wave appears due to baroclinic instability near the summer stratospheric wind jet. The quasi 2-day wave at Collm is calculated using an extended form of Eq. (3), but with linearly height-dependent coefficients:

$$\begin{aligned} v_z &= \sum_{k=0}^{1} h^k a_{0k,z} + \sum_{j=1}^{2}\left(\sum_{k=0}^{1} b_{jk,z} h^k \sin\omega_j t + \sum_{k=0}^{1} c_{jk,z} h^k \cos\omega_j t\right), \\ v_m &= \sum_{k=0}^{1} h^k a_{0k,m} + \sum_{j=1}^{2}\left(\sum_{k=0}^{1} b_{jk,m} h^k \sin\omega_j t + \sum_{k=0}^{1} c_{jk,m} h^k \cos\omega_j t\right). \end{aligned} \tag{4}$$

The frequencies included are $\omega_1 = 2\pi/12h$ for the semidiurnal tide and $\omega_2 = 2\pi/48h$ for the quasi 2-day wave. Since the period P of the quasi 2-day wave is found to be generally not exactly 48 hours and therefore is not known *a priori*, Jacobi et al. (1997b) calculated a regression analysis after Eq. (4) for each period range 43 h < P < 58 and used the one that provided the best fit between measured and calculated data. It was found that during the maximum of the events the period is smaller than 48 hours, while before and after that time the periods are longer. This was also found by Thayaparan et al. (1997) for the years 1993 and 1994 from measurements at London, Canada. However, since during a 2-day wave event the period values change from large ones to smaller ones and back to long periods, an analysis that includes only the 48-hour period also leads to reasonable results in the vicinity of the amplitude maximum. The two horizontal amplitude components of the quasi 2-day wave were calculated using:

$$\begin{aligned} v_{48,z}(h) &= \sqrt{\left(\sum_{k=0}^{1} b_{2k,z} h^k\right)^2 + \left(\sum_{k=0}^{1} c_{2k,z} h^k\right)^2}, \\ v_{48,m}(h) &= \sqrt{\left(\sum_{k=0}^{1} b_{2k,m} h^k\right)^2 + \left(\sum_{k=0}^{1} c_{2k,m} h^k\right)^2}. \end{aligned} \tag{5}$$

Each analysis was done using a 10-day data window. To give an impression of the interannual variability of the 2-day oscillation, the zonal amplitudes at 95 km, this is the height of the maximum measuring density, are shown in Figure 6. It can be seen, that the wave activity is quite variable, but there is a tendency for enhanced activity in the years 1988 to 1992. Thus a dependence of the 2-day amplitude on the solar activity is suggested. Therefore in Figure 7 the monthly mean 2-day amplitude

$$v_{48} = \sqrt{v_{48,z}^2 + v_{48,m}^2} \tag{6}$$

for a height of 95 km is shown in dependence of the sunspot number R for the months June - August. In the fourth panel the mean summer amplitudes are presented. It can be seen that the 2-day amplitude is positively correlated with the solar activity, as it was already suggested by Jacobi et al. (1997b) for the period 1983 - 1995. This correlation can be due to the fact that the

quasi 2-day wave is positively dependent on the mean mesospheric zonal prevailing wind gradient (Plumb, 1983; Pfister, 1985), such that the excitation of the wave is enhanced when the mesospheric easterly jet is stronger, or, in turn, the upper mesopause westerly winds are weaker. Since in summer the vertical zonal prevailing wind gradient is positively correlated with the solar activity, this leads to the positive correlation of v_{48} and R. However, from Figure 7 it can be seen that only in August the correlation is relatively strong and therefore statistically significant. This could be due to the fact, that the quasi 2-day wave is a very regular phenomenon that appears in nearly every summer, and additionally the events are more or less irregularly distributed, as it can be seen from Figure 6. This means that during solar maximum only an enhanced probability for the appearance of 2-day wave events is found. Since in July this probability is large in any case, the enhancement during solar maximum is not significant for July, while in August, when during solar minimum the events appear more rarely, the enhanced probability for the appearance of the events can be seen more clearly.

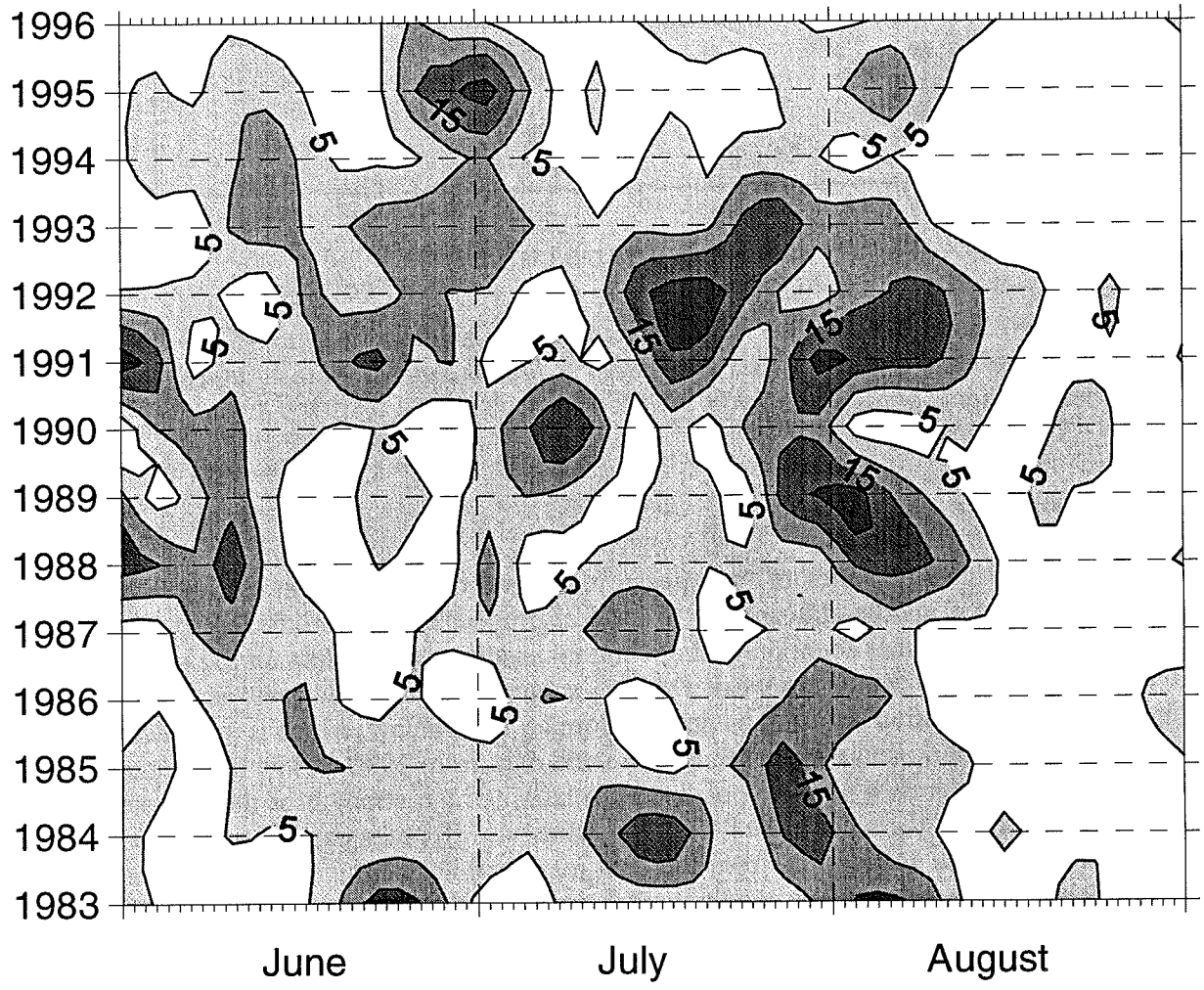

Figure 6: Zonal Amplitude $v_{48,z}$ of the 2-day wave in June - August 1983- 1996. The values are calculated from running 10-day data windows with a step rate of 1 day after Eq. (4) for an altitude of 95 km. For further details see text.

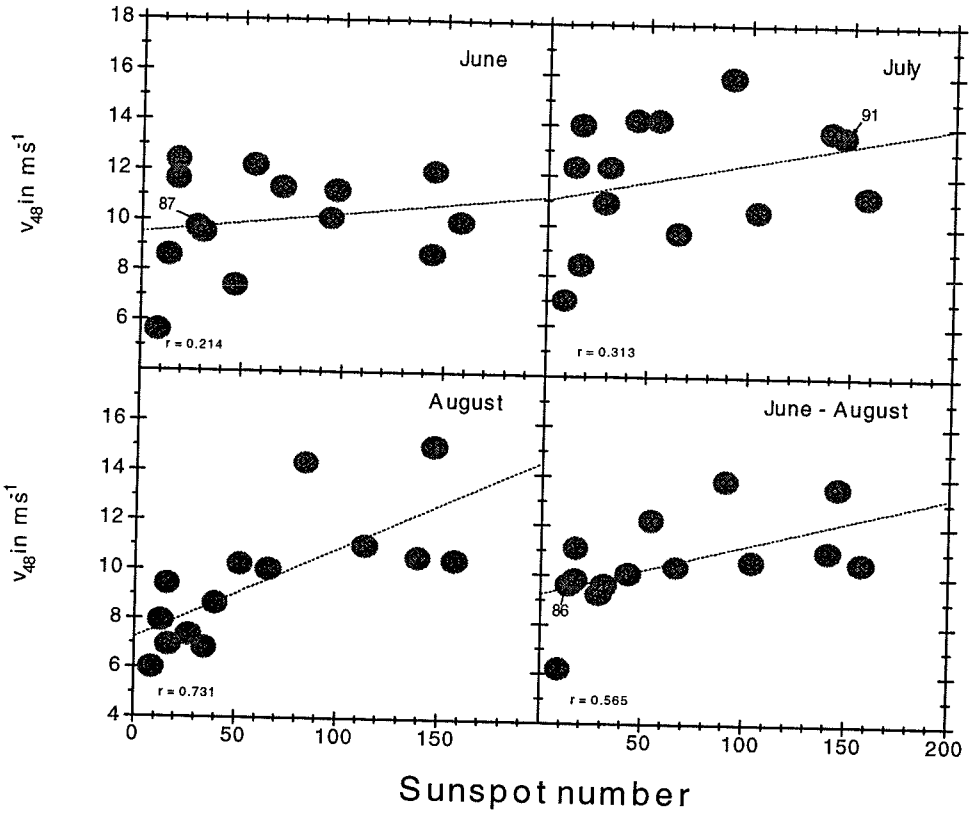

Figure 7: Correlation between the monthly mean 2-day amplitude v_{48} at 95 km altitude and the 13-monthly smoothed sunspot number R for the months June - August, from Collm measurements of the years 1983 - 1996.

6. Conclusions

From the long-term time series of mesopause region winds measured at Collm possible dependencies of upper middle atmospheric dynamical properties can be inferred. It was found, that the spring and summer zonal prevailing wind is negatively dependent on the solar activity, this means the westerly winds are weaker during solar maximum. However, as it can be seen from Figure 3, this relation seems to be due to a forcing from below, which is indicated by joint analyses of mesospheric and mesopause region wind data from 1990 - 1996 (Schminder et al., 1997). This also suggests a possible positive correlation of the strength of the summer mesospheric easterlies with the solar cycle. Although Juliusruh MF radar data are available only for a period less than one solar cycle, from the data measured so far this suggestion is also supported (Schminder et al., 1997). Additionally, regarding the vertical zonal prevailing wind gradients from 14 years of Collm measurements, one can see that the vertical zonal wind gradients are positively correlated with the solar activity, and this also hints to a forcing of the solar dependence of the mesopause region zonal winds from below. However, as it was found, for example, by Jacobi et al. (1997a), the mesosphere/lower thermosphere circulation is variable at partially very long time scales and the detection of dependencies may lead to incorrect results, if the time series used is shorter than about 2 decades. This means, considering all the measurements regarded here, that indeed a forcing of the solar cycle dependence of the mesopause region mean circulation from below is strongly suggested, but for a direct proof still longer time series of measurements may be necessary.

The interannual variability of the quasi 2-day wave activity, however, also fits into this picture. The mean summer amplitude - which is actually a mixture of maximum amplitudes and

probability of appearance - is enhanced during solar maximum, which can be explained by the stronger vertical zonal wind gradients then. This again indicates that the upper mesospheric/lower thermospheric circulation is dependent on the solar activity through a forcing of the stratosphere/mesosphere as described in the previous paragraph.

Thus the solar cycle dependence of the mesopause region mean circulation and quasi 2-day wave would be a result of a solar cycle dependence of at least the lower thermosphere and the entire middle atmosphere. Therefore the mesopause region measurements might be useful for monitoring the long-term variability and solar dependencies of the middle atmosphere.

Acknowledgements: This investigation was supported by the "Deutsche Forschungsgemeinschaft" (German Science Foundation) under contract Schm 981/2-2. I am very grateful to Dr. R. Schminder and Dr. D. Kürschner for providing the Collm wind data and for many helpful discussions. The MF radar data were provided by Dr. W. Singer and Dr. P. Hoffmann, Institute of Atmospheric Physics, Kühlungsborn.

References

Arnold, N.F., and Robinson, T.R., 1998: Solar cycle changes to planetary wave propagation and their influence on the middle atmosphere circulation. *Ann. Geophysicae* 16, 69 - 76.

Babadshanov, P.B., Kalchenko, B.V., Kashcheyev, B.L., and Fedynsky, V.V., 1973: Winds in the equatorial lower thermosphere (in russ.). *Proc. Acad. Sci. USSR* **208**, 6, 1334 - 1337.

Bremer, J., Schminder, R., Greisiger, K.M., Hoffmann, P., Kürschner, D., and Singer, W., 1997: Solar cycle dependence and long-term trends in the wind field of the mesosphere/lower thermosphere. *J. Atmos. Solar-Terr. Phys.* **59**, 497-509.

Dartt, D., Nastrom, G., and Belmont, A., 1983: Seasonal and solar cycle wind variations, 80 - 100 km. *J. Atmos. Terr. Phys.* **45**, 707-718.

Greisiger, K.M., Schminder, R., and Kürschner, D., 1987: Long-period variations of wind parameters in the mesopause region and the solar cycle dependence. *J. Atmos. Terr. Phys.* **49**, 281 - 285.

Jacobi, Ch., Schminder, R., and Kürschner, D., 1996a: Long-period (2-18 days) oscillations of mesopause winds at Collm. In: A. Raabe, J. Heintzenberg (Eds.): Meteorologische Arbeiten aus Leipzig II. *Berichte des LIM und des IFT* **4**, Leipzig, 131 - 143.

Jacobi, Ch., Schminder, R., and Kürschner, D., 1996b: On the influence of the stratospheric quasi-biennial oscillation on the mesopause zonal wind over Central Europe. *Meteorol. Zeitschrift, N.F.* **5**, 218 - 223.

Jacobi, Ch., Schminder, R., Kürschner, D., Bremer, J., Greisiger, K.M., Hoffmann, P., and Singer, W., 1997a: Long-term trends in the mesopause wind field obtained from D1 LF wind measurements at Collm, Germany. *Adv. Space Res.*, accepted.

Jacobi, Ch., Schminder, R., and Kürschner, D., 1997b: The quasi two-day wave as seen from D1 LF wind measurements over Central Europe (52°N, 15°E) at Collm. *J. Atmos. Solar-Terr. Phys.* **59**, 1277 - 1286.

Kürschner, D., 1975: Konzeption und Realisierung eines vollautomatischen Registriersystems zur Durchführung von nach der D1-Methode angelegten Routinebeobachtungen ionosphärischer Driftparameter am Observatorium Collm. *Z. Meteorol.* **25**, 218 - 221.

Kürschner, D., 1991: Ein Beitrag zur statistischen Analyse hochatmosphärischer Winddaten aus bodengebundenen Messungen. *Z. Meteorol.* **41**, 262 - 266.

Kürschner, D., Schminder, R., Singer, W., and Bremer, J., 1987: Ein neues Verfahren zur Realisierung absoluter Reflexionshöhenmessungen an Raumwellen amplitudenmodulierter Rundfunksender bei Schrägeinfall im Langwellenbereich als Hilfsmittel zur Ableitung von Windprofilen in der oberen Mesopausenregion. *Z. Meteorol.* **37**, 322 - 332.

Labitzke, K., and van Loon, H., 1992: On the association between the QBO and the extratropical stratosphere. *J. Atmos. Terr. Phys.* **54**, 1453 - 1463.

Labitzke, K., and van Loon, H., 1996: On the stratosphere, the QBO, and the sun: the winter of 1995-1996. *Meteorol Z., N.F.* **5**, 166 - 169.

Manson, A.H., Meek, C.E. Teitelbaum, H., Vial, F., Schminder, R., Kürschner, D., Smith, M.J., Fraser, G.J., and Clark, R.R. 1989: Climatologies of semi-diurnal and diurnal tides in the middle atmosphere (70 - 110 km) at middle latitudes (40 - 55°). *J. Atmos. Terr. Phys.* **51**, 579 - 593.

Muller, H.G., and Nelson, L.. 1978: A travelling quasi 2-day wave in the meteor region. *J. Atmos. Terr. Phys.* **40**, 761 - 766.

Namboothiri, S.P., Manson, A.H., and Meek, C.E., 1993: Variations of mean winds and tides in the upper middle atmosphere over a solar cycle, Saskatoon, Canada, 52°N, 107°W. *J. Atmos. Terr. Phys.* **55**, 1325 - 1334.

Plumb, R.A., 1983: Baroclinic instability of the summer mesosphere: a mechanism for the quasi-two-day wave ? *J. Atmos. Sci.* **40**, 262 - 270.

Pfister, L., 1985: Baroclinic instability of easterly jets with applications to the summer mesosphere. *J. Atmos. Sci.* **42**, 313 - 330.

Roper, R.G., and Xiao, J., 1990: The relationship between the 1974 - 1987 solar cycle and mesopause level winds over Atlanta (34N, 84W). In: Roper, R.: Climatology of meteor winds over Atlanta (34°N, 84°W): Part 2. Final Technical Report, Georgia Tech Project G-35-612, Georgia Institute of Technology, 147 - 159.

Salby, M.L., 1981a: Rossby normal modes in nonuniform background configurations. Part II: Equinox and solstice conditions. *J. Atmos. Sci.* **38**, 1827 - 1840.

Salby, M.L., 1981b: The 2-day wave in the middle atmosphere: Observations and theory. *J. Geophys. Res.* **86**, 9654 - 9660.

Schminder, R., Singer, W., Kürschner, D., Hoffmann, P., and Keuer, D., 1994: Permanent monitoring of the upper atmosphere wind field over Central Europe by a joint analysis of LF wind profiler and MF radar measurements at Collm and Juliusruh (Germany). *Meteorol. Zeitschrift, N.F.* **3**, 297 - 300.

Schminder, R., Jacobi, Ch., Kürschner, D., Hoffmann, P., Keuer, D., and Singer, W., 1997: The upper mesosphere and lower thermosphere wind field over Central Europe from 1994 through 1996 obtained from a joint analysis of LF windprofiler and MF radar measurements. *Meteorol. Zeitschrift N.F.* **6**, 225 - 229.

Sprenger, K., and Schminder, R., 1969: Solar cycle dependence of winds in the lower ionosphere. *J. Atmos. Terr. Phys.* **31**, 217 - 221.

Svensmark, H., and Friis-Cristensen, E., 1997: Variation of cosmic ray flux and global cloud coverage - a missing link in solar-climate relationships. *J. Atmos. Solar-Terr. Phys.* **59**, 1225 - 1232.

Thayaparan, T., Hocking, W.K., and MacDougall, J., 1997: Amplitude, phase, and period variations of the quasi 2-day wave in the mesosphere and lower thermosphere over London, Canada (43°N, 81°W), during 1993 and 1994. *J. Geophys. Res.* **102**, 9461 - 9478.

van Loon, H., and K. Labitzke, 1994: The 10-12-year atmospheric oscillation. *Meteorol. Zeitschrift N.F.* **3**, 259 - 166.

Christoph Jacobi
Institut für Meteorologie
Universität Leipzig
Stephanstr. 3
04103 Leipzig

The Quasi 16-day Wave in the Summer Midlatitude Mesopause Region and its Dependence on the Equatorial Quasi-Biennial Oscillation

Christoph Jacobi

Zusammenfassung:

Aus täglichen Analysen des sommerlichen zonalen Grundwindes im Mesopausenbereich, der am Observatorium Collm der Universität Leipzig gemessen wurde, werden niederfrequente Variationen im Zeitbereich planetarer Wellen (10 - 20 Tage) bestimmt. Obwohl die direkte Ausbreitung derartiger Wellen durch die stratosphärischen und mesosphärischen Ostwinde verhindert wird, werden in manchen Jahren trotzdem Oszillationen gemessen, die mit planetaren Wellen im Zusammenhang stehen können. Dies unterstützt die Theorie, daß sich planetare Wellen von der Winterhalbkugel entlang der Zonen schwachen Windes bis in die Mesopausenregion mittlerer und polarer Breiten ausbreiten. Betrachtet man die interanuelle Variabilität dieser Wellen, fällt eine Abhängigkeit von der äquatorialen quasi 2-jährigen Schwingung (QBO) auf, wobei während der Ostphase der QBO die Wellenaktivität gering ist, während sie in der Westphase der QBO stärker sein kann. Der Einfluß der QBO auf die sommerliche Wellenaktivität wird vom 11-jährigen Sonnenfleckenzyklus moduliert, wobei während des solaren Maximums stärkere Aktivität zu verzeichnen ist.

Summary:

From daily estimates of the summer mesopause region zonal prevailing wind measured at the Collm Observatory of the University of Leipzig long-term variations in the period range of planetary waves (10-20 days) are detected. Although the direct propagation of these waves from lower layers into the mesosphere is not possible because of the wave filtering in the summer stratospheric and mesospheric easterlies, in some years oscillations are found that can be connected with planetary waves, supporting the theory of the propagation of these waves from the equatorial region to the midlatitude and polar upper mesosphere along the zero wind line. The interannual variability of these waves shows a dependence on the equatorial quasi-biennial oscillation (QBO), so that in general during the east phase of the QBO the planetary wave activity is small, while during the QBO west phase it can be larger. The influence of the QBO on the planetary wave activity is modulated by the 11-year solar cycle, so that the strongest signal is found during solar maximum.

1. Introduction

In the past there has been several attempts to investigate the influence of the equatorial stratospheric quasi-biennial oscillation (QBO) on the midlatitude middle atmosphere. Sprenger and Schminder (1967) have found a 26-month oscillation in the mesospheric circulation, while Sprenger et al. (1975) found a 22-month oscillation from ionospheric drift measurements. More recently a quasi-biennial oscillation in Saskatoon medium-frequency radar wind data was found by Namboothiri et al. (1994), but there was no clear connection of the phase of the equatorial QBO to the mesopause prevailing wind oscillation with the phase of the QBO. The connection between QBO, solar activity and winter midlatitude stratospheric circulation (e.g. Labitzke and van Loon, 1992, 1996) is well known, but the reaction of the mesosphere on sudden stratospheric warmings is strongly variable, so that the QBO signal as it is to be seen in

the winter mesopause is rather weak. Jacobi et al., (1996a) found a dependence of the winter zonal prevailing wind on the equatorial QBO, but this was statistically significant only for the December data, when generally stratwarm events appear more rarely than in January and February. In summer, no statistically significant influence of the equatorial QBO on the midlatitude mesopause region could be found. This annual variability of the QBO-influence on the mean mesopause dynamics leads to secondary oscillations, which were found by Tung and Yang (1994) in stratospheric ozone. Jacobi et al. (1996a) pointed out, that secondary oscillations are also present in the midlatitude mesopause region dynamics.

Recently, however, Espy et al. (1997) found an influence of the equatorial QBO on the summer polar mesosphere that can be seen in the interannual variability of the quasi 16-day wave, which was identified as the 2nd symmetric mode of zonal wavenumber 1. They also referred to measurements of Williams and Avery (1992), who have found a 16-day wave event in summer 1984 radar measurements in Alaska. Generally, westward travelling planetary wave are filtered out by the stratospheric and mesospheric easterlies and therefore cannot propagate up to the summer upper middle atmosphere, although the 5-day wave, being the 1st symmetric mode of zonal wavenumber 1 (e.g. Rodgers, 1976), due to its high phase speed sometimes is able to propagate up to the summer mesosphere (Grollmann, 1992), and therefore can be observed in all seasons (Salby and Roper, 1980). The slower 16-day wave, however, should not be able to propagate through the stratospheric easterlies. However, some measurements have shown that in some summers the 16-day wave can be present in the mesosphere as well (Tsuda et al., 1988; Jacobi et al., 1996b).

Two mechanisms have been suggested to explain the propagation of the 16-day wave into the mesosphere. The first one is, that the wave is generated in the winter hemisphere and guided along the zero wind line to the summer mesosphere (Dickinson et al., 1968; Miyahara et al., 1991; Forbes et al., 1995). A second, or rather additional explanation is, that planetary waves are generated by oscillatory breaking of gravity waves, which are modulated in the troposphere and lower stratosphere of the summer hemisphere (Holton, 1984; Williams and Avery, 1992; Forbes et al., 1995). However, Espy et al. (1997) have shown that there is evidence for a QBO influence on the 16-day wave activity in summer, so that the former explanation is supported by their measurements. They suggest that during the easterly phase of the QBO, the waves propagation is blocked through the equatorial stratospheric easterly winds so that then the planetary wave activity in the polar mesosphere is strongly reduced.

The dataset that was used by Espy et al. (1997) contained only 4 years, and although the summer 1984 wind measurements of Williams and Avery (1992) were included into the investigation, the conclusions were based on a rather small database. Thus, to investigate a possible QBO-dependence of planetary waves on a long-term data base, in the following midlatitude mesopause region wind data of the years 1981 through 1996 are used, which were measured at the Collm Observatory of the University of Leipzig.

2. Measurements and data evaluation

The wind field of the mesopause region over Central Europe is continuously observed at the Collm Observatory of the University of Leipzig by daily total reflection (D1) nighttime radio wind measurements in the low-frequency (LF) range. The ionospherically reflected sky wave of three commercial radio transmitters on 177, 225, and 270 kHz is used (Kürschner and Schminder, 1986; Schminder and Kürschner, 1988, 1992, 1994; Jacobi et al., 1997a). The data are automatically interpreted using a modified form of the similar fade method (Kürschner, 1975) and combined to half-hourly mean values of the three measuring paths, referring to a mean reflection point at about 52°N, 15°E.

Since 1983 the reference height h is measured on 177 kHz using travel time differences between the ground wave and the reflected sky wave in a modulation frequency range near 1.8 kHz (Kürschner et al., 1987). Since this height is varying during the day and in summer due to

large absorption in the daytime D-region generally no measurements are possible then, a multiple regression analysis with height dependent coefficients is used to determine monthly mean profiles of the prevailing wind and the semidiurnal tide as well as other wind oscillations:

$$v_z = \sum_{k=0}^{q} h^k a_{0k_z} + \sum_{j=1}^{p}\left(\sum_{k=0}^{q} b_{jk_z} h^k \sin\omega_j t + \sum_{k=0}^{q} c_{jk_z} h^k \cos\omega_j t\right) + \varepsilon \,,$$
$$v_m = \sum_{k=0}^{q} h^k a_{0k_m} + \sum_{j=1}^{p}\left(\sum_{k=0}^{q} b_{jk_m} h^k \sin\omega_j t + \sum_{k=0}^{q} c_{jk_m} h^k \cos\omega_j t\right) + \varepsilon \,, \qquad (1)$$

where v_z and v_m are the measured horizontal wind data and ω_j the angular frequencies of the respective oscillations. The spectral selectivity of the separation of prevailing and tidal wind is improved through fitting the measured values for the horizontal semidiurnal tidal wind components as vector (Kürschner, 1991), which requires the assumption of clockwise circularly polarised tidal wind components:

$$b_{1k_m} = -c_{1k_z} \quad \text{and} \quad c_{1k_m} = b_{1k_z} \,. \qquad (2)$$

The tidal winds, however, are not further regarded in this investigation. The diurnal tidal components are not considered in Eq. (1), because the regularly distributed daily data gaps would lead to a large error in the calculation of these. Thus an error of the prevailing wind can occur when only nighttime measurements are performed. However, at midlatitudes the diurnal tide is a much less dominant feature than the semidiurnal tide (e.g. Manson et al., 1989), and comparison of calculations of the zonal prevailing wind calculated with and without including the diurnal tide into the regression analysis (not shown here) led to an error of less than 4 ms^{-1} in the mean values of the prevailing wind in each month that is due to omitting the diurnal period in Eq. (1). Additionally, in this investigation we are interested in the variations of the prevailing wind, which are not affected if the prevailing winds should contain a bias. The zonal and meridional prevailing wind is calculated after:

$$v_{oz}(h) = \sum_{k=0}^{q} h^k a_{0k,z} \qquad \text{and} \qquad v_{om}(h) = \sum_{k=0}^{q} h^k a_{0k,m} \,. \qquad (3)$$

with an uncertainty of 5 ms^{-1}. In addition to this, also daily estimates of the prevailing wind can be obtained by applying Eq. (1) with k = 0 (e.g. Jacobi et al., 1996b, 1997b). In this case reflection height variations are not taken into account, therefore only those nighttime wind values are used in Eq. (2) when the reflection height is found to be near its mean nighttime value and varies only slightly. In summer this mean nighttime reference height is found between 95 and 100 km.

3. Results

3.1 14-year mean periodograms

A 14-year mean periodogram of the zonal and meridional prevailing wind amplitude for July and August is shown in the upper panel of Figure 1. In the lower panel the zonal components are shown for July and August separately. The data are calculated using a regression analysis after Eq. (1) with k = 2 and j = 2, including the angular frequency $\omega_1 = 2\pi/12h$ and varying the second period $P_2 = 2\pi/\omega_2$ from 2 to 30 days, with a step rate of 6 hours. The strongest signal

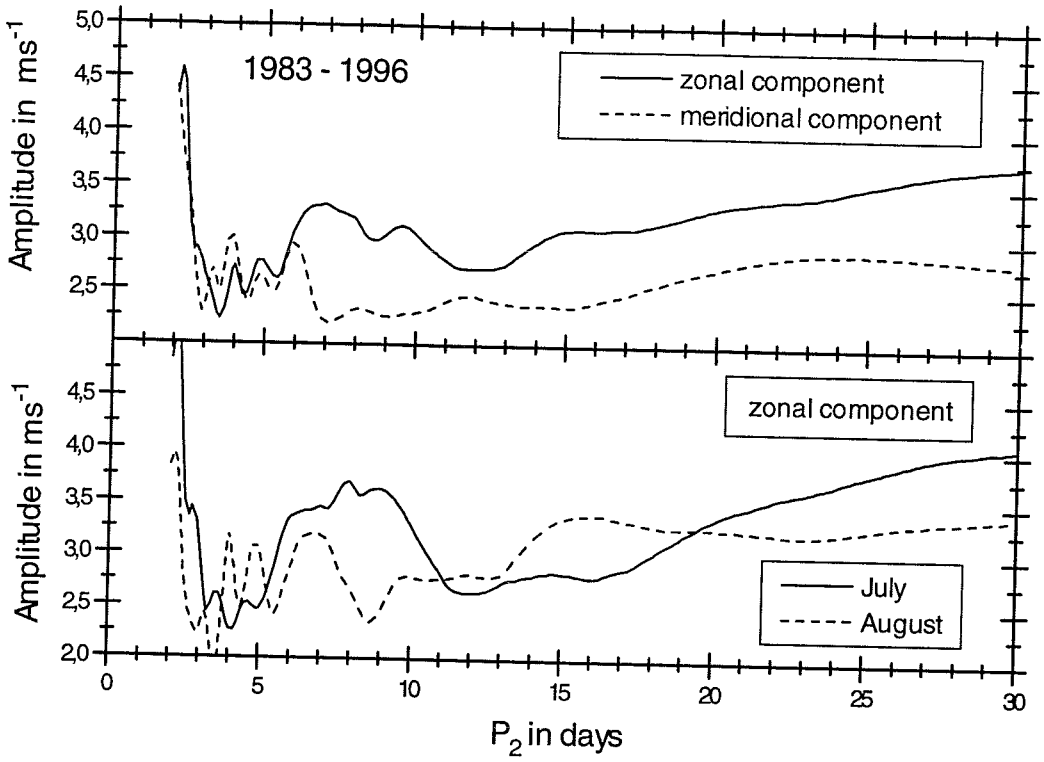

Figure 1: Amplitude spectrum of the zonal prevailing wind, calculated for each month using a regression analysis after Eq. (1) with k = 2 and j = 2, with $\omega_1 = 2\pi/12h$ and varying the second period $P_2 = 2\pi/\omega_2$ from 2 to 30 days, with a step rate of 6 hours. The data are 1983 - 1996 mean values. Upper panel: July/August means of the zonal and meridional component. Lower panel: zonal component for July and August separately.

that can be seen in Figure 1 belongs to the quasi 2-day wave. This is a well known feature in the summer mesosphere and lower thermosphere (Muller and Nelson, 1978; Clark et al., 1994; Meek et al., 1996; Jacobi et al., 1997c, and many others), which was first detected by Muller (1972). Salby (1981a,b) identified this phenomenon as a westward travelling planetary wave with wavenumber 3. In contrast to the 5- or 16-day wave, however, the 2-day wave is an in-situ effect of the mesosphere, originating from a resonant amplification of the antisymmetric (3,3)-normal mode (Salby, 1981a,b) or baroclinic instability near the summer stratospheric wind jet (Plumb, 1983; Pfister, 1985). Thus a dependence of the 2-day wave on the QBO is not to be expected. A detailed analysis of the quasi 2-day wave as measured at Collm is given by Jacobi et al. (1997c).

A large peak is found in Figure 1 at periods between 6 and 10 days. As it can be seen especially from comparison of the zonal and meridional component and from the lower panel, too, this peak obviously consists of several maximum values. The short-period one (6-7 days) possibly can be regarded as a Doppler shifted 5-day wave, which is a regular feature in the midlatitude mesosphere. In summer the mean nighttime reference heights are found above the mesospheric easterlies, and the zonal prevailing mean winds amount to more than 15 ms^{-1} there. This is shown in Figure 2, where, depending on the mean monthly variability of the wind field, mean monthly or half-monthly zonal prevailing winds for the 1983 - 1996 period are shown. The data are updates of those presented by Jacobi et al. (1997a). It can be seen that the maximum zonal prevailing winds in summer at 95 km height reach 15 ms^{-1} in August and are even stronger at higher altitudes. This means that the prevailing winds are strong enough to

influence the period even of the relatively fast 5-day wave. However, as it was pointed out in the introduction, the 5-day wave due to its high phase speed partially can propagate through the mesospheric easterlies, and thus an influence of the equatorial QBO on the summer 5-day wave is not to be expected, because the existence of this wave in the midlatitude summer mesosphere is not dependent on its propagation through the equatorial region. Lastovicka (1993) showed from ionospheric absorption measurements, that there is no evidence for an effect of the equatorial QBO on planetary waves with periods shorter than 10 days. Additionally, Jacobi et al. (1996a) could not find any QBO signal in the summer mesospheric mean winds, and numerical simulations performed by Dameris (1988) and Dameris and Ebel (1990) do not indicate an influence of the equatorial QBO on the mean summer midlatitude dynamics. Thus a possible interannual variation of the 5-day wave through the variation of the mean wind field is not likely, too. This was proved from the Collm data by comparing summer mean standard deviation calculated from daily 6 - 8 days period bandpass filtered zonal wind data with the equatorial stratospheric winds. A 75% probability for no correlation between the QBO and the planetary waves in the period window given was found.

In Figure 1 additional maximum zonal amplitudes are found at 8 and 9 days. Possibly the 8-day peak could be the result of a 16-day wave that has gone through a quadratic system. An 8-day oscillation has been reported by Salby and Roper (1980). Tsuda et al. (1988) have also found 6 - 8 day oscillations in the summer mesosphere. Salby et al. (1984) and Vincent (1993a,b) has reported 3 - 10 day oscillations in the equatorial mesosphere that are due to Kelvin waves that are only present in the zonal component, however these are restricted to near equatorial latitudes and it is doubtful that they are visible in midlatitude measurements.

In the upper panel of Figure 1 the 16-day wave is only found as a plateau in the spectrum of the zonal component, and there is some variability at larger periods that, however, is due to the general variability of the wind field of the mesopause region. In the lower panel, for August relative maximum amplitudes are found near periods of 15 - 16 days, but this peak is smeared in the summer means in the upper panel. These peaks can be regarded as the signal of the 16-day wave. Thus in the following section the interannual behaviour of this oscillation will be considered in detail.

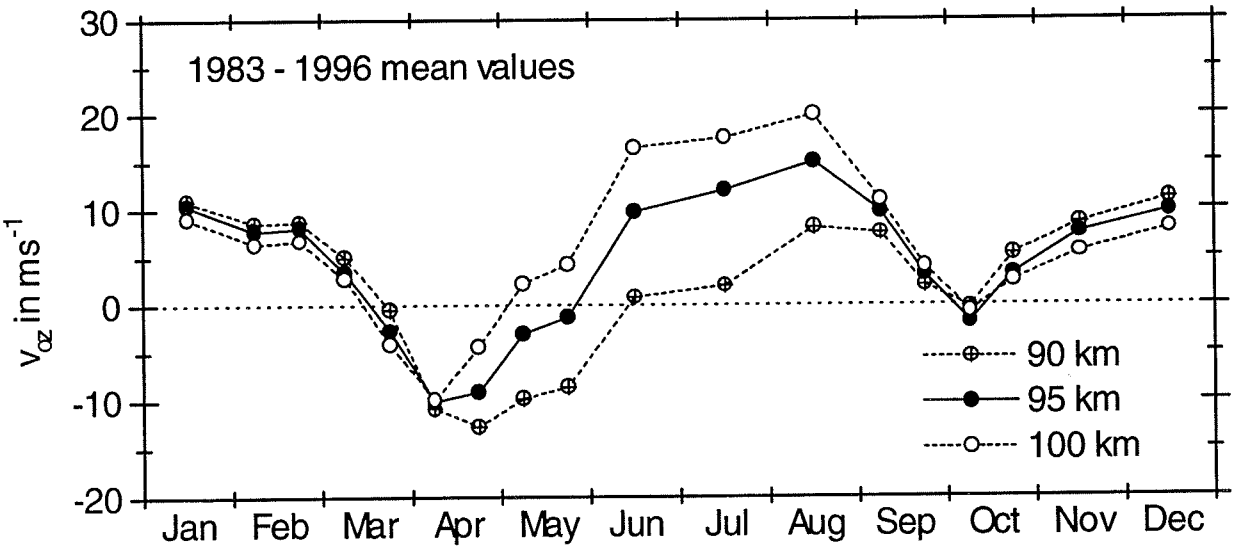

Figure 2: 1983 - 1996 mean monthly or half-monthly mean values of the zonal prevailing wind measured at Collm for three heights. The data are updates from Jacobi et al. (1997a).

3.2. Interannual variability of the 16-day wave

As an example for the interannual variability in Figure 3 the 12 - 20 day bandpass filtered time series of the zonal prevailing wind, calculated from daily analyses after Eq. (1) with k = 0, is shown for the summers of 1987 (QBO east) and 1988 (QBO west). It can be seen that generally the variation is low with amplitudes of 2 ms^{-1} and less, and only in July 1988 enhanced amplitudes are found that form a sort of burst of an oscillation with a period of about 16 days. Thus in total the 16-day wave activity is larger in 1988, although the appearance of the wave is only intermittent.

To investigate the wave activity on a long-term base and to take into account the intermittence of the planetary wave, in Figure 4 the mean standard deviation σ for July and August is shown for every year of the period 1981 - 1996, after a bandpass filter with the period windows 14 - 18 or 12 - 20 days, respectively, was applied to the time series of the daily zonal prevailing wind values. This procedure was described by Jacobi et al. (1996b, 1997b), who investigated the long-term variability of planetary wave activity on an annual base. From their monthly mean spectra they concluded that the variance or standard deviation can be considered as a signal for the planetary wave activity, thus subsequently we also refer to σ using the term „planetary wave activity". The equatorial stratospheric zonal wind v_{eq} is added to Figure 4, as well as the 13-monthly smoothed sunspot number. Considering the curve of the wave activity in the 14 - 18 day period window, its interannual variation in most of the years follows the QBO signal, so that the wave activity is reduced when the equatorial winds come from the east or conversely high planetary wave activity is only possible during periods of large v_{eq}, i.e. during QBO west years. However, this correlation is not straightforward; there are 2 years, 1983 and 1985, when despite of westerly equatorial winds the midlatitude planetary wave activity is low. This means, that the western phase of the QBO is a requirement for large planetary wave activity in the mesopause region, but not in all cases these waves are really found, while in QBO east years the propagation of planetary waves into the midlatitude mesopause is generally impossible or strongly reduced, respectively, due to the blocking mechanism of the equatorial stratospheric easterlies that was described above.

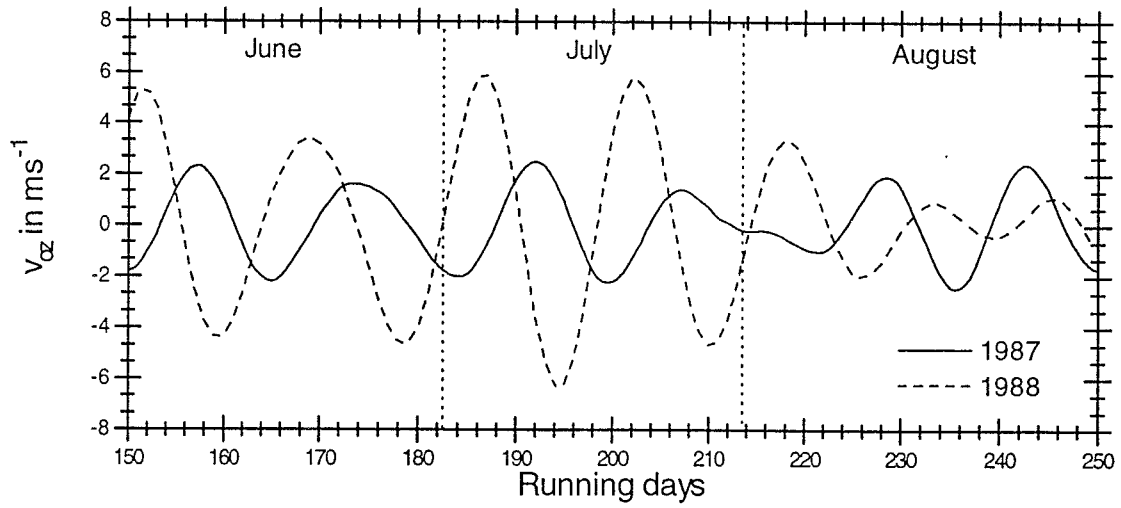

Figure 3: Two examples for the long-period variability of the mesopause region wind field in the summer mesosphere. The data are daily estimates of the zonal prevailing wind that are bandpass filtered using a Lanczos filter with 100 weights and a period window of 12 - 20 days.

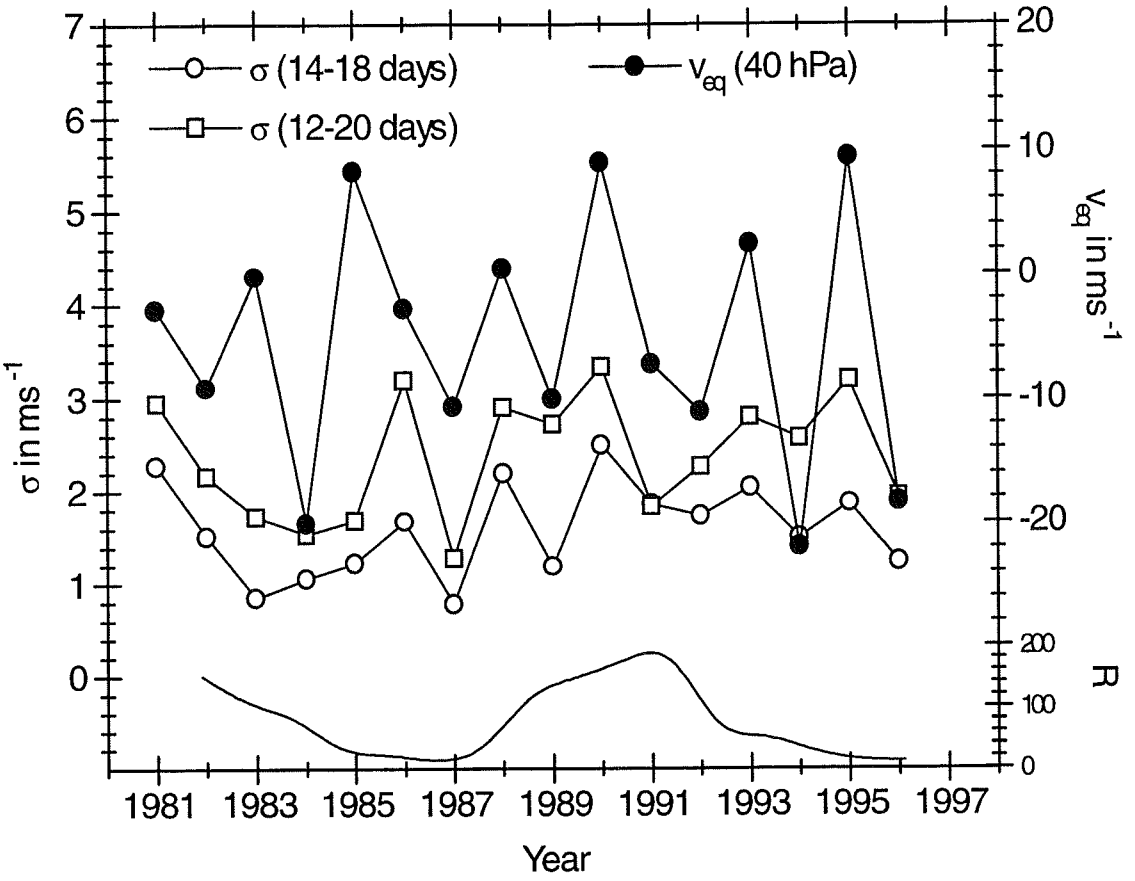

Figure 4: Summer (July/August) mean planetary wave activity, represented by the standard deviation σ of the zonal prevailing wind v_{oz}, taken from time series of daily estimates of v_{oz} that were bandpass filtered in the period windows indicated in the legend. The equatorial zonal stratospheric wind (for 40 hPa, taken as mean value of 30 and 50 hPa) is also given. In the lower part of the figure the 13-monthly smoothed sunspot number is added.

Considering a larger period window, i.e. 12 - 20 days, the general pattern is still found, although in some years (1989, 1991, 1992) the planetary wave activity curve doesn't follow the v_{eq} curve so closely. In Figure 5 the standard deviation values $\sigma_{14\text{-}18}$ and $\sigma_{12\text{-}20}$ are plotted in dependence of each other. They are, with some few exceptions, closely related to each other so that the 14 - 18 day period window may be considered as sufficient for the description of the 16-day wave activity.

3.3. Solar cycle dependence

In Figure 4 the 13-monthly smoothed sunspot number is added. During solar maximum, i.e. in the late 80s and early 90s a tendency for an enhancement of the planetary wave activity is visible, which possibly modulates the QBO-dependence of the wave activity. To investigate the time series of the planetary wave activity with respect to a possible solar influence, the monthly means of $\sigma_{14\text{-}18}$ of the years 1981 - 1996 that were normalised by their 16-year mean, were analysed using a multiple regression analysis:

$$\sigma_{14-18} = a + b \bullet \text{year} + c \bullet R. \qquad (4)$$

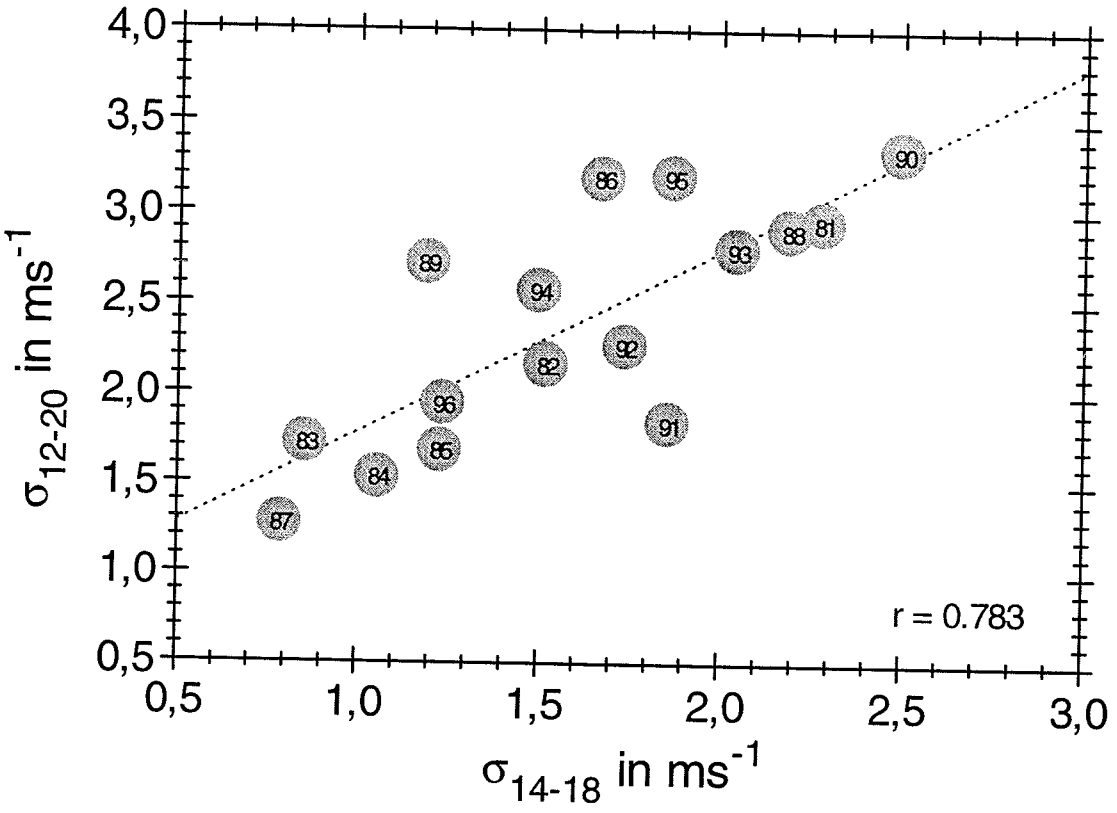

Figure 5: Standard deviation, taken from the time series of daily estimates of the zonal prevailing wind that was bandpass filtered in the period window 12 - 20 days, in dependence of the 14 - 18 days period window bandpass filtered zonal prevailing wind.

The results are shown in Figure 6. The coefficients b and c are given for each month of the year, the arrow, pointing at the July value of c in the lower panel denote a significant dependence on the 95%-level (t-test). It can be seen that no significant trend can be detected, although a weak general tendency for increasing planetary wave activity can be inferred. This coincides with the general positive long-term trend in planetary wave activity that was found by Jacobi et al. (1996b, 1997b) or Bittner et al. (1997). Considering the solar cycle dependence c, the summer values exhibit a positive correlation, as it is already suggested by Figure 4. This shows, that the planetary wave activity is variable from year to year, and thus a direct correlation with the QBO cannot be expected.

Thus the dependence of the planetary wave activity on the equatorial QBO cannot be considered as a close connection, but rather a modulation of the QBO signal on the long-term variability of σ in the course of the years. Therefore the correlation between σ and v_{eq} is relatively weak; this can be seen in Figure 7, where $\sigma_{14\text{-}18}$ is shown in dependence of the equatorial zonal wind v_{eq}. The correlation coefficient amounts to 0.472 only, although a trend is visible. If we consider the solar cycle dependence of the summer planetary wave activity, a stronger correlation, however, can be expected if the data are grouped by the solar activity, since during solar minimum the planetary wave activity is low at any rate and thus its modulation by the equatorial QBO should be less effective. Therefore in Figure 7 the data are grouped by the July/August mean of the 13-monthly smoothed sunspot number R. Now it is clearly visible that for low solar activity ($R < 50$) no significant dependence of the planetary wave on the

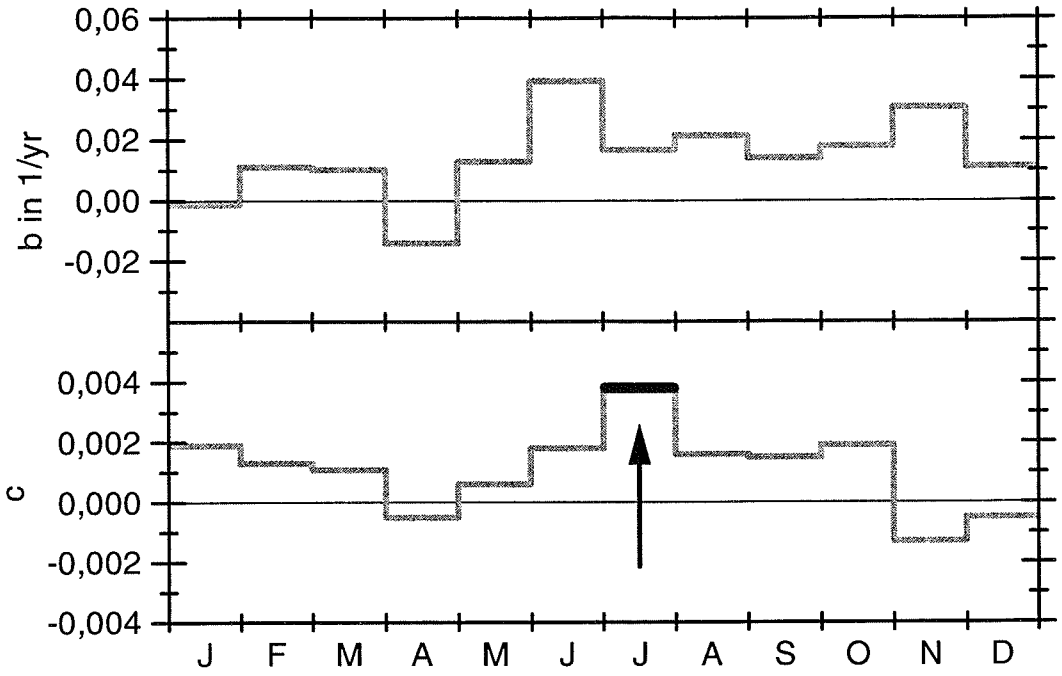

Figure 6: Coefficients b (trend) and c (solar cycle dependence), calculated after Eq. 4 for each month of the year, from normalised monthly values of $\sigma_{14\text{-}18}$.

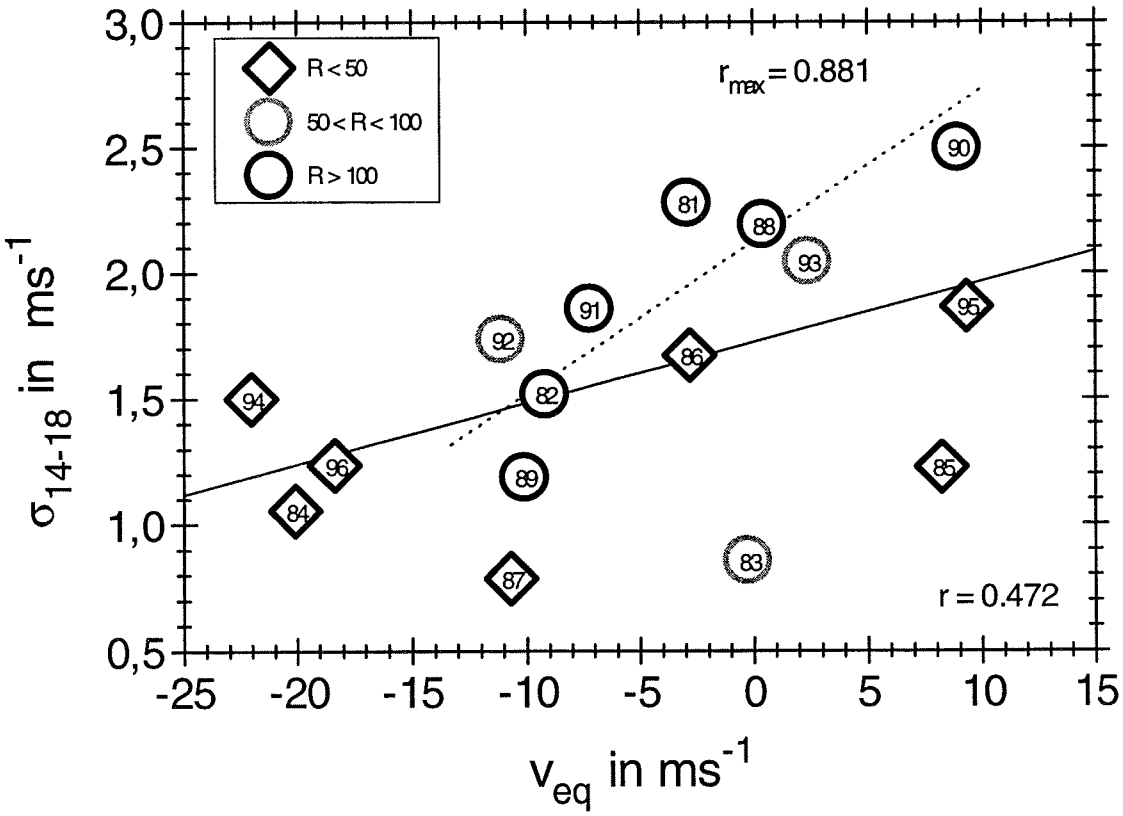

Figure 7: July/August standard deviation σ *of the zonal prevailing wind* v_{oz}*, taken from the bandpass filtered (14 - 18 days period window) time series of daily estimates of* v_{oz}*. in dependence of the equatorial zonal stratospheric wind (for 40 hPa, taken as mean value of 30 and 50 hPa). The values are classified in high, moderate and low solar activity, as indicated by the ranges of July/August mean of the 13-monthly smoothed sunspot number R in the legend.*

QBO is found, while for high solar activity (R > 100) the dependence is much stronger, as shown by the dotted regression line, and the correlation coefficient amounts to $r_{max} = 0.881$. This dependence is significant on the 95%-level, however, the database only consists of 6 years in this case and thus conclusions should be drawn with care.

4. Discussion and conclusions

Regarding the summer midlatitude upper mesosphere/lower thermosphere, planetary wave activity at time scales of more than 10 days is found in some years, despite the fact that the strong summer mesospheric easterlies generally prohibit the direct propagation of slowly westward travelling long-period planetary waves from the summer troposphere to the mesosphere. The Collm measurements presented here support results from literature (Tsuda et al., 1988; Williams and Avery, 1992; Espy et al., 1997), although the data do not necessarily correspond to each other when single years are regarded. The 15-day wave that was found, for instance, by Tsuda et al. (1985) in August 1985 as well as the July 1984 event presented by Williams and Avery (1992) could not be confirmed by the Collm measurements.

Espy et al. (1997) have proposed a QBO dependence of the planetary wave activity in the polar mesopause region and confirmed this by comparing their data with the 10 hPa Singapore winds. They pointed out that these results confirm the theory of a propagation of planetary waves, which are generated in the winter hemisphere, to the polar summer mesopause region, since a modulation of these waves can only take place in the equatorial stratosphere. From the Collm winds a QBO dependence of the 16-day wave is clearly to be seen, so that large amplitudes of the 16-day wave are only found when westerly winds are found in the equatorial stratosphere. In addition, however, this signal is modulated by the long-term variability of the planetary wave activity. Especially a solar cycle dependence is found, so that a strong influence of the QBO is found during solar maximum, while for solar minimum the influence is small.

The 40 hPa equatorial QBO signal used here, however, have a time lag of about 10 months against the 10 hPa winds (Naujokat, 1986; Jacobi et al., 1996a) that are used by Espy et al. (1997), and thus the results found here for the Collm winds are just contradicting those of Espy et al. (1997). However, as it can be seen from Figure 4, the interannual variability of the Collm $\sigma_{14\text{-}18}$ generally is not very large in the first half of the 1990s and the QBO effect seen there is relatively small, compared to the period of 1987 - 1990. It also has to be kept in mind that the definition of the QBO phase is difficult in some cases. So, for example, in the summers of 1984 and 1994 the QBO at 10 hPa had just reached the westerly phase (Naujokat, 1986; Naujokat et al., 1995) and the equatorial stratospheric winds below were still clearly in the easterly phase.

However, independently from the definition of the QBO phase, the differences in mesopause wave activity that are found between midlatitudes and polar latitudes are unexplained so far. A possible influence could be given by the different heights referred to. Espy et al. (1997) used nightglow data referring to a mean height of about 87 km, and also the 16-day wave amplitude found by Williams and Avery (1992) for July 1984 maximises at around 85 km and decreases with height. The maximum measuring density of the Collm summer wind data, in contrast to that, is found at heights between 95 and 100 km. It is, however, not quite clear why the different measuring heights should lead to a completely different dependence of the planetary wave activity on the QBO. The numerical calculations of Forbes at al. (1995) show that the region of enhanced summer 16-day wave activity is limited to a relatively small height region, and the absolute height of this region as also depending on the background wind field, so that it is conceivable that during different QBO phases the height of this region changes and thus the 16-day wave is seen by the different measuring systems at different phases of the QBO. On the other hand, numerical results presented by Dameris (1988) and Dameris and Ebel (1990) indicate that the summer hemisphere midlatitude and polar dynamics is not much influ-

enced by the QBO, and the results of Jacobi et al. (1996a) also show that the July and August mean mesopause zonal winds at Collm do not depend on the equatorial QBO. Thus the cause of the differences that arises between the polar and midlatitude planetary wave activity is still unclear. Latitudinal effects could play a role, but the model results of Forbes et al. (1995) show that for cases with enhanced leakage of planetary wave energy from the winter to the summer hemisphere the region of larger wave amplitudes is spread over a relatively wide latitude range and thus the effect of the latitudinal difference should not be dominant. Further theoretical and experimental effort seems to be necessary to explain the differences found in polar and midlatitude measurements.

Acknowledgements: This investigation was supported by the "Deutsche Forschungsgemeinschaft" (German Science Foundation) under contract Schm 981/2-2. The QBO data were contributed by the U.S. Department of Commerce, NOAA, Climate Prediction Center. I am very grateful to Dr. R. Schminder and Dr. D. Kürschner for providing the Collm wind data and for many helpful discussions.

References

Bittner, M., Offermann, D., Graef, H.H., and Donner, M., 1997: Wavelet analysis of upper mesosphere temperature variations. *Adv. Space Res.*, in press.

Clark, R.R., Current, A.C., Manson, A.H., Meek, C.E., Avery, S.K., Palo, S.E., and Aso, T., 1994: Hemispheric properties of the two-day wave from mesosphere-lower-thermosphere radar observations. *J. Atmos. Terr. Phys.* **56**, 1279 - 1288.

Dameris, M., 1988: Investigation of the influence of the equatorial quasi-biennal oscillation on the evolution of stratospheric warmings using a three-dimensional circulation model. *Beitr. Phys. Atmosph.* **61**, 355 - 366.

Dameris, M., and Ebel, A., 1990: The quasi-biennial oscillation and major stratospheric warmings: A three-dimensional model study. *Ann. Geophysicae* **8**, 79 - 86.

Dickinson, R.E., 1968: Planetary Rossby waves propagating vertically through weak westerly wind wave guides. *J. Atmos. Sci.* **25**, 984 - 1002.

Espy, P.J., Stegman, J., and Witt, G., 1997: Interannual variations of the quasi-16-day oscillation in the polar summer mesospheric temperature. *J. Geophys. Res.* **102**, 1983 - 1990.

Forbes, J.M., Hagan, M.E., Miyahara, S., Vial, F., Manson, A.H., Meek, C.E., and Portnyagin, Yu.I., 1995: Quasi 16-day oscillation in the mesosphere and lower thermosphere. *J. Geophys. Res.* **100**, 9149 - 9163.

Grollmann, Th., 1992: Wechselwirkung freier Moden, Gezeiten und Schwerewellen in der mittleren Atmosphäre. *Mitt. Inst. f. Geophys. u. Meteorol. d. Univ. Köln* **84**, 141 p.

Holton, J.R., 1984: The generation of mesospheric planetary waves by zonally asymmetric gravity wave breaking. *J. Atmos. Sci.* **41**, 3427 - 3430.

Jacobi, Ch., Schminder, R., and Kürschner, D., 1996a: On the influence of the stratospheric quasi-biennial oscillation on the mesopause zonal wind over Central Europe. *Meteorol. Zeitschrift, N.F.* **5**, 218 - 223.

Jacobi, Ch., Schminder, R., and Kürschner, D., 1996b: Long-period (2-18 days) oscillations of mesopause winds at Collm. In: A. Raabe, J. Heintzenberg (Hrsg.): Meteorologische Arbeiten aus Leipzig II. *Wiss. Mitt. des LIM und des IFT* **4**, Leipzig, 131 - 143.

Jacobi, Ch., Schminder, R., and Kürschner, D., 1997a: Measurements of mesopause region winds over Central Europe from 1983 through 1995 at Collm, Germany. Beitr. Phys. Atmosph. **70**, 181 - 200.

Jacobi, Ch., Schminder, R.., and Kürschner, D., 1997b: Planetary wave activity obtained from long-term (2-18 days) variations of mesopause region winds over Central Europe (52°N, 15°E). *J. Atmos. Solar-Terr. Phys.*, accepted.

Jacobi, Ch., Schminder, R., and Kürschner, D., 1997c: The quasi two-day wave as seen from D1 LF wind measurements over Central Europe (52°N, 15°E) at Collm. *J. Atmos. Solar-Terr. Phys.* **59**, 1277 - 1286.

Kürschner, D., 1975: Konzeption und Realisierung eines vollautomatischen Registriersystems zur Durchführung von nach der D1-Methode angelegten Routinebeobachtungen ionosphärischer Driftparameter am Observatorium Collm. *Z. Meteorol.* **25**, 218 - 221.

Kürschner, D., 1991: Ein Beitrag zur statistischen Analyse hochatmosphärischer Winddaten aus bodengebundenen Messungen. *Z. Meteorol.* **41**, 262 - 266.

Kürschner, D., and Schminder, R., 1986: High-atmosphere wind profiles for altitudes between 90 and 110 km obtained from D1 LF measurements over Central Europe in 1983/1984. *J. Atmos. Terr. Phys.* **48**, 447 - 453.

Kürschner, D., Schminder, R., Singer, W., and Bremer, J., 1987: Ein neues Verfahren zur Realisierung absoluter Reflexionshöhenmessungen an Raumwellen amplitudenmodulierter Rundfunksender bei Schrägeinfall im Langwellenbereich als Hilfsmittel zur Ableitung von Windprofilen in der oberen Mesopausenregion. *Z. Meteorol.* **37**, 322 - 332.

Labitzke, K., and van Loon, H., 1992: On the association between the QBO and the extratropical stratosphere. *J. Atmos. Terr. Phys.* **54**, 1453 - 1463.

Labitzke, K., and van Loon, H., 1996: On the stratosphere, the QBO, and the sun: the winter of 1995-1996. *Meteorol Z., N.F.* **5**, 166 - 169.

Lastovicka, J., 1993: Planetary wave activity in the upper middle atmosphere inferred from radio wave absorption and the quasi-biennial oscillation. *Ann. Geophysicae* **11**, 820 - 827.

Manson, A.H., Meek, C.E., Teitelbaum, H., Vial, F., Schminder, R., Kürschner, D., Smith, M.J., Fraser, G.J., and Clark, R.R., 1989: Climatologies of semi-diurnal and diurnal tides in the middle atmosphere (70 - 110 km) at middle latitudes (40 - 55°). *J. Atmos. Terr. Phys.* **51**, 579 - 593.

Meek C.E., Manson, A.H., Franke, S.J., Singer, W., Hoffmann, P., Clark, R.R., Tsuda, T., Nakaura, T., Tsutsumi, M., Hagan, M., Fritts, D.C., Isler, J., and Portnyagin, Yu.I., 1996: Global study of northern hemisphere quasi-2-day events in recent summers near 90 km altitude. *J. Atmos. Terr. Phys.* **58**, 1401 - 1411.

Miyahara, S., Portnyagin, Yu.I., Forbes, J.M., and Solovjava, T.V., 1991: Mean zonal acceleration and heating of the 70- to 100-km region. *J. Geophys. Res.* **96**, 1225 - 1238.

Muller, H.G., 1972: Long-period wind oscillations. *Phil. Trans. Roy. Soc.* **A272**, 585 - 598.

Muller, H.G., and Nelson, L., 1978: A travelling quasi 2-day wave in the meteor region. *J. Atmos. Terr. Phys.* **40**, 761 - 766.

Namboothiri, S.P., Meek, C.E., and Manson, A.H., 1994: Variations of mean winds and solar tides in the mesosphere and lower thermosphere over time scales ranging from 6 months to 11 yr: Saskatoon, 52°N, 107°W. *J. Atmos. Terr. Phys.* **56**, 1313 - 1325.

Naujokat, B., 1986: An update of the observed quasi-biennial oscillation of the stratospheric winds over the tropics. *J. Atmos. Sci.* **43**, 1873 - 1877.

Naujokat, B., Labitzke, K., Lenschow, R., Rajewski, B., Wiesner, M., and Wohlfart, R.-C., 1995: The stratospheric winter 1994/95: A cold winter with a strong minor warming. *Beilage zur Berliner Wetterkarte* SO **24/95**, 24p.

Plumb, R.A., 1983: Baroclinic instability of the summer mesosphere: a mechanism for the quasi-two-day wave ? *J. Atmos. Sci.* **40**, 262 - 270.

Pfister, L., 1985: Baroclinic instability of easterly jets with applications to the summer mesosphere. *J. Atmos. Sci.* **42**, 313 - 330.

Rodgers, C.D., 1976: Evidence for the five-day wave in the upper stratosphere. *J. Atmos. Sci.* **33**, 710 - 711.

Salby, M.L., 1981a: Rossby normal modes in nonuniform background configurations. Part II: Equinox and solstice conditions. *J. Atmos. Sci.* **38**, 1827 - 1840.

Salby, M.L., 1981b: The 2-day wave in the middle atmosphere: Observations and theory. *J. Geophys. Res.* **86**, 9654 - 9660.

Salby, M.L., and Roper, R., 1980: Long-period oscillations in the meteor region. *J. Atmos. Sci.* **37**, 237 - 244.

Salby, M.L., Hartmann, D.L., Bailey, P.L., and Gille, J.C., 1984: Evidence for equatorial Kelvin modes in Nimbus-7 LIMS. *J. Atmos. Sci.* 41, 220 - 235.

Schminder, R., and Kürschner, D., 1988: Mean winds and tides in the 85- to 110-km region over Central Europe in 1983 - 1986. *J. Geophys. Res.* **93**, 2493 - 2497.

Schminder, R., and Kürschner, D., 1992: Höhen-Zeit-Schnitte der Windfelder (Grund- und Gezeitenwind) zwischen 85 und 105 km Höhe über Mitteleuropa für 1990 aus funktechnischen D1-Windmessungen am Observatorium Collm. *Kleinheubacher Berichte* **35**, 137 - 145.

Schminder, R., and Kürschner, D., 1994: Permanent monitoring of the upper mesosphere and lower thermosphere wind fields (prevailing and semidiurnal tidal components) obtained from LF D1 measurements in 1991 at the Collm Geophysical Observatory, *J. Atmos. Terr. Phys.* **56**, 1263 - 1269.

Sprenger, K., and Schminder, R., 1967: Evidence of a 26-month wind oscillation in the lower ionosphere over Central Europe. *Z. Meteorol.* **19**, 168 - 170.

Sprenger, K., Greisiger, K.M., and Schminder, R., 1975: Evidence of quasi-biennial wind oscillation in the mid-latitude lower thermosphere, obtained from ionospheric drift measurements in the LF range. *J. Atmos. Terr. Phys.* **37**, 1391 - 1393.

Thayaparan, T., Hocking, W.K., and MacDougall, J., 1997: Amplitude, phase, and period variations of the quasi 2-day wave in the mesosphere and lower thermosphere over London, Canada (43°N, 81°W), during 1993 and 1994. *J. Geophys. Res.* **102**, 9461 - 9478.

Tsuda, T., Kato, S., and Vincent, R.A., 1988: Long-period wind oscillations observed by the Kyoto meteor radar and comparison of the quasi-2-day wave with Adelaide HF radar observations. *J. Atmos. Terr. Phys.* **50**, 225 - 230.

Tung, K.K., and Yang, H., 1994: Global QBO in circulations and ozone. Part I: Reexamination of observational evidence. *J. Atmos. Sci.* **51**, 2699 - 2707.

Vincent, R.A., 1993a: Low frequency dynamics of the equatorial mesosphere. In: Thrane, E.V., Blix, T.A., Fritts, D.C. (Eds.): Coupling processes in the lower and middle atmosphere. *NATO ASI Series* Vol. **387**. Kluver, Dordrecht, 125 - 135.

Vincent, R.A., 1993b: Long-period motions in the equatorial mesosphere. *J. Atmos. Terr. Phys.* **55**, 1067 - 1080.

Williams, C.R., and Avery, S.K., 1992: Analysis of long-period waves using the mesosphere-stratosphere-troposphere radar at Poker Flat, Alaska. *J. Geophys. Res.* **97**, 855- 861.

Christoph Jacobi
Institut für Meteorologie - Universität Leipzig
Stephanstr. 3
04103 Leipzig

Rossby wave propagation in a bounded ocean current

Uwe Harlander, Werner Metz

Zusammenfassung

Die Ausbreitungspfade und die strukturelle Veränderung von quasi-geostrophischen Rossby-Wellenpaketen werden mittels der WKB-Methode untersucht. Es wird angenommen, daß die Wellenpakete an einem in Ost-West-Richtung verlaufenden festen Rand reflektiert werden können. Die Dynamik der Rossby-Wellenpakete wird auf der β-Ebene aber auch auf der sogenannten δ-Oberfläche—-wo auch die zweite Ableitung des Coriolis-Parameters eine Rolle spielt—-studiert. Es wird gezeigt, daß die Wellenpakete unter bestimmten Umständen große Entfernungen in zonaler Richtung entlang der Küste zurücklegen können und damit die Strömung weit stromab beeinflussen. Die Wellenpakete sind dabei zwischen dem reflektierenden Rand und einer Umkehrbreite gefangen im Unterschied zu freien Rossbywellen in der Atmosphäre, die zwischen zwei Umkehrbreiten gefangen werden können. Es zeigt sich, daß der δ-Term keine besonders wichtige Rolle für die Ausbreitung der Rossby-Wellenpakete spielt, am wichtigsten ist er noch bei der Dynamik von Wellen mit negativer Phasengeschwindigkeit. Es wird vorgeschlagen, daß ein selektiver Rossby-Wellenleiter wie er hier diskutiert wird eine Rolle in der Dynamik des Antarktik-Zirkumpolarstromes spielt.

Abstract

We study the propagation and the structural change of quasi-geostrophic Rossby wave packets by means of a WKB-method. Our approach involves the introduction of a rigid boundary, where the wave packets can be reflected elastically. We study Rossby wave packet dynamics at high latitudes on a modified β-plane, where the second derivative of the Coriolis parameter with respect to latitude is taken into account (δ-term). We show that under certain conditions synoptic-scale wave packets can propagate far distances along an east-west oriented "coast" and may affect the flow far downstream of the source region. In contrast to free propagating Rossby wave packets (e.g. in the atmosphere), which can be trapped between two turning latitudes, the wave packets considered here are trapped between a turning latitude and the reflecting boundary. It turns out that the δ-term is most important for wave packets with negative phase speeds. Finally, we suggest that such a selective Rossby waveguide may play a role in the dynamics of the Antarctic Circumpolar Current.

1 Introduction

Rossby waveguides are latitude belts where locally excited stationary Rossby wave packets in a zonal mean basic flow are captured between two turning latitudes and thus able to propagate long distances in a zonal direction. In the framework of the linear ray tracing theory (cf. e.g. Hoskins and Karoly, 1981, or Hoskins and Ambrizzi, 1993, HA) in the atmosphere such waveguides are associated with local maxima (with respect to latitude) of the total wavenumber and turning latitudes are found where the zonal wavenumber equals the total wavenumber. Normally, when considering observed atmospheric zonally symmetric basic states (e.g. 300 mb) any local maxima of the stationary wavenumber (the total wavenumber for stationary waves) seems to be not pronounced enough to be able to act as a waveguide (James 1988). Therefore, the waveguide concept has been applied to an asymmetric environment, i.e. a basic state that varies also in the zonal direction although the strict validity of the linear ray theory is here in doubt (Karoly 1983). However, it has been shown that the concept remains a valuable interpretation tool in this case, too. In particular, HA, Ambrizzi et al. (1995) and Ambrizzi and Hoskins (1997) have integrated linear barotropic and baroclinic models on the sphere with a zonally asymmetric basic state and found that many of the preferred Rossby wave propagation paths in their model integrations tended to follow "local" waveguides, where the latter were defined using local values of the basic state.

In this short note we shall envisage some simple variation of the Rossby waveguide concept, where a waveguide is confined not within two turning latitudes, but within one turning latitude and one reflecting wall. Clearly, such a configuration will hardly be relevant for the large-scale atmospheric flow, however, a natural application could be the flow in the southern polar ocean with Antarctica as its southern boundary. Rossby wave propagation in the ocean has already been studied previously; e.g. Chang and Philander (1989) documented the existence of an equatorial waveguide for Rossby waves with a zonal wavelength of about 1000 km. Also a coastal waveguide for gravity water waves with reflection at the coast and a turning near the coastline has been studied, e.g. by Craik 1985. However, the possible existence of a Rossby waveguide in a strong polar current with reflection at the coastline appears not to have been considered before.

We shall investigate the problem by applying the simplest model appropriate for that purpose, namely the quasi-geostrophically scaled shallow water model of Pedlosky (1987) on a polar β-plane. To achieve a more realistic approximation of the effects of the sphericity of the earth in high southern latitudes, we retain also the second order term in the Taylor series expansion of the Coriolis parameter. Such a modified β-plane has been introduced by Yang (1988, 1991) who called it "δ-surface". While the dynamical effects of this modification is in general small for typical atmospheric flows, we shall show that it can become important for strong oceanic currents at high latitudes.

To be more precise, we will study the propagation of oceanic Rossby wave packets on the modified β-plane which is bounded to the south by a rigid wall but of infinite extend

in the northward and east-west directions. The equation governing our problem is the linearized barotropic quasi-geostrophic potential vorticity equation. To keep things as simple as possible we assume a basic state $\bar{U} = \bar{U}(y)$. We follow then Yang (1991) in the application of the WKB method[1] derive equations for the wave packet path and the associated changes of the local wavenumbers and frequency on the modified β-plane. Note, however, that the theory can be readily modified to deal also with a more general basic state. Using a basic state $\bar{U} = \bar{U}(y)$ implies that the local frequency and zonal wavenumber are conserved along a ray path and makes our analysis formally similar to the atmospheric Rossby wave propagation studies of e.g. Hoskins and Karoly (1981) or Hoskins and Ambrizzi (1993). However, in contradistinction to these studies we apply the modified β-plane geometry and place a rigid wall at the southern boundary of the integration domain. Furthermore, we shall study not only the propagation of stationary Rossby waves but also that of waves of non-zero frequency. Such a proceeding appears to be resonable in view of the fact that the mechanism that exites the Rossby wave packets is rather unspecified and in view of significant differences among atmospheric Rossby wave packets of zero, positive and negative frequencies reported recently by Yang and Hoskins (1996).

For reasonable profiles of the basic flow the placement of a rigid southern boundary clearly forces a Rossby waveguide along this boundary. The purpose of the present note is to investigate how the structure of this waveguide depends on the model parameters, e.g., on the δ-term or the frequency of the waves.

The paper is organized as follows. In section 2 we first briefly recapitulate the quasi-geostrophic scaling of the shallow-water equations with particular emphasis on the occurrence of the δ-term. We present then the wave packet equations resulting from the application of the WKB method to the linearized quasi-geostrophic potential vorticity equation. We also discuss the boundary conditions implied by the rigid wall. In section 3 some Rossby wave paths are explicitely computed and the dependence of the waveguide on different basic states and the δ-effect is investigated. In section 4 we discuss our results and drawn some conclusions.

2 Model

In this section we first briefly discuss the relevance of the so-called δ-term in thc quasi-geostrophic vorticity equation. Then we derive the wave packet equations and discuss finally the boundary conditions required.

2.1 Quasi-geostrophic scaling of the shallow-water equations

As pointed out in the introduction we are concerned with a high-latitude flow on a modified β-plane where the β-term alone may not be sufficient to provide an adequate

[1] In recognition of Wenzel, Kramers and Brillouin. Sometimes also called BKW or WKBJ (by adding J for Jeffreys) or LG method (for Liouville and Green). For more details see the historical notes of Olver (1997).

representation of the effects of sphericity of the earth. Therefore, we retain the second term in the Taylor-series expansion of the Coriolis parameter on this β-plane and write:

$$f \approx \gamma f_0 + \beta_0 L y - \frac{1}{2}\gamma f_0 \frac{L^2}{a^2} y^2 \quad , \tag{1}$$

where $f_0 = 2\Omega \sin \mid \phi_0 \mid$, $\gamma = 1$ for the northern and $\gamma = -1$ for the southern hemisphere, respectively, $\beta_0 = 2\Omega/a \cos \phi_0$, L is a length scale and y the dimensionless meridional coordinate. ϕ_0 is the tangential latitude of the β-plane and the other symbols have their conventional meanings. Note that (1) approximates the Coriolis parameter as a quadratic function of the dimensionless y-coordinate. Proceeding as in the classical quasi-geostrophic scaling of the shallow-water equations (Pedlosky 1987), i.e. using a velocity scale U and a time scale L/U the quasi-geostrophic vorticity equation is obtained from the $\mathcal{O}(\epsilon_R^1)$-problem after expanding the (dimensionless) variables in a power series in the small parameter ϵ_R, namely the Rossby number

$$\epsilon_R = \frac{U}{f_0 L} \quad . \tag{2}$$

Here, we focus on the Coriolis term as it occurs for example in the dimensionless zonal momentum equation

$$\epsilon_R \frac{\partial u}{\partial t} + \cdots + \left(\gamma + \beta y - \gamma \frac{\delta}{2} y^2\right) v = \cdots \quad , \tag{3}$$

where the dots represent the remaining terms in the equation which are not relevant for our purposes. Here, $\beta = \beta_0 L/f_0$ and $\delta = L^2/a^2$. Clearly, δ must be of the same order as β, namely of $\mathcal{O}(\epsilon_R)$ to be retained in the $\mathcal{O}(\epsilon_R^1)$-problem, i.e. in the quasi-geostrophic vorticity equation.

We consider here large-scale flow systems, hence we assume that $L = 10^6 m$ which implies $\delta \approx 10^{-2}$. Under usual midlatitude atmospheric conditions $U = 10 m s^{-1}$, $f_0 = 10^{-4} s^{-1}$ and $\epsilon_R = 0.1$. Thus, δ is at most of $\mathcal{O}(\epsilon_R^2)$ and can be neglected. The same is also true for high-latitude atmospheric flow. If, however, we assume a large-scale high-latitude oceanic flow with $U = 1 m s^{-1}$ then the Rossby number decreases to 10^{-2} and thus $\delta = \mathcal{O}(\epsilon_R)$ and the δ-term should be retained. Even in this case, however, β is still larger than δ but for polar regions we may assume $\beta = \mathcal{O}(\epsilon_R)$.

Note that e.g. observations of the austral winter mean surface circumpolar current around Antarctica (Peixoto and Oort, 1992) suggest that the assumption of $U = 1 m s^{-1}$ must not be entirely unrealistic.

2.2 WKB solution of the quasi-geostrophic vorticity equation

Assuming a (geostrophic) zonally symmetric basic flow $\bar{U}$ that depends only on the y-coordinate, the linearized (dimensionless) quasi-geostrophic potential vorticity equation

for the perturbation streamfunction ψ_0 is written as

$$\left(\frac{\partial}{\partial t}+\bar{U}\frac{\partial}{\partial x}\right)(\nabla^2\psi_0 - F\psi_0) + B_1\frac{\partial\psi_0}{\partial x} = 0 \quad , \tag{4}$$

with

$$B_1 = F\bar{U} + \bar{\beta} - \gamma\bar{\delta}y - \frac{\partial^2\bar{U}}{\partial y^2} \quad , \tag{5}$$

where ψ_0 is the $\mathcal{O}(\epsilon_R^0)$ streamfunction, $\bar{\beta} = \frac{\beta}{\epsilon_R} = \mathcal{O}(1)$, $\bar{\delta} = \frac{\delta}{\epsilon_R} = \mathcal{O}(1)$ and all the other symbols have their conventional meanings. Note that we have included in (4) the effects of an upper free surface ("Froude"-parameter $F = f_0^2L^2/gD = \mathcal{O}(1)$), where D is the vertical scale height. Except for the δ-term (4) is of standard form.

We restrict our discussion to the case where $\bar{U}$ and B_1 vary in such a way (cf. Appendix B) that we may apply the WKB method to the quasi-geostrophic potential vorticity equation (QGV). Following e.g. Yang (1991) (see Appendix A) we may write the equations describing the ray of propagation and the change of the local frequency and the local wavenumbers of a quasi-geostrophic Rossby wave packet:

$$\sigma = \bar{U}m - \frac{m}{K^2}B_1 \quad , \tag{6}$$

$$C_{gX} =: \frac{D_gX}{DT} = \bar{U} - K^{-4}B_1\left(n^2 - m^2 + F\right) \quad , \tag{7}$$

$$C_{gY} =: \frac{D_gY}{DT} := K^{-4}2nmB_1 \quad , \tag{8}$$

$$\frac{D_g\sigma}{DT} = 0 \quad , \tag{9}$$

$$\frac{D_gm}{DT} = 0 \quad , \tag{10}$$

$$\frac{D_gn}{DT} = -\left(m\frac{\partial\bar{U}}{\partial Y} - \frac{m}{K^2}\frac{\partial B_1}{\partial Y}\right) \quad , \tag{11}$$

with

$$B_1 = F\bar{U} + \bar{\beta} - \gamma\bar{\delta}\frac{Y}{\epsilon} - \epsilon^2\frac{\partial^2\bar{U}}{\partial Y^2} \quad , \tag{12}$$

where $T = \epsilon t$, $X = \epsilon x$, $Y = \epsilon y$ are "slow" variables with $\epsilon = 0.1$ (see Appendix A), $\frac{D_g}{DT} := \frac{\partial}{\partial T} + C_{gX}\frac{\partial}{\partial X} + C_{gY}\frac{\partial}{\partial Y}$, $K^2 = m^2 + n^2 + F$ and σ, m and n denote the local frequency and the local wavenumbers in zonal and meridional direction, respectively.

We consider a half plane, i.e. an in east-west and north direction infinite extended domain which is bounded at $Y = -0.2$ (dimensional $y^* = -2000km$) by a rigid wall. At this latitude Rossby wave propagation is allowed in all direction except to the south. Hence we assume Rossby wave reflection at the southern boundary at $Y = -0.2$. It is well known (e.g. Pedlosky 1987) that the energy flux vector of the Rossby wave packet bounces off the wall elastically, i.e., with angle of reflection equal to angle of incidence for the energy and wave packet trajectory. A helpful geometrical representation of the reflection process was introduced by Longuet-Higgins (1964) and Pedlosky (1987).

Table 1: **Different experiments described in the text. Here y_t denotes the turning latitude (computed in Appendix B from $q(y_t) = 0$), x_R denotes the distance of two reflection points and t_R denotes the time a wave packet needs to propagate from one reflection point to the next.**

	$\bar{U}$	U_0	F	β	δ	m	$n(0)$	$2\pi/\sigma[year]$	$y_t[km]$	$x_R[km]$	$t_R[day]$
E1	eq.(17)	0.5	1	5	1	2	12.08	0	900	13100	360
E2	eq.(17)	0.5	1	5	1	2	4.5	-1	600	10200	172
E3	eq.(18)	1	1	5	1	3	11.98	0	-1100	2500	530
E4	eq.(18)	1	1	5	1	3	4.75	-1	-1150	1650	165
E5	eq.(18)	1	1	5	1	3	2.85	-0.5	-1350	1480	105

For the reflection at an east-west oriented boundary it can be shown that the zonal wavenumber is conserved, but the meridional wavenumber reverses its sign. Thus the following conditions for the wavenumber and group velocity changes at the boundary are implied:

$$m_r = m_i \quad , \tag{13}$$

$$n_r = -n_i \quad , \tag{14}$$

$$C_{gXr} = C_{gXi} \quad , \tag{15}$$

$$C_{gYr} = -C_{gYi} \quad . \tag{16}$$

Here, "reflection" and "incidence" is indicated by "r" and "i", respectively.

3 Results

In this section we investigate the solution of (7)-(11) together with the boundary conditions (13)-(16) for different basic flow profiles and local frequencies. Thereby we focus on the Rossby wave propagation properties in sheared high-latitude westerly ocean currents where β becomes smaller than in middle latitudes and the second derivative of the Coriolis parameter becomes more important. The current is assumed to be i) bounded at its southern side by a rigid east-west oriented boundary and ii) situated in the southern hemisphere (i.e. $\gamma = -1$ in (12)).

In the experiments performed two different basic flows are used, i) a linear flow profile

$$\bar{U} = \frac{U_0}{\epsilon} Y + 1.02 \tag{17}$$

and ii) a jet-like basic flow profile

$$\bar{U} = U_0 \exp\left\{ -\left(\frac{Y}{\epsilon}\right)^2 \right\} \quad , \tag{18}$$

where U_0 is constant.

The order of magnitude of the different effects considered are

$$\bar{U} \sim \mathcal{O}(1) \quad , \quad F \sim \mathcal{O}(1) \quad , \quad \bar{\beta} \sim \mathcal{O}(1) \quad , \quad \bar{\delta} \sim \mathcal{O}(1) \quad . \tag{19}$$

It is worth to mention that the specific setting of U_0, F, $\bar{\beta}$ and $\bar{\delta}$ of the experiments performed (cf. Table 1) is consistent with these order of magnitudes. As shown in Tab. 1 we assumed that the β-effect is half as strong than in middle latitudes and that the δ-effect is five times smaller than the β-effect. The use of $U_0 = 0.5$ in experiment E1 and E2 corresponds to a velocity gradient of $1ms^{-1}/2000km$ and $U_0 = 1$ in experiment E3, E4 and E5 corresponds to a maximal jet velocity of $1ms^{-1}$ 2000km north of the "coast".

Note that the WKB concept for studying Rossby wave dynamics is suitable only for qualitative statements and does not allow for quantitative discussions, at least in geophysical applications. The range of validity of the WKB approximation for the parameters used in Tab. 1 is given in Appendix B.

3.1 Critical lines and turning latitudes

From (6) the total wavenumber for a purely zonal only y-dependent basic flow is given by

$$K_\sigma^2 := m^2 + n^2 = \frac{B_1}{\bar{U} - \sigma/m} - F \quad . \tag{20}$$

Thus, Rossby wave propagation is possible only when the total wavenumber is real. A critical line is defined as a region where K_σ (or $q(Y)$ as defined in Appendix B) tends to infinity, i.e. where $\sigma = \bar{U}m$. According to linear theory, it will take a wave packet an infinite time to reach a critical line, which will act as something of a "black hole" to Rossby wave information (James 1994). When nonlinear effects are considered, too, Killworth and McIntyre (1985) showed that under quite general conditions a critical line could absorb only a finite amount of wave activity, and so must act as a perfect reflector in the long time average.

Usually, Rossby wave packets are refracted towards higher values of K_σ and a turning latitude is approached when $n = 0$ and $K_\sigma^2 = m^2$ (or $q(Y) = 0$ as defined in Appendix B), respectively (cf. Hoskins and Ambrizzi 1993, Yang and Hoskins 1996). Note that neither at the critical lines nor at the turning latitudes WKB-solutions are valid (cf. Appendix B).

In Fig. 1 a) we plot the turning latitude as a function of the zonal wavenumber for experiment E1 with (black line) and without the δ-term (grey line) to study the combined effect of the meridional shear and the δ-effect on the position of the turning latitude. In this most simple situation E1, long waves can propagate far to the north, whereas short waves are strongly trapped and hardly leave the "coast". It can be shown that no turning latitude exists for waves with $m < 1.5$ if the δ-term is present. On the other hand, without the δ-term almost all waves have a turning latitude, even if very far to the north (not shown). Fig. 1 b) shows the position of the turning latitude when

the jet-like basic flow profile is used (E3). Now long waves can leave the current and may reach regions with a very weak basic flow to the north of the jet. Wave packets excited near the rigid boundary with zonal wavenumbers larger than three are trapped between the "coast" and the turning latitude, whereas waves excited to the north of the jet center cannot propagate far in the zonal direction since they are not trapped. As shown in Figs. 1 a) and b) the δ-effect does not change the situation fundamentally.

The δ-effect becomes more important when non-stationary wave packets are considered. Fig. 1 c) shows the position of the turning latitudes for waves with a period of 0.5years and a negative phase speed (E5 of Table 1). Now the waveguide south of the jet center is more selective than in the stationary case, i.e. only waves in a relatively small wavenumber range are trapped; the δ-term enhances this wavenumber selection.

3.2 Rays of propagation

In this section we present examples of rays of Rossby wave propagation for the different basic flow profiles used and for different phase speeds. Note that a linear dependence of $\bar{U}$ from Y decouples the meridional wavenumber evolution from the Rossby wave path. Therefore (11) can be computed independenly from the actual path and thus can be considered as a single ordinary non-linear differential equation. In that case the "independence theorem", first mentioned by Yang (1991), is valid. However, only when a rigid ocean surface is assumed ($F = 0$), closed analytical solutions to (7),(8) and (11) can be found. Hence, we solve the equations by using a forth order Runge-Kutta scheme and use in all experiments a small WKB-number of $\epsilon = 0.1$ (see Appendix A).

In E1 and E2 the parameter U_0 corresponds to a shear of $\frac{0.5ms^{-1}}{1000km}$ — a value observable e.g. in some regions of the ACC (Nowlin and Klinck 1986) — and $m = 2$ corresponds to a zonal wavelength of 3000km. As initial conditions we always apply $X(0) = 0$ and $Y(0) = -0.2$ (dimensional $y^* = -2000km$). The local frequency σ (given in Table 1) can easily be computed from (6) when the boundary condition for $\bar{U}$, the initial meridional wavenumber $n(0)$ and the constant zonal wavenumber m is used.

Besides stationary Rossby waves we also computed some rays of Rossby waves with non-zero frequency. A plausible physical mechanism for the occurrence of non-zero frequency Rossby waves is e.g. a fluctuating current over an ocean ridge (Yang and Hoskins 1996). Note that only negative frequencies are considered although a "topographic wavemaker" would also cause oscillations with a positive phase speed. The restriction to negative frequencies is justified because for the parameters used only highly trapped short waves with large wavenumbers can propagate with a positive phase speed near the reflective wall. In Fig. 2 we plot n^2 as a function of m for $\sigma = \frac{2\pi}{-1\text{year}}$, $\sigma = \frac{2\pi}{-0.5\text{year}}$, $\sigma = \frac{2\pi}{1\text{year}}$ and $\sigma = \frac{2\pi}{0.5\text{year}}$ along the boundary at $Y = -0.2$. Clearly, Rossby wave propagation and also Rossby wave reflection is only possible when $n^2 > 0$. From Fig. 2 we find that for negative frequencies, waves with a relatively large zonal wavelength can be reflected at the rigid boundary whereas for positive frequencies only short Rossby waves with zonal wavenumbers in the shaded intervalls can propagate.

Furthermore, critical lines are located at the boundary for zonal wavenumber 11 (21) for waves with $\sigma = \frac{2\Pi}{1\text{year}}$ ($\sigma = \frac{2\Pi}{0.5\text{year}}$). As we are only interested in larger scale waves which can be reflected at the boundary and propagate larger distances away from the "coast" we don't consider waves with positive phase speeds.

The different frequencies used are given in Table 1 and correspond to periods of the order 0.5-1 year. In that frequency range the zonal phase speeds are comparable to the basic flow speeds $500km$ to the north of the boundary and the non-zero frequencies of the Rossby wave packets can be expected to influence their propagation. The associated zonal phase speeds are $c = -0.1m\,s^{-1}$ in E2, $c = -0.06m\,s^{-1}$ in E4 and $c = -0.13m\,s^{-1}$ in E5.

The rays of propagation between two reflection points of the experiments E1, E2, E3, E4 and the associated meridional changes of the synoptic-scale Rossby wave packets are shown in Fig. 3 a) and b). Initially, the wave packets propagate northward and the meridional wavenumbers decrease, i.e., the meridional extension of the disturbances increase. For small meridional wavenumbers the WKB-approximation is no longer valid (see Appendix B), however, when the meridional wavenumbers change their sign, the wave packets are at their turning points and from now on they propagate southward until they reach the southern boundary, where they are reflected to northern directions, and so forth. Thus, the gradient of the basic flow together with the defined boundary reflection lead to a waveguide in the current and the Rossby wave packets may propagate far distances along the "coast". Such a propagation is illustrated in Fig. 4 a). We display 7.5 complete cycles of the wave packet "oscillation" of experiment E4. The wave packet propagates in a clockwise manner from left to right. At the boundary, the meridional wavenumber change its sign instantaniously (see Fig. 4 b)) because of the defined reflection condition. Therefore the structural oscillation of the packet has a see-saw-like character. With the parameter setting of E4 it takes about 3.4 years for the wave packet to travel 12500km along the rigid wall. The maximal distance of that path from the boundary is 850km and the distance between two reflection points is about 1250km. As can be seen from Fig. 3 a) (and also from Figs. 1 a), b)), wave rays in the linear basic flow for $m = 2$ have the form of large arcs, whereas in the jet-like current the arcs for $m = 3$ are less extended. Note that zonal wavenumber 2 is no longer trapped for the jet-like profile. However, the periods the wave packets need for the propagation between two reflection points are comparable for the different basic flow profiles considered (cf. Fig 3 b)). A summary of the characteristic features (turning latitude, distance of two reflection points, period between two reflection points) of the different experiments performed is given in Table 1.

The effect of the δ-term on the paths showed is not fundamental. But generally speaking, the δ-effect can be significant (cf. Yang 1991), e.g. in regions with very weak basic flows. This can be demonstrated if we remove the rigid wall and allow the wave packets to propagate freely southward in regions with almost no basic flow. Therefore we repeated experiment E5 but without a reflecting wall. As shown in Fig. 4 c) the packet propagates far to the south but because of the δ-term it is still trapped, now between two turning latitudes. However, significance of such a waveguide in ocean

currents is questionable because the situation considered is quite unrealistic.

4 Discussion and conclusion

In the previous sections we studied the propagation of quasi-geostrophic barotropic Rossby wave packets along an east-west oriented boundary situated in the southern part of the model domain by applying the well known WKB technique. We used a purely zonal and only meridional dependent basic flow without considering topography. The study showed that under certain conditions synoptic scale Rossby wave packets on the β-plane or the δ-surface can propagate far distances away from their source region in zonal directions. Essencial for the occurrence of the waveguides discussed here is a boundary at the southern side of the flow where Rossby wave packets can be reflected. Furthermore we showed that the sphericity of the earth in polar regions can have some effect on the Rossby wave propagation properties in ocean currents. The sphericity influences not only the non-linear behavior of the wavenumbers in the so called WKB-phasespace (cf. Yang 1988, 1991), it also leads to a more selective waveguide for non-stationary waves (cf. Fig. 1 c)) and is important for the propagation of Rossby waves in almost vanishing basic flows (cf. Fig. 4 c)).

The question arises if the Rossby waveguides discussed have some relevance for the "real world". Obviously, the southern part of the ACC is a region where at least similar conditions to the one assumed here can be found (cf. Nowlin and Klinck, 1986). Therefore it is suggested that synoptic scale disturbances may affect the ACC far away from the region where the disturbances have developed.

Resently, Hughes (1996) discussed the occurrence of a waveguide for Rossby waves in the ACC of the Fine Resolution Antarctic Model (FRAM). In contrast to our study, he considered meso-scale Rossby waves trapped between two critical lines situated to the north and to the south of the jet center. Killworth and McIntyre (1985) showed, that critical lines could only absorb a finite amount of wave activity, and so must act as a perfect reflector in the long time average. Such "reflectors" cannot be described with the linear WKB concept since nonlinear processes are essential. Another crucial difference between the waves discussed by Hughes and the waves considered here is the phase speed. In our case the phase speed is either zero or negative because otherwise large-scale zonal waves cannot propagate at the boundary and a critical line can exist very close (or even northward) to the rigid wall; in that case synoptic-scale Rossby waves can not be reflected at the "coast", at least in the linear sense (see Fig. 2). It should be mentioned that the meso-scale Rossby waves discussed by Hughes can only propagate in regions where the basic flow is not to strong. For the scaling we applied in section 2.1 short Rossby waves cannot propagate near the jet center (see Fig. 3 b)).

Note that the largest meridional scale of the trapped wave packets considered here occurs when they are closest to the maximum in the jet-like zonal flow. It is known that wave packets with a small meridional scale (large meridional wavenumber) and a large zonal scale (small zonal wavenumber) can easily be absorbed by the zonal flow (Zeng 1979). In the situation considered here such an absorption is not very likely and

the disturbance may affect the flow. Furthermore, from the equivalent wave action conservation equation (Bretherton and Garrett 1968), propagation of pseudomomentum to a region of increasing intrinsic frequency $(\sigma - m\bar{U})$ will be associated with an increase in wave energy. Therefore the wave energy is at its maximum near the turning latitude where $\bar{U}$ is relatively large. This can also be shown directly by considering the $\mathcal{O}(\epsilon)$-problem of (4) (the so called amplitude equation) and the total wavenumber evolution derived from (10) and (11) (cf. Yang 1991).

Finally we should mention that one must be careful when applying the results of the previous sections to "real" geophysical flows. The WKB-method is only an approximation technique and the strict mathematical validity for the application of the theory to large scale wave packets is still in doubt (see Appendix B), even though it has been found by Hoskins and Karoly (1981) that the theory is qualitatively useful even in such situations where the WKB small number ϵ approaches unity.

A more complete discussion with a more realistic model which can also deal with a "realistic" basic flow and coastline is postponed to a forthcoming investigation to study the relationship between Rossby wave packets and the observed variability of the ACC (Meredith et al., 1996).

APPENDIX A

The WKB approximation assumes a separation between "slow" and "fast" variables. Hence we introduce the following time and space variables:

$$T = \epsilon t \quad , \quad X = \epsilon x \quad , \quad Y = \epsilon y \tag{21}$$

with $\epsilon = 0.1$ and use the WKB-ansatz

$$\psi_0 = \psi(X, Y, T, \epsilon) \exp(i\theta(X, Y, T)/\epsilon) \quad , \tag{22}$$

where

$$\psi(X, Y, T, \epsilon) = \tilde{\psi}_0(X, Y, T) + \epsilon\tilde{\psi}_1(X, Y, T) + \epsilon^2\tilde{\psi}_2(X, Y, T) + \cdots \quad , \tag{23}$$

and further we define the local frequency and the local wavenumbers in zonal and meridional direction as

$$\sigma = -\frac{\partial\theta}{\partial T} \quad , \quad m = \frac{\partial\theta}{\partial X} \quad , \quad n = \frac{\partial\theta}{\partial Y} \quad . \tag{24}$$

From this definition we have the relations

$$\frac{\partial\sigma}{\partial X} = -\frac{\partial m}{\partial T} \quad , \quad \frac{\partial\sigma}{\partial Y} = -\frac{\partial}{\partial T} \quad , \quad \frac{\partial m}{\partial Y} = \frac{\partial n}{\partial X} \quad . \tag{25}$$

Substituting (22) in (4) we obtain from the order ϵ^0 problem the dispersion relation (6) and by differentiating σ with respect to the local wavenumbers we get (7) and (8). Differentiating σ with respect to T, X and Y, respectively, using (25), (7) and (8), we find (9), (10) and (11).

APPENDIX B

Usually the slow variation of the coefficients in (4) is considered as condition for the validity of the WKB-approximation. In many situations relavant in meteorology or oceanography this slow variation is questionable. Therfore a more careful analysis is necessary to decide if the WKB-solution is an accurate approximation of the exact solution.

Let us use $\psi_0 = \tilde{\psi}(y) \exp i(mx - \sigma t)$ to transform (4) to

$$\frac{d^2\tilde{\psi}}{dy^2} - q(y)\tilde{\psi} = 0 \quad , \tag{26}$$

where

$$q(y) = \frac{\sigma(m^2 - F) - \bar{U}(m^3 + Fm) + B_1 m}{\sigma - \bar{U}m} \quad . \tag{27}$$

If we try a solution of the form $\tilde{\psi} \approx \exp(\pm \int q(y)^{1/2} dy)$ it can be found that the solution is accurate if the condition

$$\frac{1}{2} \mid \frac{q(y)'}{q(y)^{3/2}} \mid \ll 1 \tag{28}$$

holds, i.e. $q(y)$ must either be slowly varying, or else of large magnitude, or both (cf. Dingle 1973, Hoskins and Karoly 1981). However, a more accurate condition for the validity of the WKB-assumption can be found if we directly compare the orders of magnitude of two following leading terms of the WKB-expansion (cf. Holmes 1995). If we use the wave-ansatz and the transformation $Y = \epsilon y$, where $\epsilon \ll 1$, (26) reads

$$\epsilon^2 \frac{d^2\tilde{\psi}}{dY^2} - q(Y)\tilde{\psi} = 0 \quad . \tag{29}$$

Using a WKB-ansatz of the form (22) and (23) for $\tilde{\psi}$ we find from the $\mathcal{O}(1)$-problem

$$\theta(Y) = \pm \int q(Y)^{1/2} dY \quad , \tag{30}$$

and from the $\mathcal{O}(\epsilon)$-problem

$$\tilde{\psi}_0(Y) = \frac{c_1}{\theta'^{1/2}} \quad , \tag{31}$$

where c_1 is an arbitrary integration constant. Assuming $\tilde{\psi}_1(Y) = \tilde{\psi}_0(Y) W(Y)$ it follows from the $\mathcal{O}(\epsilon^2)$-problem

$$W(Y) = c_2 + \frac{1}{4}\frac{\theta''}{(\theta')^2} + \frac{1}{8}\int \frac{(\theta'')^2}{(\theta')^3} dY \quad , \tag{32}$$

where c_2 is an arbitrary constant. Now, given a small value of ϵ, the expression in (22) will be an accurate approximation of the solution, if $\epsilon\tilde{\psi}_1(Y) \ll \tilde{\psi}_0(Y)$. Therefore, using

Table 2: **Left hand side (LHS) of the validity expression for the different experiments.**

	Y_t	Y_0	Y_1	LHS(33)
E1	0.09	0.01	-0.2	0.55
E2	0.06	0.02	-0.2	0.58
E3	-0.11	-0.13	-0.2	0.51
E4	-0.115	-0.137	-0.2	0.53
E5	-0.135	-0.148	-0.2	0.54

(30), (31), (32), for the intervall $Y_0 \leq Y \leq Y_1$, we will have an accurate expression if the following holds:

$$\epsilon\Big(\mid c_2 \mid + \frac{1}{32} \mid \frac{q(Y)'}{q(Y)^{3/2}} \mid_\infty \Big(4 + \int_{Y_0}^{Y_1} \mid \frac{q(Y)'}{q(Y)} \mid dY\Big)\Big) \ll 1 \quad , \tag{33}$$

where $\mid \cdot \mid_\infty \equiv \max_{Y_0 \leq Y \leq Y_1} \mid \cdot \mid$. As might be expected, this shows that the WKB-expansion becomes nonuniform as a turning point ($q(Y_t) = 0$) is approached. The Y-component group velocity of the Rossby wave packet falls to zero at Y_t and wave energy can propagate no further in the Y-direction. A caustic forms at Y_t (the meridional wavenumber becomes zero and the mean energy density of the wave becomes infinity) and elementary wave theory breaks down. A more complete analysis (e.g. Lighthill 1978 or Holmes 1995), but still based on linear approximation, resolves the singularity and founds the solution neat Y_t to have the form of an Airy function. The waves are turned back as a reflected wave-train with equal and opposite magnitude to the incoming one and the solution beyond Y_t decays rapidly to zero.

Note that (33) can be formulated independently of the scale separation parameter ϵ if (33) is written in the "fast" variable y. Hence mathematically there is no need for discussing the scale separation; we only need to estimate the range of validity of the WKB-method via (33).

Assuming that the constant of integration does not determine the order of magnitude of (33) we computed the left hand side of the validity condition for the experiments described in section 3. The result is summarized in Table 2. Following Li and Nathan (1994) we assumed $LHS(33) \leq \mathcal{O}(0.5)$ to be sufficient for the WKB-approximation. Obviously the linear basic flow profile is the "more critical" one, i.e. the WKB-solutions break down in larger distances from the turning latitude.

References

Ambrizzi T and H.-H. Hsu 1995: Rossby wave propagation and teleconnection patterns in the Austral winter. *J. Atmos. Sci.*, **52**, 3661-3672.

Bretherton F.P. and C.J.R. Garrett 1968: Wavetrains in inhomogenious moving media. *Proc. Roy. Soc. Lond.*, **A302**, 529-554.

Chang P. and S.G.H. Philander 1989: Rossby wave packets in baroclinic mean currents. *Deep-Sea Research*, **36**, 17-37.

Craik A.D.D. 1985: *Wave interactions and fluid flows.* Cambridge University Press, 322pp.

Dingle R.B. 1973: *Asymptotic expansions: Their derivation and interpretation.* Academic Press, 521pp.

Holmes M.H. 1995: *Introduction to perturbation methods.* Texts in applied math.,**20**, Springer Verlag, 337pp.

Hoskins B.J. and D.J. Karoly 1981: The steady linear response of a spherical atmosphere to thermal and orographic forcing. *J. Atmos. Sci.*, **38**, 1179-1196.

Hoskins B.J. and T. Ambrizzi 1993: Rossby wave propagation on a realistic longitudinally varying flow. *J. Atmos. Sci.*, **50**, 1661-1671.

Hughes C.W. 1996: The antarctic circumpolar current as a waveguide for Rossby waves. *J. Phys. Oceanogr.*, **26**, 1375-1387.

James I.N. 1988: On the forcing of planetary-scale Rossby waves by Antarctica. *Q. J. Roy. Met. Soc.*, **114**, 619-637.

James I.N. 1994:*Introduction to circulating atmospheres.* Cambridge University Press, 422pp.

Karoly D.J. 1983: Rossby wave propagation in a barotropic atmosphere. *Dyn. Atmos. Oceans*, **7**, 111-125.

Li L. and T.R. Nathan 1994: The global atmospheric response to low-frequency tropical forcing: Zonally averaged basic states. *J. Atmos. Sci.*, **51**, 3412-3426.

Longuet-Higgins M.S. 1964: On group velocity and energy flux in planetary wave motions. *Deep-Sea Research*, **11**, 35-42.

Meredith, M.P., J.M. Vassie, K.J. Heywood, R. Spencer 1996: On the temporal variability of the transport through Drake Passage. *J. Geophys. Res.*, **101**, 22485-22494.

Nowlin W.D. and J.M. Klinck 1986: The physics of the Antarctic Circumpolar Current. *Rev. Geophys.*, **24**, 469-491.

Olver F.W.J. 1997: *Asymptotics and special functions.* A K Peters, 572pp.

Pedlosky J. 1987: *Geophysical fluid dynamics.* Springer Verlag, 710pp.

Yang H. 1988: Global behavior of the evolution of a Rossby wave packet in barotropic flows on the earth's δ-surface. *J. Atmos. Sci.*, **45**, 133-146.

Yang H. 1991: *Wave packets and their bifurcations in geophysical fluid dynamics.* Springer Verlag, Appl. Math. Sci. 85, 247pp.

Yang G.-Y. and B.J. Hoskins 1996: Propagation of Rossby waves of nonzero frequency. *J. Atmos. Sci.*, **53**, 2365-2378.

Zeng Q.-C. 1979: On nonlinear interaction of motion and process of rotational adaption in rotating atmosphere. *Sci. Sinica*, **22**, 945-957.

Authors: Uwe Harlander, Werner Metz, Institut für Meteorologie (LIM), Universität Leipzig, Stephanstr. 3, 04103 Leipzig

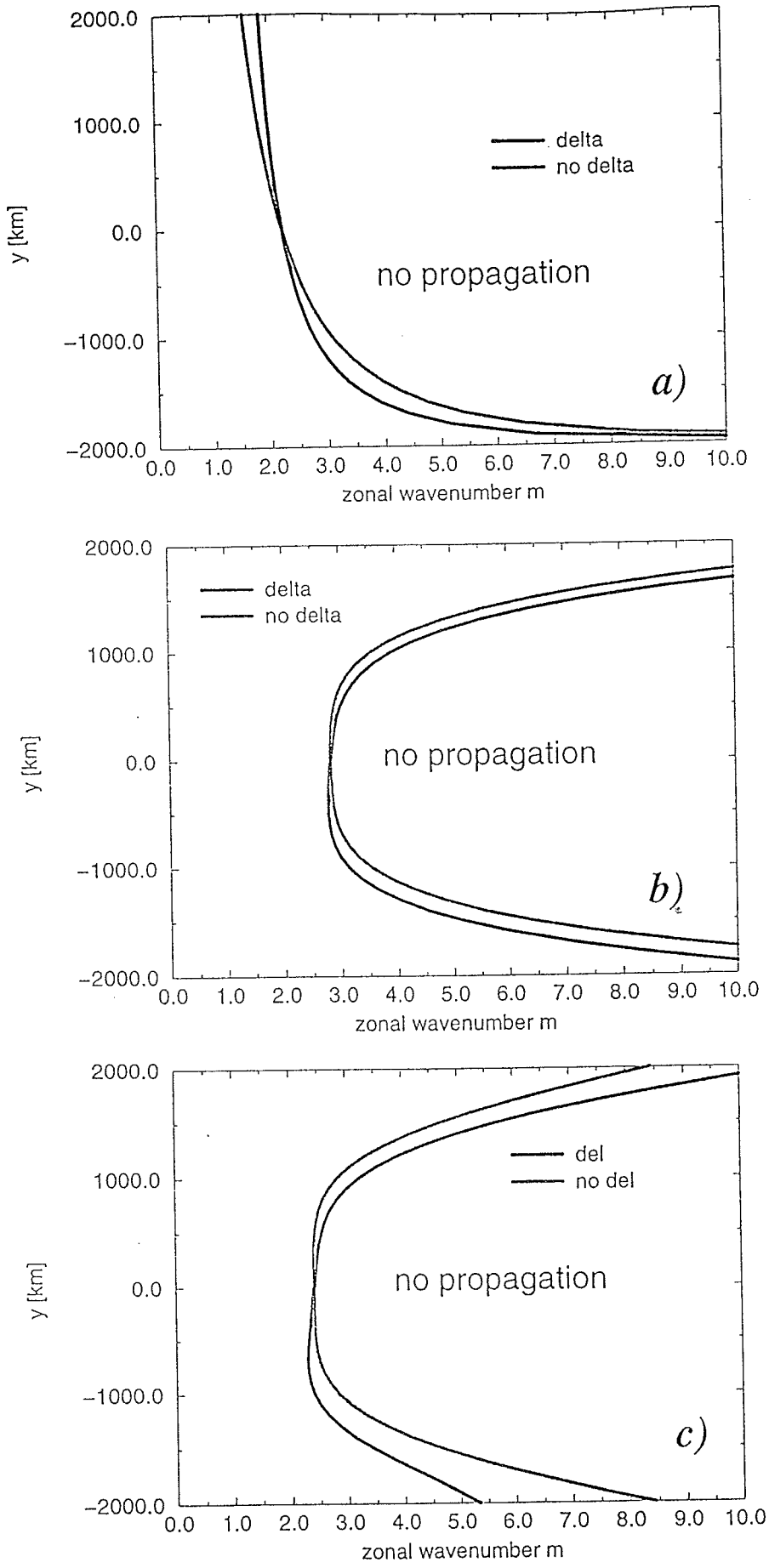

Figure 1: Turning latitude $y_t(m)$ of experiment E1 (a), of experiment E3 (b) and of experiment E5 (c) with and without the δ-term.

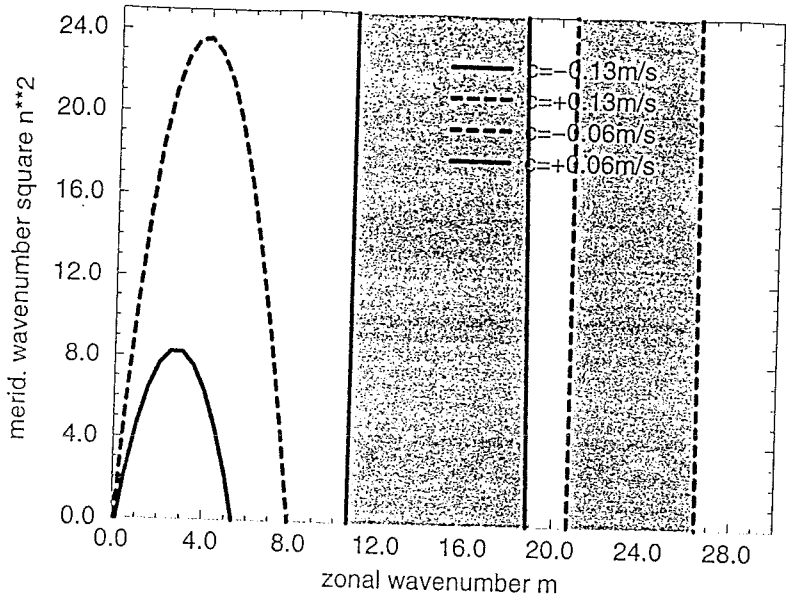

Figure 2: Square of the meridional wavenumber as a function of the zonal wavenumber along the boundary $Y = -0.2$ for the jet-like basic flow profile and different zonal wave speeds.

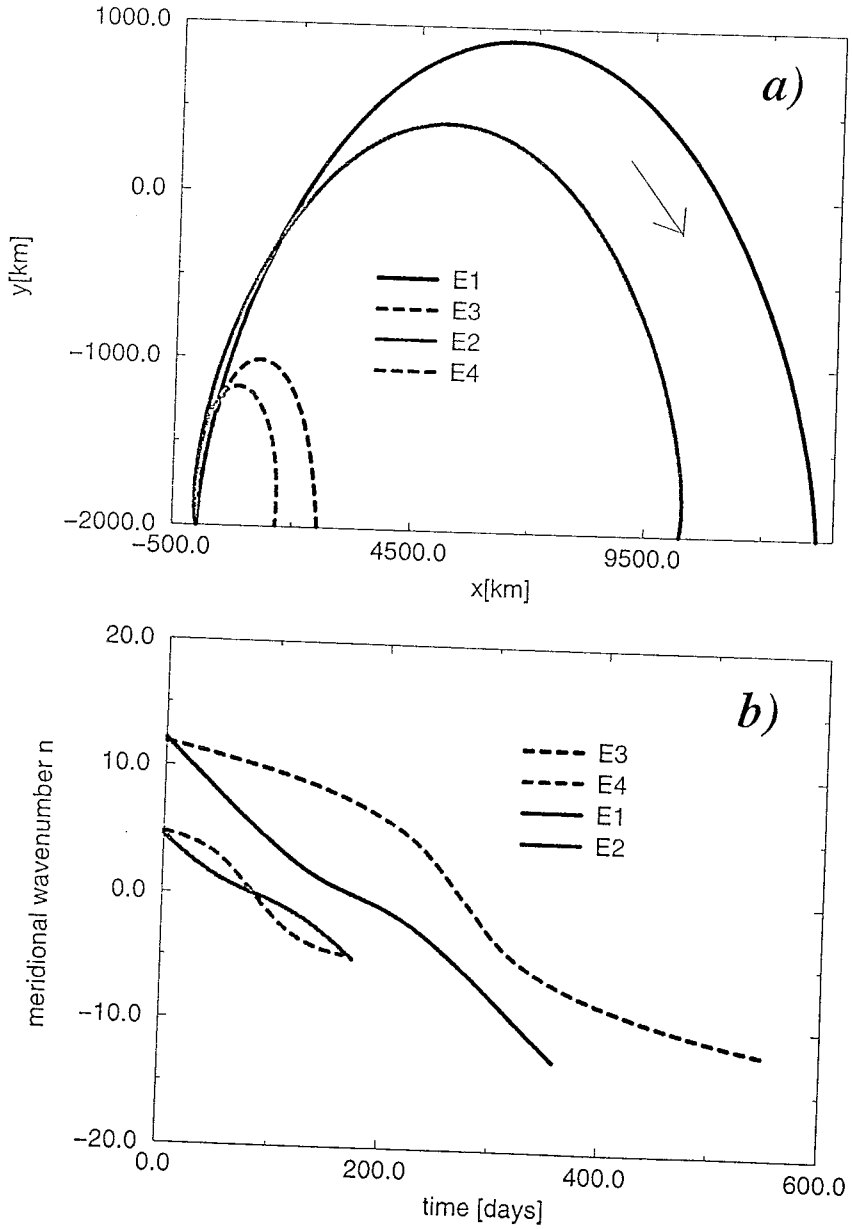

Figure 3: Different paths of Rossby wave packets (a) and corresponding meridional wavenumber evolution (b) between two reflection points (see Tab. 1). Initial positions are $x(0) = 0$, $y(0) = -2000km$. All packets move in clockwise direction (marked by an arrow). The boundary is located at $y = -2000km$.

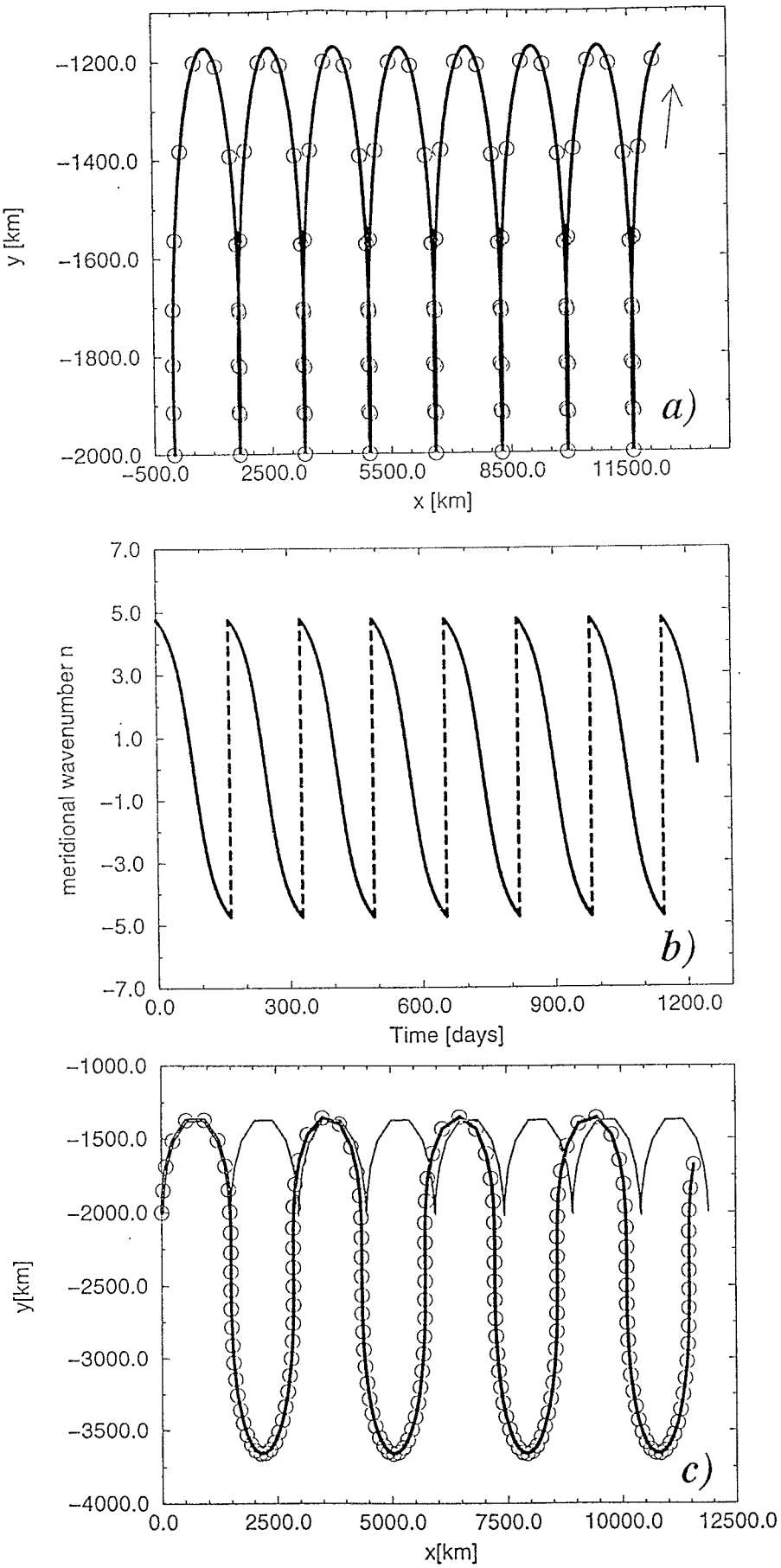

Figure 4: Rossby wave packet path of E4 when 7 reflections occur at $y = -2000km$ (a), corresponding meridional wavenumber evolution (b) and Rossby wave packet path of E5 with the rigid boundary (grey line) and without the rigid boundary (black line) (c). Waves are excited at $x = 0$, $y = -2000km$, circles show 11.5day time intervalls.

A note on the Eady problem with $\beta \neq 0$

Robby Griesche and Werner Metz

Abstract

The Eady problem is modified to allow for a non-zero β parameter but retaining a zero meridional gradient of potential vorticity. Two different basic states are examined for which analytical solutions of the linearized quasi-geostrophic potential vorticity equation were obtained. As has to be expected in addition to the short wave cutoff to instability a non-zero β parameter implies a long wave cutoff, too. In both cases the solutions turn out to converge towards the classical Eady solution if $\beta \rightarrow 0$. It is found that the qualitative structure of the phase speed diagramm and also the qualitative shape of the vertical structure of the unstable solutions turned out to be rather insensitive to the specific settings of the basic state.

Zusammenfassung

Das klassische Eadyproblem wird auf die β-Ebene verlagert, wobei der Grundstrom so modifiziert wird, daß der meridionalen Gradienten der potentiellen Vorticity nach wie vor verschwindet. Zwei verschiedene Grundzustände werden untersucht, für die analytische Lösungen der linearisierten potentiellen Vorticitygleichung erhalten werden konnten. Wie man erwarten konnte, bedingt die Einführung eines von Null verschiedenen β-Parameters das Auftreten einer Langwelleninstabilitätsgrenze zusätzlich zu der Kurzwelleninstabilitätsgrenze des klassischen Problems. In beiden Fällen konnte weiterhin gezeigt werden, daß die Lösungen für $\beta \rightarrow 0$ gegen die klassischen Eadylösungen konvergieren. Ferner stellte sich heraus, daß die qualitative Struktur des Phasengeschwindigkeitsdiagramms und die qualitative Gestalt der Vertikalstruktur der instabilen Lösungen relativ unempfindlich gegenüber der genauen funktionalen Darstellung des Grundzustandes sind.

1. Introduction

Since the classical treatments by Charney (1947) and Eady (1949) baroclinic instability appears to be one of the most extensively studied problems in dynamical meteorology (cf. e.g. Drazin, 1978 and references therein). Only recently, the theme of Eady has been taken up by Lindzen (1994, in the following L94) who investigated the implications of retaining the key feature of Eady's problem, namely a zero gradient of potential vorticity, but modifying the basic state such that a non-zero β-parameter can be accounted for. By assuming the reciprocal of the Brunt-Väisäla frequency to be a linear function of height and adjusting the basic state wind profile accordingly L94 obtained solutions of the modified Eady problem in terms of modified Bessel functions of zero order. Not unexpectedly L94 found that the inclusion of the β-effect adds a long wave cutoff to instability to the classical Eady problem while it does retain the short wave cutoff. Furthermore, it turned out that the real part of the phase speed for the unstable modes exhibits now a dispersive behavior where the longer waves are slowed down towards the speed of the basic state at the lower boundary.

It is the purpose of the present note to extend the work of L94 by re-examining the modified Eady problem for some other basic states for which analytical solutions can still be obtained. In section 2 we recapitulate briefly the basic equations of the modified Eady problem. The different basic states used and the results obtained are presented in section 3. In section 4 a discussion is given and some conclusions are drawn.

2. Basic equations for the modified Eady problem

The governing equation is the linearized quasigeostrophic potential vorticity equation which states the conservation of quasigeostrophic potential vorticity for an adiabatic and frictionless flow. In particular, the Eady problem considers a flow on a mid-latitude β-plane which is confined in the vertical direction between two rigid lids at $z = 0$ and $z = D$, so that D defines the vertical scale of the fluid motion. Also, the vertical variation of density is approximated by an exponential of constant scale height H and it is assumed that $H \gg D$. In dimensionless form the linearized quasigeostrophic potential vorticity equation may be written (cf. e.g. Pedlosky, 1987) as:

$$\left(\frac{\partial}{\partial t}+U\frac{\partial}{\partial x}\right)q'+\frac{\partial \psi}{\partial x}\frac{\partial Q}{\partial y}=0 \tag{1}$$

where $U = U(z)$ is the (dimensionless) zonal basic flow, ψ is the perturbation streamfunction, $z = z_* D$ the dimensionless vertical coordinate and

$$q' = \nabla^2\psi+\frac{\partial}{\partial z}\left(\frac{1}{S}\frac{\partial \psi}{\partial z}\right) \tag{2}$$

is the perturbation potential vorticity and

$$\frac{\partial Q}{\partial y}=\beta-\frac{\partial}{\partial z}\left(\frac{1}{S}\frac{\partial U}{\partial z}\right) \tag{3}$$

is the meridional gradient of the basic state's potential vorticity. In (3), $\beta = \beta_0 L^2/U_0$ is the dimensionless β parameter, L the horizontal length scale, U_0 the velocity scale and $S = N^2D^2/f_0^2L^2$ the dimensionless static stability parameter with N the Brunt-Väisäla frequency. The vanishing of the vertical velocity at the upper and lower rigid lids implies the vertical boundary condition for (1):

$$\left(\frac{\partial}{\partial t}+U\frac{\partial}{\partial x}\right)\frac{\partial \psi}{\partial z}-\frac{\partial \psi}{\partial x}\frac{dU}{dz}=0,\ z=0,1 \tag{4}$$

The basic assumption of the Eady problem is $\partial Q/\partial y=0$ which makes the solution of (1) analytically feasible while retaining $\partial Q/\partial y\neq 0$ implies a dramatic complication of the mathematics (cf. e.g. Green, 1960). In the classical Eady problem $\partial Q/\partial y=0$ is achieved by assuming a constant static stability ($S=const.$), a constant vertical shear of the basic zonal flow ($dU/dz=const.$) and a f-plane geometry ($\beta=0$).

With $\partial Q/\partial y=0$ a separation Ansatz is made for the variable ψ :

$$\psi = \Phi(z)\sin(ly)e^{ik(x-ct)} \tag{5}$$

where Φ is a (complex) amplitude function, k and l are the horizontal wave numbers and $c = c_r + i\, c_i$ is the complex phase speed which plays the role of an eigenvalue of the problem. Note that a solution is called *unstable* if $c_i > 0$. The governing equations (1) and (4) may then be written as:

$$(U-c)\left(\frac{d}{dz}\frac{1}{S}\frac{d\Phi}{dz} - \left(k^2+l^2\right)\Phi\right) = 0, \tag{6}$$

$$(U-c)\frac{d\Phi}{dz} - \Phi\frac{dU}{dz} = 0, \quad z = 0,1 \tag{7}$$

In the following we shall examine some modification based on (6) and (7) of the classical Eady problem where $\partial Q/\partial y=0$ is retained but we shall allow for a β-plane geometry i.e. $\beta\neq 0$.

3. Results

a. Variations of the basic state

To achieve $\partial Q/\partial y=0$ with $\beta\neq 0$ one has to adjust U or S or both in such a way that the rhs of (3) vanishes. Integrating (3) with respect to z gives the required relationship between U and S namely

$$S(z) = \frac{dU}{dz}\Big/(\beta z + \alpha), \tag{8}$$

where $\alpha = U'(0)/S(0)$ is an integration constant. Note that the values of $U'(0)$ and $S(0)$ are not individually fixed but only their ratio α is constant. The following variations are possible:

1. $S=S_0=const.$:

   In this case the solutions to (6) can be expressed in terms of $sinh(\mu z)$ and $cosh(\mu z)$ as in the classical Eady problem where μ is a scaled total wave number ($\mu^2 = (k^2+l^2)\, S_0$). The necessary adjustment of the basic state zonal wind from (8) is:

   $$U(z) = \frac{1}{2}\beta S_0 z^2 + U'(0)z + U(0) \tag{9}$$

2. This means, however, that the boundary conditions (7) and thus the eigenvalues c are different from the classical Eady problem. This variation is discussed below.

3. $U'=m_0=const.$:

   Here, S must be adjusted as $S(z) = S_0/(S_0\beta z/m_0 + 1)$ and as discussed by L94 one can

obtain solutions to (6) in terms of the zero-order Bessel functions I_0 and K_0.

4. $S=S(z)$ and $U=U(z)$:

In this case one can prescribe either $S(z)$ or $U(z)$ and adjust the other according to (8), however, subject to the constraint that one can still find a solution to (6). Such a case has also been considered by L94 with $S(z) = S_0 / (\delta S_0 \beta z / m_0 + 1)$, $\delta<1$ a free parameter and U adjusted accordingly. As this $S(z)$ has the same functional form as that for the case 2 L94 obtained solutions again in terms of the zero-order Bessel functions I_0 and K_0. In the present paper we shall discuss the case $U(z) \sim ln(S_0 \beta z / m_0 + 1)$ which yields $S(z) \sim 1/(S_0 \beta z / m_0 + 1)^2$ so that a solution in terms of Bessel functions is no longer possible.

b. Results for case 1: $S=S_0$=const.

The basic zonal flow equation for the case of a constant static stability is (9) where we specify $U(0) = 0$ and $U(1) = 1$ which yields $U'(0) = 1 - 1/2\ \beta S_0$, thus:

$$U(z) = \frac{B}{2} z^2 + \left(1 - \frac{B}{2}\right) z, \quad B = \beta S_0 . \tag{10}$$

The adjusted $U(z)$ is illustrated in Fig. 1 (open diamonds) for $\beta=1.62$ and $S_0=1/4$. One can see that for these parameters the modification of $U(z)$ produces only a small deviation from the classical problem wind profile (dashed line). As S_0=*const.*, the general solution of (6) is identical to that of the classical Eady problem:

$$\Phi(z) = a\ sinh(\mu z) + b\ cosh(\mu z), \tag{11}$$

where a and b are (in general) complex constants. Inserting (10) and (11) into the boundary conditions (7) yields a homogeneous system of equations for a and b. The phase speed c is then obtained from the condition for non-trivial solutions (i.e. the system determinant must be zero) as:

$$c_{1,2} = \frac{1}{2}\left(1 - \frac{B\ coth\mu}{\mu}\right) \pm \frac{1}{2\mu}\sqrt{\Delta}, \quad \Delta = \mu^2 - 4\mu\ coth\mu + 4 + \left(coth^2\mu - 1\right)B^2 . \tag{12}$$

In (12) the stabilization of long waves ($\mu \ll 1$) due to the β-term is evident. Thus, in addition to the short wave instability limit of the classical Eady problem a long wave instability limit is implied by the β-effect. On the other hand for short waves ($\mu \gg 1$) c in (12) approaches the phase speed for the classical Eady problem. Instability, i.e. a negative discriminante Δ in (12) can only occur if the parameter B is smaller than some a critical value B_{crit}. This B_{crit} can be explicitly obtained by solving the equation $\Delta = 0$ for B where Δ is defined in (12). The dependence of B_{crit} on the scaled wavenumber μ is displayed in Fig. 2a. Note that because $\mu^2 = (k^2+l^2)$ S_0 the displayed B_{crit} must be interpreted as $\beta_{crit}S_0$ for some fixed value of S_0. Not surprisingly,

the short wave instability cutoff in the scaled wavenumber in Fig. 2a is nearly independent of β_{crit} and approaches the classical Eady limit at μ_{crit} = 2.3994 (cf. Pedlosky, 1987) for $\beta \rightarrow 0$. On the other hand, with decreasing β the long wave instability cutoff approaches μ = 0. The maximal β_{crit} for which instability is still possible is $\approx 2/S_0$ which can be achieved only for large horizontal length scales L or small wind scales U_0. An alternative view of the instability cutoff is presented in Fig. 2b where we have plotted $S_{crit}=B_{crit}/\beta$ for some standard value of β as a function of the total wavenumber $K=(k^2+l^2)^{1/2}$. One can recognize that in this display the long wave cutoff due to the β-effect is virtually independent of the stability parameter S_0 while the short wave cutoff depends strongly on stability.

The real and imaginary parts of the phase speeds $c_{1,2}$ according to (12) are displayed in Fig. 3 for some standard values of S_0 and β as a function of the scaled wavenumber μ. It is clear from (12) that due to the β-effect the real part of the phase speed c_r for unstable waves is always less than the value 1/2 of the classical problem and that c_r exhibits now a dispersive behavior. The steering level of the unstable waves lies always in the lower half of the fluid and approaches $U(0)$ for long waves. For short neutral waves $c_{r(1,2)} \rightarrow \pm 1$ for $\mu \rightarrow \infty$ as in the classical problem, however, for long neutral waves one branch of c_r behaves somewhat peculiar in that it approaches -∞ as $\mu \rightarrow 0$. Please note, however, that the structure of Fig. 3 agrees qualitatively with the results obtained by L94 for his different basic state.

It is well known that the structure of the solutions of the Eady problem is entirely determined by the boundary conditions (7). In particular, the boundary conditions force the solutions to attain their maximal amplitude at the boundaries. In the classical Eady problem these extrema are equal while the inclusion of the β-effect allows now for a vertical asymmetry of the wave solutions. This will become immediately clear if one looks at the necessary condition for instability (cf. e.g. Pedlosky, 1987) which using (6) and (7) may be written as

$$\frac{|\Phi_1|^2}{|\Phi_0|^2} = \frac{U'(0)}{S(0)} \frac{S(1)}{U'(1)} \frac{|1-c|^2}{|c|^2} = \frac{1}{1+\beta S(0)/U'(0)} \frac{|1-c|^2}{|c|^2}, \qquad (13)$$

where the last equality comes from (8). As β, $S(0)$ and $U'(0)$ are all positive, the first factor on the rhs of (13) tends to cause a larger amplitude at the lower boundary. However, as $c_r<1/2$ due to the β-term the phase speed factor tends to counteract this behavior by increasing the wave amplitude at the upper boundary. From the structure of the phase speed diagram (Fig. 3) one can see that the latter effect is particularly pronounced for the longer waves. The ratio $|\Phi_1|/|\Phi_0|$ is displayed in Fig. 4 for three different stability factors S_0. One can see that this ratio is always greater than one and for small wavenumbers μ near the longwave cutoff the amplitude of the unstable waves at the upper boundary can exceed four times the amplitude at the lower boundary. The ratio generally increases with increasing stability S_0. Finally, the description of the vertical structure of the unstable waves is completed by the phase function $arg(\Phi)$ (not shown) which -similar to the classical Eady solution - increases monotonically with height consistent with an westward vertical tilt of the wave solutions.

c. Solution to case 3: Prescribed zonal wind profile

In this variation we prescribe the basic state zonal wind and adjust the static stability accordingly. In particular, we consider a wind profile:

$$U(z)=\frac{ln(\tilde{B}z+1)}{ln(\tilde{B}+1)},\quad \tilde{B}=\frac{\beta}{\alpha}, \tag{14}$$

where again we choose $U(0)=0$ and $U(1)=1$. This profile is also displayed in Fig.1 (open circles) and it can be seen that $U(z)$ is now concave with respect to height. From (8) the associated profile of the stability parameter is:

$$S(z)=\frac{\tilde{B}}{\alpha(\tilde{B}z+1)^2\,ln(\tilde{B}+1)}. \tag{15}$$

Some profiles S(z) according to (15) for different values of $\tilde{B}$ are illustrated in Fig. 5. One can recognize that increasing $\tilde{B}$, i.e. decreasing the integration constant α in (8) has the effect of increasing the static stability at the lower boundary and decreasing it at the upper. As this behavior near the lower boundary is somewhat unrealistic, but not unexpected (recall that there is no boundary layer in the problem), physically reasonable results can be expected only for relatively small values of $\tilde{B}$.

As the factor $1/S$ in the governing DGL (6) is now a quadratic function in z, important consequences for the solutions of (6) are implied. In particular, one can show that a solution in terms of zero-order Besselfunctions as in the problem considered by L94 is not possible. Instead, we may find a solution of (6) in terms of a general power-Ansatz (Griesche, 1996)

For that purpose we first assume:

$$\Phi(z)=\frac{d}{dz}A(z) \tag{16}$$

and integrate (6) once with respect to z using (16). Ignoring an integration constant which is irrelevant for the solution of our problem one obtains the following homogeneous DGL for $A(z)$:

$$\frac{d^2}{dz^2}A(z)-\frac{\tilde{B}(k^2+l^2)}{\alpha(\tilde{B}z+1)^2\,ln(\tilde{B}+1)}A(z)=0. \tag{17}$$

Defining a new scaled wavenumber via

$$\tilde{\mu}^2=\frac{k^2+l^2}{\alpha}=(k^2+l^2)\frac{S(0)}{U'(0)}, \tag{18}$$

the general power Ansatz for $A(z)$

$$A(z) = (\tilde{B}z + 1)^{\rho} \tag{19}$$

transforms the governing DGL (17) into a quadratic equation in the unknown exponent ρ:

$$\rho(\rho - 1) - \frac{\tilde{\mu}^2}{\tilde{B}\, ln(\tilde{B} + 1)} = 0. \tag{20}$$

Thus, the general solution of (17) can be written as:

$$A(z) = a(\tilde{B}z + 1)^{\rho_1} + b(\tilde{B}z + 1)^{\rho_2} \tag{21}$$

where ρ_1 and ρ_2 are the two (real) roots of (20) and a and b are unknown constants. The dispersion relation for the phase speed c is then obtained in a straightforward but clumsy manner by inserting (21), (16), (15) and (14) into the boundary conditions (7) and requiring that the determinante of the resulting homogeneous system for a and b be zero. After some algebra one gets:

$$\begin{aligned} c_{1,2} &= \frac{1}{2}\left(1 - \frac{\tilde{B}}{\tilde{\mu}^2}\right) \pm \frac{1}{2\tilde{\mu}^2}\sqrt{\Delta}, \\ \Delta &= (\tilde{B} - \tilde{\mu}^2)^2 - \tilde{B}(\tilde{B}(1 - W^2) - 2\tilde{\mu}^2 + 2\frac{W\tilde{\mu}^2((\tilde{B}+1)^W + 1)}{(\tilde{B}+1)^W - 1}, \\ W &= \sqrt{1 + 4\tilde{\mu}^2 / \tilde{B}\, ln(\tilde{B} + 1)}. \end{aligned} \tag{22}$$

First, we would like to remark that using l'Hospital's rule one can show that (22) approaches the classical formula as $\tilde{B} \to 0$. Furthermore, also in this variation the real part of the phase speed for unstable solutions ($\Delta<0$) is always less than 1/2 and exhibits a dispersive behavior. The phase speed diagram $c(\tilde{\mu})$ according to (22) (not shown) turns out to be qualitatively similar to that obtained above for a constant static stability (Fig. 3) and also to that obtained by L94. In particular, also in this case short and long wave cutoffs to instability exist and the variation of these cutoffs with the parameter $\tilde{B}$ is illustrated in Fig. 6 where we display $c_i(\tilde{\mu})$ for different values of $\tilde{B}$. One can see that in this case an increasing $\tilde{B}$ has the effect to move the short wave cutoff to higher scaled wavenumbers $\tilde{\mu}$ while with decreasing $\tilde{B}$ the cutoff approaches the classical value of 2.3994. Although $\Delta = 0$ in (22) can't be solved explicitly for $\tilde{B}$ a numerical solution is still possible and we have verified that until very high (and physically very unrealistically) values of $\tilde{B}$ the equation $\Delta = 0$ from (22) has always two real roots. This means, that unlike in the previous case we were not able to find a limiting value of $\tilde{B}$ which inhibits instability. Instead, the region of instability is merely shifted towards higher values of $\tilde{\mu}$.

For reasonable values of $\tilde{B}$ the vertical structure of the unstable solutions turns out to be similar to that of the previous case. With respect to the ratio of the amplitudes of the solutions at the upper and the lower boundary still (13) applies. This ratio is illustrated in Fig. 7 for three different values of $\tilde{B}$. One can recognize that in this case the ratio is generally smaller than in

the previous case with S=const. and that it decreases with increasing $\tilde{B}$. Furthermore, for high values of $\tilde{B}$ and sufficiently short waves the ratio can become < 1 so that the unstable waves attain their maximal amplitude at the lower boundary.

4. Summary

We have modified the classical Eady problem and used two different basic states that retain a zero meridional gradient of potential vorticity in the presence of a non-zero β-term. In particular, the one basic state (case 1) had S=const. and an adjusted basic zonal wind, while for the other basic state (case 3) we prescribed $U(z)$ with a logarithmic height profile and accordingly adjusted $S(z)$. The solutions to the basic state case 1 were particularly simple and equal to the classical Eady solutions. However, due to the implied change in $U(z)$ the boundary conditions and thus the phase speed equation were different from the classical solution. In the other case 3 basic state the functional form of the changed $S(z)$ suggested a solution in terms of a general power-Ansatz. In both cases, as has to be expected, the non-zero β-parameter implied a long wave cutoff to instability in addition to the short wave cutoff of the classical problem. Furthermore, for both cases the solutions converged towards the classical Eady solution if $\beta \to 0$. It was also found that the qualitative structure of the phase speed diagram the qualitative shape of the vertical structure of the unstable solutions were similar for both solutions. This suggests the modified Eady problem to be rather insensitive to the specific settings of the basic state.

References

Charney, J.G., 1947: The dynamics of long waves in a baroclinic westerly current. *J. Meteor.*, **4**, 135-163.

Drazin, P.G., 1978: Variations on a theme of Eady. In: Rotating Fluids in Geophysics. P.H. Roberts and A.M. Soward, Eds., Academic Press, 139-169.

Eady, E.T., 1949: Long waves and cyclone waves. *Tellus*, **1**, 33-52.

Green, J.S.A., 1960: A problem in baroclinic instability. *Quart. J. Roy. Met. Soc.*, **86**, 237-251.

Griesche, R., 1996: Einige Variationen zum Problem der klassischen baroklinen Instabilität. Diploma thesis, University of Leipzig, Faculty of Mathematics and Informatics, 35 pp., reprint available from the author.

Lindzen, R.S., 1994: The Eady problem for a basic state with zero PV gradient but $\beta \neq 0$. *J. Atmos. Sci.*, **51**, 3221-3226.

Pedlosky, J., 1987: Geophysical fluid dynamics. *Springer-Verlag*, New York. 710pp.

Werner Metz
Institut für Meteorologie
Stephanstr. 3
D-04103 Leipzig

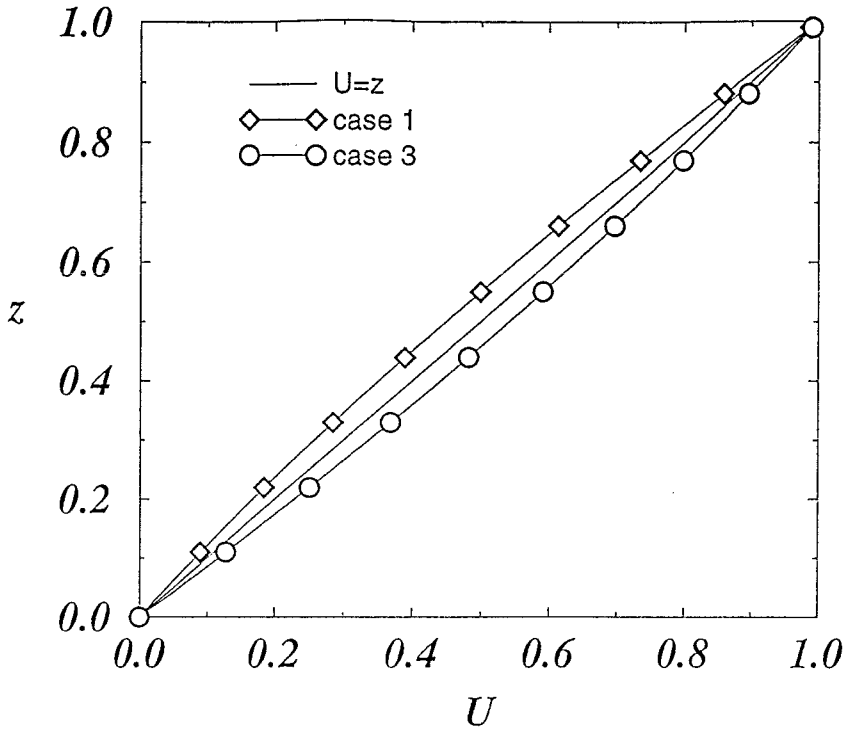

Figure 1: Vertical profiles of the dimensionless basic state zonal wind for the modified Eady problem, case 1 (open diamonds) and case 3 (open circles). The classical Eady profile is indicated by the thin line.

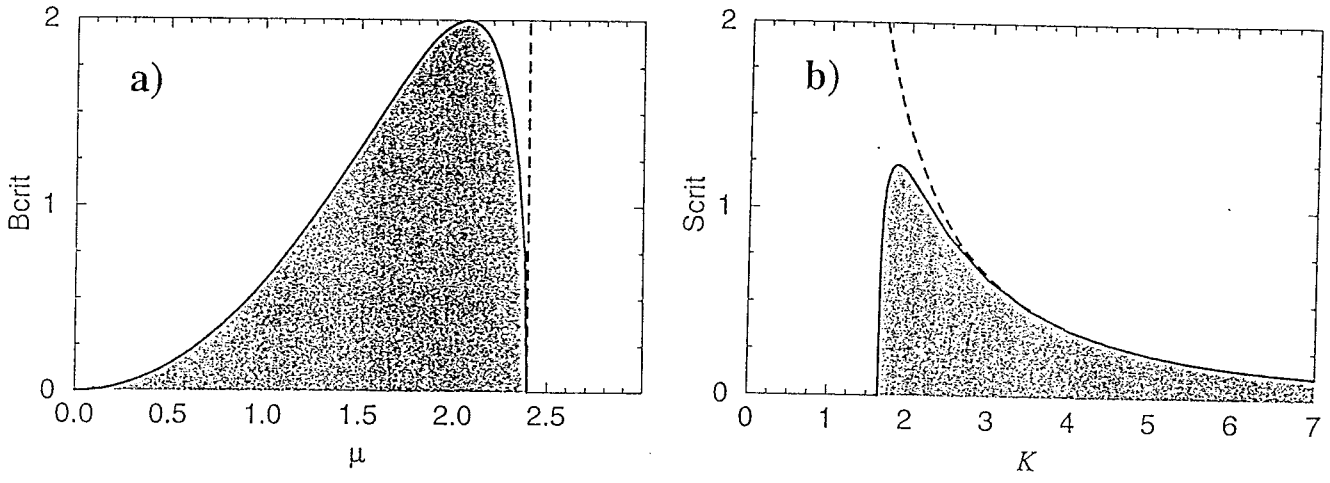

Figure 2: Instability cutoff for the modified Eady problem, case1. a) Parameter $B_{crit}=\beta_{crit}S_0$ as a function of the scaled wavenumber μ. The region of possible instability is shaded. The dashed curves denotes the constant short wave cutoff for the classical Eady problem. b) Parameter $S_{crit}=B_{crit}/\beta$ as a function of the two dimensional wavenumber $K=(k^2+l^2)^{1/2}$. Instability region shaded. The dashed curves denotes the constant short wave cutoff for the classical Eady problem.

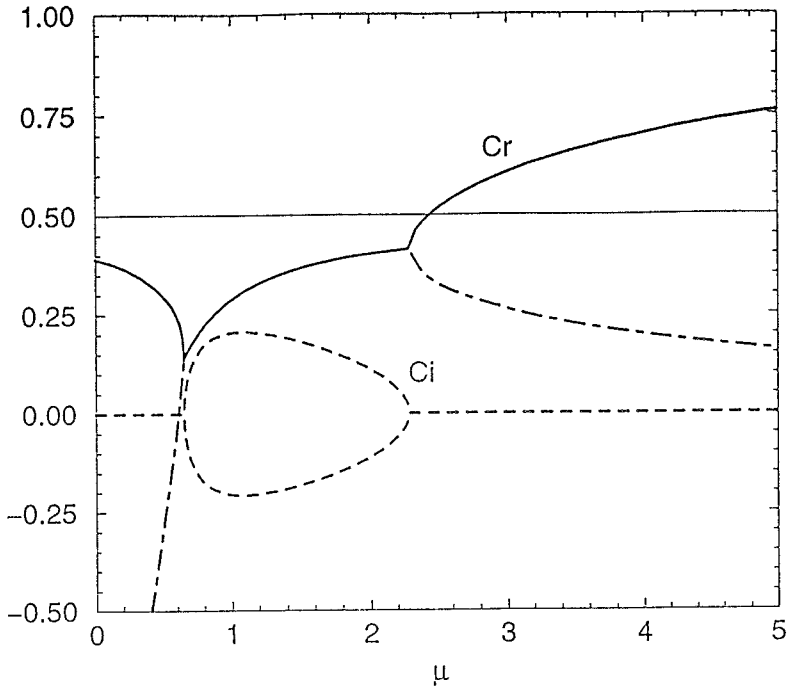

Figure 3: Phase speed diagram for the modified Eady problem, case1. Shown are the real (Cr, full and dash-dotted lines) and imaginary (Ci, dashed lines) parts for both modes of c.

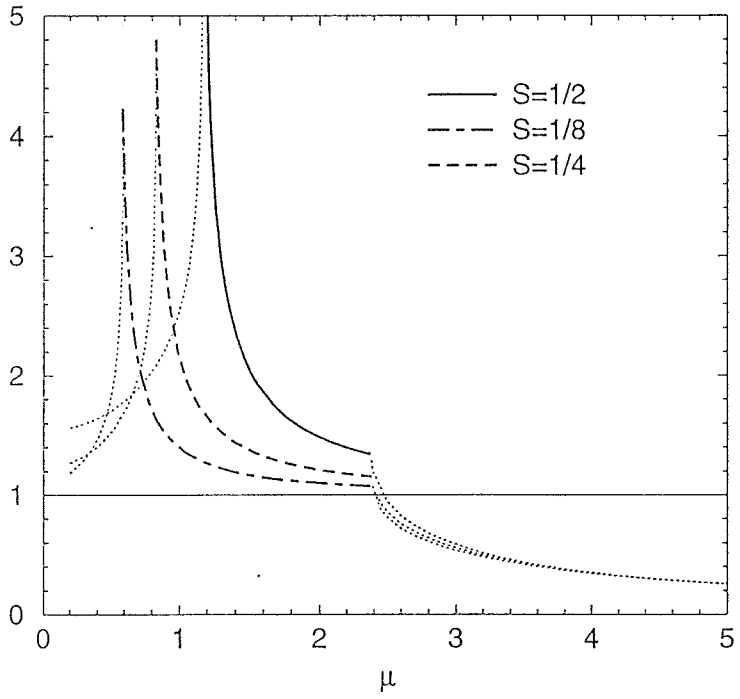

Figure 4: The ratio of the streamfunction amplitudes of the $|\Phi_1|/|\Phi_0|$ according to (13) for the modified Eady problem, case 1. The curves displayed are relevant only in the unstable regions (thick lines). Shown the ratios for S_0=1/8 (dash-dotted), S_0=1/4 (dashed) and S_0=1/2 (full).

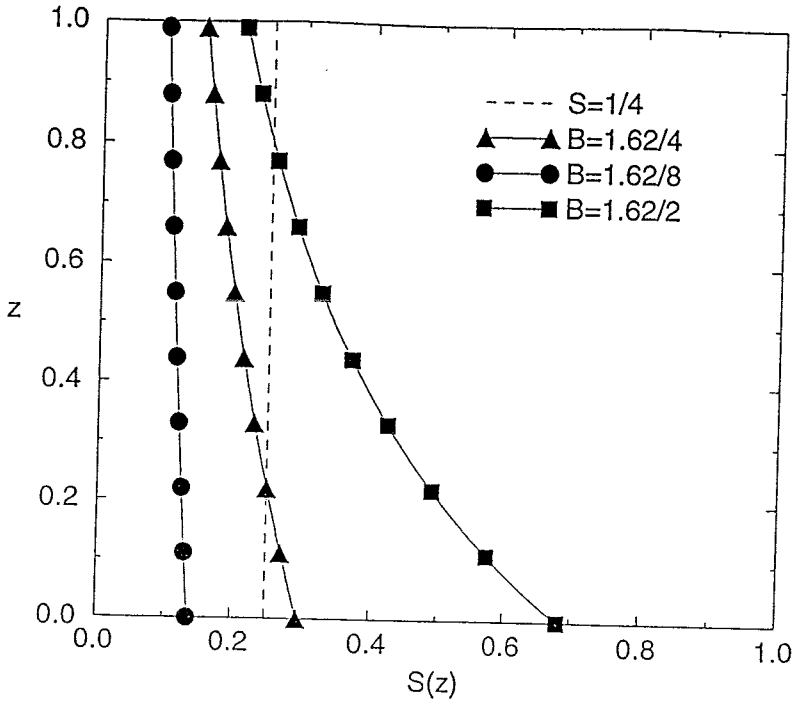

Figure 5: Vertical profiles of the static stability parameter $S(z)$ for the modified Eady problem, case 3, according to (15). Shown are the profiles for $\widetilde{B}$ = 1.62/8 (full circles), $\widetilde{B}$ = 1.62/4 (full triangles) and $\widetilde{B}$ = 1.62/2 (full squares). The thin dashed line represents $S(z)$ = 1/4.

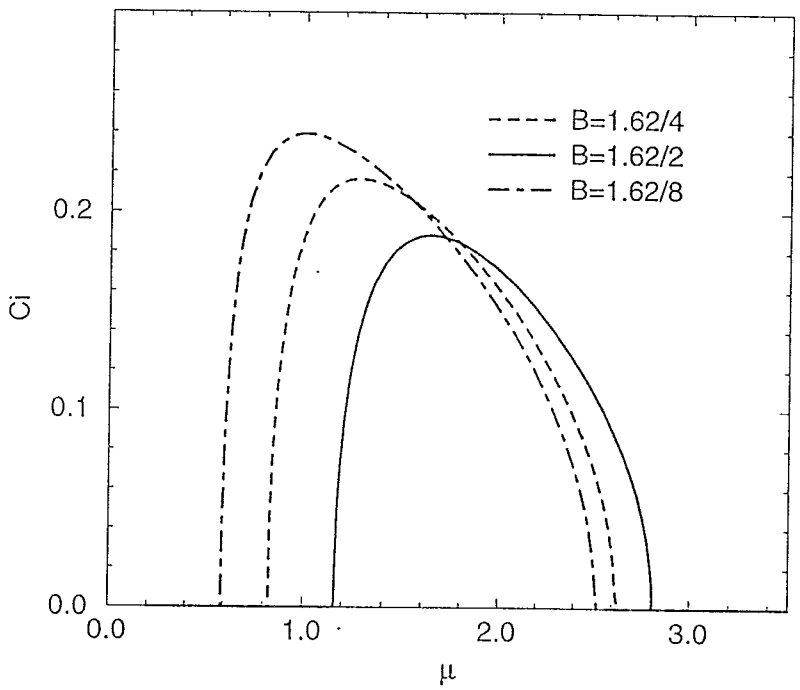

Figure 6: The imaginary part c_i of the phase speed c for the modified Eady problem, case 3, according to (22). Shown is only the growing mode for $\widetilde{B}$ = 1.62/8 (dash-dotted), $\widetilde{B}$ = 1.62/4 (dashed) and $\widetilde{B}$ = 1.62/2 (full).

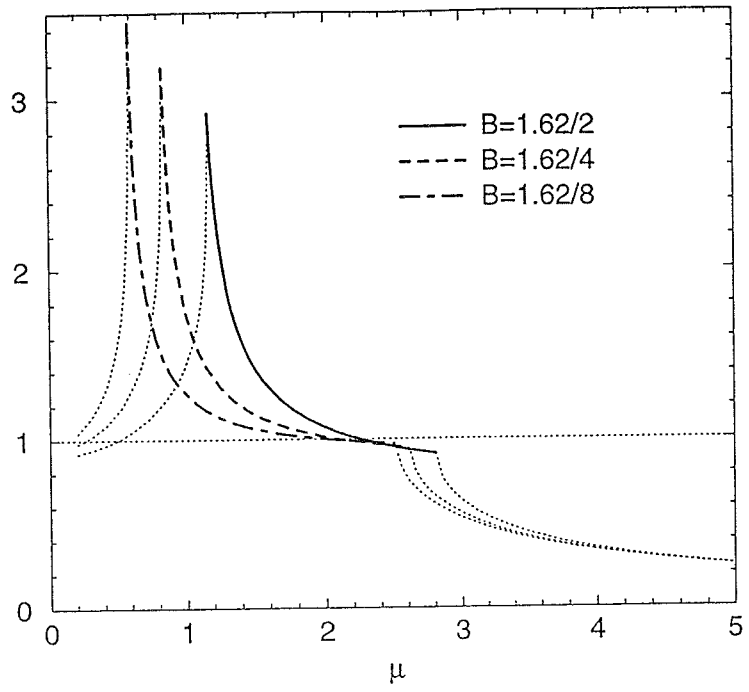

Figure 7: As Fig. 4 but for case 3 of the modified Eady problem. Shown are the ratios for $\widetilde{B}$ = 1.62/8 (dash-dotted), $\widetilde{B}$ = 1.62/4 (dashed) and $\widetilde{B}$ = 1.62/2 (full).